



Numerical analysis of broken regular wave forces on a shoal-mounted cylinder

J.J.L. van Gorsel

Numerical analysis of broken regular wave forces on a shoal-mounted cylinder

by

J.J.L. van Gorsel

Department of Hydraulic Engineering
Section: Coastal Engineering

in partial fulfilment of the requirements for the degree of

Master of Science
in Civil Engineering

at the Delft University of Technology,
to be defended publicly on 28 May 2021, at 15:00.

Committee Chair:	Dr. ir. A. Antonini	TU Delft
Committee members:	Dr. ir. J.D. Bricker,	TU Delft
	Ir. S.G. Pearson,	TU Delft/Deltares
	Ir. A.L. Patil	Stanford University

An electronic version of this thesis is available at <http://repository.tudelft.nl/>.



Reference: front cover by Rivrin (2016).

Acknowledgements

This report concludes the final stage of my master's degree in Hydraulic Engineering at the Delft University of Technology. Conducting the research and summarizing everything in this report has been one of the largest challenges I encountered so far. During this period, I learned a lot of lessons and gained a lot of experience that allowed me to grow in both a professional and personal level. I would like to thank everyone that supported me in any way during this period.

Firstly, I would like to thank the members of my graduation committee who helped and supported me during this period. Dr. ir. A. Antonini, thank you for introducing me to this wonderful topic and for supervising me. Thanks for always having the time to discuss any difficulties I ran into. Dr. ir. Jeremy Bricker, thank you for your input and insights during the progress meetings. Ir. Stuart Pearson, thank you for the positive energy and support on both an academic and personal level. Ir. Akshay Patil, thank you for our late night CFD talks and helping me to get to know OpenFOAM. Without your help I would not have been able to develop the model. Next, I would also like to thank Christian, Mieke and Nikola for giving me comments and feedback on the report.

I would like to thank the Environmental Fluid Mechanics section for allowing me to use the HCP cluster for my simulations. I would also like to express my thanks for the computing time on SHERLOCK at Stanford University.

Furthermore, I want to thank my friends and fellow classmates for making this period less lonely. Finally, I would like to thank my parents and stepparents for their unconditional support during my studies and always being there for me.

Jan van Gorsel

Delft, May 2021

Abstract

Lighthouses have guided seafarers for centuries and still play an essential role in navigating marine vessels and bringing them to safe harbours. With climate change, the already harsh ocean environment may become more severe. It is expected that future wave conditions can compromise the structural integrity of the lighthouses with their violent impact. The hydrodynamic processes of wave transition before, at, and after the point of impact are complex, highly non-linear, and turbulent. There is no exact description of these processes. Therefore, there is a need to further study them in order to better understand the broken wave load and its effect on the structural integrity of lighthouses.

From the very beginning, wave breaking processes are complex. For instance, prior to impact with shoal-mounted cylindrical structures, waves undergo a rapid transition from deep to shallow water. During this transition the waves shoal, start to break, and once broken they hit the cylindrical structure of the lighthouse. It is therefore necessary to approximate the hydrodynamics. Since, it is difficult to measure the processes using only physical models. Consequently, this research focuses on broken wave load analysis using a process-based numerical model.

An approach widely used for analysing wave forces on slender cylindrical structures is calibrated for breaking wave loads. Critical factors for determining these loads are the curling factor and slamming coefficient. However, there is still no scientific consensus regarding the exact values for these parameters. Further research, like this study, can help in determining these values.

The main goal of this thesis is to assess the pressure distribution on the structure and quantify the values for the curling factor and slamming coefficient for a shoal-mounted slender cylindrical structure. The STORMLAMP (STructural behaviour Of Rock Mounted Lighthouses At the Mercy of imPulsive waves) project's experimental data of Dassanayake et al. (2019) is used as a benchmark case to validate the proposed computational framework. In addition, the performance of two different Volume of Fluid methods, isoAdvector and MULES, are assessed.

This study demonstrates that the curling factor and slamming coefficient are significantly different for the broken wave load compared to the breaking wave load. The curling factor is found to be twice as large in the case of a broken wave load. On the other hand, the peak slamming coefficient is five times smaller. Moreover, the isoAdvector solver in comparison to the MULES solver produces results that better resemble the benchmark case results. Although the two solvers do not produce the same peak impact forces, they do both produce similar values for the aforementioned critical parameters. Also, it was found that the isoAdvector solver is faster and more efficient than the MULES solver in the case of a 3D simulation.

From the results it can be concluded that the chosen numerical framework represents the benchmark case well, and that the methodology used for breaking wave loads can be applied for broken wave loads with adjustment of the curling factor and slamming coefficient.

KEY WORDS

OpenFOAM, STORMLAMP, broken wave load, isoAdvector, MULES

Table of Contents

1	Introduction.....	1
1.1	Background.....	1
1.2	Problem statement.....	2
1.3	Goal and objectives.....	3
1.4	Outline.....	3
2	Methodology.....	4
2.1	Force characteristics.....	5
2.2	Benchmark case.....	6
2.2.1	Wave conditions.....	7
2.3	Numerical framework.....	7
2.3.1	Key parameters.....	8
2.3.2	Boundary and initial conditions.....	8
2.3.3	Numerical schemes and solvers.....	9
2.3.4	isoAdvectord.....	10
2.3.5	Turbulence.....	11
2.3.6	Numerical wave tank.....	11
2.3.7	Mesh.....	12
2.3.8	Measurement locations.....	14
2.4	2D Model validation.....	14
2.4.1	Alignment of data.....	15
2.4.2	Data processing.....	15
2.5	3D Model validation.....	17
2.5.1	Water level elevation.....	17
2.5.2	Ensemble average force signal.....	17
2.5.3	Single peak analysis.....	17
2.5.4	Rising time and force of peak.....	18
2.6	Calibration of coefficients.....	18
2.6.1	Pressure distribution on the cylinder.....	18
2.6.2	Curling factor and slamming coefficient.....	20
2.7	Computation cost.....	21
3	Results.....	22
3.1	2D Model validation.....	22
3.2	Wave states.....	27
3.3	3D Model validation.....	28
3.3.1	Water level elevation.....	29

3.3.2	Force comparison.....	29
3.4	Calibration of coefficients.....	33
3.4.1	Pressure distribution.....	34
3.4.2	Curling factor and slamming coefficient	37
3.5	Computational cost.....	40
3.5.1	2D simulation.....	40
3.5.2	3D simulation.....	40
4	Discussion	42
5	Conclusions and recommendations	44
5.1	Conclusions	44
5.2	Recommendations.....	45
	Bibliography	46
	Appendices.....	50

Symbols & Abbreviations

Abbreviations

CFD: Computational Fluid Dynamics

CPWH: Cells Per Wave Height

CRMSE: Centred Root Mean Square Error

DILU: Diagonal-based Incomplete LU

FFT: Fast Fourier Transform

GAMG: Generalised Geometric-Algebraic Multi Grid

MULES: Multidimensional Universal Limiter for Explicit Solution

MUSCL: Monotone Upstream-centered Schemes for Conservation Laws

NWT: Numerical Wave Tank

OCW3D: OceanWave3D

OpenFOAM: Open Field Operation And Manipulation

PCC: Pearson Correlation Coefficient

PIMPLE: Pressure-Implicit Method for Pressure-Linked Equations

PISO: Pressure Implicit with Splitting of Operators

PoA: Point of Application

SD: Standard Deviation

SFCD: Self-Filtered Central Differencing

SIMPLE: Semi-Implicit Method for Pressure-Linked Equations

STORMLAMP: SStructural behaviour Of Rock Mounted Lighthouses At the Mercy of imPulsive waves

SWL: Still Water level

TKE: Turbulent Kinetic Energy

VOF: Volume of Fluid

Relevant terms

Computational costs: The effort needed to run the numerical framework and generate results. Can be described in the time needed for the whole simulation or the time needed per time step.

Curling factor: An empirical factor for the part of the breaking wave water level elevation that impacts on the structure (λ).

Ensemble average: an average of several signals for which the datapoints at $t=0$, $t=1$, ..., $t=n$ are averaged.

isoAdvector: A geometric Volume of Fluids method. One of the two methods used in the numerical framework.

MULES: An algebraic Volume of Fluids method. One of the two methods used in the numerical framework.

Numerical experiment(s): The experiments done using the numerical framework.

Numerical framework: the collection equations and programming that is used to set-up of the numerical wave tank.

OceanWave3D: A robust model for non-linear wave problems. In this study used to generate the boundary conditions.

OpenFOAM: The open-source software used to model the numerical wave tank.

Laboratory experiments: The experiments done in real life in a physical wave flume.

Point of application: The centroid of the pressure.

Relaxation zone: A zone in the numerical wave tank where the reflected waves are filtered out and the solution forced to the supplied boundary conditions.

Slamming coefficient: An empirical factor used in the formula for the peak impact force.

STORMLAMP: A research project that assesses the structural performance of offshore lighthouses and characterises the wave loading on those structures (“STORMLAMP,” n.d.).

Wavse2Foam toolbox: a OpenFOAM toolbox that can be used to create the numerical wave tank.

List of Symbols

Symbol	Description	Unit
$\langle F_T \rangle_E$	Ensemble average of the total force	[N]
$\langle P \rangle_E$	Ensemble average pressure	[N/m ²]
h_0	Water depth	[m]
C_D	Drag coefficient	[-]
C_M	Inertia coefficient	[-]
C_S	Slamming coefficient	[-]
F_D	Drag force	[N]
F_I	Impact force	[N]
F_M	Inertia force	[N]
$F_{T,p}$	Peak total force	[N]
F_T	Total force	[N]
F_{max}	Maximum force in the signal	[N]
H_{mean}	Mean wave height	[-]

S_x	Standard deviation of x	[–]
$T_{T,p,r}$	Rising time of the force signal	[s]
f_I	In-line impact force	[N/m]
s_I	Height of the impact	[m]
u_*	Friction velocity	[m/s]
\tilde{x}	Median value of x	[–]
\bar{x}	Mean value of x	[–]
y^+	Dimensionless wall distance	[–]
y_a	Locations on the cylinder where the pressure is above a set limit	[m]
$y_{i,OF}$	Value computed by OpenFOAM	[–]
$y_{i,e}$	Value measured in the experiment	[–]
$\eta_{b,WG11}$	Water level elevation at wave gauge 11	[m]
η_b	Water level elevation of the breaking wave	[m]
λ_1	Stress limiting coefficient	[–]
λ_2	Stress limiting coefficient	[–]
μ_{OF}	Mean value of the OpenFOAM time series	[–]
μ_e	Mean value of the experiment time series	[–]
ν_t	Turbulent viscosity	[m ² /s]
σ_{x_i}	Variance	[–]
C	Wave celerity	[m/s]
D	Pile diameter	[m]
F	Force	[N]
H	Wave height	[m]
L	Wavelength	[m]
N	Total number of datapoints	[–]
P	Pressure	[N/m ²]
R	Radius of the cylinder	[m]
T	Wave period	[s]
U	Velocity	[m/s]
a	Amplitude	[m]

d	Water depth	[m]
f	Frequency	[Hz]
g	Gravity	[m/s^2]
k	Turbulent kinetic energy	[m^2/s]
p	Pressure	[N/m^2]
t	Time	[s]
u	Water velocity	[m/s]
y	Distance to the nearest wall	[m]
α	Phase of the cell during the simulation	[$-$]
η	Water surface elevation,	[m]
λ	Curling factor	[$-$]
ν	Kinematic viscosity	[m^2/s]
ρ	Density of water	[kg/m^3]
ω	Turbulence specific dissipation rate	[$1/s$]

1 Introduction

1.1 Background

Lighthouses have played a vital role throughout history in safe navigation and maritime transport, and thus have a direct impact on the economy. With time, these structures age and continue to be affected by the harsh ocean environment (e.g. high ocean waves (Wang et al., 2004) and increasing sea level rise (Kulp and Strauss, 2019)). This is especially the case for offshore lighthouses, which are built on shallow outcrops and rocky platforms in the middle of the ocean. As part of the STORMLAMP (STructural behaviour Of Rock Mounted Lighthouses At the Mercy of imPulsive waves) project Antonini et. al. (2019) and Raby et al. (2019) note that it is necessary to assess the structural integrity of these aging lighthouses. Overall, there is a need to further understand the complex hydrodynamic processes that occur just before, during and after breaking of waves near and against an offshore lighthouse.

An example of such a lighthouse is La Jument lighthouse in France, located 2 kilometres from the closest island and 26 kilometres from the mainland (Figure 1-1). As it can be seen from the figure, the impact of breaking waves on an offshore lighthouse can be immense. Another example is the Wolf Rock lighthouse, located 13 kilometres from the British mainland. Both lighthouses are over 40 metres tall and have been vital components of marine infrastructure for more than a hundred years.

A numerical framework can be used to assess the impact of the waves on such lighthouses. The main question is how the impact load of the broken wave force can be quantified and how the pressure is distributed on the lighthouse. This information is necessary to perform assessments of structural safety.



Figure 1-1 Waves breaking against La Jument lighthouse on the French coast (Image: Mathieu Rivrin/Solent News (2016))

1.2 Problem statement

Von Karman (1929) and Wagner (1932) were the first ones to describe the impact of water onto a slender cylindrical structure and the theory behind it. The theory for the in-line force on a cylinder contains the (peak) slamming coefficient (C_s). This coefficient describes the contribution of the unknown processes that influence the impact of water into a structure. The values found for this coefficient vary from π to 2π by Van Karman and Wagner, respectively. The difference can be explained by the fact that Wagner included the pile up effect of the water against the cylinder. The pile-up effect leads to an earlier immersion of the structure, which leads to a shorter duration of the impact and thus an increase in the maximum force. Von Karman did not include this and therefore found a lower value for the slamming coefficient. With extensive laboratory experiments, Wienke and Oumeraci (2005) verified a value of 2π for the slamming coefficient, but also note that the value is not constant but varies in time as the wave passes the structure and the force on the structure weakens. As a continuation on that, Veic and Sulisz (2018) note that the value not only varies in time, but also along the height of the cylinder.

Later, Goda et al. (1966) expanded the equation to include the height of the impact ($\lambda * \eta_b$). This allows for the calculation of the force of waves on piles. The height of the impact is the height over which the wave impacts the structure. This value is dependent on the curling factor (λ) and the water level elevation of the breaking wave (η_b). The curling factor describes the contribution of the wave crest to the area of impact of the total impact force. There is no agreement on the value for the curling factor, with values in the range of 0.14 to 0.67 for a flat seabed and a vertical cylinder (Arntsen et al., 2013; Goda et al., 1966; Veic and Sulisz, 2018; Wienke and Oumeraci, 2005). While for a mildly sloping bed of 1:10, Irschik et al. (2005) and Veic and Sulisz (2018) note values between 0.40 and 0.65.

Ghadirian et al. (2016) did both laboratory and numerical experiments to compute the in-line force on a cylinder placed on a flat seabed using a focused wave group. It was found that the troughs of the waves were marginally but consistently overpredicted by the model. Next, they also state that the numerical results sometimes underpredict the peak force for the waves preceding the main wave in the focused wave group. No information is given about the curling factor and the slamming coefficient. For both steep slopes and broken waves, no information is known about the curling factor and the slamming coefficient and thus remains a key knowledge gap in assessing the wave load on a shoal mounted cylindrical structure.

Most numerical research into breaking wave forces utilises the algebraic MULES (Multidimensional Universal Limiter for Explicit Solution) (Deshpande et al., 2012; Weller, 2008) to compute the interface. With the development of the geometric isoAdvector method by Roenby et al. (2016) a new, more accurate method is available. This approach is specially developed to improve the analysis of wave-structure interaction and wave loads on coastal and marine structures. The method produces a sharp and smooth interface which is needed to accurately compute the impact of the wave on the structure (Roenby et al., 2017). Furthermore, recent research of Larsen and Fuhrman (2018) indicates that most turbulence models overestimate the turbulence produced. They show that by adjusting the closure models this overestimation can be removed. Therefore, they proposed a new formulation for the $k - \omega$ closure models that elegantly stabilises the model in nearly potential flow regions. This results in a better approximation of the turbulence levels and less wave decay than exhibited by the standard closure models. Further validations of this closure model were carried out by Patil (2019).

Dassanayake et al. (2019) carried out laboratory experiments to assess the impact and runup on a slender cylinder located on a shoal with a relatively steep slope. To the author's knowledge, no numerical study has been carried out which assesses the pressure distribution, curling factor and slamming coefficient for such conditions. This represents a key research gap in our understanding of wave impact on lighthouses. The study of Dassanayake et al. (2019) provides a valuable reference on which to base such a numerical assessment.

1.3 Goal and objectives

The main goal of this thesis is to assess the pressure distribution on the structure and quantify the values for the curling factor and slamming coefficient for a shoal-mounted slender cylindrical structure.

The main objectives of this research are:

1. To validate the numerical framework using a benchmark case by Dassanayake et al. (2019).
2. To evaluate the effectiveness of the proven methods for breaking wave loads and to quantify the curling factor and slamming coefficient in the case of broken wave loads.
3. To assess the performance and results of the MULES and isoAdvectord methods.

By quantifying the curling factor and slamming coefficient, the impact force on such a structure can be quantified; hence the structural integrity of these structures located on rocky shoals can be further assessed and evaluated. Comparing the results computed by the isoAdvectord and MULES solvers will clarify which solver is more accurate in representing the benchmark case. This will lead to more accurate and efficient estimates of wave impacts, which is essential given the high computational load and numerical complexity of these simulations.

1.4 Outline

Chapter 2 discusses the benchmark case, the methodology to set-up the numerical framework, how the numerical framework is validated, what is done to calibrate the slamming coefficient and curling factor and how the computational costs for isoAdvectord and MULES are assessed. **Chapter 3** presents the results of the 2D and 3D simulations and analyses. In **Chapter 4** the results are discussed, and the conclusions and recommendations are gathered in **Chapter 5**.

2 Methodology

A series of numerical analyses were applied to assess wave impact on slender cylinders (i.e. idealized representation of a lighthouse). To set-up and assess the model, there are seven steps in this methodology (Figure 2-1).

First, a description of the wave impact and force characteristics is given. Secondly, the benchmark case used to validate the model is presented. Further, the set-up of the numerical framework for assessment of the impact of the wave onto a cylindrical structure is described, followed by the model validation using the water level elevation time series of the benchmark case. After the 2D validation, a 3D model validation with the available force time series on the cylinder is presented. The sixth subchapter describes the calibration methodology for the coefficients and how the pressure distribution on the cylinder is assessed. Finally, computational effort of the two different solvers is compared and presented.

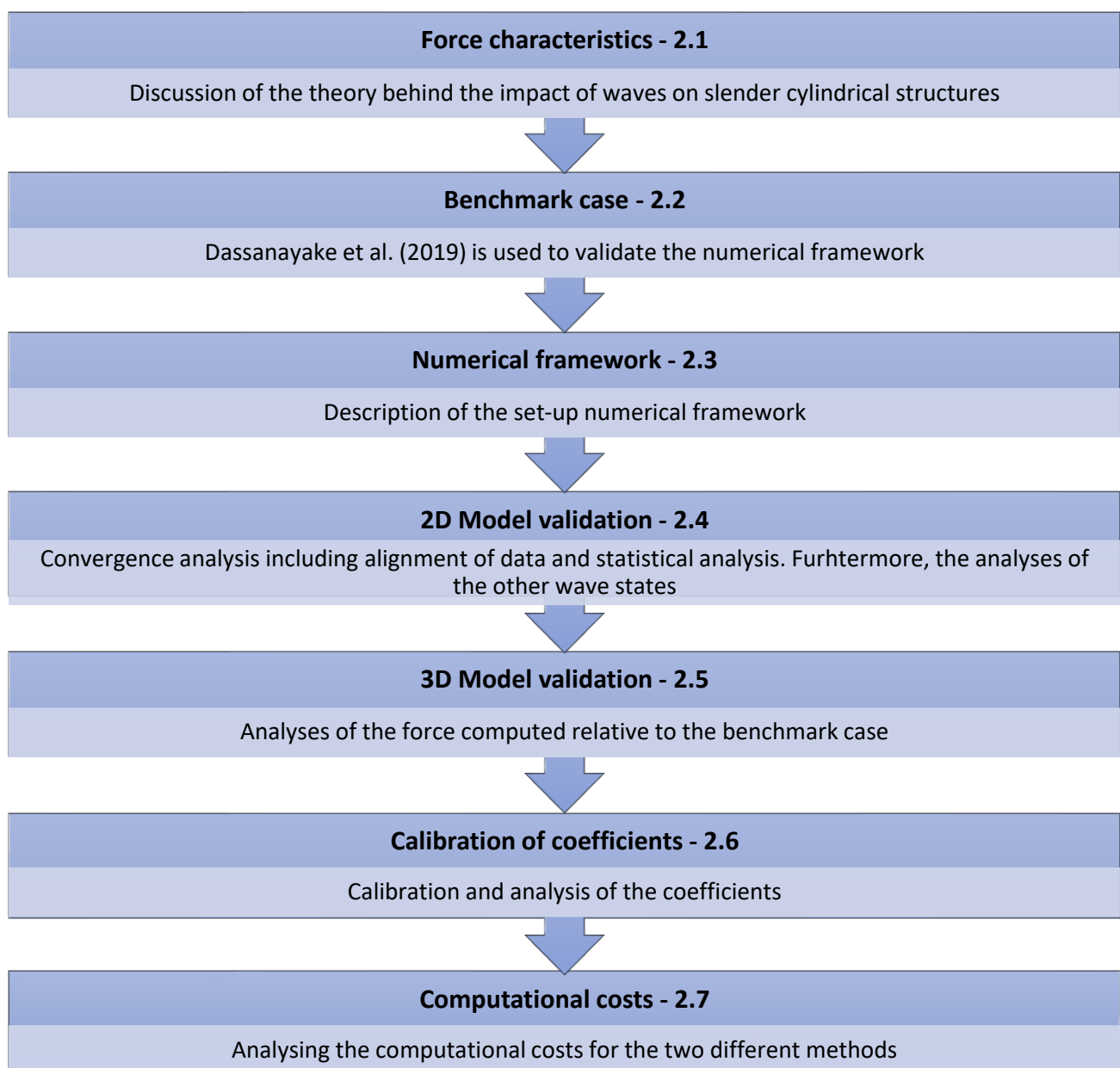


Figure 2-1 Overview of methodology

2.1 Force characteristics

The force exerted on a (slender) cylinder for non-breaking waves can be approximated with the Morison equation (Morison et al., 1950). This equation includes the inertia forces (F_M) and the drag force (F_D) applied on the cylinder (Equation 1).

Equation 1 Morison equation

$$F = F_D + F_M = \int_{-d}^{\eta} \frac{1}{2} * \rho * C_D * D * u(z)|u(z)|dz + \int_{-d}^{\eta} \rho * C_M * \frac{\pi * D^2}{4} * \dot{u}(z)dz$$

Where F [N] is the force, η [m] the water surface elevation, d [m] the water depth, ρ [kg/m³] the water density, C_D [-] and C_M [-] are empirical coefficients, D [m] is the pile diameter and u [m/s] the water particle velocity.

The Shore Protection Manual (1984) states that this equation can also be used for breaking waves by multiplying the drag component of the force by 2.5. However, further research should be done into the wave conditions for which the formula can and cannot be used. The specific case of breaking waves can cause a large impact force on the structure which cannot be described with the Morison equation, especially the short duration of the peak impact forces. Therefore, for breaking waves an additional term for the impact force (F_I) should be added to Morison equation (Equation 2):

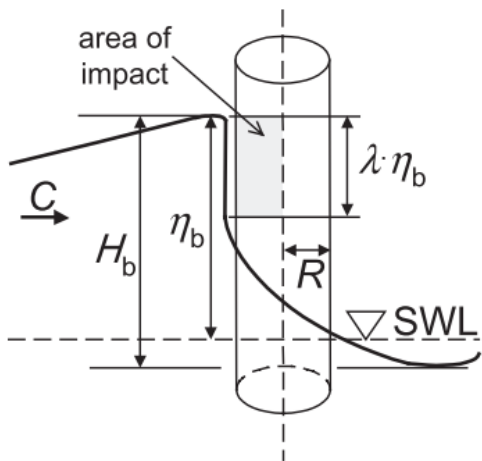
Equation 2 Adjusted Morison equation

$$F = \underbrace{F_M + F_D}_{\text{Morison equation}} + \underbrace{F_I}_{\text{Impact term}}$$

The total force must be divided into two parts in order to assess the load on the cylinder during the moment of impact. One part is the quasi-static force as described by the Morison equation and a second part describing the impact force due to the violent impact of the water. Secondly, the characteristics of the wave must be assessed as they largely determine the magnitude and duration of the wave-structure interaction. The magnitude of the impact force is mainly determined by the momentum of the wave and two dimensionless empirical factors. There is no consensus on the values of these two parameters (Wienke and Oumeraci, 2005). This is especially the case for broken waves, as the geometry (i.e. the slope of the shoal) can have a large influence on the behaviour of the wave and thus the factors. The impact force can be described with Equation 3, and an overview of the values can be found in Figure 2-2:

Equation 3 Impact force

$$F_I = f_I * \lambda * \eta_b = \rho * R * C^2 * C_s * \lambda * \eta_b$$



- F_I [N]: impact force
- f_I [N/m]: impact line force
- λ [-]: curling factor
- η_b [m]: elevation of the wave above SWL
- ρ [kg/m^3]: mass density of water
- C_s [-]: slamming coefficient
- R [m]: cylinder radius
- C [m/s]: wave celerity

Figure 2-2 Overview definitions of the process of a wave breaking against a cylinder (retrieved from: (Wienke and Oumeraci, 2005))

Naturally, the force on the cylinder varies in time and space. Peregrine (2003) notes that the highest run-up on a structure corresponds with the lowest pressure and thus a lower force on the structure. This is at the point where the water is in free-fall and exerts little to no pressure on the water particles below. When the water runs down the cylinder or wall, a second peak in the forces occurs. This is due to the pressure build-up in the water column from the falling water that must decelerate as it arrives at the bottom of the cylinder.

Furthermore, at the point that the wave passes the axis of the cylinder, a secondary load cycle is present (Grue et al., 1993). Liu et al. (2019) used a numerical framework to assess the higher harmonics of the secondary load cycle on a vertical cylinder with a 1:10 sloping bed. It is thought to be caused by the local breaking of the wave around the cylinder when the water is forced up the back of the structure. It was found that the peak of the secondary load cycle is approximately 4.2% of the peak-to-peak value of the horizontal force and its period was found to be approximately 16.4% of the wave period, whereas Grue et al. (1993) found 11% and 15% for the force intensity and period, respectively.

2.2 Benchmark case

The laboratory experiments done by Dassanayake et al. (2019) for the research project STORMLAMP are used to validate the numerical framework. The experiments executed during this project focused on small-scale wave flume tests to assess the wave run-up and impact on shoal mounted lighthouses. The tests were executed in a 35-metre-long flume, 0.6 metres wide, and 1.2 metres deep, in the COAST Laboratory of the University of Plymouth, Great Britain. Experiments were done using different, regular wave conditions, a slope of 1:5, and a fixed water level of 0.5 metres. During the experiments, the water level elevation along the flume was measured by multiple wave gauges and the impact of the wave was measured by a six-axis load cell (see Figure 2-3). The cylinder is 0.12 metres in diameter and placed in the middle of the shoal that is 3 times the cylinder radius wide.

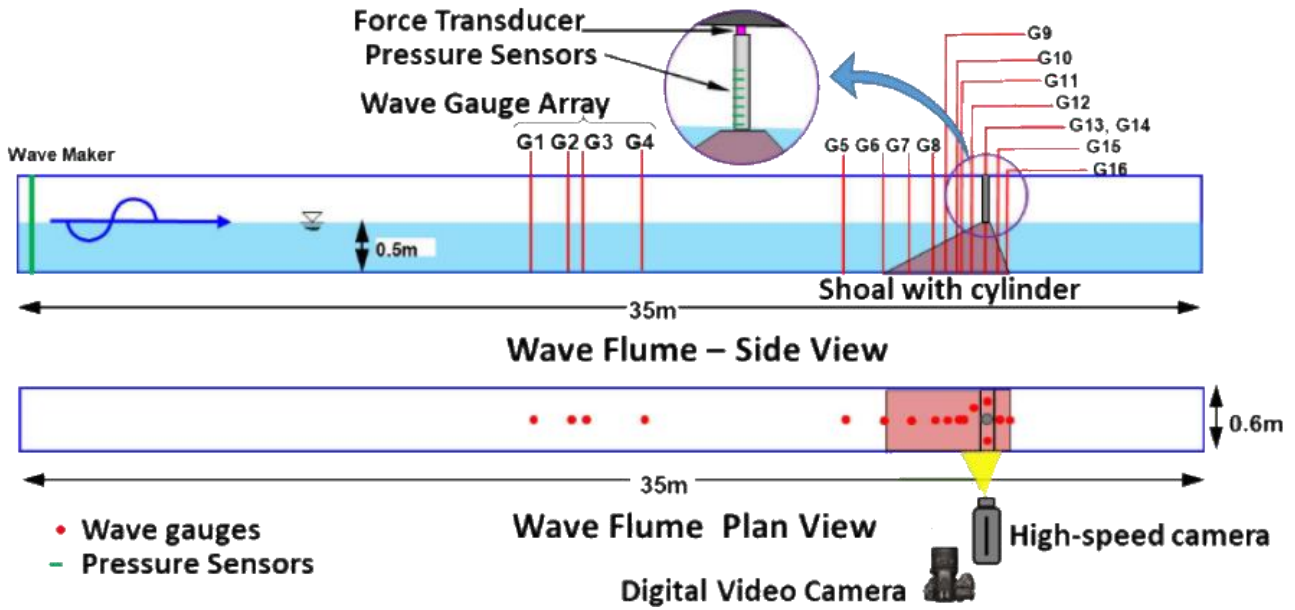


Figure 2-3 Experimental set-up of the STORMLAMP small-scale wave flume tests in the COAST Laboratory of the University of Plymouth. Retrieved from Dassanayake et al (2019)

2.2.1 Wave conditions

Table 1 shows the regular wave conditions used in this study to validate the numerical framework according to the 1:81 Froude similitude. These conditions were simulated with a fixed 1:5 slope.

Table 1 Overview of the model scale wave properties for the wave flume tests of the STORMLAMP project.

Case #	H [m]	T [s]	L [m]	Ursell number [-]
1	0.05	1.20	2.05	1.68
2	0.05	2.44	5.09	10.36
3	0.10	1.20	2.05	3.36
4	0.10	2.44	5.09	20.72
5	0.15	1.50	2.83	9.61
6	0.15	1.96	3.96	18.82

2.3 Numerical framework

The processes on the shoal (wave breaking and propagation after breaking of the wave) are highly non-linear and vary rapidly in space and time. The type of measurements needed to capture these complex processes in high spatiotemporal resolution are not possible with physical models such as that of Dassanayake et al. (2019). Doing so can obstruct wave propagation, is expensive, and would result in an unrealistic number of measurement devices. Next, it can also influence the interaction between the wave and the structure, and thus introducing bias to the results. In order to overcome this limitation, a high-resolution numerical simulation was carried out to assess the impact of the wave onto the structure. First, a 2D numerical model was set-up for a validation of the water level elevation. Further, this model was extended to a 3D model and validated with the force time series of experimental data set of Dassanayake et al. (2019).

The numerical framework was set-up with OpenFOAM as a basis. This is the free open-source CFD (Computational Fluid Dynamics) software developed by OpenCFD Ltd. since 2004 (OpenFOAM®, n.d.). The software can be used in a range of applications such as complex fluid flows, chemical

reactions, and heat transfer. It was chosen as it can (fully) capture the impact of the broken waves and the complex processes of wave breaking. Comparable frameworks have been used with similar cases (e.g., Ghadirian and Bredmose, 2019; Liu et al., 2019; Veic and Sulisz, 2018) which have proven to produce accurate results.

The numerical wave tank (NWT) consists of the finite volume framework OpenFOAM-v1912 (OpenFOAM®, n.d.) and the waves2Foam toolbox (Jacobsen et al., 2012). The recently developed Volume of Fluid (VOF) based isoAdvector algorithm by Roenby et al. (2016) was used to model the multiphase nature of the flow and resolve the sharp discontinuities in the propagation of broken waves. This method was compared with the MULES approach. Additionally, to limit the over-production of turbulent kinetic energy (TKE) under breaking waves, the stabilization closure developed by Larsen and Fuhrman (2018) was preferred. To reduce the computational cost and maintain the nonlinear nature of the shallow water waves, the numerical domain consists of an NWT coupled with a nonlinear potential wave model (i.e., OceanWave3D (OCW3D), (Engsig-Karup et al., 2009)) as presented by (Paulsen et al., 2014a) and (Jacobsen et al., 2015).

2.3.1 Key parameters

During the simulations, the time step is an important aspect to keep the simulation stable. In the 2D simulations, the used time step was optimised by adjusting the Courant number to the set limits. For the 3D simulations, the time step was fixed at a value of 1/10,000 seconds to ensure a stable simulation.

For isoAdvector, a Courant number up to 0.5 can be used, as stated by Roenby et al. (2016) but for MULES the optimal value is 0.05 as stated by Larsen et al. (2019). However, the Courant number for MULES can go up to 0.4 and still have a stable simulation. Therefore, for both solvers, a value of 0.25 was used. This is still in the range of stability for MULES and isoAdvector.

2.3.2 Boundary and initial conditions

For the various patches in the numerical domain, the boundary condition(s) (b.c.) are specified per field (Figure 2-4). In the 2D simulation, the cylinder is absent in the numerical domain.

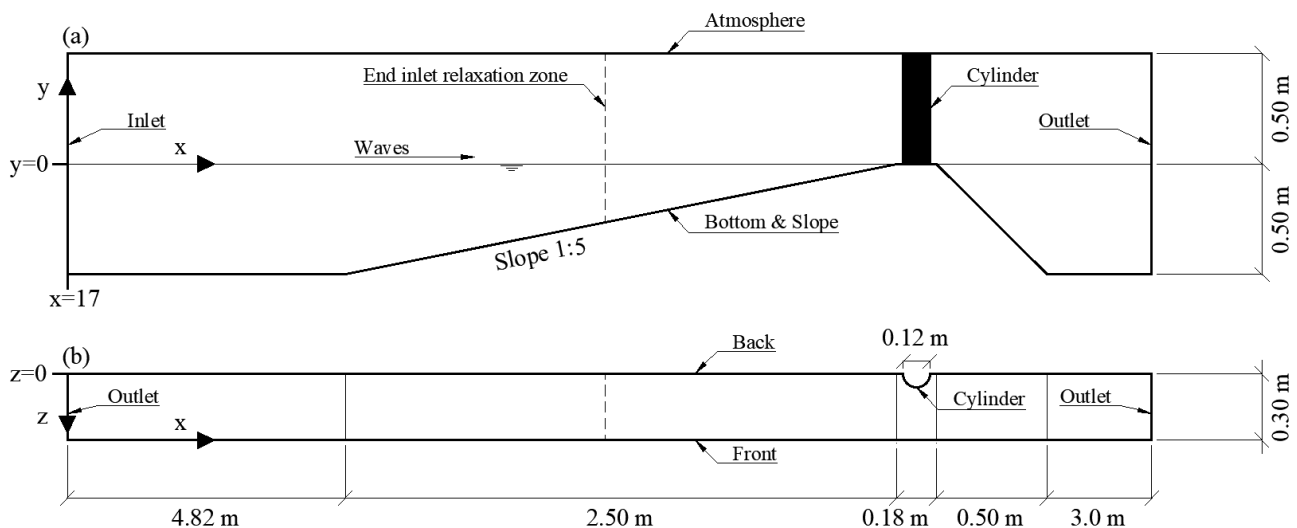


Figure 2-4 Overview of the numerical domain including the numerical patches for the 3D case. (a) Shows the longitudinal profile. (b) Show the plan view.

There are several variables present in the numerical domain and used in the boundary and initial conditions:

- I. the phase fraction of the given phase where 1 means fully filled with water and 0 means fully filled with air (α , [-])

- II. the turbulent kinetic energy (k , [m^2/s^2])
- III. the turbulent viscosity (ν_t , [m^2/s])
- IV. the turbulence specific dissipation rate (ω , [$1/s$])
- V. the pressure (p , [N/m^2])
- VI. the velocity (U , [m/s])

As shown in Figure 2-4, the following patches and the corresponding b.c. are present in the numerical domain:

- i. **Inlet:** The location where the waves enter the domain.

The inlet mostly applies a zero gradient b.c. except for the fields α (applies the standard waves2Foam toolbox b.c. for α), k (applies an inlet outlet b.c. based on (Larsen and Fuhrman, 2018)) and U (applies the standard waves2Foam toolbox b.c.).

- ii. **Outlet:** The end of the numerical wave tank where the waves exit the domain.

The outlet applies a zero gradient b.c. for all fields.

- iii. **Atmosphere**

The atmosphere utilises an inlet-outlet b.c. for α and for ω and k based on (Larsen and Fuhrman, 2018)), U (applies a pressure-inlet-outlet-velocity b.c.), ν_t (applies a calculated b.c.) and the pressure (which applies a total pressure b.c.)

- iv. **Bottom, Slope and Cylinder**

For all walls (bottom, slope, and cylinder), a wall function was applied, except for U which utilises a no slip b.c., and the α and pressure which apply a zero gradient b.c..

- v. **Front:** This is the lateral side of the numerical domain that represents the glass wall of the experiment set-up.

In the case of 2D flow the b.c. was set to empty as there is no interaction between the wall and the water. For 3D flow, a slip b.c. was applied as the flow can be non-zero on the glass wall.

- vi. **Back:** This is the back side of the numerical domain and represents the middle of the wave flume in the experiment set-up.

For 2D flow the b.c. was set to empty as there is no interaction between the middle and the water. For 3D flow, as the problem is symmetrical, a symmetry boundary conditions was applied. This means that the NWT only entails half of the physical flume with the assumption that the problem is fully symmetrical. This saved significant computational costs as the cell count for the 3D case was halved.

2.3.3 Numerical schemes and solvers

The following numerical schemes and solvers were used in the simulations. For the time discretisation Euler's method was applied, for the gradient discretisation Gauss linear (OpenFOAM®, n.d.), the divergence discretisation Gauss Minmod (Harten, 1983) for both k and ω was used, and Gauss SFCD (Self-Filtered Central Differencing) (Ziman, 1990) for the velocity. For the Laplacian schemes, Gauss linear corrected (OpenFOAM®, n.d.) is utilised, and for the viscous diffusion term Gauss linear (OpenFOAM®, n.d.) is applied. The isoAdvector (Roenby et al., 2016) approach was used for α and thus the interface. When MULES (Deshpande et al., 2012; Weller, 2008) is used Gauss interfaceCompression (OpenFOAM®, n.d.) and Gauss MUSCL (Monotone Upstream-centered Schemes for Conservation Laws) (van Leer, 1977) were used for the interface.

The GAMG (Generalised Geometric-Algebraic Multi Grid) solver (Ferziger et al., 2020) was used for the pressure together with a Gauss Seidel preconditioner and smoother (Ferziger et al., 2020). The GAMG solver was used as it is especially developed for large geometries. The smoothSolver (OpenFOAM®, n.d.) combined with a DILU (Diagonal-based Incomplete LU) preconditioner (OpenFOAM®, n.d.) and Gauss Seidel smoother (Ferziger et al., 2020) is utilised for the U , k and ω .

The PIMPLE (Pressure-Implicit Method for Pressure-Linked Equations) algorithm (Barton, 1998) was applied for the pressure velocity coupling. The PIMPLE algorithm is a combination of the SIMPLE (Semi-Implicit Method for Pressure-Linked Equations) algorithm (Patankar and Spalding, 1972) and the PISO (Pressure Implicit with Splitting of Operators) algorithm (Issa, 1986).

The choices for these numerical schemes and solvers are based on the work done by Jacobsen et al. (2018) and Patil (2019).

2.3.4 isoAdvector

The standard algebraic VOF method to compute the interface has been tested in numerous cases for regular and irregular waves (e.g., Jacobsen et al., 2012; Larsen et al., 2019; Paulsen et al., 2014b). Although, the traditional MULES solver has the tendency to smear the interface and thus leads to less accurate results (Larsen et al., 2019; Roenby et al., 2016). The algebraic VOF schemes are much simpler to implement, more efficient and not limited to structured meshes. They are however not as accurate as geometric VOF schemes (López et al., 2008). The new solver based on the isoAdvector principle developed by Roenby et al. (2016) utilises a geometric approach to compute the interface. In addition to the advection of the passive scalar, the isoAdvector method improves the interface prediction step by advection of the interface itself. This leads to a smoother and sharper interface (Figure 2-5). This figure shows the two interfaces for both solver for the same timestep. It shows that the interface of the breaking wave and the interface on the shoal for MULES (Top) is more spread out over different cells while for isoAdvector (bottom), the interface is sharper and spread out over fewer cells.

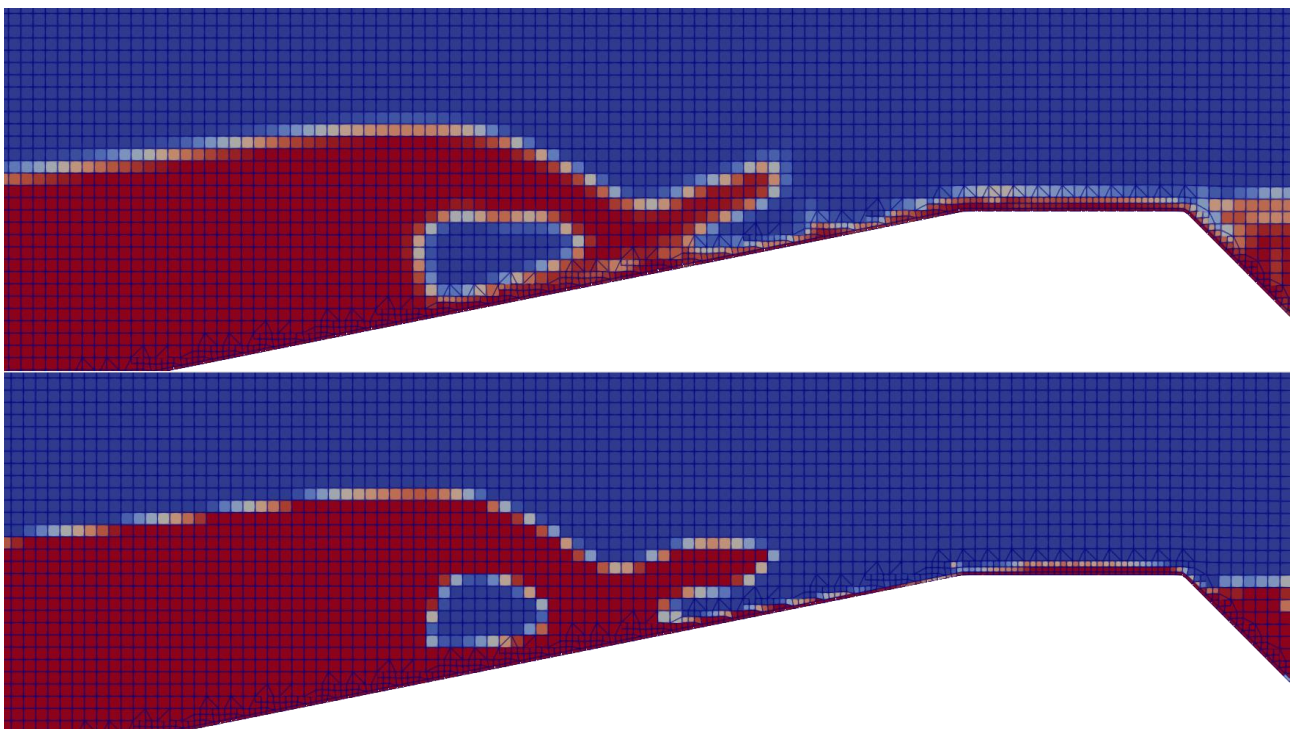


Figure 2-5 The interface between air and water for the same time step in a 2D simulation for MULES (top) and isoAdvector (bottom).

Geometric VOF schemes include complex geometric operations that make the computations slow. That is why the main goal of Roenby et al. (2016) was to develop a VOF-based interface advection method that retains the accuracy of the geometric schemes but keeping the geometric operations to a minimum to achieve acceptable calculations times. Roenby et al. (2017) state that depending on the cell size and the time discretisation, either isoAdvector or MULES can be fastest when simulating 10 wave periods. They furthermore state that the isoAdvector solver is less sensitive to different

aspect ratio's (the cell's dx/dy ratio) of the cells than MULES. This new VOF approach was validated using experimental data of breaking waves by Patil (2019).

2.3.5 Turbulence

As the specific situation modelled will result in breaking and broken waves, the correct prediction of the produced turbulence is crucial. According to Larsen et al. (2018), most two-equation turbulence models are unconditionally unstable, instead of conditionally unstable when applied in regions of nearly potential flow. This is due to exponential growth of the turbulent kinetic energy and eddy viscosity (Larsen and Fuhrman, 2018). This can lead to premature wave decay and influence the results throughout the entire numerical domain, thus affecting the computed force. To prevent the overprediction of the turbulence under breaking waves, Larsen et al. (2018) proposed an adjustment to the equations. This adjustment to the turbulence closure model creates a stable set of Reynolds Averaged Navier-Stokes (RANS) equations that can be used for wave propagation over long durations while the wave holds its original form. The new proposed model accurately predicts the water surface elevation throughout the breaking process. This is important as the waves are already broken by the time they hit the lighthouse, so a correct prediction of the water level during the breaking process, and thus the wave slamming, into the lighthouse is needed to acquire accurate results.

The parameters in the turbulence model, are λ_1 and λ_2 , for which 0.8 and 0.1 were applied, respectively, in the numerical model, based on Patil (2019). Patil (2019) validated the adjusted $k - \omega$ closure model with the mentioned values for λ_1 and λ_2 for a case with plunging waves.

2.3.6 Numerical wave tank

Within OpenFOAM there is the possibility to use the waves2Foam toolbox (Jacobsen et al., 2012) to set-up an NWT. By coupling OpenFOAM and OCW3D, the numerical domain for OpenFOAM is reduced significantly because OCW3D can be used to model the area of the NWT that is not of interest in the research. For this research that is everything that happens before the shoal (Figure 2-6). This reduces the computational costs of the simulation.

Figure 2-6 shows that the first 17 metres of the NWT are modelled by OCW3D, at 17 metres the model is coupled with OpenFOAM. At 17 metres the inlet relaxation zone starts. This zone filters out the reflected waves and ends at 23 metres, where the full OpenFOAM domain starts, and the waves break and hit the shoal.

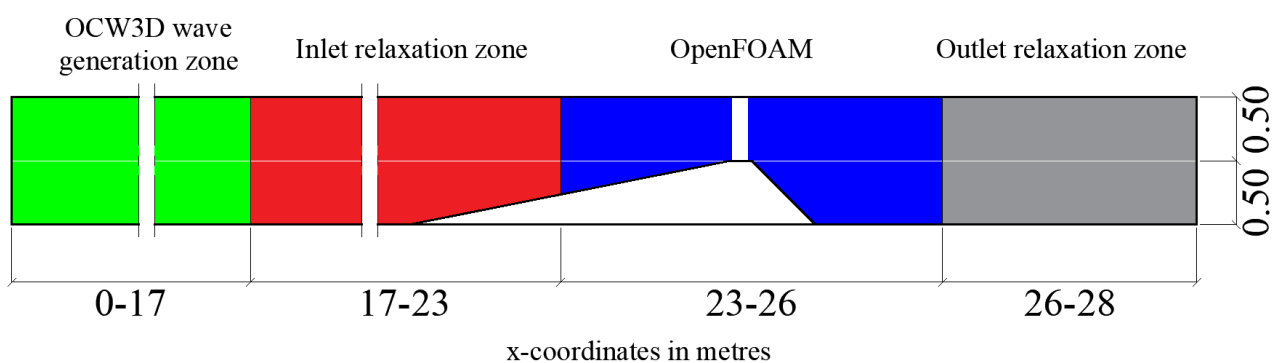


Figure 2-6 Overview coupling OCW3D and OpenFOAM for waves of 0.15 metre and 1.5 seconds. At the bottom, the streamwise coordinates in metres of the different areas in the numerical wave tank can be found (not to scale).

OceanWave3D

OCW3D makes use of an efficient solution scheme for the 3D Laplace problem using a higher-order discretization (Runge-Kutta method) for nonlinear waves on a variable depth. The solutions given by OCW3D are found to be robust for general nonlinear wave problems, with no need for additional smoothing or filtering over that imposed naturally by the finite difference schemes (Engsig-Karup et al., 2009). When applying regular waves, a stream function which takes the wave height, wave period

and water depth as input is used. The results computed by OCW3D are used as input for the OpenFOAM inlet relaxation zone. The model itself is not suitable for breaking waves and applies a filter that limits the vertical particle velocity when a wave is about to break. For the breaking filter, the standard option in the OCW3D graphical user interface is used.

As the first section of the NWT is not part of the area of interest in this study, OCW3D was used to handle and propagate the waves over this part. OCW3D propagates the waves until the start of the relaxation zone where the solution provided by OCW3D is used as a boundary condition in OpenFOAM. Paulsen et al. (2014b), Jacobsen et al. (2015), Veic and Sulisz (2018), Patil (2019) and Jonker (2020) have all demonstrated and validated the coupling of OpenFOAM and OCW3D in an NWT.

Relaxation zone

The relaxation zones were introduced by Jacobsen et al. (2012) as a continuation on the work of Mayer et al. (1998). The relaxation zone filters out the reflected waves so that the wave conditions at the beginning of the inlet relaxation zone match the solution provided by OCW3D. For all cases, the inlet relaxation zone was made to be two times the wavelength of the used wave state. This ensured that nearly all reflected waves were filtered out (Jacobsen et al., 2012). However, some exceptionally long waves can still occur in the domain and cannot be filtered out by the relaxation zone. For the current NWT, the period of this wave is approximately 20 seconds when it is assumed that the basin is closed and approximately 23 metres long. The distance to halfway up the shoal (Equation 4).

Equation 4 Eigen frequency of basin

$$T_1 = \frac{2 * L}{\sqrt{g * h_0}} = \frac{2 * 23}{\sqrt{9.81 * 0.5}} \approx 20 \text{ seconds}$$

Where T_1 [s] is the wave period, L [m] the length of the basin, g [m/s^2] the gravity and h_0 [m] is the water depth.

The start and end of the inlet relaxation zone for the different wave states can be found in Table 2. After the shoal at 26 metres, the outlet relaxation zone starts. Here the velocity field is set to zero metres per second so the waves are damped out and cannot return to the shoal. This zone ends at 28 metres. For each relaxation zone, a ramping time of one wave period is applied. The ramping time is the time over which the numerical framework gradually is exposed to the forcing conditions. If this is not done, the simulation can crash when the numerical framework is suddenly exposed to the full forcing conditions.

Table 2 Overview of the start and end of the inlet relaxation zone for the different wave states.

Case #	L [m]	Start inlet relaxation zone	End inlet relaxation zone
1	2.05	18.80	23.00
2	5.09	12.60	23.00
3	2.05	18.80	23.00
4	5.09	12.60	23.00
5	2.83	17.00	23.00
6	3.96	15.00	23.00

2.3.7 Mesh

The physical wave flume (Figure 2-7a) is recreated as both a 2D model (Figure 2-7b) and a 3D model (Figure 2-7c) using the native OpenFOAM mesh generators blockMesh and snappyHexMesh.

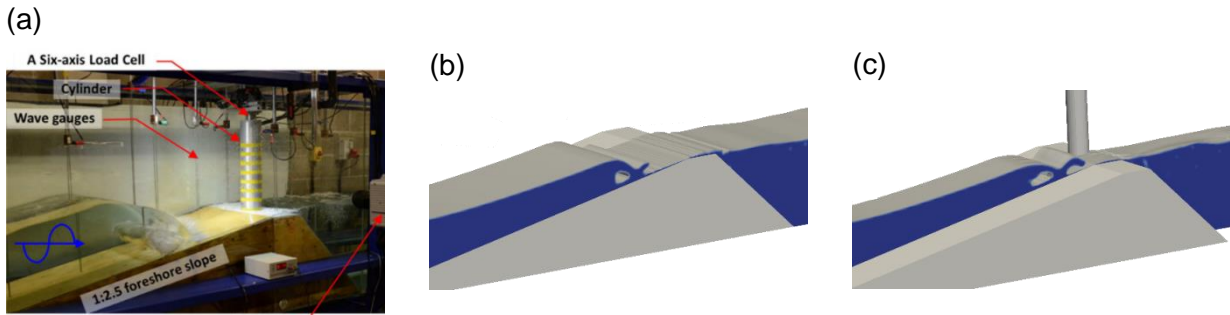


Figure 2-7 An overview of the meshes compared to the experiment. (a): The experiment set-up for a 1:2.5 slope (retrieved from D.T. Dassanayake et al.(2019)). (b): The geometry for a 2D simulation, without cylinder and a 1:5 slope. (c) The geometry for the 3D case, with cylinder and a 1:5 slope.

First a background mesh was created using blockMesh with half the required cells per wave height (CPWH), level 0 in Table 3. With snappyHexMesh the slope was cut out from this background mesh and the area around the water level was refined to the needed resolution (level 1). Table 3 shows an overview of the cell sizes for the different resolutions and levels per resolution for 0.15-metre waves. On the shoal, a level 2 refinement was applied.

Table 3 Overview cell sizes for a different number of CPWH based on 0.15 m and 1.5 s waves.

Level	5 CPWH [m]	10 CPWH [m]	15 CPWH [m]	20 CPWH [m]	25 CPWH [m]
0	0.060	0.030	0.020	0.0150	0.012
1	0.030	0.015	0.010	0.0075	0.006
2	0.015	0.0075	0.005	0.00375	0.003
3	0.0075	0.00375	0.0025	0.001875	0.0015

The refinement along the water is made with 75% of the wave height of case 5 from Table 1 (0.1125 m) below the water line and 120% (0.18 m) above the water line (see Figure 2-8a). The refinement was placed up to the outlet relaxation zone. This range of the refinement was also used for the other wave states.

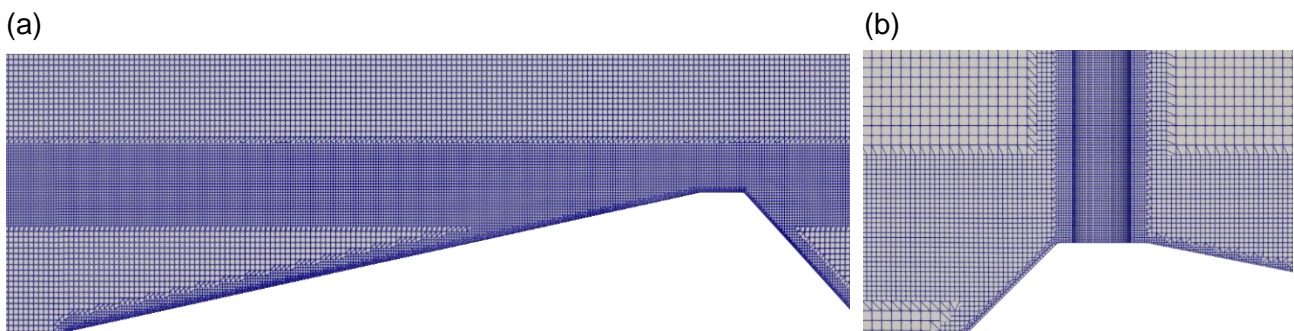


Figure 2-8 Overview of set-up of the used meshes. (a) Overview of a 2D mesh. Along the water line a refinement of level 1 is applied. On the slope a refinement of level 2 is used, everywhere else a refinement of level 0 is used. (b) Detail of the resolution applied on the face of the cylinder for the 3D mesh. The refinement around the cylinder is of level 2.

In the 3D mesh, the cylinder is added and the same level 2 refinement as was used on the slope is applied (Figure 2-8b). The resolution around the cylinder is chosen to be one level higher than the resolution around the water level to fully capture the impact of the wave into the structure.

Jacobsen et al. (2012) recommended that the aspect ratio should be kept as close to 1 as possible. This recommendation is kept in mind when setting up the mesh. See Appendix A for an overview of the aspect ratio per geometry. The dimensionless wall distance (y^+) is determined per case and

simulation and is discussed in the results section of the specific simulation or case. The value of y^+ can be determined with Equation 5:

Equation 5 Dimensionless wall distance

$$y^+ = \frac{u_* * y}{\nu}$$

Where $u_* [m/s]$ is the friction velocity, $y [m]$ the distance to the nearest wall and $\nu [m^2/s]$ is the kinematic viscosity.

The value of y^+ is important as it influences the turbulence modelling through the wall functions used for the boundary and initial conditions. According to Larsen and Fuhrman (2018), this value should be kept below 30 during the simulations.

2.3.8 Measurement locations

In the numerical domain, there are several locations where values were measured, e.g. the water level elevation, velocity, pressure and force. For the 2D simulations, the most important measurement locations are the wave gauges which are placed at the same locations as in the experiments of Dassanayake et al. (2019). The results from these wave gauges can be used to validate the results of the 2D NWT and therefore define the mesh to use for the 3D case, see Table 4 and Figure 2-9 for an overview of the locations of the wave gauges.

Table 4 Overview locations wave gauges

Wave gauge	WG08	WG09	WG10	WG11	WG12
x-coordinate [m]	23.08	23.40	23.70	23.82	24.07

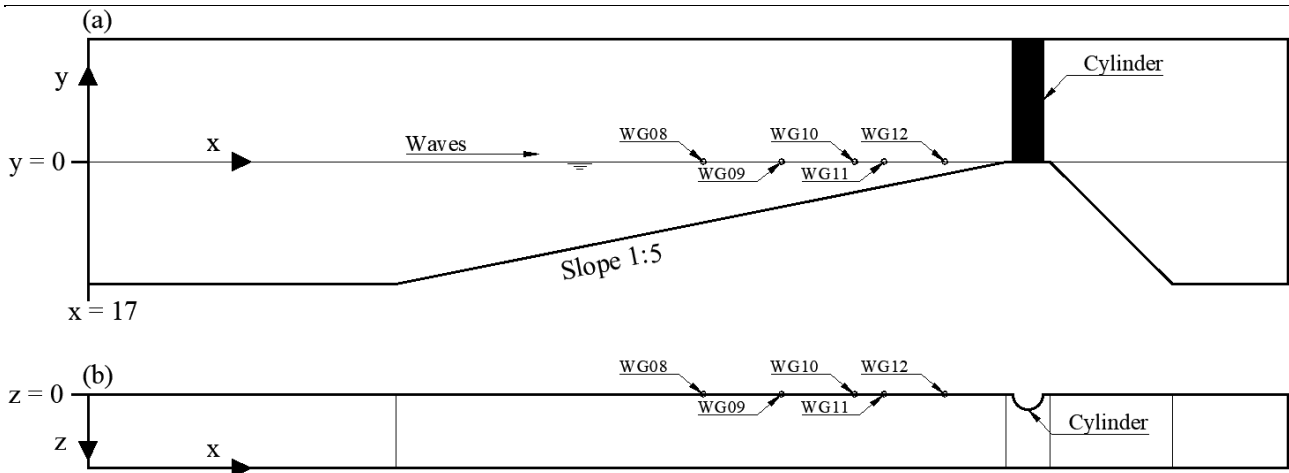


Figure 2-9 Overview of the placed wave gauges in the domain and the cylinder on which values were measured. (a) Shows the longitudinal profile. (b) Show the plan view.

For the 3D simulations, not only the water level at the locations of the wave gauges was measured but also several other fields such as p , U , v_t , k and ω . These variables were measured from the bottom of the slope to the atmosphere with a line of gauges. Next, the total force on the cylinder is measured. This is used to validate the 3D model set-up. Furthermore, the interpolated cell values of the variables p , U , and α on the cylinder were measured.

2.4 2D Model validation

The 2D model validation includes a convergence analysis to determine the cell size needed to compute a correct water level elevation. In the convergence analysis the results for the different mesh resolutions are compared to the results of the experimental data. This is done for wave state 5 of the

benchmark case (Table 1). The different resolutions assessed are 5, 10, 15, 20 and 25 CPWH. The validation is performed by aligning the data and by comparing the correlation and error between the computed and measured data. The analyses discussed in this paragraph were performed for all the wave gauges in the NWT. It should be noted that all the water level elevation data from the benchmark case has the cylinder present on the shoal. This could influence the results of the verification and is therefore considered when assessing the results.

The found resolution in the convergence analysis was used to analyse the other wave states mentioned in Table 1 for each wave state the necessary changes are made to the mesh and inlet relaxation zone.

2.4.1 Alignment of data

Even though the wave conditions entail regular waves, the data sets cannot be compared unless they both have the same start and endpoint, i.e. they are synchronized. As both data sets have different starting points in time (e.g. as in Figure 2-10a), the two data sets should be aligned before they can be compared. The data was aligned using a cross-correlation analysis which determined the similarity between the two signals and gave the time delay between the two signals to achieve the maximum correlation as output. Overall, it gave the time delay when the correlation between two data sets is largest. This time delay is then used to shift the starting point in time of the data set and aligns the two signals (see Figure 2-10b).

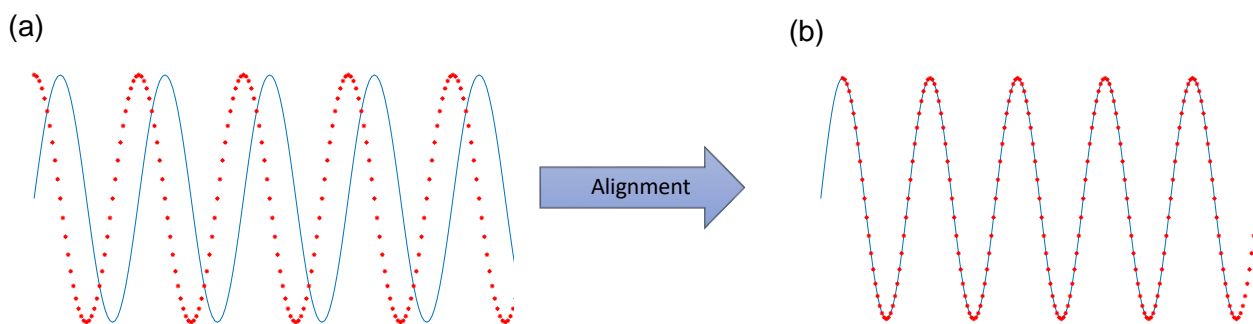


Figure 2-10 Overview of alignment procedure. (a): The experimental and OpenFOAM data sets that are not aligned. (b): The experimental and OpenFOAM data sets that are aligned

As a result of aligning the data, there is a small shift in time that occurs (e.g. as in Figure 2-10b) and thus the start and endpoints of one of the data sets do not correspond anymore. This was solved by cropping the data sets at the third and third-last zero-down crossing of the experimental data. The third crossing was used after determining through trial and error that is the first crossing that exists in both the experimental and OpenFOAM data sets. Next, a low-pass filter was used to remove the small oscillations of the wave gauges of the experimental data above 8 Hz. The data range selected from the alignment is used for the further analyses in the 2D validation of the numerical framework.

2.4.2 Data processing

The post-processing of the data sets consists of the following five steps:

1. Fast Fourier Transform (FFT) to assess the analyse the frequency domain.
2. Ensemble average wave shape to analyse the average wave shape produced by the model to the experimental data.
3. Pearson Correlation Coefficient (PCC) to analyse the correlation between the OpenFOAM and experimental data.
4. Centred Root Mean Square Error (CRMSE) to determine the error between the OpenFOAM and experimental data.
5. Standard Deviation (SD) to assess the variation in the water level time series.

To assess if the model computes the correct wave period as the experiment, a FFT on the water level elevation was applied. Furthermore, as the waves state entails only regular waves, an ensemble average wave shape was determined to assess how well the numerical framework represents the laboratory experiments. From the selected time series, the individual waves were determined using a zero-down crossing analysis. From the zero-down crossing, one wave period of data was used to create the individual wave. This ensured that all waves selected for the ensemble average had the same number of datapoints. For all selected waves, the data per datapoint were averaged to create the ensemble average. To give the ensemble average of the different data sets at a common point they, were aligned at the zero-up crossing of the mean wave height. This ensured that the different waves could be compared to each other.

The correlation between the numerical and experimental data was assessed using the PCC (Equation 6). This shows the correlation between two data sets where the coefficient can vary between -1 and 1, showing either full negative linear correlation or full positive linear correlation, respectively.

Equation 6 Pearson Correlation Coefficient

$$PCC = \frac{cov(X_1, X_2)}{\sigma_{X_1} * \sigma_{X_2}}$$

In which, PCC is the Pearson Correlation Coefficient, $cov(X_1, X_2)$ the covariance between the data and σ_{X_i} is the variance of the data sets.

CRMSE was used to assess the error between OpenFOAM and the experimental data (Equation 7). In the procedure, the mean value of the data set is removed from the water level elevation data. This makes it a useful tool in comparing the difference in amplitude between data sets.

Equation 7 Centred Root Mean Square Error

$$CRMSE = \sqrt{\frac{\sum_{i=1}^N ((y_{i,e} - \mu_e) - (y_{i,OF} - \mu_{OF}))^2}{N}}$$

In which, CRMSE is the Centred Root Mean Square Error, $y_{i,e}$ is the value measured in the experiment, μ_e is the mean value of the experiment time series, $y_{i,OF}$ is the value computed by OpenFOAM, μ_{OF} is the mean value of the OpenFOAM time series and N the total number of datapoints.

The CRMSE was normalised with the local mean wave height (H_{mean}). Normalising the CRMSE creates the possibility to assess the numerical framework at the different locations in the NWT, and for different wave states (Equation 8).

Equation 8 Normalisation of the Centred Root Mean Square Error

$$CRMSE_n = \frac{CRMSE}{H_{mean}}$$

To compare the variation in the water level between the experimental data and OpenFOAM, the Standard Deviation (SD) for all data sets was determined (Equation 9).

Equation 9 Standard Deviation

$$SD = \sqrt{\frac{1}{N-1} \sum_{i=1}^N |y_{i,n} - \mu_{OF}|^2}$$

To assess the difference in the water level variation of the OpenFOAM and experimental results the SD for the OpenFOAM results was normalised with the experimental SD (Equation 10).

Equation 10 Normalisation of the Standard Deviation

$$SD_n = \frac{SD_{OF}}{SD_{Exp}}$$

In which SD_n is the normalised SD, SD_{OF} the SD of the OpenFOAM data and SD_{Exp} the SD of the experimental data.

2.5 3D Model validation

The 3D validation of the numerical framework focused mainly on the forces computed by OpenFOAM and a comparison with the experimental results. Additionally, the water level elevation was also assessed. The comparison of the force focused on three aspects: the ensemble average force signal, a single peak analysis, and the rising time of the peak force.

2.5.1 Water level elevation

The same analyses are done for the 3D validation as for the 2D validation. The methodology is discussed in detail in section 2.4.

2.5.2 Ensemble average force signal

The ensemble average of the force signal was computed by assessing the locations of the peaks (F_{max} in Figure 2-11) and the location of the threshold of the force. From the location of the threshold, 1.2 seconds of datapoints was selected and used to create the ensemble average. The value of the threshold was set to 0.05 N.

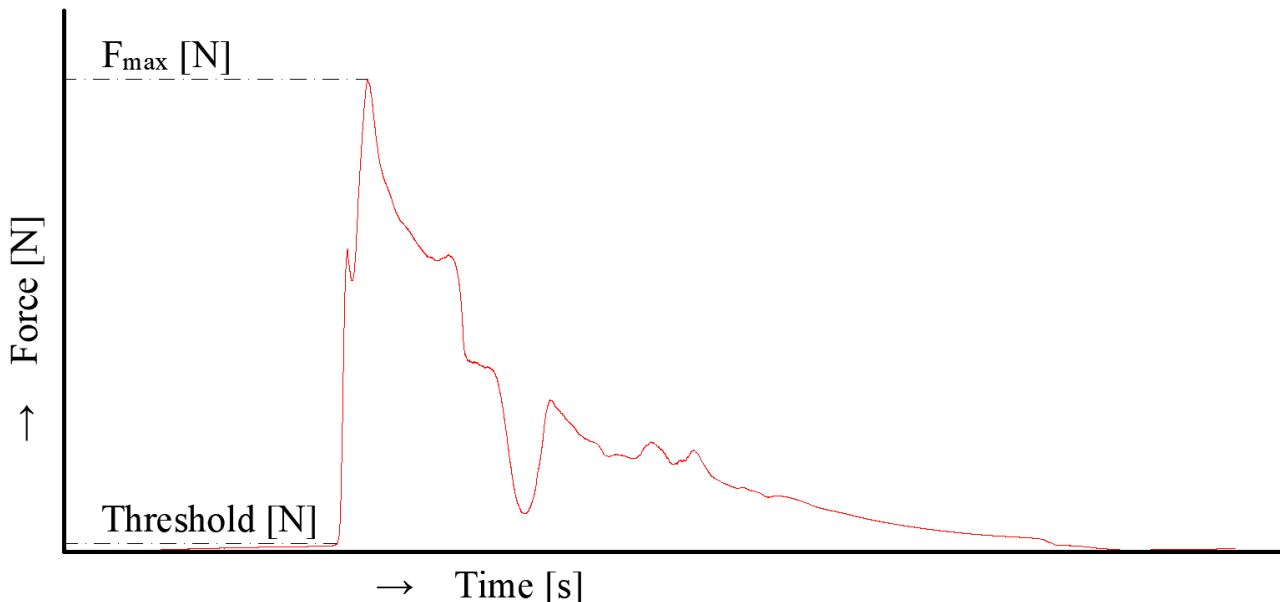


Figure 2-11 Overview of the total force on the cylinder over time

2.5.3 Single peak analysis

Comparing individual peaks was proposed because the features of the individual force signal are smeared by the averaging process used for the ensemble. This is due to the slight difference in timing of each event. Comparing a single force signal from all three data sets was done by determining the maximum peak force of the MULES data set and comparing this signal to isoAdvector and

experimental signals that have a similar peak magnitude. The signals used in the comparison were extracted using the same methodology as for the ensemble averaged force signal.

2.5.4 Rising time and force of peak

The rising time indicates how long it takes for the force signal to reach its maximum value from the given threshold (Figure 2-11). The rising time was determined for all peaks in the data sets. Further, the peak forces of the selected time series of the different data sets were analysed.

2.6 Calibration of coefficients

The following aspects are important to calibrate the coefficients and assess the pressure distribution on the cylinder. The pressure exerted on the cylinder, the point of application of the force on the cylinder, the height of the impact ($\lambda * \eta_b$), the curling factor (λ), the decomposition of the total force exerted on the cylinder and the slamming coefficient (C_s).

2.6.1 Pressure distribution on the cylinder

The pressure on the centreline of the cylinder was determined for every instance of the peak force on the cylinder (Figure 2-12). The pressure profiles were averaged in an ensemble average profile to assess the average pressure distribution in the centreline of the cylinder. The height over which the pressure distribution works was determined (red line in Figure 2-12) to assess the height of the impact at the time of the peak force. A threshold was set at 50 N/m² below which the height of the impact does not apply anymore. To filter out small peaks in the pressure distribution, as at 0.13 metre in Figure 2-12.

The height of the impact can also be measured as the multiplication of water level elevation of the breaking wave (η_b) with the curling factor (λ) in Equation 11.

Equation 11 Height of the wave impact during the maximum impact force

$$s_I = \lambda * \eta_{b,WG11} = \max(y_a) - \min(y_a)$$

In which s_I [m] is the height of the impact, y_a [m] the locations on the cylinder where the pressure is above a set limit of 50 N/m², λ [-] the curling factor and $\eta_{b,WG11}$ [m] the water level elevation at wave gauge 11. Wave gauge 11 is located at $x = 23.82$ metre.

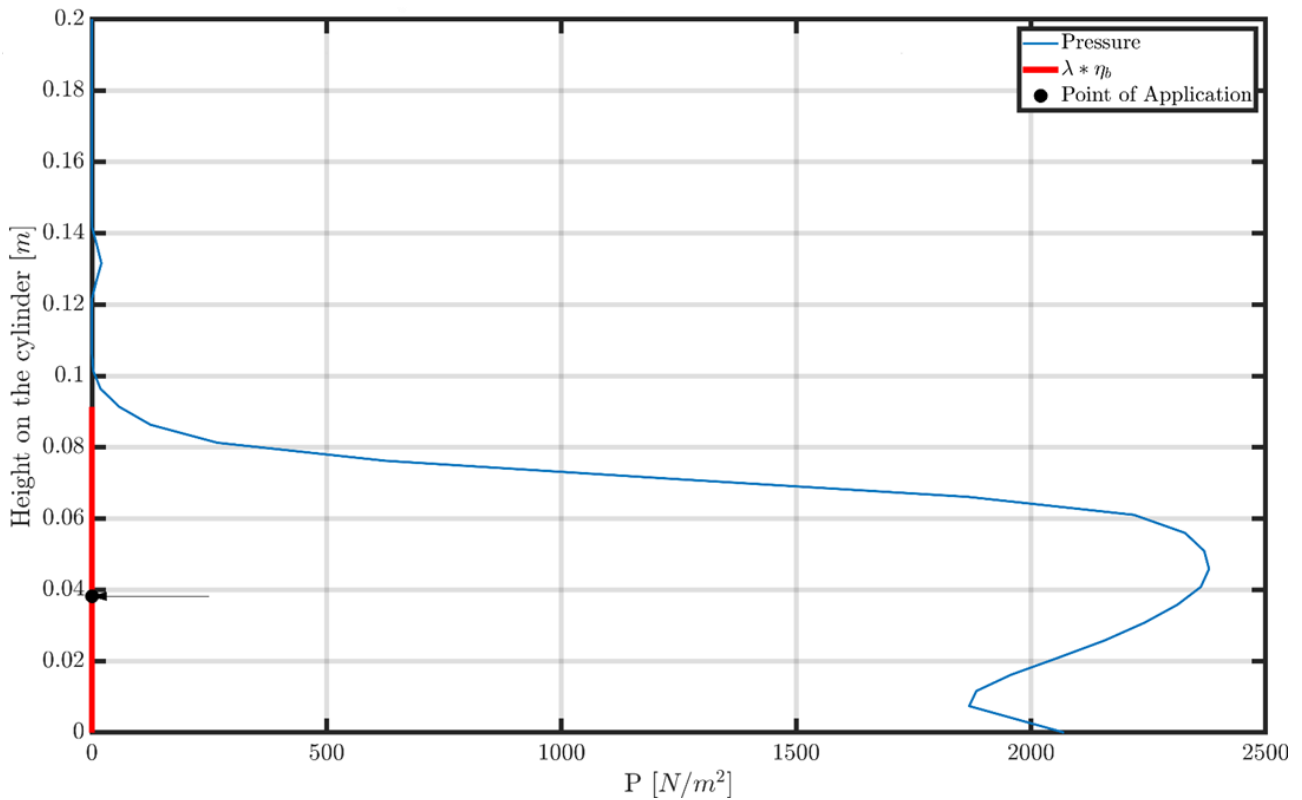


Figure 2-12 Example of the pressure distribution on the centre of the cylinder during the peak of a force signal. The figure also shows the height of the impact (red line) and the centre of the pressure distribution (black arrow).

The point of the force application is determined from the pressure distribution. One should know where the pressure is applied and where the approximate centre of the pressure on the centreline of the cylinder lies. This can be used in assessing the structural integrity of real-life lighthouses.

The pressure from the peak forces at different locations around the structure (0, 13, 28, 48, 62 and 90 degrees) was analysed. The pressure distributions at these locations were averaged to analyse the spread of the pressure on the structure during the moment of the peak forces.

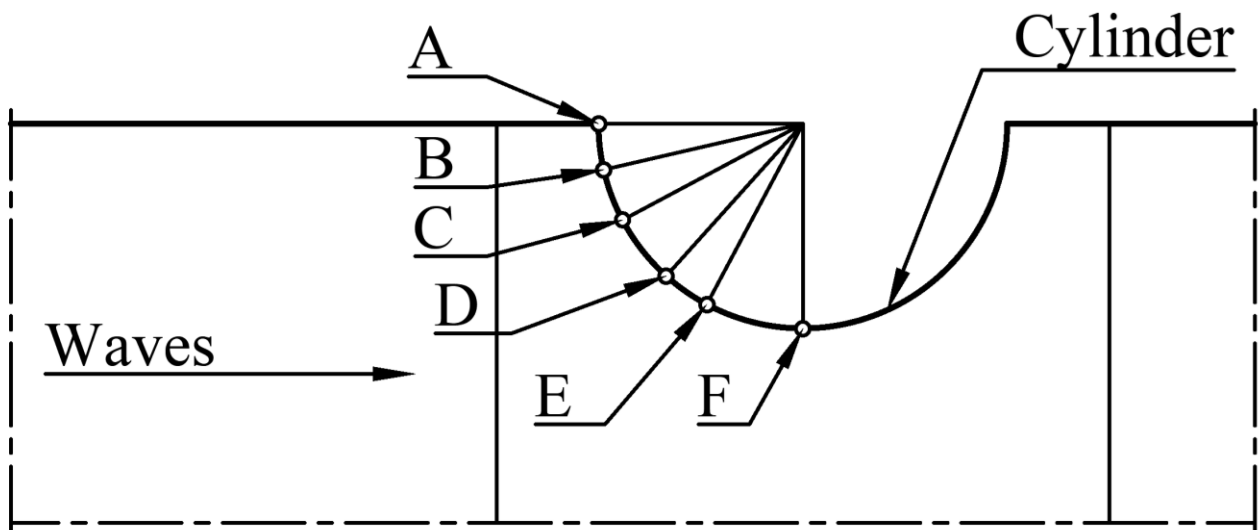


Figure 2-13 Overview of the locations where the pressure distribution around the cylinder is measured. A=0°, B=13°, C=28°, D=48°, E=62°, F=90°

2.6.2 Curling factor and slamming coefficient

The value of the curling factor was determined by the height over which the peak pressure (and thus force) is exerted on the cylinder. To determine the curling factor, the height of the impact was divided by η_b to find the value of λ by using Equation 12.

Equation 12 Curling factor

$$\lambda = \frac{S_I}{\eta_{b,WG11}}$$

This approach is different from Wienke and Oumeraci (2005) as they first determined the slamming coefficient using the in-line force around the cylinder at the location of the wave crest and then the curling factor. In this study, the curling factor was determined before the slamming coefficient. Veic and Sulisz (2018) did the same, first they determined the curling factor and then the slamming coefficient using the total impact force and not the in-line impact force. Using the total impact force is possible, as in a numerical study the total forces on the total structure can be accurately measured. However, the methodology of how they determined the curling factor is different than done in this study. They use the ratio of the overturning jet to the wave crest, while in this study the height over which the pressure is applied on the cylinder was used.

OpenFOAM only gives the total force in x-direction on the cylinder. To compute the value of the slamming coefficient, the force must be decomposed into a quasi-static and impact force. The separation was done using a smoother that applies a robust Locally Estimated Scatterplot Smoothing (LOESS). This method has been shown to be able to accurately separate the forces into the different parts and does not overestimate the peak of the quasi-static part (Tu and Muskulus, 2016) for waves breaking on a jacket structure. The span they apply for the smoother is 5% of the total length of the time series, which was also used in this research. Using the known impact force, the slamming coefficient was determined by rewriting Equation 3 to Equation 13 in the following format:

Equation 13 Slamming coefficient

$$C_s = \frac{F_I}{\rho * R * C_{WG11}^2 * \lambda * \eta_{b,WG11}}$$

Where C_s [-] is the slamming coefficient, F_I [N] the impact force, ρ [kg/m³] the density of the water, R [m] the radius of the cylinder, C_{WG11} [m/s] the wave celerity at wave gauge 11, λ [-] the curling factor and $\eta_{b,WG11}$ [m] the water level elevation at wave gauge 11.

η_b is taken from wave gauge 11, where the wave is almost breaking. According to the methodology by Wienke and Oumeraci (2005), the wave velocity was measured at the breaking location and averaged over the wave crest (Figure 2-14). The density is 1000 kg/m³ and the radius of the cylinder is 0.06 m, in accordance with the experiments of Dassanayake et al. (2019).

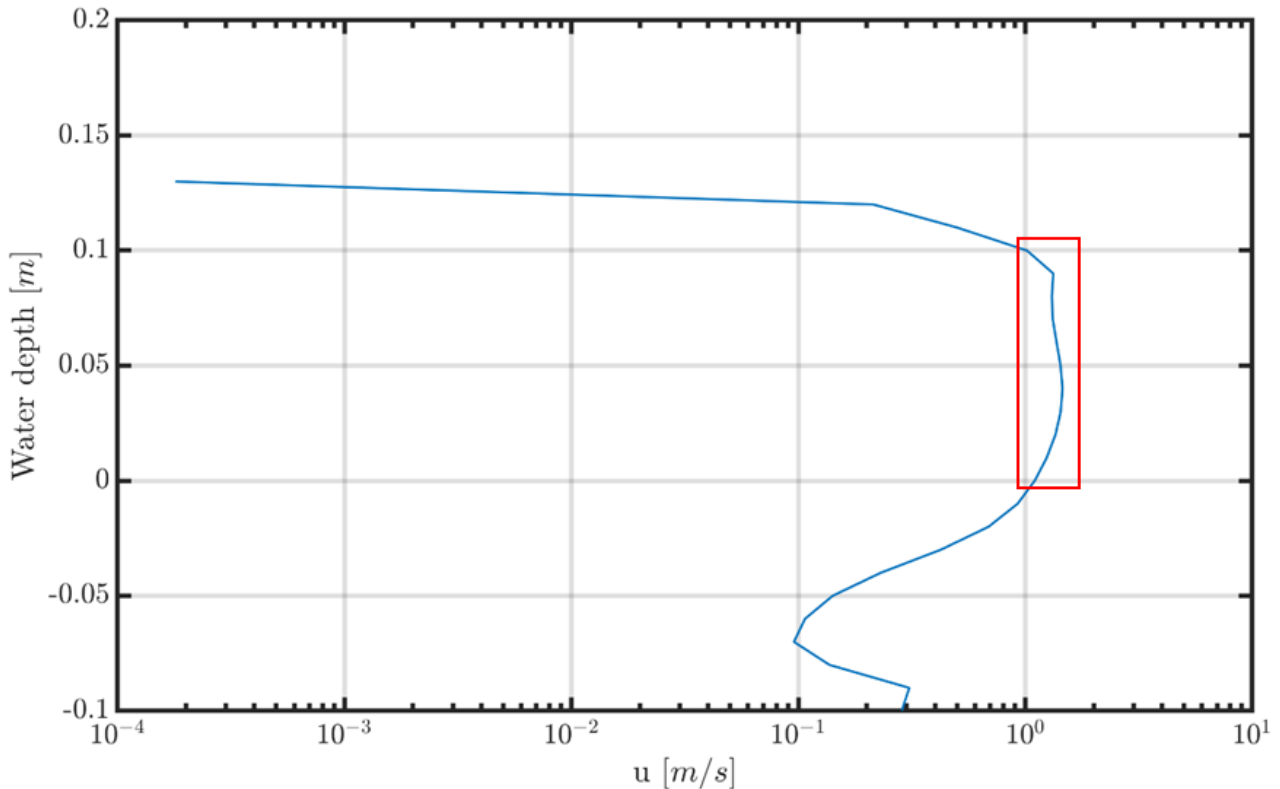


Figure 2-14 Example of used velocity profile. The average value of the part where the velocity profile is constant (red area) is used to determine the average velocity of the wave.

2.7 Computation cost

Four simulations were done to compare the computational cost for the two different solvers. First, the computational costs in 2D were compared and later the computational costs for a 3D simulation. For the 2D simulations 70 wave periods were compared. For the 3D simulations, the available data from before the simulations were stopped was used. They unfortunately were stopped due to a required reallocation of the computational resources.

Next, the 3D simulations did not start at the same time. The time difference between the starting points was determined to compare the computational costs. The range of data of the isoAdvect solver, which started earlier, that falls within this range was removed from the data set. This makes it possible to compare the data sets and analyse the computational costs per solver for a 3D simulation.

The simulations done for the 2D comparison of the computational effort were all run on the HPC (High Performance Computing) cluster of the Environmental Fluid Mechanics section of the Hydraulic Engineering department at the Faculty Of Civil Engineering and Geosciences of the Delft University of Technology. The 2D simulations ran at the same time on the same node with two processors for each of the simulations. The 3D simulations were done at the SHERLOCK HPC cluster of Stanford University. Both solvers utilised 20 processors in the 3D simulation.

The time step for the 2D simulations was set to a variable value to optimally make use of the Courant number. For the 3D simulations, the time step was set to a fixed value of 1/10,000 seconds.

3 Results

During the wave structure interaction, a lot of processes occur at the same time. Examples are wave breaking, the interaction of the wave with the shoal and then the interaction of the wave with the cylinder (Figure 3-1). The following sections include the results of the 2D model validation (3.1), the other wave states in 2D (3.2), the 3D model validation (3.3) and the calibration of the force components (3.4).

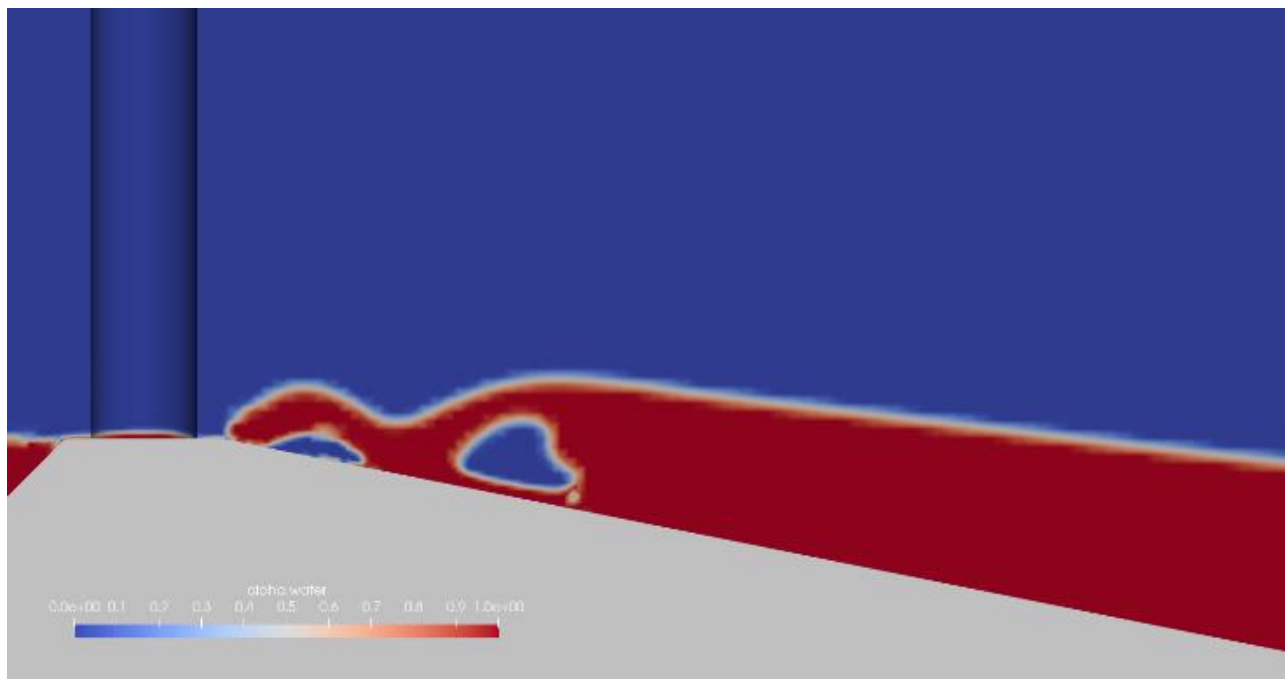


Figure 3-1 Impact of the wave onto the cylinder in the 3D simulation with isoAdvect

3.1 2D Model validation

Figure 3-2 shows the time series of the water level elevation for the different resolutions in OpenFOAM and the experimental data. In the numerical results, an oscillating trend with a return period of approximately 20 seconds is present in the NWT. This long wave can influence the results in terms of the computed amplitude, and thus the correlation between OpenFOAM and the experimental data. A range of data was selected which includes the long wave twice to average out its effect on the data set. In addition, the selected range of data excludes the first 60 seconds as there is some spin-up present in both the experimental and the OpenFOAM data. This results in using a data range of approximately 60-110 seconds in the 2D model validation.

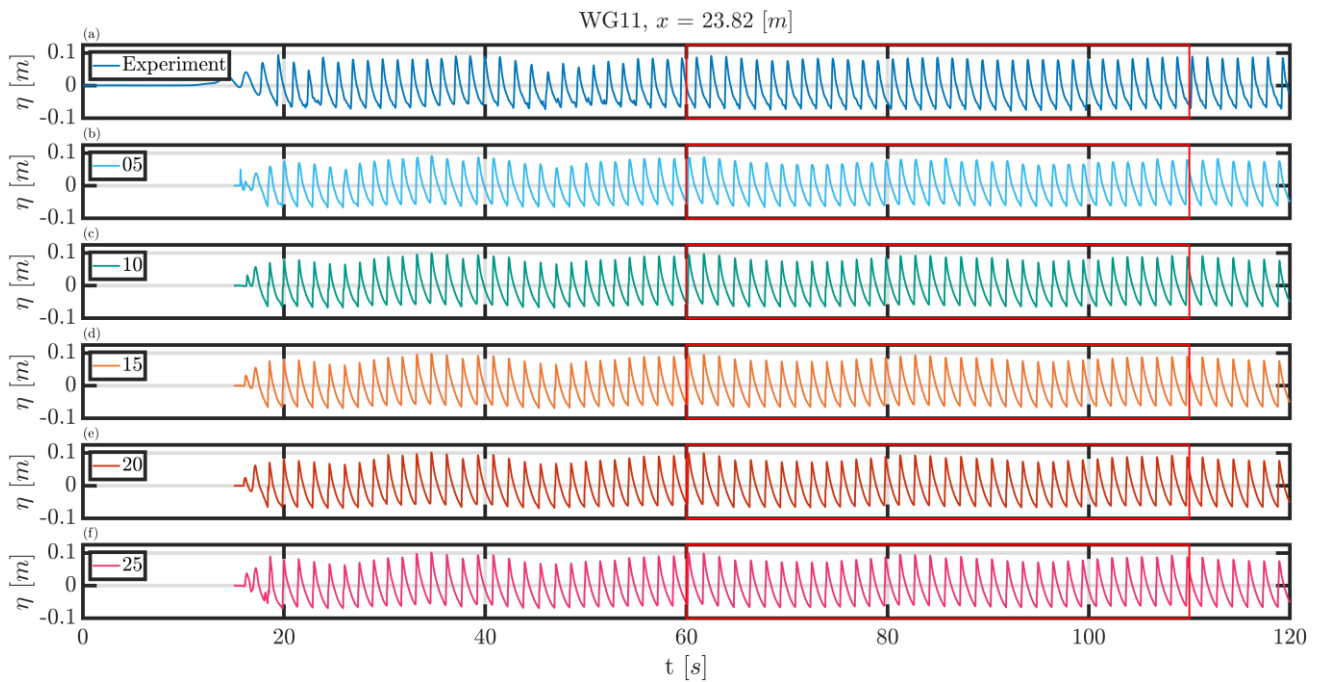


Figure 3-2 Overview of water level elevation at WG11. (a): the water level elevation as measured during the experiment. (b-f): the water level elevation measured with a resolution of respectively 5, 10, 15, 20 and 25 CPWH.

The frequency and amplitude of the data sets were assessed using a FFT (Figure 3-3). In the low frequency domain, i.e. around 0.05 Hz, a small peak in the data can be found. This small peak corresponds with the predicted 20 second period and thus corroborates the presence of the long oscillating wave in the NWT. The water level elevation time series show multiple higher harmonics in the frequency domain. A stream function was used to compute the water level elevation. According to Méhauté (1976), a stream function is of a 5th order and the data should then approximately contain 5 peaks. Figure 3-3 shows 6 distinctive peaks in the frequency domain, at a multiple of the theoretical frequency of 0.67 Hz. However, there are also some smaller peaks present at 4 Hz and higher.

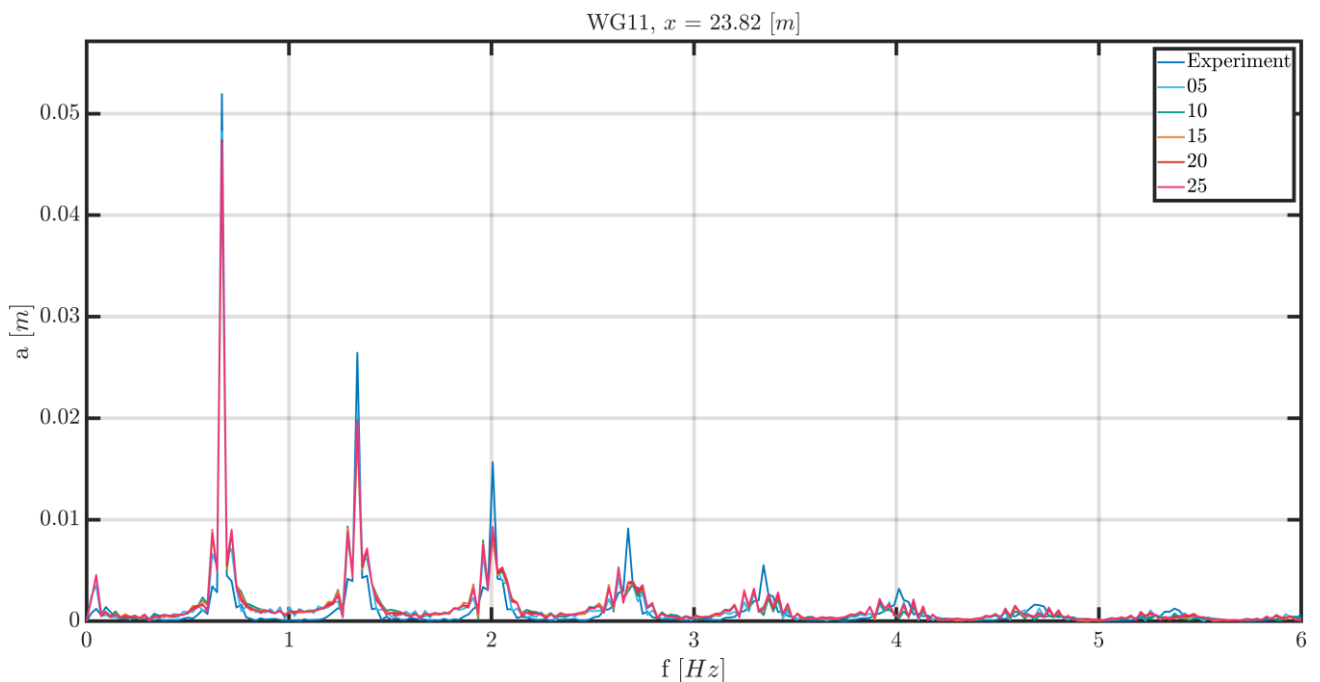


Figure 3-3 Overview of data at WG11. FFT of all resolutions compared with the experiment to analyse the frequency and amplitude of the waves.

There is a good agreement between the numerical and the experimental results regarding the wave period and wave amplitude (Figure 3-3 and Figure 3-4). However, there is a small difference in amplitude of the wave between the OpenFOAM and experimental results. Furthermore, there is a minimal difference between the amplitudes computed for the different resolutions in OpenFOAM.

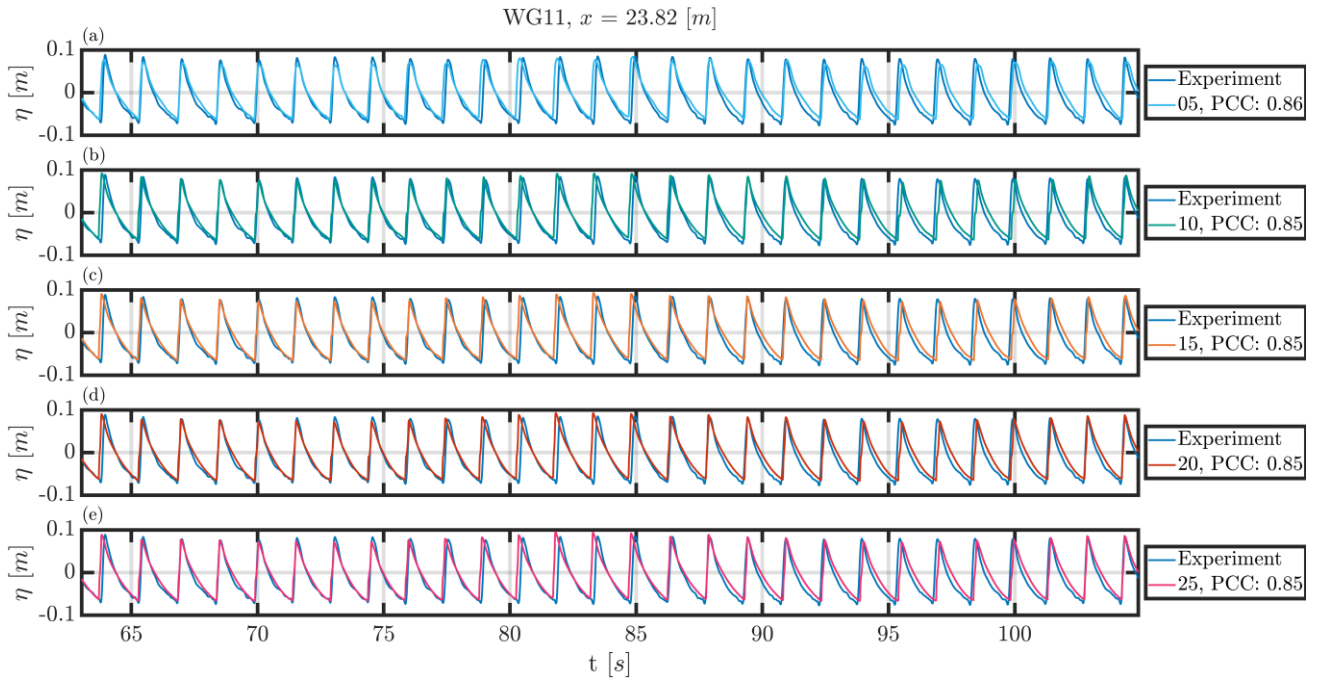


Figure 3-4(a-e): Overview of the selected time series for the different resolutions (b-e) per wave height compared to the experimental results (a).

Alignment of the data and comparing OpenFOAM with the numerical results presents a nearly identical time series with only a minimal difference in the crests and troughs of the waves (Figure 3-4). There is a small difference in time between the numerical and experimental peaks, but this can be caused by the procedure of aligning the data and possible small vibrations of the wave gauges in the experimental set-up. This is corroborated with the data in Figure 3-5 and Table 5, which show that the mean and median of the data sets are nearly identical. This strengthens the assumption that the numerical framework can generate waves with a similar wave period as the experimental data.

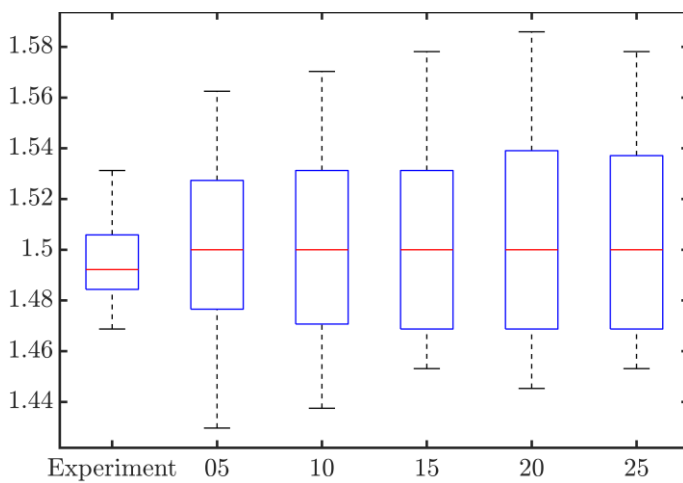


Figure 3-5 A boxplot of the wave period

Table 5 Overview of the median, mean and standard deviation for the wave period.

Data set	\tilde{x} [s]	\bar{x} [s]	S_X [s]
Experiment	1.49	1.50	0.017
05 CPWH	1.50	1.50	0.034
10 CPWH	1.50	1.50	0.038
15 CPWH	1.50	1.50	0.037
20 CPWH	1.50	1.50	0.038
25 CPWH	1.50	1.50	0.038

The comparison of the ensemble averages clearly shows that the numerical results slightly underpredict the peaks and troughs of the average wave shape (Figure 3-6). The wave shapes do not start and end at the same locations due to aligning of the shapes at their mean zero-up-crossing.

However, it is possible that the averaging process slightly influences the results by averaging out the peaks and troughs, the finer resolutions (15 CPWH and above) seem to generate better results when only assessing the shape of the wave (Figure 3-6). This is corroborated by an analysis of the wave height. The mean and median of the numerical and experimental results for 15 CPWH and higher are identical (Figure 3-7 and Table 5). There is a larger variation in the wave height for the numerical results, but this can be explained by the presence of the long wave in the NWT. Overall, the model can compute 0.15 metre and 1.5 seconds waves corresponding to the experimental data with a slight underprediction of approximately 6% of the wave height.

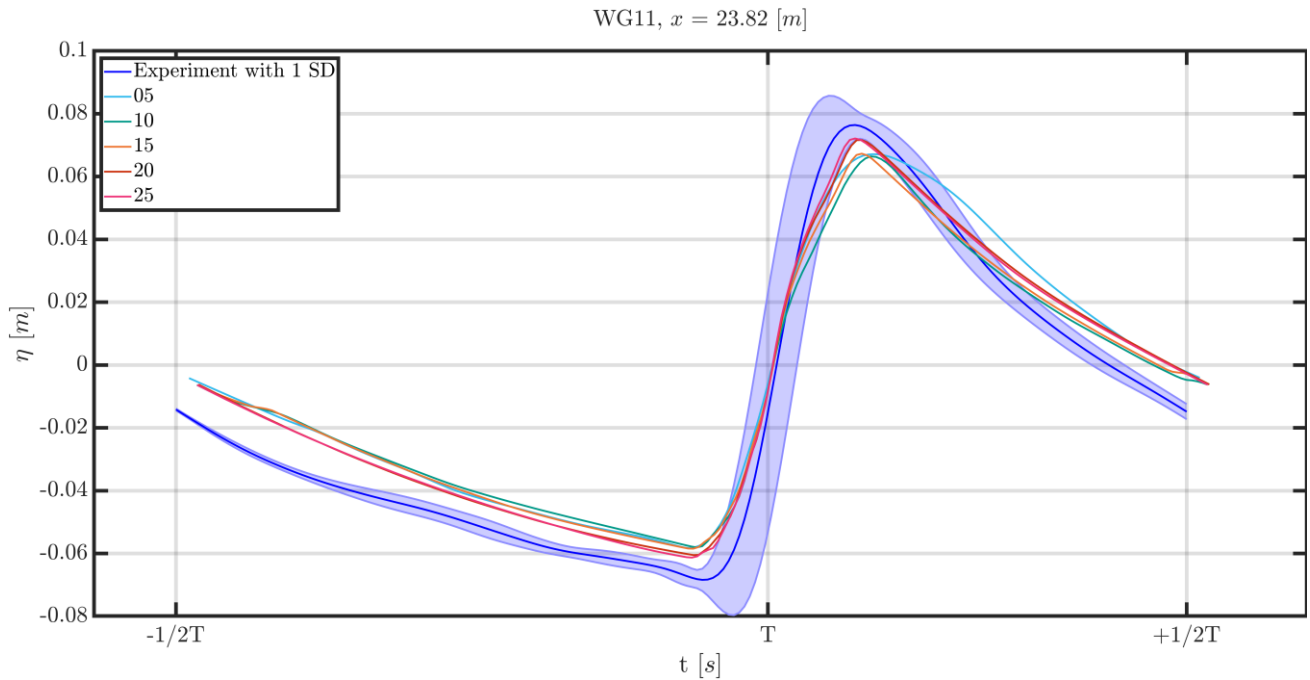


Figure 3-6 Comparison of the ensemble average wave shapes for the different resolutions and the experimental data at the location of $x = 23.82 \text{ m}$ where the experiment result is shown with 1 standard deviation. The OpenFOAM data shows only the ensemble mean without a standard deviation.

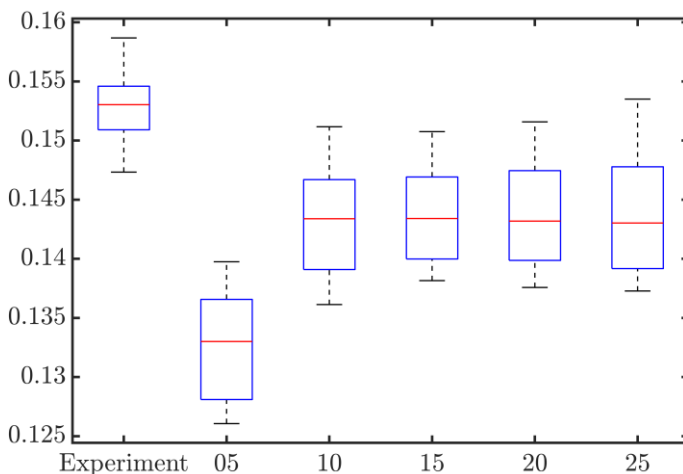


Figure 3-7 A boxplot of the wave height

Table 6 Overview of the median, mean and standard deviation for the wave height.

Data set	$\tilde{x} \text{ [m]}$	$\bar{x} \text{ [m]}$	$S_x \text{ [m]}$
Experiment	0.153	0.153	0.003
05 CPWH	0.133	0.133	0.004
10 CPWH	0.143	0.143	0.004
15 CPWH	0.143	0.144	0.004
20 CPWH	0.143	0.144	0.005
25 CPWH	0.143	0.144	0.005

The correlation with the experimental data is relatively high, the closer the waves get to the top of the shoal, the correlation between the experiment and OpenFOAM goes down (Figure 3-8a). The correlation is still close to 0.8 for broken waves. Furthermore, the error is a maximum 20% for regular and breaking waves but can go up to 24% for broken waves. Next, as can be clearly seen in Figure 3-8c, the numerical framework does underpredict the variation of the water level for all locations

except when the wave is already broken at WG12 where the model overpredicts the variance in the water level elevation.

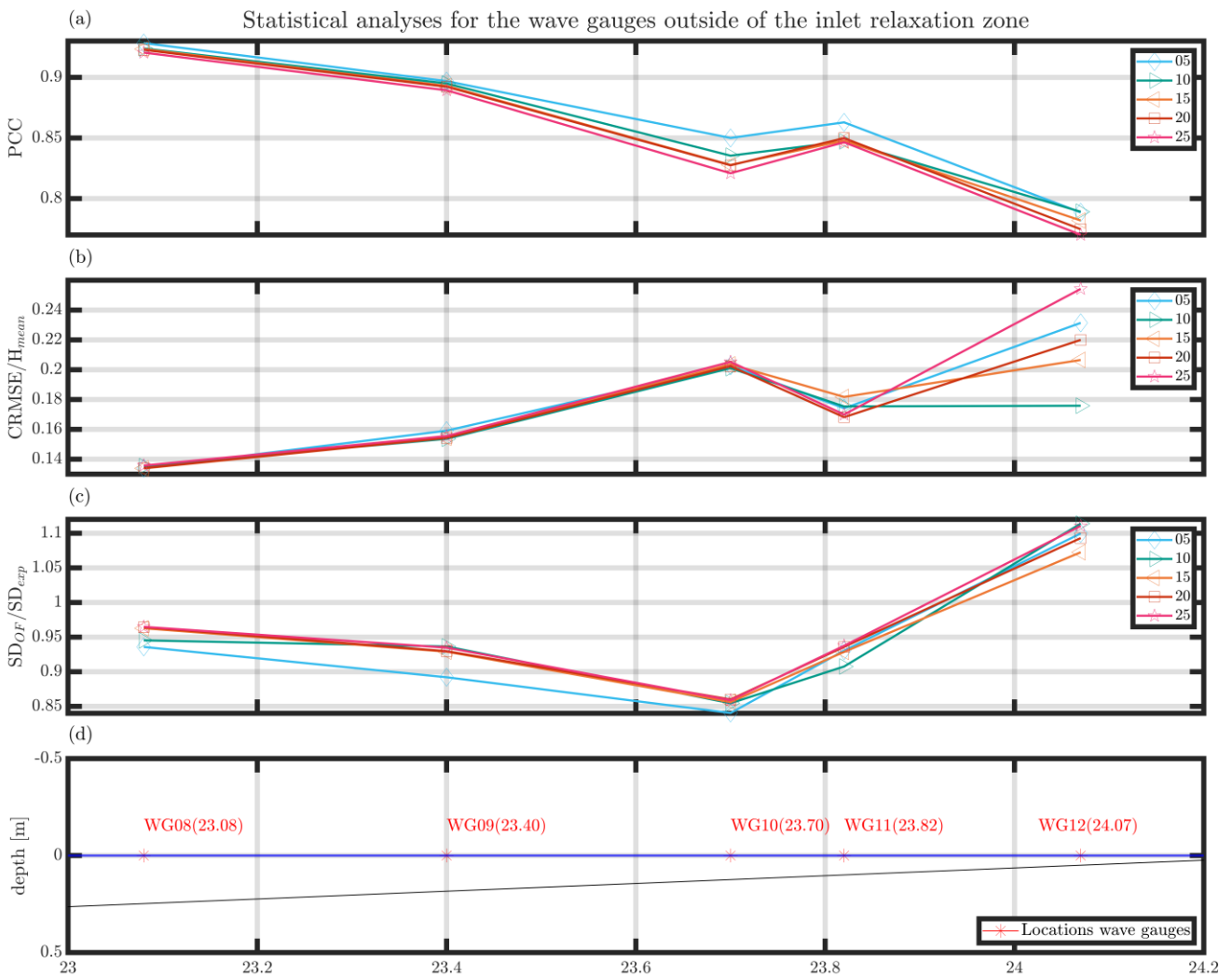


Figure 3-8 Overview of the performance of the model throughout the numerical wave tank, for 0.15 m and 1.5 s waves. (a): The Pearson Correlation Coefficient for the comparison of the time series. (b): The CRMSE/ H_{mean} for the time series. (c): The normalised Standard Deviation. (d): Indication of where on the slope measurements were taken.

All grid sizes at all locations perform similarly, except for WG12, where the waves are already broken (breaking of the wave happens between wave gauge 11 and 12). There is some difference between the 5, 10 and 15 CPWH but not much between 15, 20 and 25 CPWH. 15 CPWH appears to perform better after the wave is broken with the one of the lowest errors, highest correlation and the standard deviation that is closest to the experiment. Also, considering the needed computational resources 15 CPWH was chosen above 20 or 25 CPWH as the domain then already contains 1.5 million cells. Using a higher resolution than 15 CPWH would have resulted in a larger number of cells and consequently higher computational costs. The results of the other wave gauges can be found in Appendix B.

In the OpenFOAM simulations the dimensionless wall distance (y^+) is an important factor in the numerical simulation. This variable is important in the turbulence modelling and influences the wall functions used for the boundary and initial conditions. For the 2D model validation, the mean and median values per grid size were determined for the whole time series. The values of y^+ per resolution can be found in Table 7. y^+ is optimal below 30, as stated by Larsen and Fuhrman (2018).

Table 7 Overview y^+ values 2D model validation for 0.15 metre and 1.5 second waves

Grid size	Median	Mean
05 CPWH	53.05	100.29
10 CPWH	31.42	60.62
15 CWPH	23.60	46.62
20 CPWH	17.55	36.43
25 CWPH	14.91	29.10

Histograms of y^+ per grid size can be found in Appendix B.

3.2 Wave states

In addition to wave state 5, five other wave states were tested with the identified optimum resolution. Table 8 shows the results between the numerical and experimental results for wave gauge 11. The correlation for all wave states is relatively high with an error of 22% or lower.

Table 8 Overview statistics for wave gauge 11 ($x=23.82$ m) for all different wave states.

Variable	#1	#2	#3	#4	#5	#6
PCC	0.94	0.97	0.77	0.93	0.85	0.89
CRMSE/ H_{mean}	0.13	0.12	0.22	0.14	0.18	0.13
$SD_{\text{OF}}/SD_{\text{Exp}}$	0.89	0.82	0.93	1.11	0.93	0.94

As well there is a high correlation with the experimental data for the other locations in the NWT (Figure 3-9). All the different wave states are comparable to the experimental results with a high correlation. Except for two aspects, the correlation is always above 0.8 and the error is always below 25% of the mean wave height. The results vary from a near perfect representation of the experimental data for 0.05 metre and 2.44 second waves (Appendix D.2). However, there are also results where the trough of the wave is overpredicted and the crest is underpredicted, e.g. for 0.10 metre and 2.44 second waves (Appendix D.4).

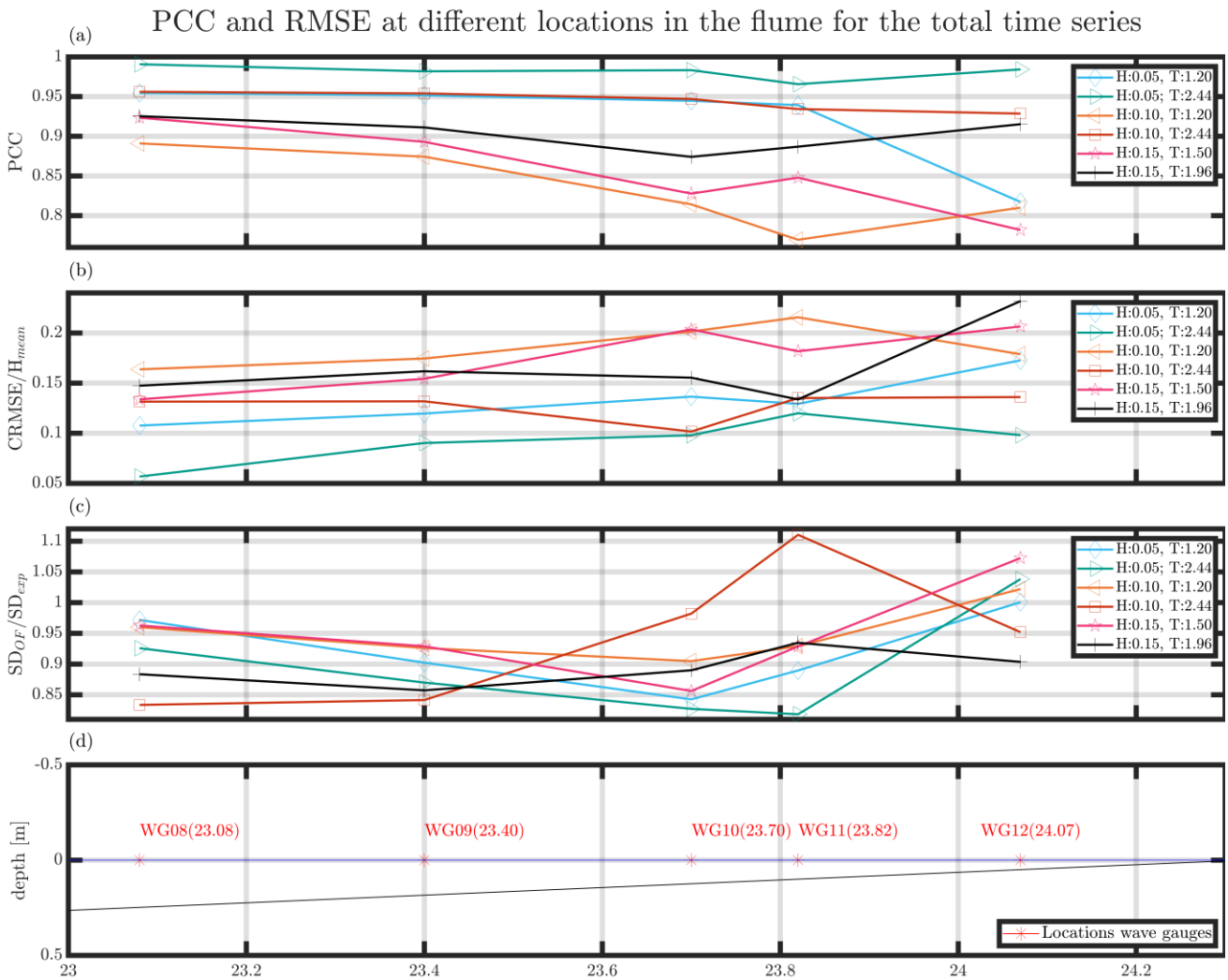


Figure 3-9 Overview of the performance of the numerical set-up for the different wave characteristics throughout the numerical wave tank compared to the experiments. (a): The Pearson correlation coefficient for the comparison of the time series. (b): The CRMSE/ H_{mean} for the time series. (c): The normalised Standard Deviation. (d): Indication of where on the slope measurements were taken.

A detailed overview of the plots for the different wave states, per wave gauge and histograms for y^+ can be found in Appendix D.

3.3 3D Model validation

The 3D model validation focused on two aspects. The water level elevation and the total force in the x-direction computed by OpenFOAM. Unfortunately, the 3D OpenFOAM simulations had to be stopped prematurely due to reallocating of the computational resources and thus the data sets do not have the same number of datapoints. Since the MULES data set is the shortest, the same range of the datapoints was taken from both the experimental and isoAdvectord data sets.

The force time series of the experiment appears to have a pattern where there is a downward trend of the peak force over time (Figure 3-11). This makes the peaks at the end of the time series correspond better with the isoAdvectord and MULES results. Therefore, a range of data from the last part of the experimental and isoAdvectord data set is used in the analyses. The data range used for the three data sets are:

- Experiment: 77.51 - 119.06 seconds
- isoAdvectord: 17.23 – 58.78 seconds
- MULES 17.22 – 58.77 seconds.

3.3.1 Water level elevation

Figure 3-10 shows a summary of the water level elevation comparison for the 3D simulation. There is a significant difference between the 3D and 2D simulations, especially in the correlation with the experimental data set. The maximum correlation of 0.95 versus a maximum correlation of 0.8 for the 2D and 3D simulations, respectively (Figure 3-10 versus Figure 3-8). This indicates that there is a larger error for the 3D simulation compared to the 2D simulation. However, the differences can be attributed to the limited amount of data that can be compared and the fact that the data is not from the same time range. Which is the case for the 2D simulation.

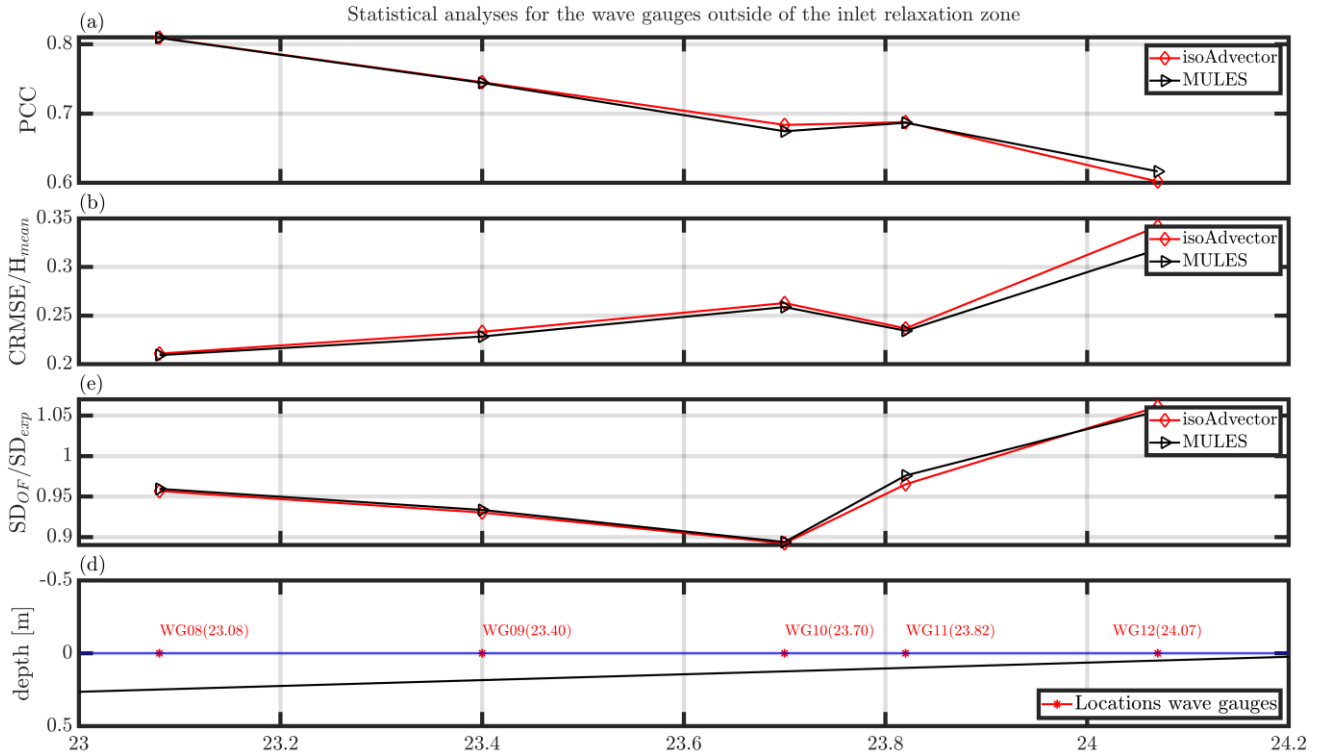


Figure 3-10 Overview of the performance of the two solvers for the 3D case throughout the numerical wave tank compared to the experiment. (a): The Pearson correlation coefficient for the comparison of the time series. (b): The CRMSE/H_{mean} for the time series. (c): The normalised Standard Deviation. (d): Indication of where on the slope measurements were taken.

However, both isoAdvect and MULES computed comparable results with minimal differences between the two solvers. Furthermore, the numerical results still have a significant correlation with the experimental data. Plots of the water level elevation, frequency analysis and ensemble average wave per wave gauge can be found in Appendix E.

Table 9 shows an overview of the y^+ values for the 3D simulations. It is noteworthy that with the exact same mesh, the values for isoAdvect are slightly larger than for MULES. The slightly larger values for isoAdvect can be caused by a larger velocity computed by isoAdvect. The histograms and average values of y^+ per cell can be found in Appendix F.

Table 9 Overview y^+ values 3D simulations

Data set	Median [-]	Mean [-]
isoAdvect	20.56	35.45
MULES	19.97	33.59

3.3.2 Force comparison

The force time series used in the analyses for the three different data sets are shown in Figure 3-11. This figure shows that there seems to be a long regular wave present of approximately 20 seconds in

the numerical results. This is confirmed by the frequency domain of the force time series (Figure 3-12). This long wave is not present in the experimental results. An overview of the complete force time series and the parts that are selected can be found in Appendix G.

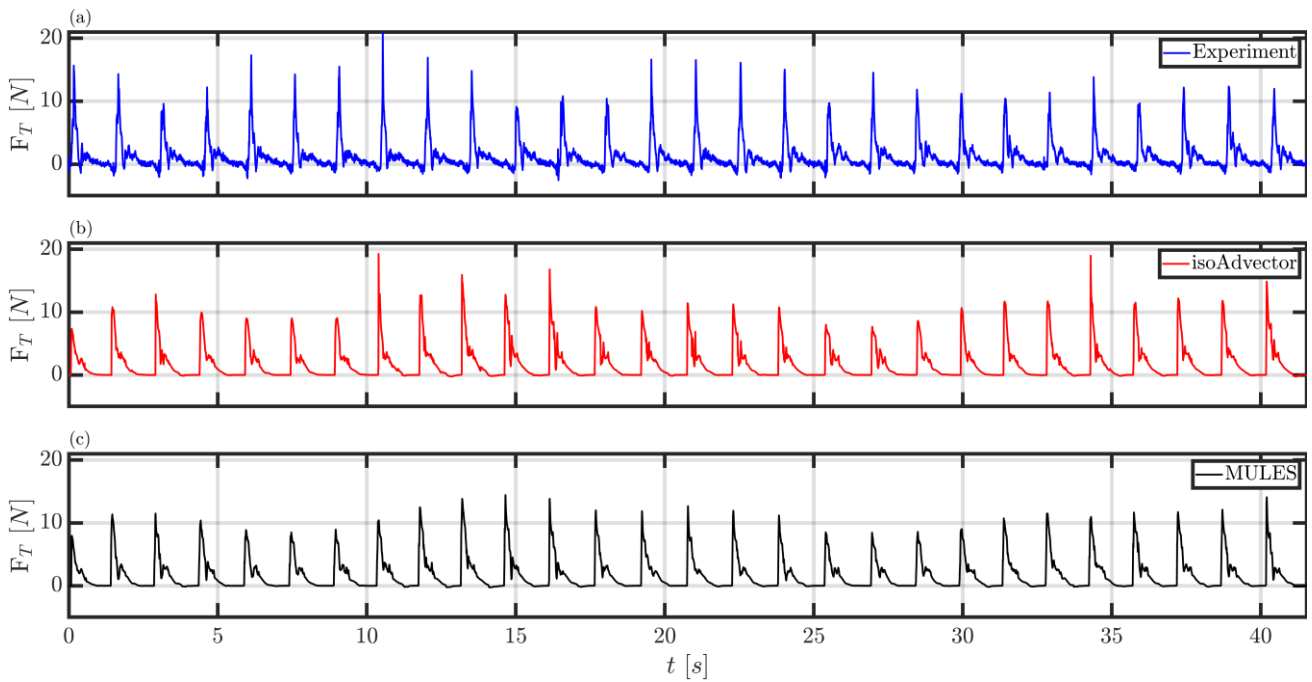


Figure 3-11 Overview time series force from the used in the analyses. (a): Experimental, data used: 78.60 - 119.35 seconds. (b) isoAdvectord, data used: 64.63 - 105.38 seconds. (c) MULES, data used: 16.57 - 57.32 seconds.

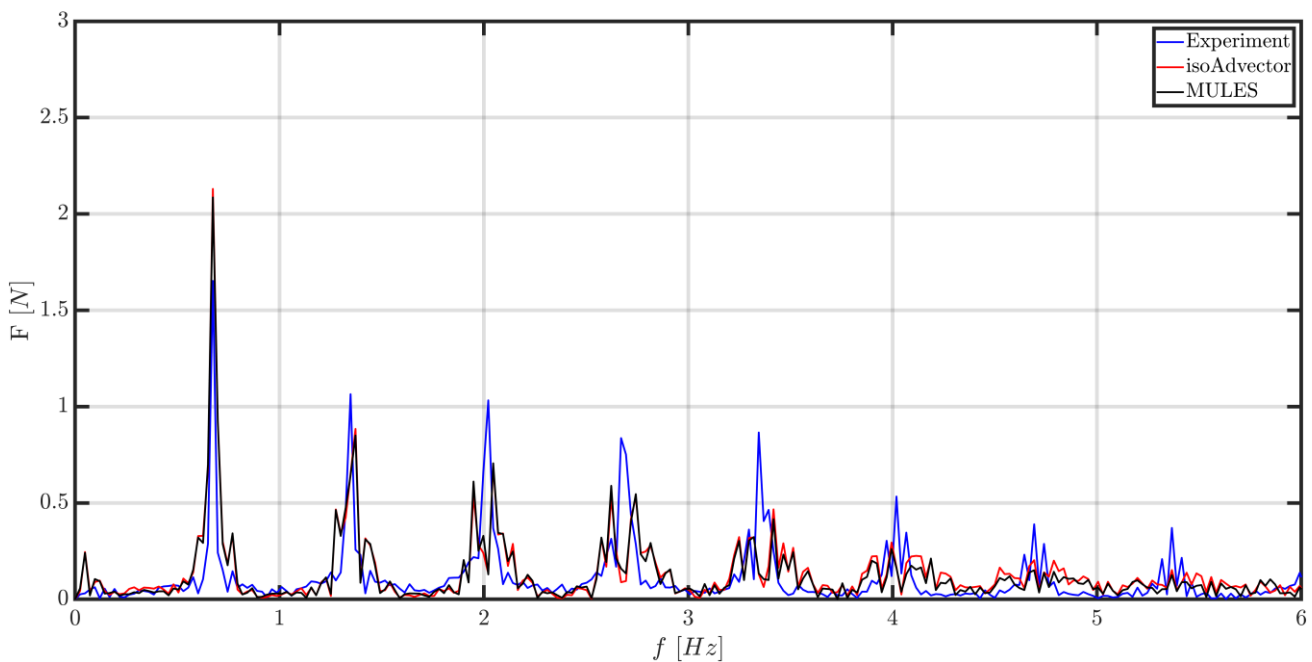


Figure 3-12 Overview time spectral analysis of the force. (a): Experimental (b) isoAdvectord (c) MULES

The clear difference between the three data sets is the magnitude of the peak forces. In the experimental data set, there are more peaks of a larger magnitude than MULES or isoAdvectord. This is confirmed by the statistical analyses of the peak forces (Figure 3-13 and Table 10). The medians for the three data sets are relatively close to each other and for the OpenFOAM results nearly identical. The mean values are also relatively close to each other with small differences, as can be seen when assessing the average force signal shape (Figure 3-14). However, the MULES data set

does seem to have significantly fewer peaks of a large magnitude (maximum 14 N) compared to isoAdvectord (maximum 19 N) and the experimental data (maximum 21 N). This is confirmed with the smaller spread of the data in the boxplot and the smaller standard deviation. The difference between the OpenFOAM results can be explained by the sharper interface of isoAdvectord. With a sharper interface, the wave is spread out over fewer cells, the incoming wave then contains less air. When hitting the structure, the wave is less spread out and the energy of the wave is more focused. Furthermore, the force is dependent on the velocity of the wave. The isoAdvectord method can generate higher velocities at the interface compared to MULES. This is important as the velocity also influences the magnitude of the force. The combination of either of these processes can explain the difference between isoAdvectord and MULES.

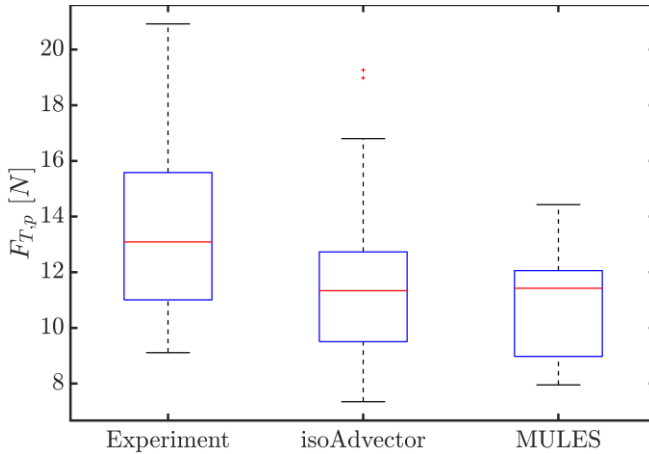


Table 10 Overview of the median, mean and standard deviation for the peak total force.

Data set	\tilde{x} [N]	\bar{x} [N]	S_x [N]
Experiment	13.10	13.40	2.93
isoAdvectord	11.30	11.70	3.08
MULES	11.40	11.10	1.88

Figure 3-13 A boxplot of the peak total force in x-direction

The slight difference between the mean peak forces for MULES and isoAdvectord can also be found in the ensemble average of the force signals (Figure 3-14). Since the waves are regular, an ensemble average of the force signal is made. This was used to analyse the average force and compare the results between the three data sets. Same as for the previous figures (Figure 3-11; Figure 3-13), the experimental data has a slightly larger mean peak value compared to isoAdvectord and MULES. Overall, the differences between the ensemble averaged signal are minimal. The largest differences are the rising time and the trough in the force at 0.2 seconds (Figure 3-14).

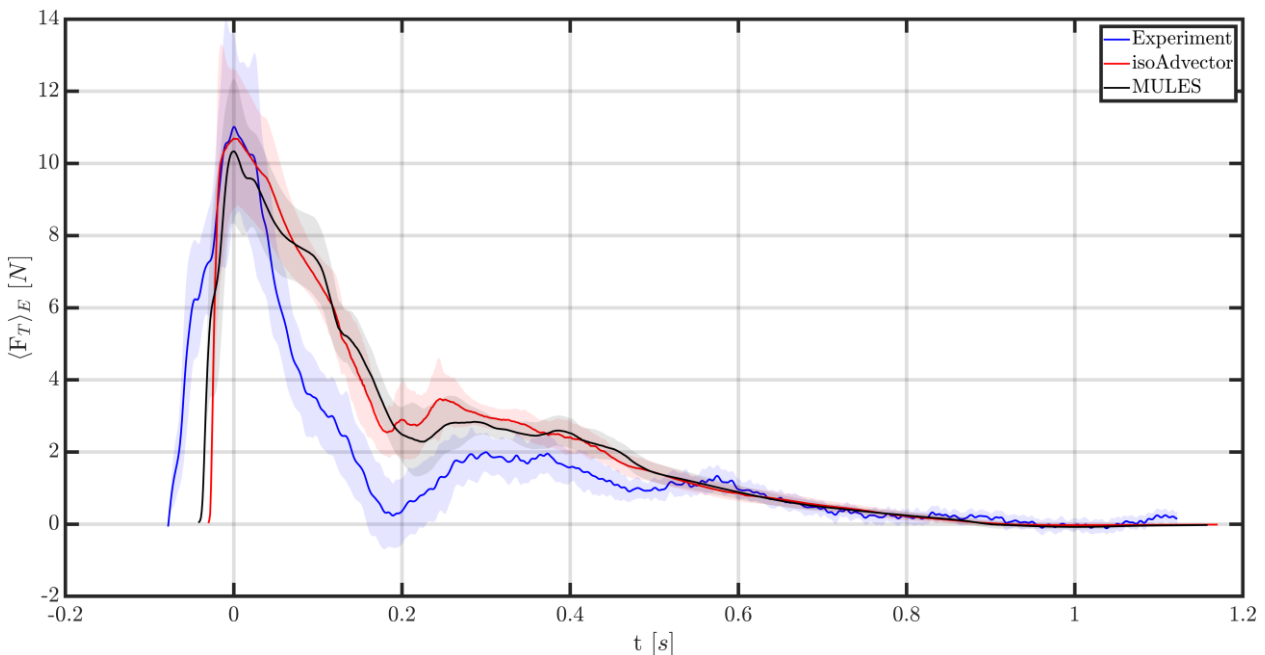


Figure 3-14 Ensemble average force signal for the three different data sets. The signals are aligned at the peak force.

The difference in rising time between the numerical and physical results can be explained by the post-processing of the experimental results, this can lead to a longer rising time. Overall, the rising time for the OpenFOAM results is less than half of the rising time for the experimental data (Figure 3-15 and Table 11). The difference between the OpenFOAM results can again be explained by the sharper interface for isoAdvector. With the sharper interface, the first part of the wave will reach the structure just a bit later than for MULES. This creates a more instantaneous impact and thus results in a shorter rising time for isoAdvector.

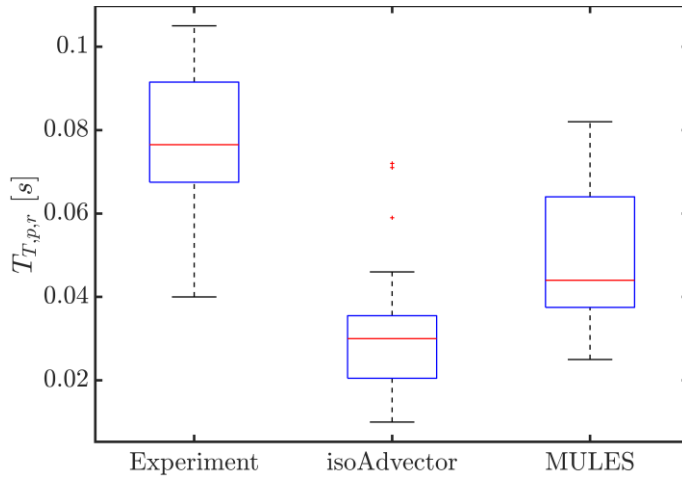


Table 11 Overview of the median, mean and standard deviation for the rising time.

Data set	\tilde{x} [s]	\bar{x} [s]	S_x [s]
Experiment	0.077	0.078	0.015
isoAdvector	0.030	0.031	0.016
MULES	0.044	0.047	0.015

Figure 3-15 A boxplot of the rising time for the total force on the cylinder in x-direction

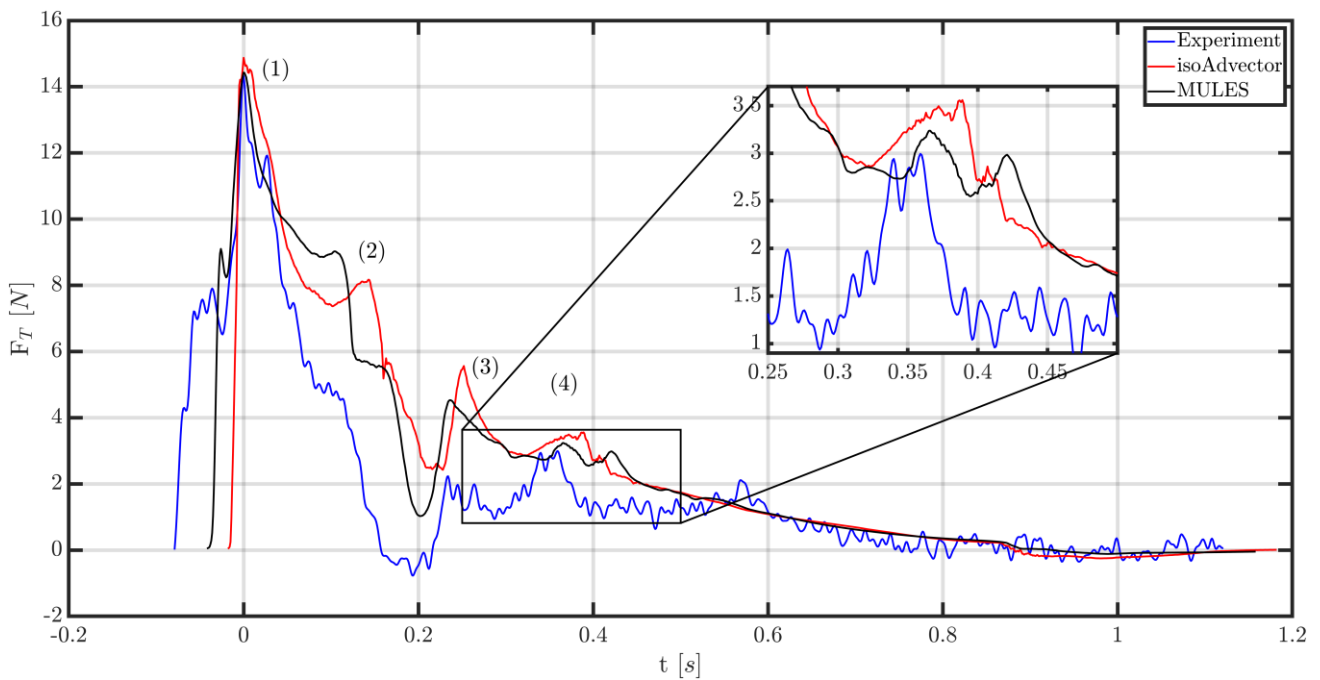


Figure 3-16 Single peak analysis for the three different data sets where the data sets are aligned at the peak. The experiment peak is from $t=1.66$ seconds, isoAdvector, $t=40.20$ seconds and MULES $t=14.65$ seconds. (1), (2) and (3) indicate the peaks present in the signals. The secondary load cycle is shown in the zoomed in plot.

Figure 3-16 shows a comparison of a single force signal from each of the three data sets. This comparison is proposed because the features of the individual force signals are smeared out by the averaging process used for the ensemble. This is due to the slightly different timing of each event. For the comparison, the maximum peak of the MULES data set was used and peaks that are as close to this peak value were selected from the isoAdvector and experimental results. The figure again clearly shows the difference in the rising time and the behaviour of the signal after the peak force (Figure 3-16).

There are several peaks present in the force signal. First there is a peak at 0 seconds (1), this peak is caused by the initial and violent impact of the (aerated) water body on the cylinder. Then there is a peak just after 0.2 seconds (2), this peak is caused by the water body that initially moved upwards now decelerates and starts falling downwards until it reaches the bottom of the shoal. This generates a large pressure gradient and thus a peak in the force. The third peak (3) is at approximately 0.25 seconds and is caused by the remainder of the water mass that arrives at the structure.

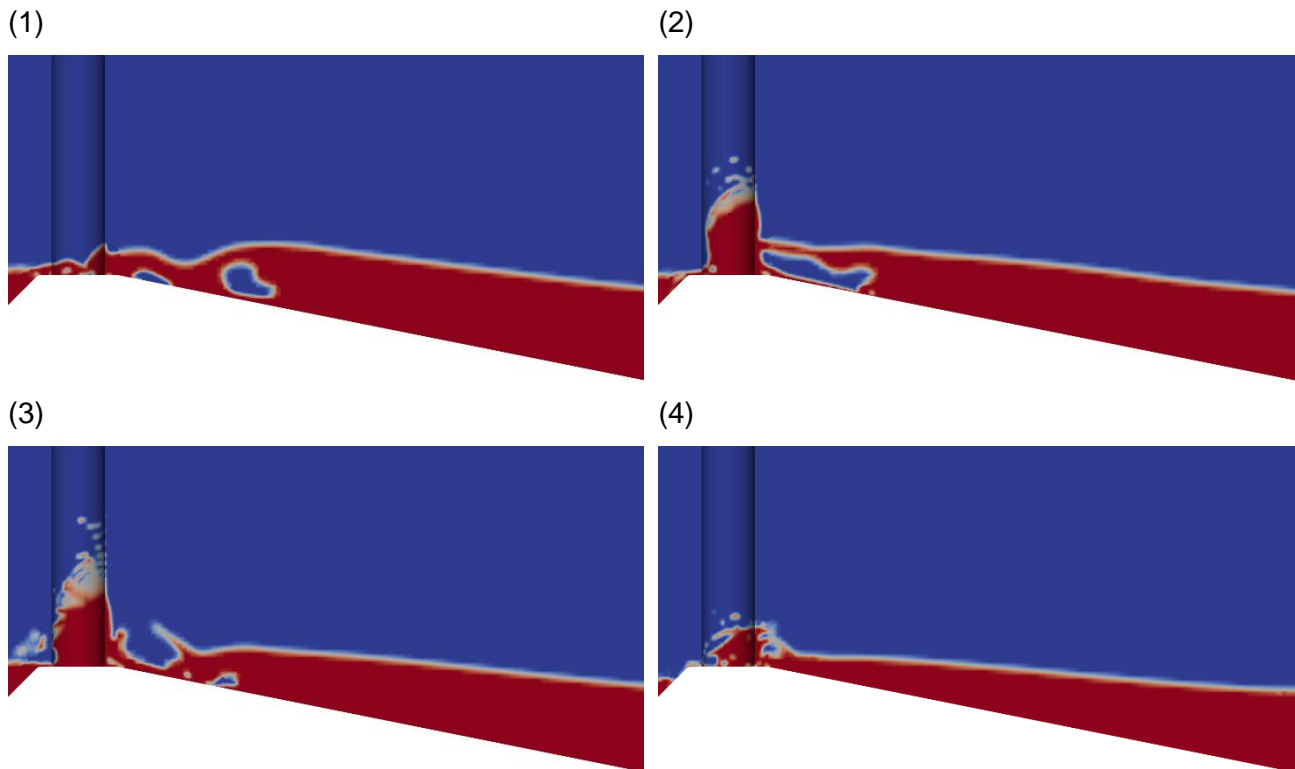


Figure 3-17 Overview of the instances of the peaks in the force signal for isoAdvector. Where white is the shoal, red is only water, dark blue is air and everything between is a mix of water and air.

The fourth peak (4) present in the signal is another small load cycle around 0.4 s. The peak is almost invisible when compared to the preceding ones, but it is present as can be seen in the zoomed plot in Figure 3-16. The magnitude of the secondary load cycle peaks for isoAdvector, MULES and the experiment are 6.4%, 4.4% and 12.5% of the total peak force. The period of the secondary load cycle for isoAdvector, MULES and the experiment are 6%, 6.67% and 6.67% of the wave and thus force period, respectively.

Overall, the model can compute force signals that are comparable to the experimental data. Even with smaller peak values of the force signals, the average and single peak comparison correspond well with the experimental data. This is the case for both MULES and isoAdvector. This indicates that the model is able to compute similar results as the experimental data. Therefore, the model can be used to calibrate the coefficients of the breaking wave methodology for broken waves.

3.4 Calibration of coefficients

The OpenFOAM data sets was used to assess the pressure on the cylinder, the point of application of the force, the curling factor, the decomposition of the forces and the slamming coefficient for the two different solvers. Furthermore, the differences between the results computed with isoAdvector and MULES were assessed.

3.4.1 Pressure distribution

The figures with the pressure distribution at the centre line of the cylinder due to the wave impact for isoAdvect (Figure 3-18) and MULES (Figure 3-19) show several variables. First, the average pressure distribution was computed. This was done by taking the average of all the instances of the pressure distribution at the time of the peak impact forces. Furthermore, based on the average pressure distribution, the height of the impact ($\lambda * \eta_b$) and centre point of the pressure are presented.

There are two distinct differences between the two average pressure distributions: The shape and the magnitude of the standard variation. Interestingly, both solvers have a double peaked, rather than triangular or uniform, distribution of the pressure. All previous research on breaking wave impact noted a uniform or triangular pressure distribution (Kyte and Tørum, 1996; Wienke and Oumeraci, 2005). The shape of the pressure for MULES has a larger difference between the peak (2500 N/m²) and the trough (1900 N/m²) than the peak (2500 N/m²) and trough (2300 N/m²) for isoAdvect. This makes the MULES pressure distribution more double peaked than isoAdvect. Next, the difference in the standard deviation is explained by the larger peak forces present in the isoAdvect time series as shown in Figure 3-13 and Table 10. Besides these differences, the centroid, and the height of the impact for the average pressure are almost identical. The application point and pressure distribution can be used in stability and strength calculations of structures located on a similar location.

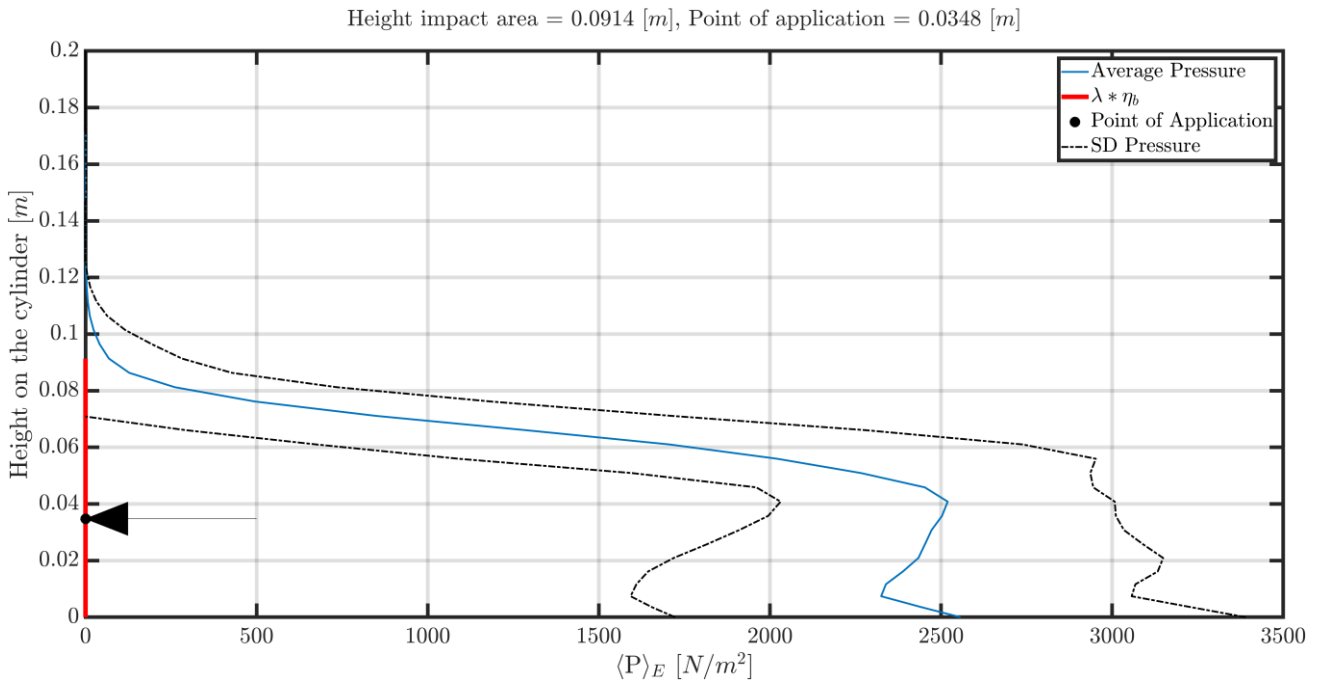


Figure 3-18 Average pressure distribution for the instances of the peak forces on the cylinder for the isoAdvect solver. Both the height of the impact and the point of application are determined based on the mean pressure profile

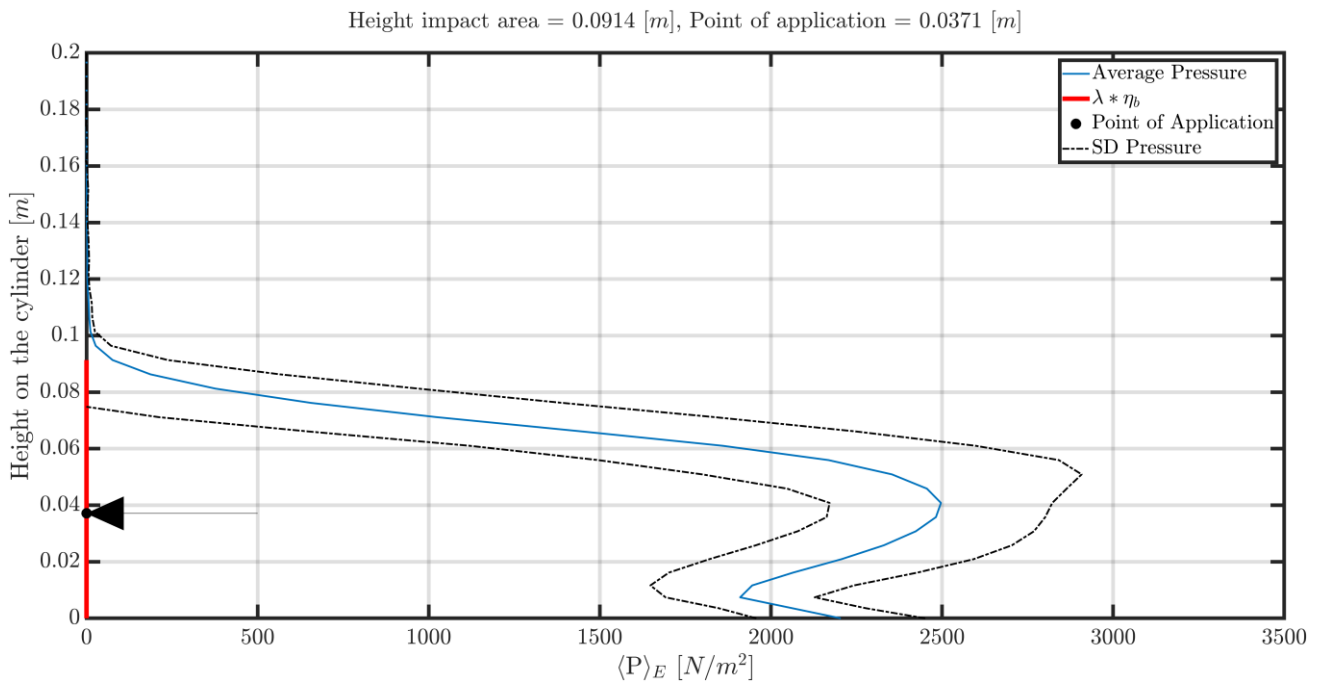


Figure 3-19 Average pressure distribution for the instances of the peak forces on the cylinder for the MULES solver. Both the height of the impact and the point of application are determined based on the mean pressure profile

The centre point of the pressure is normalised with the height of the impact to assess the point of application on the structure. The point of application is approximately 43% of the height over which the pressure affects the cylinder (Figure 3-20 and Table 12). Both data sets show similar results in both mean, median and the standard deviation.

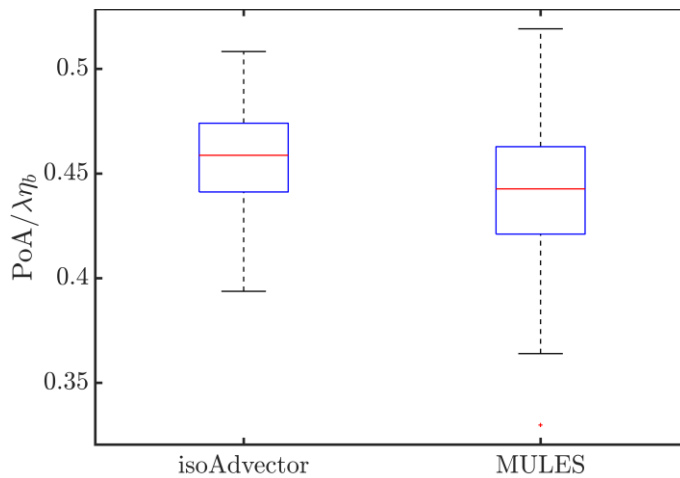


Figure 3-20 A boxplot of the point of application normalised with the height of the impact

Table 12 Overview of the median, mean and standard deviation for the normalised point of application of the force.

Data set	\tilde{x} [-]	\bar{x} [-]	S_x [-]
isoAdvectord	0.44	0.44	0.030
MULES	0.42	0.42	0.039

The radial pressure distribution is the next point of interest. The pressure distribution for both solvers is largest in the first 30 degrees and then goes rapidly down to approximately 20% of the maximum (Figure 3-21 and Figure 3-22). At 28 degrees, the pressure is already significantly lower and from 48 degrees onwards the contribution seems to be nearly insignificant compared to the middle of the cylinder. This corresponds with previous findings from Wienke and Oumeraci (2005) who also note that the pressure is focused in the first 30 degrees of the cylinder during the peak impact.

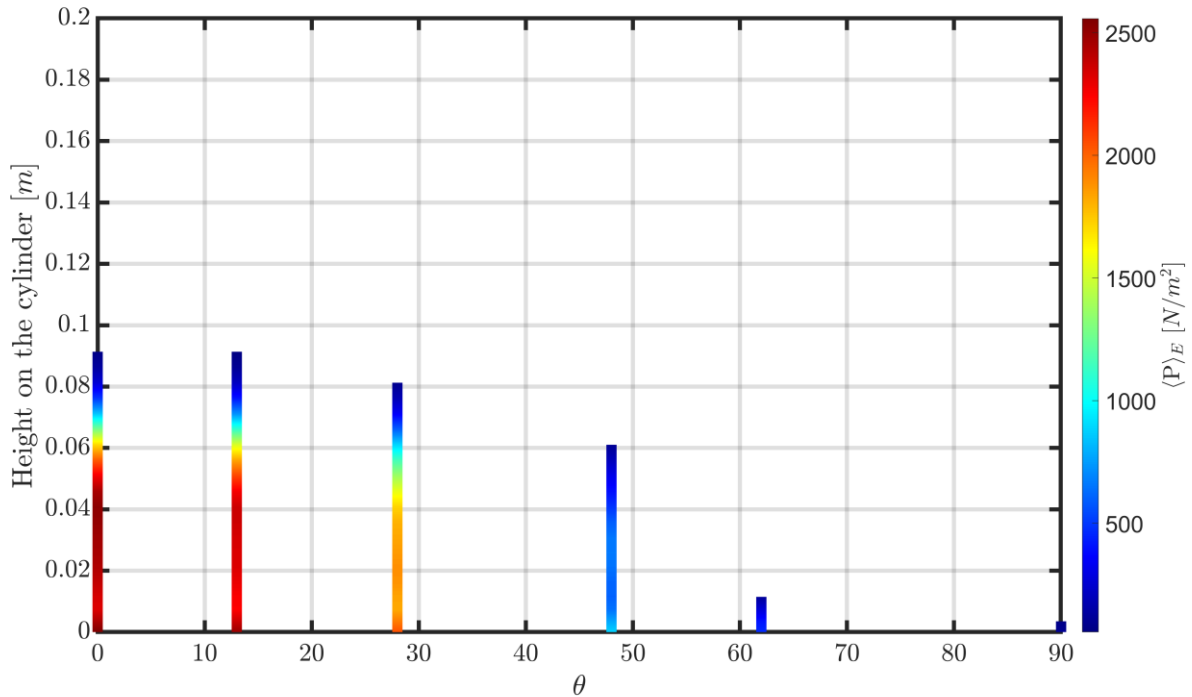


Figure 3-21 Average pressure distribution on the different locations of the cylinder for the isoAdvector solver

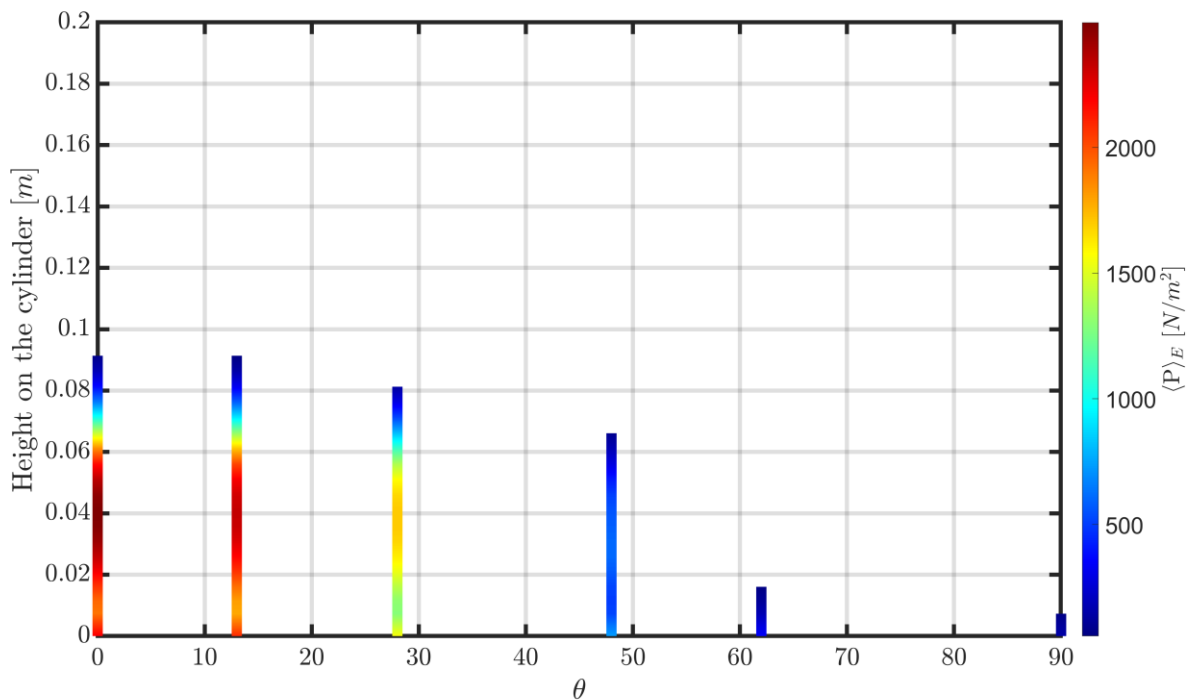


Figure 3-22 Average pressure distribution on the different locations of the cylinder for the MULES solver

These results can lay the foundation for the development of the formulation of impulsive loads due to broken waves and improve the assessment of lighthouses. Both Antonini et al. (2019) and Dassanayake et al. (2021) used the formulation proposed by Wienke and Oumeraci (2005) with a clear overestimation of the load. However, the radial distribution proposed by Wienke and Oumeraci (2005) is in good agreement with the proposed findings in Figure 3-21 and Figure 3-22.

3.4.2 Curling factor and slamming coefficient

The curling factor for both solvers varies significantly (Figure 3-23 and Table 13). Even though the interquartile ranges of the boxplot overlap, there is a large difference between the two data sets. However, despite the disagreement between the MULES and isoAdvectord solver, the curling factor is nearly twice larger than the proposed value of 0.46 for breaking waves by Wienke and Oumeraci (2005) or Goda et al. (1966). For isoAdvectord a value of 0.81 was found, while for MULES a value of 0.93 was found. The main difference in the results can, again, be explained by how the two solvers compute the interface between water and air. The sharper interface computed by isoAdvectord can lead to the water being less spread out on the cylinder and thus leading to a smaller curling factor compared to MULES.

Furthermore, from the data indicates that the curling factor can be larger than 1. This indicates that the height of the pressure is distributed on the cylinder can be larger than the water level elevation of the breaking wave. This can be mainly due to the bounce of the water jet generated by the broken wave on the shoal (Figure 3-24).

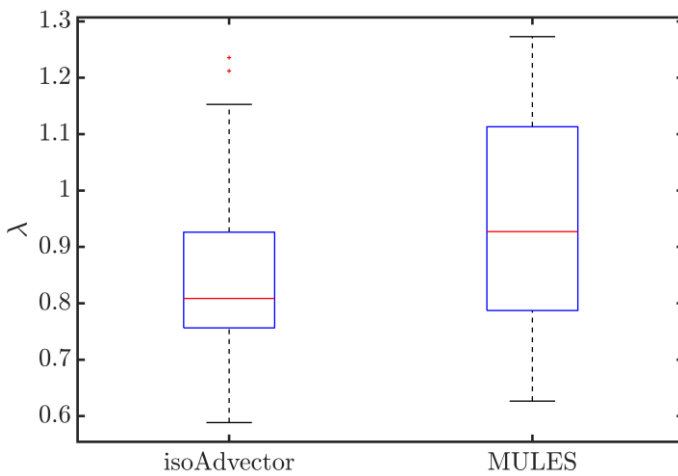


Figure 3-23 A boxplot of the curling factor

Table 13 Overview of the median, mean and standard deviation of the curling factor.

Data set	\tilde{x} [-]	\bar{x} [-]	S_x [-]
isoAdvectord	0.81	0.85	0.168
MULES	0.93	0.95	0.187

The larger value of the curling factor compared to breaking wave cases can be attributed to how the shoal affects the propagating of the wave to the cylinder. The influence of the shoal after the wave is broken highly influences the curling factor. When the wave is breaking due to the shoal, the wave first slams into the shoal (Figure 3-24a), generating an upward bore that propagates towards the cylinder (Figure 3-24b). Which again hits the shoal at the toe of the structure before violently impacting the cylinder (Figure 3-24c). During the moment of impact, the wave spreads out over the cylinder as shown in Figure 3-21 and Figure 3-22 and Figure 3-24d. Figure 3-25 shows the same process for the MULES solver. A comparison of Figure 3-24b with Figure 3-25b shows that for the same time step the results computed by the MULES solver show a bore that is closer to the cylinder than for the isoAdvectord solver. Furthermore, comparing Figure 3-24c with Figure 3-25c shows that indeed for MULES the wave reaches higher up the cylinder than for isoAdvectord.

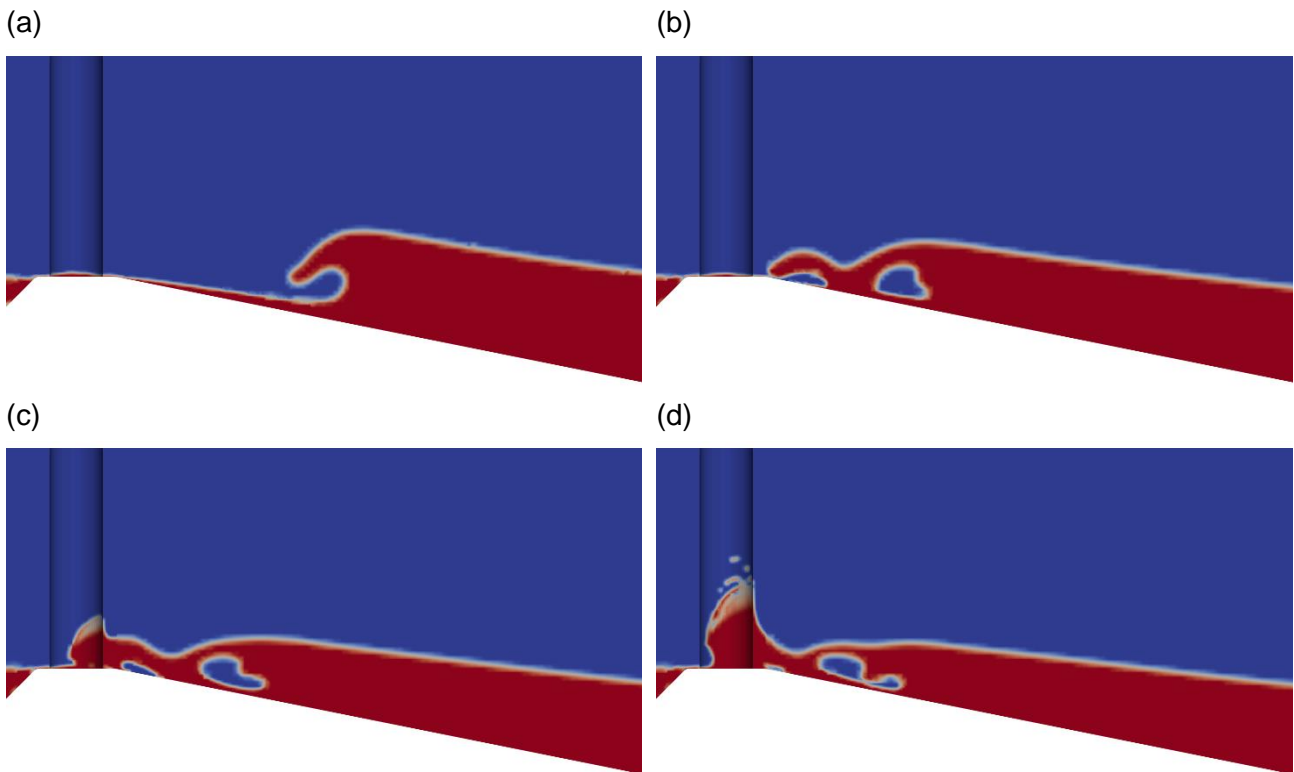


Figure 3-24 Overview of breaking process for isoAdvector. Where white is the shoal, red is only water, dark blue is air and everything between is a mix of water and air. (a) $t_1=55.7$ s. (b): $t=t_1+0.2$ s. (c): $t=t_1+0.25$ s. (d): $t=t_1+0.3$ s

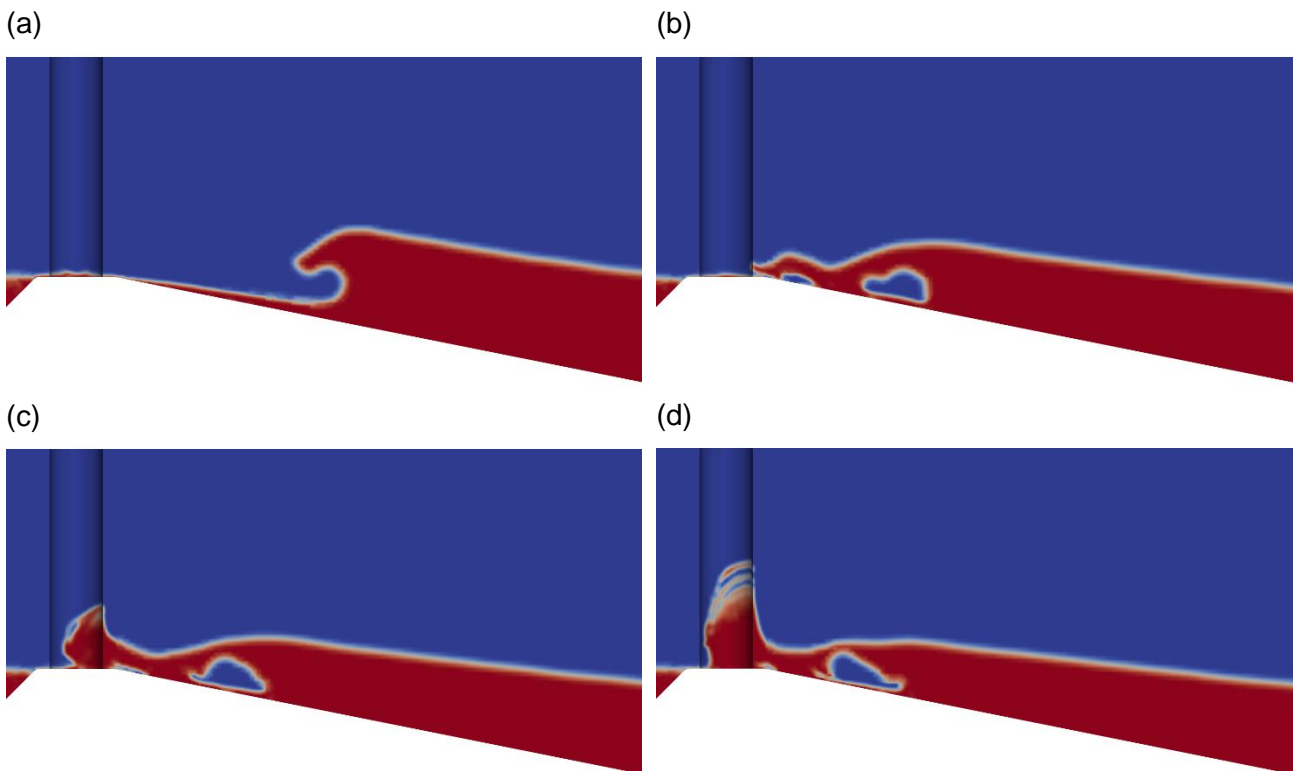


Figure 3-25 Overview of breaking process for MULES. Where white is the shoal, red is only water, dark blue is air and everything between is a mix of water and air. (a) $t_1=55.7$ s. (b): $t=t_1+0.2$ s. (c): $t=t_1+0.25$ s. (d): $t=t_1+0.3$ s

Next, to assess the slamming coefficient, the total force first was decomposed into a quasi-static and impulsive part (Figure 3-26). Figure 3-26 shows that there is a strange peak in the quasi-static force for $t=0$. This is a result of a numerical error due to the decomposition method. Due to selecting only a part of the force time series, the decomposition method suggests that a large quasi static force is

present in the time series. This only affects the first peak which was excluded from the analysis. The impact force is of the same order of magnitude as the total force while the quasi-static force is a magnitude smaller with peaks closer to 1 N.

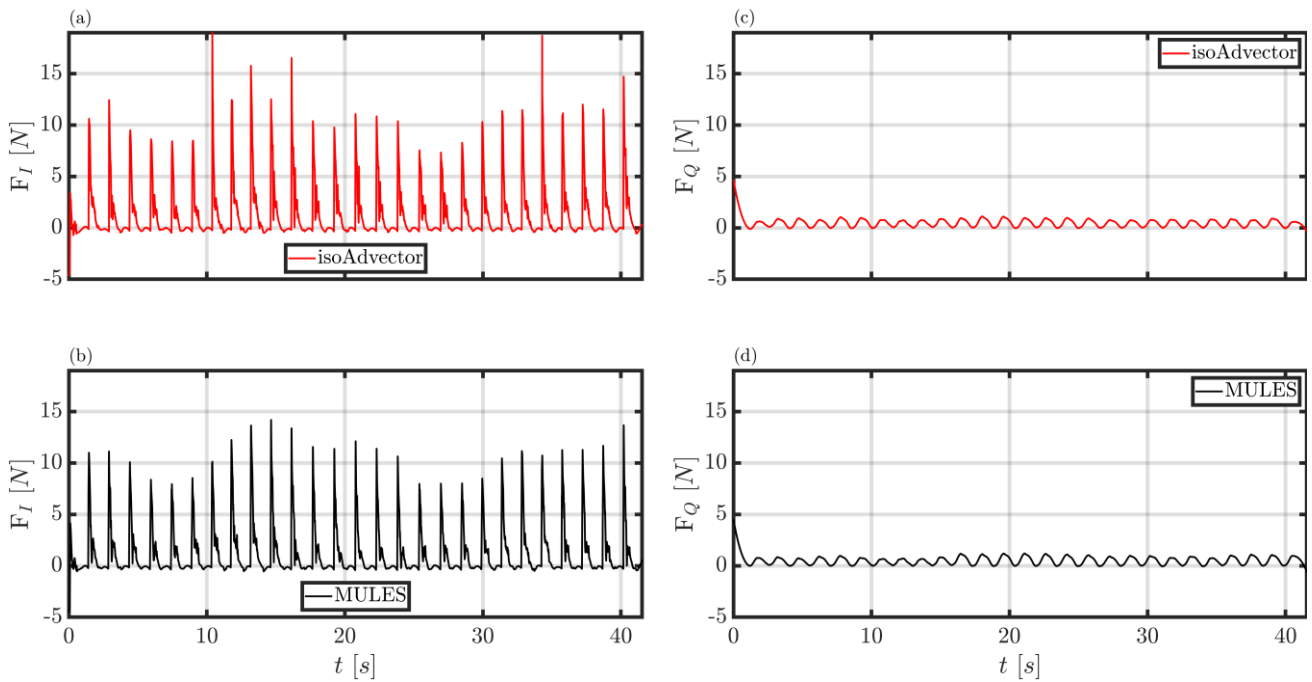


Figure 3-26 Overview of the decomposition from the total force to the impact and quasi-static force. (a): impact force for isoAdvectord. (b): impact force for MULES. (c): quasi-static force for isoAdvectord. (d): quasi-static force for MULES.

With both impact force and the curling factor known, the slamming coefficient was determined. There is a minimal difference between the slamming coefficients for the two solvers (Figure 3-27 and Table 14). The isoAdvectord solver has some outliers that can be explained with the larger peaks present in the data set. This value is nearly 5 times as small compared to the value of 2π found by Wienke and Oumeraci (2005) for breaking waves. The difference between the breaking wave and broken wave case is the interaction of the wave with the shoal. Due to the wave breaking on the shoal, energy is dissipated from the wave which results in a lower value for the slamming coefficient.

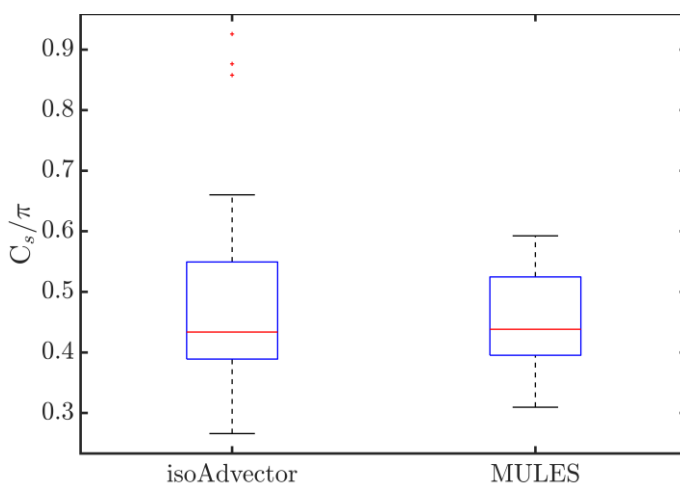


Figure 3-27 A boxplot of the slamming coefficient normalised with π

Table 14 Overview of the median, mean and standard deviation for the slamming coefficient normalised with π

Data set	\tilde{x} [-]	\bar{x} [-]	S_x [-]
isoAdvectord	0.43	0.49	0.17
MULES	0.44	0.45	0.085

3.5 Computational cost

3.5.1 2D simulation

For the 2D simulation the MULES solver performs better in terms of computational costs. The MULES solver finished the simulation in 91.7 hours while this isoAdvector solver took 109.2 hours (Figure 3-28b). This is a difference of 17.5 hours and thus the isoAdvector solver is nearly 20% slower than the MULES solver for the entire 120 second simulation.

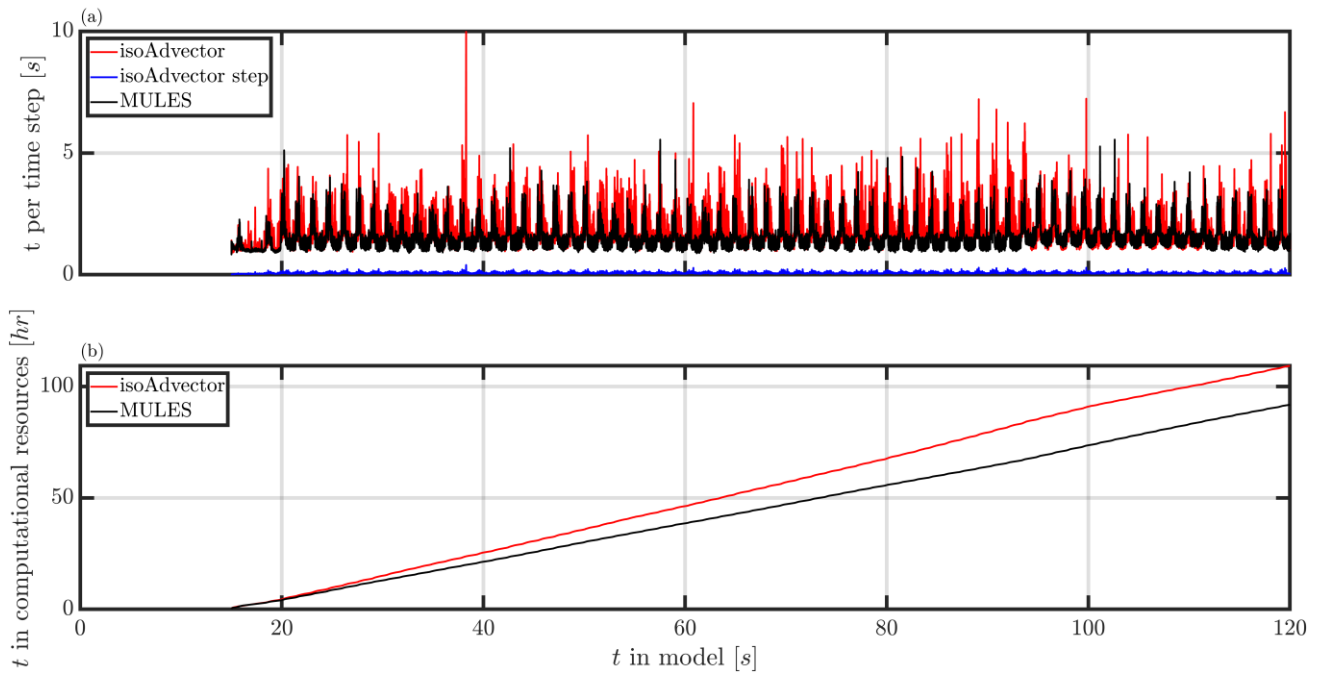


Figure 3-28 Overview of the computational costs for the two different solvers. (a) Shows the total time needed per time step (isoAdvector =red and MULES=black) and the time needed for the extra isoAdvector step in the VOF method (blue). (b): Shows the total time needed in real life for isoAdvector (red) and MULES (black).

Figure 3-28a clearly shows that peaks for the time needed per time step are larger for isoAdvector than for MULES. Table 15 confirms this. The MULES solver is approximately 0.2 seconds faster per time step. The isoAdvector solver thus takes 13.7% more time per time step than the MULES solver. On tens of thousands of time steps this can quickly lead to a significant difference in the time needed per simulation.

Table 15 Overview of the median, mean and standard deviation of the time needed per time step for the 2D simulations of MULES and isoAdvector.

Data set	\tilde{x} [s]	\bar{x} [s]	S_x [s]
isoAdvector	1.67	1.74	0.51
MULES	1.33	1.53	0.48

In this specific case, for a 2D simulation, the MULES solver is faster than the isoAdvector solver.

3.5.2 3D simulation

The 3D simulations did not start simultaneously. Therefore, the data where the solvers were not running at the same time were removed from the data sets (Figure 3-29). This figure clearly shows that the isoAdvector solver has a lower computational costs per time step compared to the MULES solver.

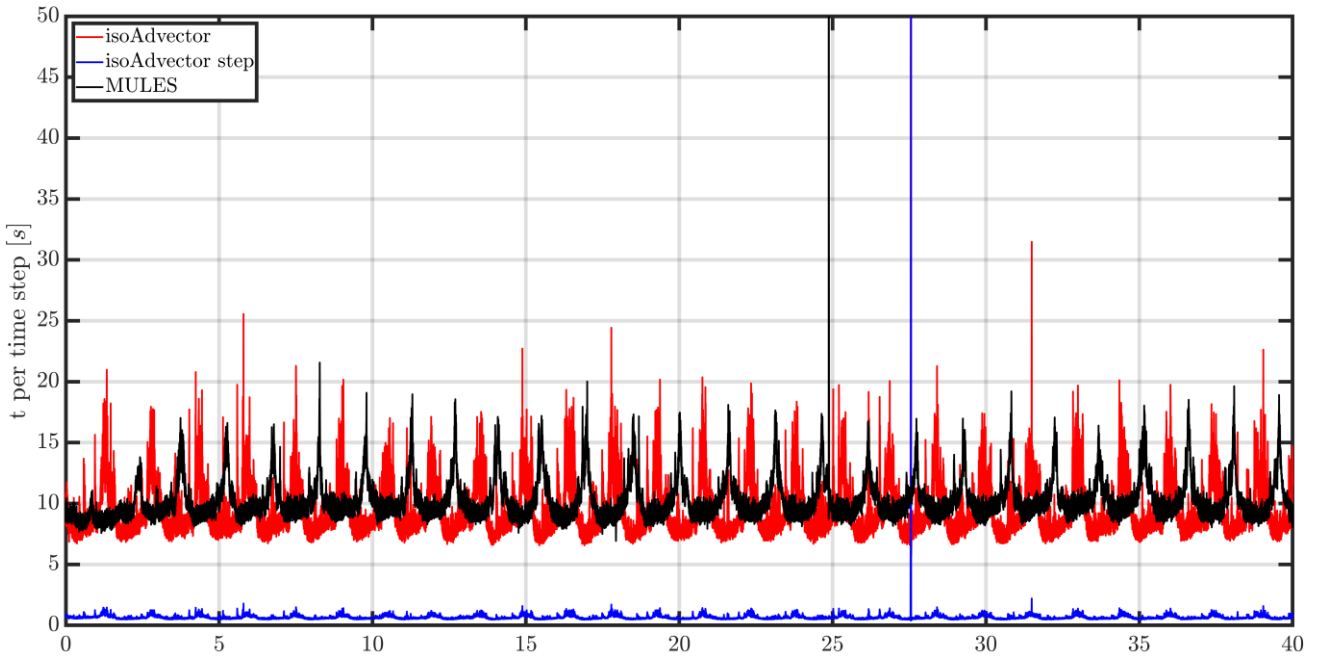


Figure 3-29 Overview of the computational costs for the two different solvers. (a) Shows the total time needed per time step (isoAdvector =red and MULES=black) and the time needed for the extra isoAdvector step in the VOF method (blue)

The time required per time step for both solvers for the 3D simulation show a similar trend (Figure 3-29). However, there are larger peaks for isoAdvector than for MULES, but the average time per time step for isoAdvector is smaller than for MULES (Table 16). The mean value for MULES (10.23) is approximately 11% larger than for isoAdvector (9.22).

The peaks in the time needed per time step for isoAdvector are higher but the troughs are lower. This indicates that the MULES solver performs better for the violent impact but that isoAdvector performs better for the period between the impact of the wave on the cylinder.

Table 16 Overview of the median, mean and standard deviation of the time needed per time step for the 3D simulations of MULES and isoAdvector.

Data set	\tilde{x} [s]	\bar{x} [s]	S_x [s]
isoAdvector	8.57	9.22	2.65
MULES	9.68	10.23	2.57

Contrary to the 2D simulation for this specific model set-up, the isoAdvector solver is faster than the MULES solver for a 3D simulation.

4 Discussion

The values for the curling factor obtained in this study vary significantly from previous research such as Wienke and Oumeraci (2005), Goda et al. (1966). These studies note a maximum value of 0.46 for breaking waves against a cylinder. This is nearly twice as small as the values of 0.81 and 0.93 found in this study. This is also larger than the range the range of 0.40 – 0.65 noted by Irschik et al. (2005) and Veic and Sulisz (2018) for a 1:10 sloping bed. Further, the value found for the slamming coefficient differs significantly compared to Wienke and Oumeraci (2005). This study notes a value of 0.45π for broken waves while for breaking waves a value of 2π is noted by Wienke and Oumeraci (2005), which is a reduction of nearly five times.

The main and largest difference between this study and Wienke and Oumeraci (2005) is the presence of a shoal and the shallow nature of the surrounding water that induce the waves to interact with the cylinder once already broken. After breaking on the shoal, the wave propagates towards the cylinder (Figure 3-24 and Figure 3-25). Even though the time needed to reach the cylinder is short, the effect is significant the wave loses energy. The velocity of the wave is measured at the same location as for Wienke and Oumeraci (2005), but the forces are smaller in comparison. This is due to the loss of energy of the wave and thus results in a lower slamming coefficient.

The larger curling factor can be attributed to the behaviour of the wave on the shoal, after it is broken. During this short period between being fully broken and hitting the cylinder, the wave turns into a small bore. The bore surges upwards towards the cylinder and pushes the water upwards. This results in a height that is nearly twice as large as the 0.46 as stated by Wienke and Oumeraci (2005) and Goda et al. (1966).

Two differences between the OpenFOAM simulations and experimental results are the slight underprediction of the wave crest and the slight overprediction of the wave trough. Moreover, the numerical results produce a shorter rising time while the experimental results contain larger peak forces, this aspect can be likely due to some inaccuracy in the physical model results rather than in the numerical ones.

For a 0.15-metre wave height and 1.5 seconds wave period, the model computes a smaller amplitude of the wave compared to the experimental data. However, for other wave states, the model computes the water level elevation without any errors, i.e. for 0.05 metre and 1.20 second waves. This small difference between the OpenFOAM and experimental data can be explained by the placement of the wave gauges. If one wave gauge is placed a few millimetres to the right or left, there can be a notable difference in the measured results.

The difference in the peak forces between the OpenFOAM results and the experimental data is significant but the averaging the signals the peak forces are similar. However, the experimental data shows a downward trend in the peak forces towards the end of the simulation. At the beginning of the experimental data, the peak force is more than twice as large as the largest peak in the MULES data set. While in the last part of the simulation, which is used in the analyses, the difference is reduced to 45%. There is no clear indication of what is causing this difference in peak forces and further analysis of this aspect is needed. What is causing the differences in force should be further analysed by analysing the loads due to the other wave states in Table 1.

Furthermore, the difference in the rising time can be explained by the complex post-processing of the experimental data and by the movement of the cylinder during the loading phase. These could have led to an unrealistic large rising time compared to numerical results. However, the OpenFOAM results have a near instantaneous rising time that is also unrealistic for such aerated water bore. This difference could be the result of the OpenFOAM computation producing less aerated water compared to the physical experiments. This would lead to the physical wave arriving at the cylinder just a bit earlier than the numerical wave and suddenly inducing the maximum load.

The largest difference in the results between isoAdvector and MULES lies in the curling factor and the peak values of the force on the cylinder. The difference in the computed water level elevation is nearly negligible, as shown in Figure 3-10 and Appendix E. The curling factor is approximately 15% larger for MULES (0.93) than for isoAdvector (0.81). The difference is most likely attributed to the differences in the computed interface, as shown in Figure 3-24 and Figure 3-25. The sharper interface computed by isoAdvector leads to a thinner interface and thus the water is less divided over the cylinder during the moment of impact. While for MULES, with a thicker interface, the water is more spread out over the cylinder during the moment of impact. This can explain the difference in the computed curling factor.

The second large difference between the two solvers is the magnitude of the peak forces. The largest peak force (19.3 N) present in the isoAdvector data set is approximately 34% larger than for MULES (14.4 N). The difference can be traced back to several instances of a larger pressure distribution for isoAdvector than for MULES. There are two possible reasons to which the larger pressure distribution and forces can be attributed to: the interface thickness and the presence of larger velocities near the water surface (Larsen et al., 2019). Due to a larger velocity at the water surface during the moment of impact, a larger force can occur on the cylinder. These incorrect velocities can be prevented by applying a Ghost Fluid Method for the consistent treatment of density and pressure gradient discontinuities at the free surface (Vukčević et al., 2017). Whether the difference is due to the interface or a larger velocity during the moment of impact should be further investigated.

The pressure distribution computed by both solvers is double peaked instead of uniform or triangular (Kyte and Tørum, 1996; Wienke and Oumeraci, 2005). This difference can be attributed to the shoal. The pressure is focused and thus a second peak occurs where the shoal and the cylinder are connected.

The MULES solver is faster for the 2D simulation but not for the 3D simulation. In the 2D simulation the isoAdvector solver takes 13.7% more time per time step than the MULES solver. However, in the 3D simulation the MULES solver takes 11% more time per time step than the isoAdvector solver. This indicates that the isoAdvector solver can handle the impact or 3D simulation better than MULES, but for simple wave propagation, MULES is faster than isoAdvector with similar results.

5 Conclusions and recommendations

5.1 Conclusions

This study presents a novel analysis of broken wave loads on shoal-mounted cylindrical structures, building on the methodology commonly used for investigating breaking waves. With no prior research done into this specific situation, calibrating the methodology for broken waves is essential in the structural assessment of marine infrastructure such as lighthouses. This will result in a better approximation of the forces on such structures and greatly improves the accuracy of the structural assessment. The results of the newly developed geometric VOF method (i.e., isoAdvector) are compared to the standard algebraic VOF method (i.e., MULES).

To address the problem, a numerical framework was set-up according to the physical experiment done by Dassanayake et al. (2019) as part of the STORMLAMP project. The model was validated in 2D using the water level elevation time series of the physical experiments. This was done by varying the cell sizes until an optimum was found that represents the physical experiments best. This optimum is a resolution of 15 cells per wave height around the mean water level. Even though the numerical results slightly underpredict the wave crest and trough, there is a good agreement in both the wave period and wave height. The same numerical set-up is used for different wave states. For these wave states the model computes results comparable to the experimental data with the same slight under-, and overprediction of the wave crest and trough, respectively.

With the identified optimum resolution of 15 cells per wave height, the model was extended to 3D. The 3D model was then validated using the available force time series from the experimental case. When comparing the individual and ensemble average of the force signal there is relatively a good agreement between all three data sets. The only thing that stands out are the larger peak forces in the experimental data. Neither one of the numerical data sets can match those peaks even though the mean values of the OpenFOAM results are relatively close to the mean of experimental data.

Using the validated model, the empirical factors in the formulation of the impact force were calibrated and the results between the two solvers were assessed. The curling factor for the isoAdvector case is found to be 0.81 and for MULES 0.95. The slamming coefficient is found to be approximately 0.45π for both MULES and isoAdvector. Overall, the methodology for breaking waves can be applied for waves with a wave height of 0.15 metres and a period of 1.5 seconds when changing the slamming coefficient and curling factor to 0.45π and 0.81, respectively. However, further validation in terms of different wave states and geometries is needed. Furthermore, the double peaked pressure distribution computed by both solvers is of similar shape and magnitude, and the radial distribution corresponds with the findings of Wienke and Oumeraci (2005).

During the comparison of the computational costs of the 2D simulations, the isoAdvector solver has proven to take 13.7% more time per time step than the MULES solver. However, in the 3D simulations the MULES solver needs 11% more time per time step than the isoAdvector solver. Furthermore, the results of the isoAdvector solver resemble the experimental data better.

Taking everything into account, the isoAdvector solver is the preferred solver to analyse the wave-structure interaction of cylindrical structures. The results of this study can be used as a foundation for the development of the formulation of the impact of broken waves onto lighthouses. This would significantly improve the accuracy of the strength and stability calculations for lighthouses and similar structures.

5.2 Recommendations

Developing this approach into a simple empirical equation instead of a time-consuming numerical model would be extremely beneficial and would result in quick and simple assessment of broken wave loads on marine infrastructure such as lighthouses.

Furthermore, the found values for the slamming coefficient and curling factor should be verified for different wave states. The effect of the slope on the force, slamming coefficient and curling factor should also be analysed. This would contribute to the development of a simple empirical solution to analyse the impact force on a slender cylinder.

However, before such a simple empirical equation can be made, several other aspects should be further investigated. First, a convergence analysis for the cell size around the cylinder should be done. This would verify if the used resolution of the cells is small enough to capture the total force on the cylinder. Second, it can be an option to explore the use of a larger cell size for the water level elevation and vary the cell size around the cylinder to find an optimum. This would save time but would result in a less accurate representation of the water level elevation.

If the findings of this study can be put into practice, it is hoped that the lights of these impressive structures will continue to shine for many years to come.

Bibliography

- Antonini, A., Raby, A., Brownjohn, J.M.W., Pappas, A., D'Ayala, D., 2019. Survivability assessment of fastnet lighthouse. *Coastal Engineering* 150, 18–38. <https://doi.org/10.1016/j.coastaleng.2019.03.007>
- Arntsen, Ø.A., Ros Collados, X., Tørum, A., 2013. Impact Forces on a Vertical Pile From Plunging Breaking Waves 533–544. https://doi.org/10.1142/9789814412216_0046
- Barton, I.E., 1998. Comparison of SIMPLE- and PISO-type algorithms for transient flows. *International Journal for Numerical Methods in Fluids* 26, 459–483. [https://doi.org/10.1002/\(SICI\)1097-0363\(19980228\)26:4<459::AID-FLD645>3.0.CO;2-U](https://doi.org/10.1002/(SICI)1097-0363(19980228)26:4<459::AID-FLD645>3.0.CO;2-U)
- Dassanayake, D.T., Antonini, A., Pappas, A., Raby, A., Brownjohn, J.M.W., D'Ayala, D., 2021. Influence of the Spatial Pressure Distribution of Breaking Wave Loading on the Dynamic Response of Wolf Rock Lighthouse. *Journal of Marine Science and Engineering* 9, 55. <https://doi.org/10.3390/jmse9010055>
- Dassanayake, D.T., Raby, A., Antonini, A., 2019. Physical Modelling of the Effect of Shoal Geometry on Wave Loading and Runup on a Cylinder. *Coastal Structures 2019* 851–861. https://doi.org/https://doi.org/10.18451/978-3-939230-64-9_022
- Deshpande, S.S., Anumolu, L., Trujillo, M.F., 2012. Evaluating the performance of the two-phase flow solver interFoam. *Computational Science and Discovery* 5, 014016. <https://doi.org/10.1088/1749-4699/5/1/014016>
- Engsig-Karup, A.P., Bingham, H.B., Lindberg, O., 2009. An efficient flexible-order model for 3D nonlinear water waves. *Journal of Computational Physics* 228, 2100–2118. <https://doi.org/10.1016/j.jcp.2008.11.028>
- Ferziger, J.H., Perić, M., Street, R.L., 2020. *Computational Methods for Fluid Dynamics*, 4th ed. Springer International Publishing, Cham. <https://doi.org/10.1007/978-3-319-99693-6>
- Ghadirian, A., Bredmose, H., 2019. Pressure impulse theory for a slamming wave on a vertical circular cylinder. *Journal of Fluid Mechanics* 867, R1. <https://doi.org/10.1017/jfm.2019.151>
- Ghadirian, A., Bredmose, H., Dixen, M., 2016. Breaking phase focused wave group loads on offshore wind turbine monopiles. *Journal of Physics: Conference Series* 753. <https://doi.org/10.1088/1742-6596/753/9/092004>
- Goda, Y., Haranaka, S., Kitahata, M., 1966. Study on impulsive breaking wave forces on piles. Report Port and Harbour Technical Research Institute 5, 1–30.
- Grue, J., Bjorshol, G., Strand, O., 1993. Higher harmonic wave exciting forces on a vertical cylinder. *Applied Mathematics* 2.
- Harten, A., 1983. High resolution schemes for hyperbolic conservation laws. *Journal of Computational Physics* 49, 357–393. [https://doi.org/10.1016/0021-9991\(83\)90136-5](https://doi.org/10.1016/0021-9991(83)90136-5)
- Irschik, K., Sparboom, U., Oumeraci, H., 2005. BREAKING WAVE LOADS ON A SLENDER PILE IN SHALLOW WATER, in: *Coastal Engineering 2004*. World Scientific Publishing Company, pp. 568–580. https://doi.org/10.1142/9789812701916_0045
- Issa, R.I., 1986. Solution of the implicitly discretised fluid flow equations by operator-splitting. *Journal of Computational Physics* 62, 40–65. [https://doi.org/10.1016/0021-9991\(86\)90099-9](https://doi.org/10.1016/0021-9991(86)90099-9)

- Jacobsen, N.G., Fuhrman, D.R., Fredsøe, J., 2012. A wave generation toolbox for the open-source CFD library: OpenFoam®. *International Journal for Numerical Methods in Fluids* 70, 1073–1088. <https://doi.org/10.1002/fld.2726>
- Jacobsen, N.G., van Gent, M.R.A., Capel, A., Borsboom, M., 2018. Numerical prediction of integrated wave loads on crest walls on top of rubble mound structures. *Coastal Engineering* 142, 110–124. <https://doi.org/10.1016/j.coastaleng.2018.10.004>
- Jacobsen, N.G., van Gent, M.R.A., Wolters, G., 2015. Numerical analysis of the interaction of irregular waves with two dimensional permeable coastal structures. *Coastal Engineering* 102, 13–29. <https://doi.org/10.1016/j.coastaleng.2015.05.004>
- Jonker, R.G., 2020. Homogeneous detached composite breakwater.
- Kulp, S.A., Strauss, B.H., 2019. New elevation data triple estimates of global vulnerability to sea-level rise and coastal flooding. *Nature Communications* 10, 1–12. <https://doi.org/10.1038/s41467-019-12808-z>
- Kyte, A., Tørum, A., 1996. Wave forces on vertical cylinders upon shoals. *Coastal Engineering* 27, 263–286. [https://doi.org/10.1016/0378-3839\(96\)00003-8](https://doi.org/10.1016/0378-3839(96)00003-8)
- Larsen, B.E., Fuhrman, D.R., 2018. On the over-production of turbulence beneath surface waves in Reynolds-averaged Navier-Stokes models. *Journal of Fluid Mechanics* 853, 419–460. <https://doi.org/10.1017/jfm.2018.577>
- Larsen, B.E., Fuhrman, D.R., Roenby, J., 2019. Performance of interFoam on the simulation of progressive waves. *Coastal Engineering Journal* 61, 380–400. <https://doi.org/10.1080/21664250.2019.1609713>
- Liu, S., Jose, J., Ong, M.C., Gudmestad, O.T., 2019. Characteristics of higher-harmonic breaking wave forces and secondary load cycles on a single vertical circular cylinder at different Froude numbers. *Marine Structures* 64, 54–77. <https://doi.org/10.1016/j.marstruc.2018.10.007>
- López, J., Zanzi, C., Gómez, P., Faura, F., Hernández, J., 2008. A new volume of fluid method in three dimensions-Part II: Piecewise-planar interface reconstruction with cubic-Bézier fit. *International Journal for Numerical Methods in Fluids* 58, 923–944. <https://doi.org/10.1002/fld.1775>
- Mayer, S., Garapon, A., Sørensen, L.S., 1998. A fractional step method for unsteady free-surface flow with applications to non-linear wave dynamics. *International Journal for Numerical Methods in Fluids* 28, 293–315. [https://doi.org/10.1002/\(SICI\)1097-0363\(19980815\)28:2<293::AID-FLD719>3.0.CO;2-1](https://doi.org/10.1002/(SICI)1097-0363(19980815)28:2<293::AID-FLD719>3.0.CO;2-1)
- Méhauté, B., 1976. *An Introduction to Hydrodynamics and Water Waves*. Springer Berlin Heidelberg, Berlin, Heidelberg. <https://doi.org/10.1007/978-3-642-85567-2>
- Morison, J.R., Johnson, J.W., Schaaf, S.A., 1950. The Force Exerted by Surface Waves on Piles. *Journal of Petroleum Technology* 2, 149–154. <https://doi.org/10.2118/950149-G>
- OpenFOAM®, n.d. OpenFOAM® [WWW Document]. URL <https://www.openfoam.com/> (accessed 4.30.20).
- Patankar, S.V., Spalding, D.B., 1972. A calculation procedure for heat, mass and momentum transfer in three-dimensional parabolic flows. *International Journal of Heat and Mass Transfer* 15, 1787–1806. [https://doi.org/10.1016/0017-9310\(72\)90054-3](https://doi.org/10.1016/0017-9310(72)90054-3)
- Patil, A., 2019. Numerical investigation of nearshore wave transformation and surf zone hydrodynamics.

- Paulsen, B.T., Bredmose, H., Bingham, H.B., 2014a. An efficient domain decomposition strategy for wave loads on surface piercing circular cylinders. *Coastal Engineering* 86, 57–76. <https://doi.org/10.1016/j.coastaleng.2014.01.006>
- Paulsen, B.T., Bredmose, H., Bingham, H.B., Jacobsen, N.G., 2014b. Forcing of a bottom-mounted circular cylinder by steep regular water waves at finite depth. *Journal of Fluid Mechanics* 755, 1–34. <https://doi.org/10.1017/jfm.2014.386>
- Peregrine, D.H., 2003. Water - Wave Impact on Walls. *Annual Review of Fluid Mechanics* 35, 23–43. <https://doi.org/10.1146/annurev.fluid.35.101101.161153>
- Qu, S., Liu, S., Ong, M.C., Sun, S., Ren, H., 2020. Numerical Simulation of Breaking Wave Loading on Standing Circular Cylinders with Different Transverse Inclined Angles. *Applied Sciences* 10, 1347. <https://doi.org/10.3390/app10041347>
- Raby, A.C., Antonini, A., Pappas, A., Dassanayake, D.T., Brownjohn, J.M.W., D’Ayala, D., 2019. Wolf Rock lighthouse: past developments and future survivability under wave loading. *Philosophical Transactions of the Royal Society A: Mathematical, Physical and Engineering Sciences* 377, 20190027. <https://doi.org/10.1098/rsta.2019.0027>
- Rivrin, M., 2016. Mathieu Rivrin photographs.
- Roenby, J., Bredmose, H., Jasak, H., 2016. A computational method for sharp interface advection. *Royal Society Open Science* 3. <https://doi.org/10.1098/rsos.160405>
- Roenby, J., Larsen, B.E., Bredmose, H., Jasak, H., 2017. A new volume-of-fluid method in openfoam. 7th International Conference on Computational Methods in Marine Engineering, MARINE 2017 2017-May, 266–277.
- STORMLAMP [WWW Document], n.d. URL <https://stormlamp.org.uk/> (accessed 5.11.20).
- Tu, Y., Muskulus, M., 2016. Statistical properties of local slamming forces on a jacket structure in offshore wind applications. *Proceedings of the International Offshore and Polar Engineering Conference 2016-Janua*, 206–213.
- US Army, C. of E., 1984. Shore protection manual. Shore protection manual. II.
- van Leer, B., 1977. Towards the ultimate conservative difference scheme. IV. A new approach to numerical convection. *Journal of Computational Physics* 23, 276–299. [https://doi.org/10.1016/0021-9991\(77\)90095-X](https://doi.org/10.1016/0021-9991(77)90095-X)
- Veic, D., Sulisz, W., 2018. Impact Pressure Distribution on a Monopile Structure Excited by Irregular Breaking Wave. *Polish Maritime Research* 25, 29–35. <https://doi.org/10.2478/pomr-2018-0019>
- von Karman, T., 1929. The impact on seaplane floats during landing. National Advisory Committee for Aeronautics Technical Notes.
- Vukčević, V., Jasak, H., Gatin, I., 2017. Implementation of the Ghost Fluid Method for free surface flows in polyhedral Finite Volume framework. *Computers & Fluids* 153, 1–19. <https://doi.org/10.1016/j.compfluid.2017.05.003>
- Wagner, H., 1932. Uber Stoss- und Gleitvorgange an der Oberflache von Flussigkeiten. *Zeitschrift fur angewandte Mathematik und Mechanik* 12, 193–215.
- Wang, X.L., Zwiens, F.W., Swail, V.R., 2004. North Atlantic Ocean Wave Climate Change Scenarios for the Twenty-First Century. *Journal of Climate* 17, 2368–2383. [https://doi.org/10.1175/1520-0442\(2004\)017<2368:NAOWCC>2.0.CO;2](https://doi.org/10.1175/1520-0442(2004)017<2368:NAOWCC>2.0.CO;2)

- Weller, H.G., 2008. A new approach to VOF-based interface capturing methods for incompressible and compressible flow. OpenCFD Ltd., Report TR/HGW 4, 35.
- Wienke, J., Oumeraci, H., 2005. Breaking wave impact force on a vertical and inclined slender pile - Theoretical and large-scale model investigations. *Coastal Engineering* 52, 435–462. <https://doi.org/10.1016/j.coastaleng.2004.12.008>
- Ziman, H.J., 1990. A computer prediction for chemically reacting flows in stirred tanks.

Appendices

Appendix A	Mesh aspect ratio.....	i
Appendix B	Results wave gauges	vii
Appendix C	y^+ values 2D model validation	xvi
Appendix D	Wave states	xix
Appendix D.1	H=0.05 m, T=1.20 s	xix
Appendix D.2	H=0.05 m, T=2.44 s	xxii
Appendix D.3	H=0.10 m, T=1.20 s	xxv
Appendix D.4	H=0.10 m, T=2.44 s	xxviii
Appendix D.5	H=0.15 m, T=1.96 s	xxxi
Appendix E	Results of water level analysis 3D simulation	xxxv
Appendix F	y^+ values 3D model validation.....	xxxviii
Appendix G	Overview selected data force time series	xl

Appendix A contains the aspect ratios for all different geometries. Appendix B contains the plots per wave gauge, except wave gauge 11, for the convergence analysis. Appendix B contains the y^+ values for the simulations run for the 2D model validation. Appendix D contains the plots for the different wave conditions with the resolution selected from the convergence analysis. Appendix E contains the plots of the analysis of the water level elevation of the 3D simulations. Appendix F contains the y^+ values for the simulations run for the 3D model validation and Appendix G contains the overview of the total force time series.

Appendix A Mesh aspect ratio.

This appendix contains the histograms with the different aspect ratios of all the following cases.

- Convergence analysis CPWH 05
- Convergence analysis CPWH 10
- Convergence analysis CPWH 15
- Convergence analysis CPWH 20
- Convergence analysis CPWH 25
- Wave state H=0.05 m, T=1.20s
- Wave state H=0.05 m, T=2.44s
- Wave state H=0.10 m, T=1.20s
- Wave state H=0.10 m, T=2.44s
- Wave state H=0.15 m, T=1.96s
- 3D simulation isoAdvectord
- 3D simulation MULES

Results of aspect ratio for all time steps for the case WIF-2D-05
Mean 1.05, Median: 1.02

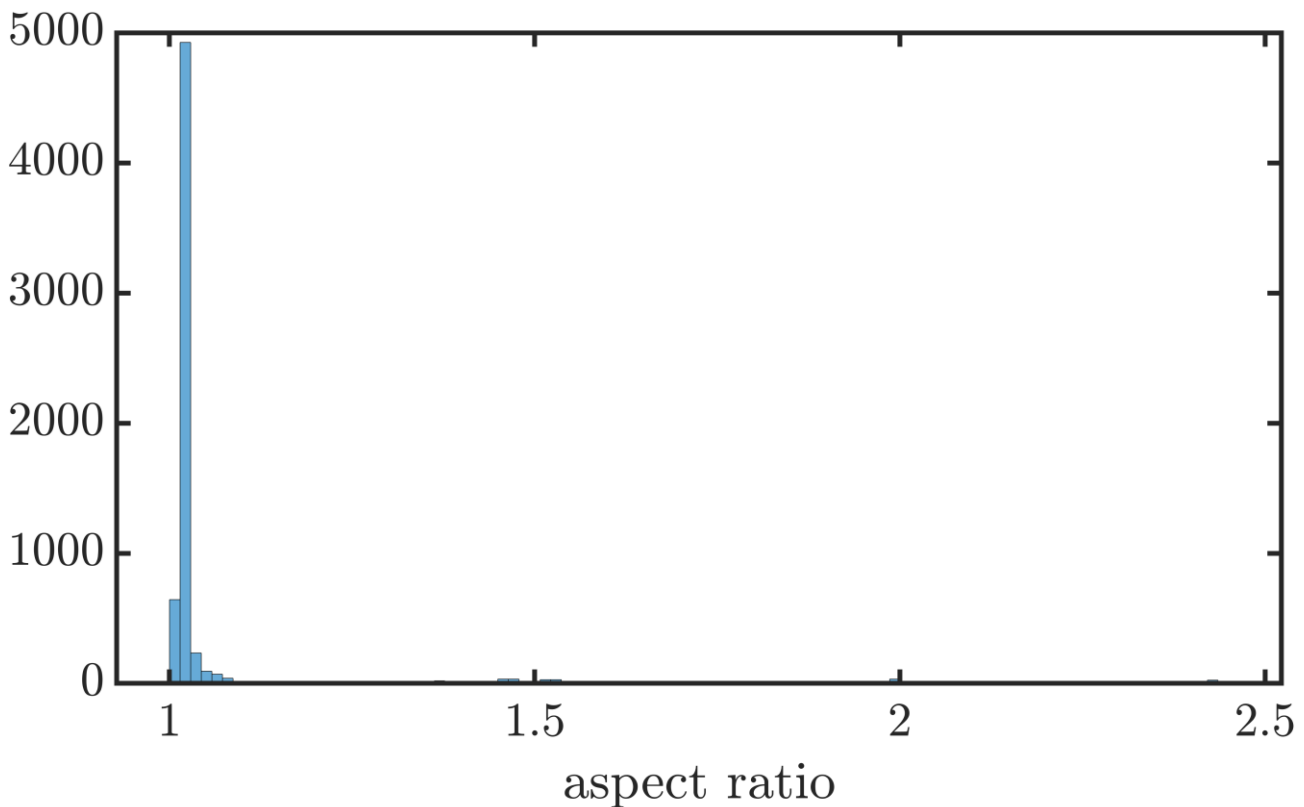


Figure A. 1 Histogram aspect ratio for the 2D isoAdvectord case with 05 CPWH

Results of aspect ratio for all time steps for the case WIF-2D-10
Mean 1.04, Median: 1.02

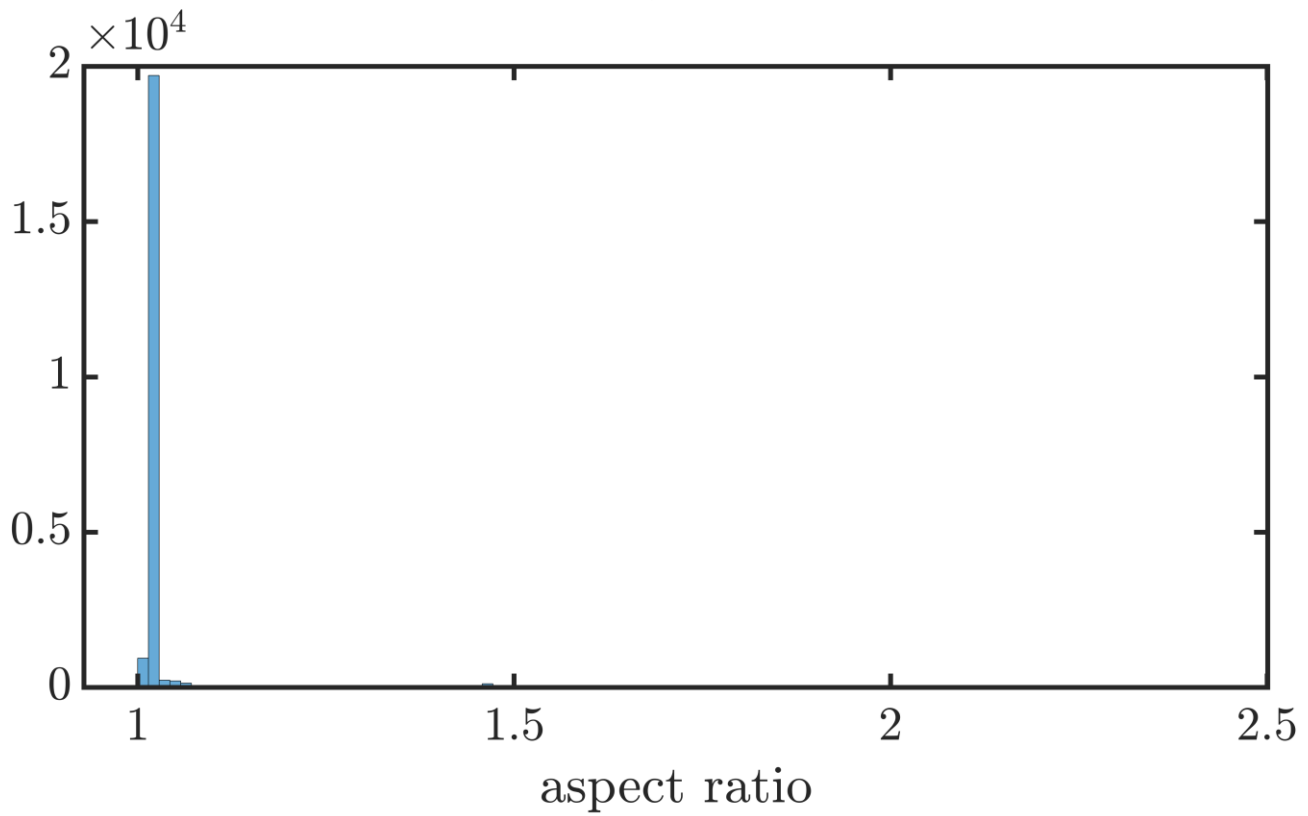


Figure A. 2 Histogram aspect ratio for the 2D isoAdvectord case with 10 CPWH

Results of aspect ratio for all time steps for the case WIF-2D-15
Mean 1.01, Median: 1.00

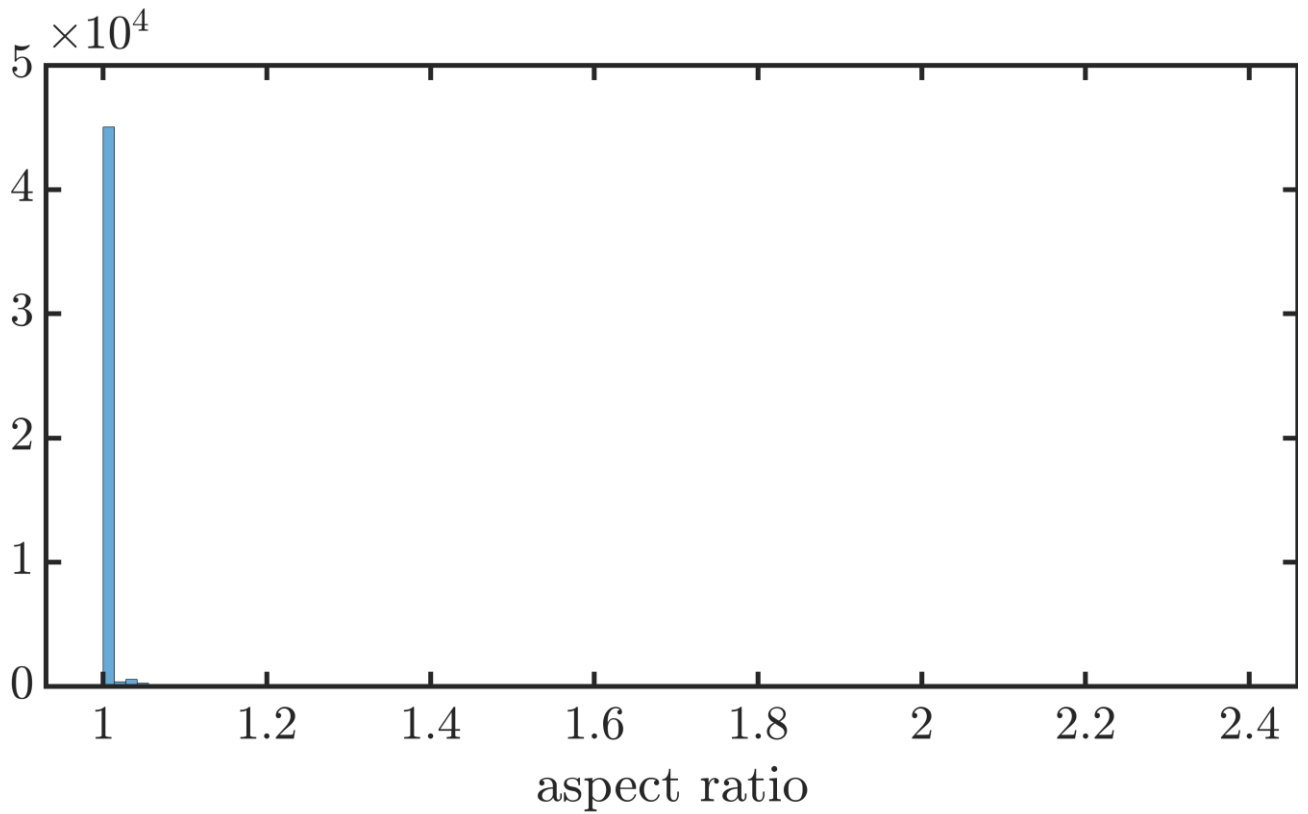


Figure A. 3 Histogram aspect ratio for the 2D isoAdvectord case with 15 CPWH

Results of aspect ratio for all time steps for the case WIF-2D-20
Mean 1.01, Median: 1.00

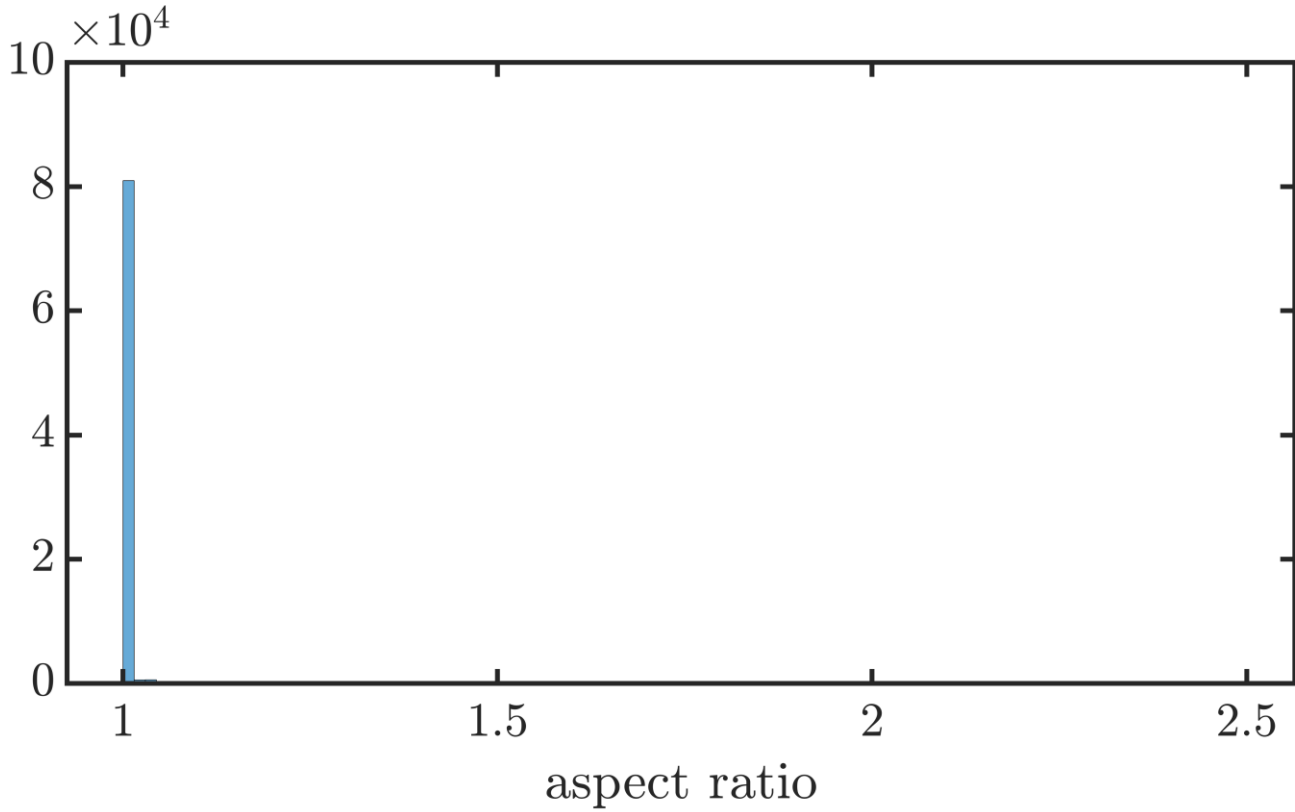


Figure A. 4 Histogram aspect ratio for the 2D isoAdvector case with 20 CPWH

Results of aspect ratio for all time steps for the case WIF-2D-25
Mean 1.02, Median: 1.01

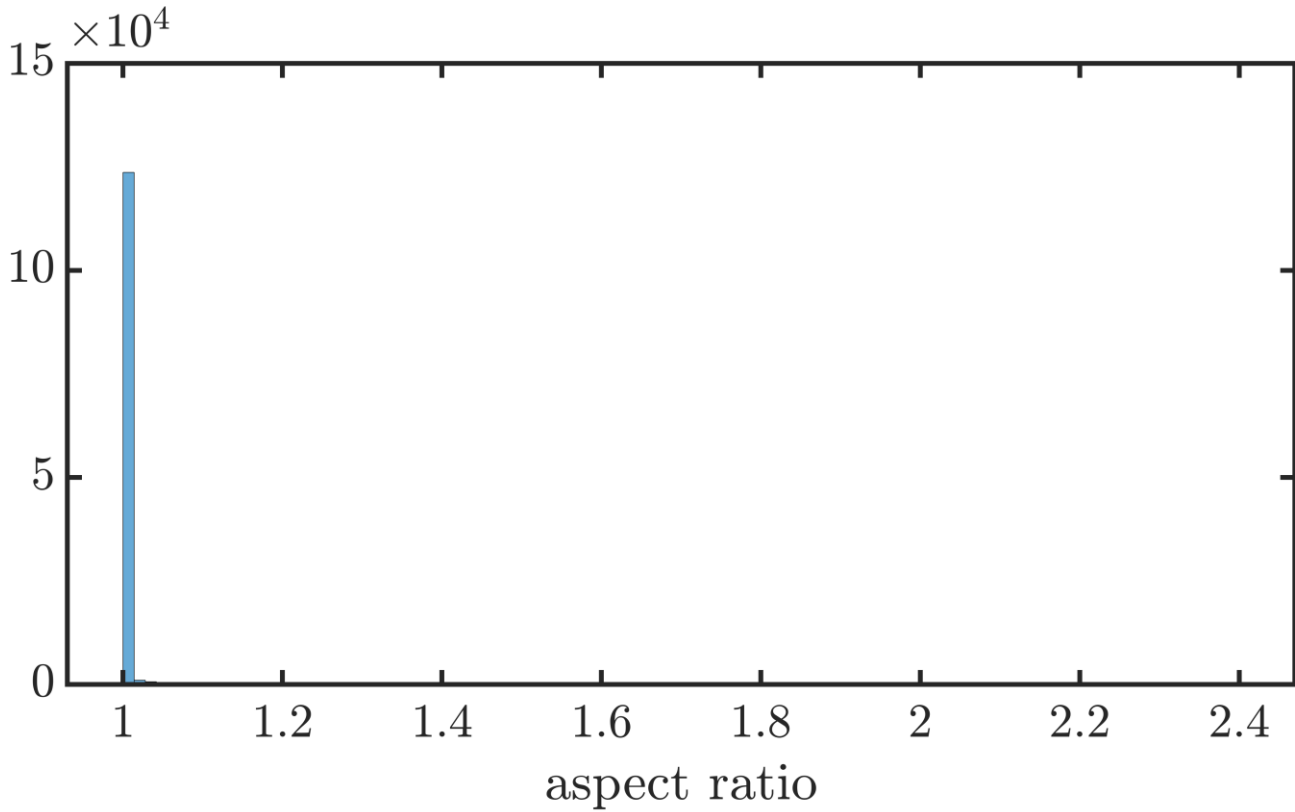


Figure A. 5 Histogram aspect ratio for the 2D isoAdvector case with 25 CPWH

Results of aspect ratio for all time steps for the case WIF-005120
Mean 1.01, Median: 1.00

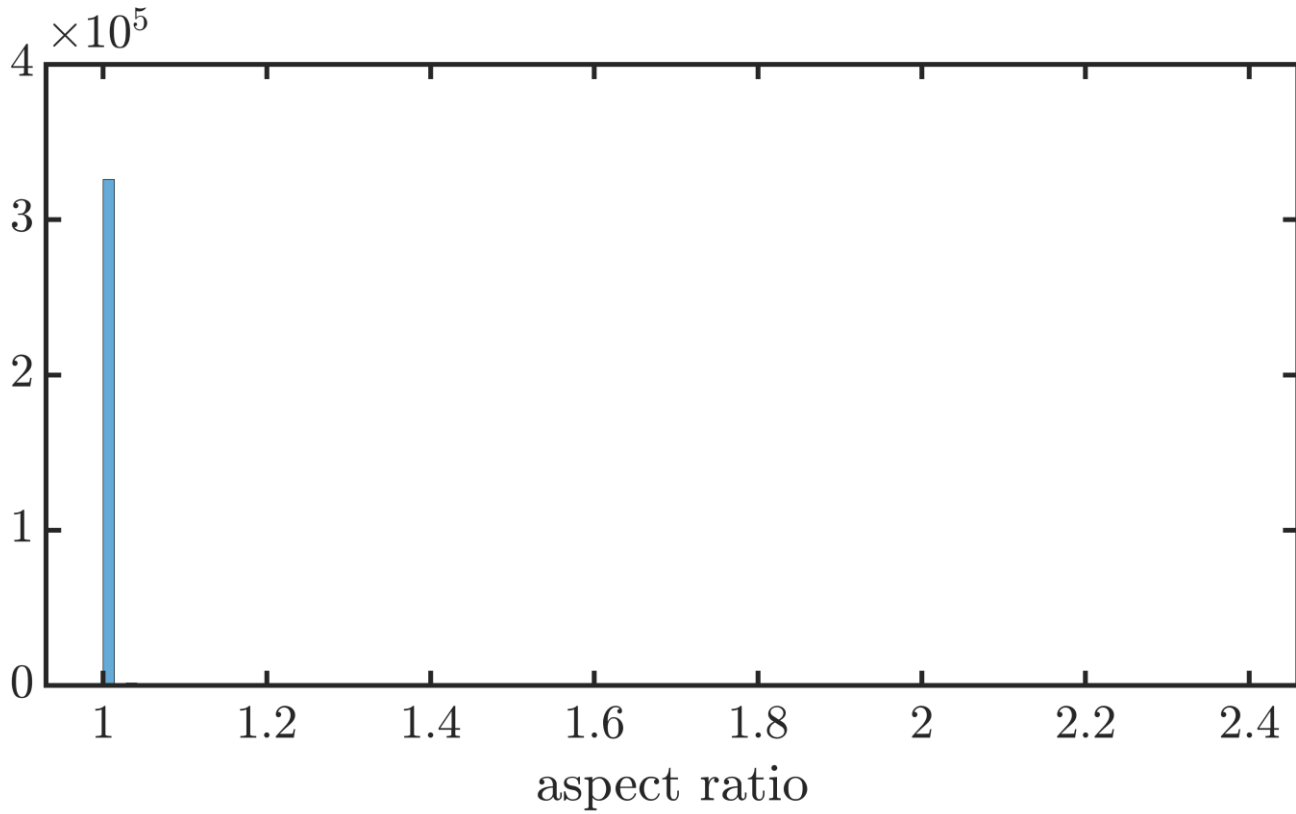


Figure A. 6 Histogram aspect ratio for the 2D isoAdvectord case of $H=0.05$ m, $T=1.20$ s

Results of aspect ratio for all time steps for the case WIF-005244
Mean 1.00, Median: 1.00

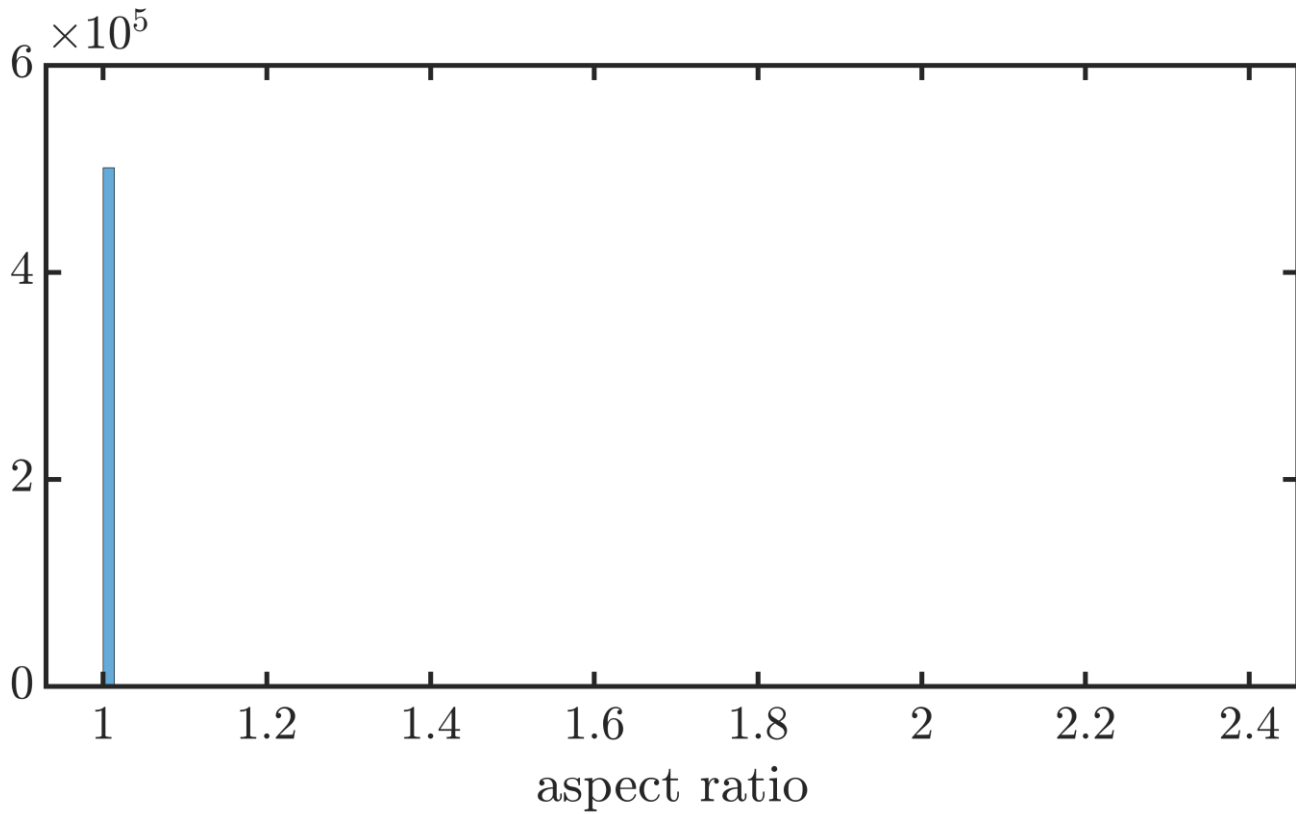


Figure A. 7 Histogram aspect ratio for the 2D isoAdvectord case of $H=0.05$ m, $T=2.44$

Results of aspect ratio for all time steps for the case WIF-010120
Mean 1.01, Median: 1.00

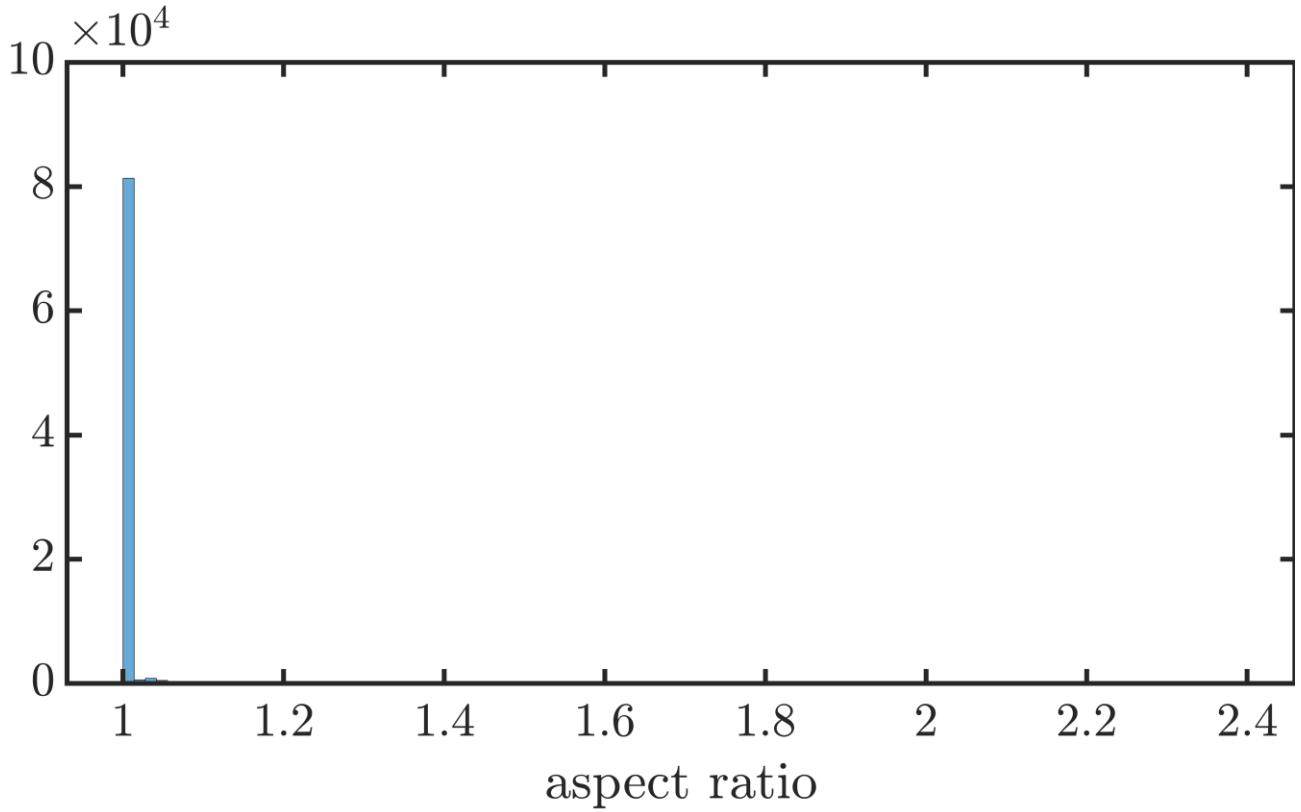


Figure A. 8 Histogram aspect ratio for the 2D isoAdvectord case of $H=0.10$ m, $T=1.20$ s

Results of aspect ratio for all time steps for the case WIF-010244
Mean 1.01, Median: 1.00

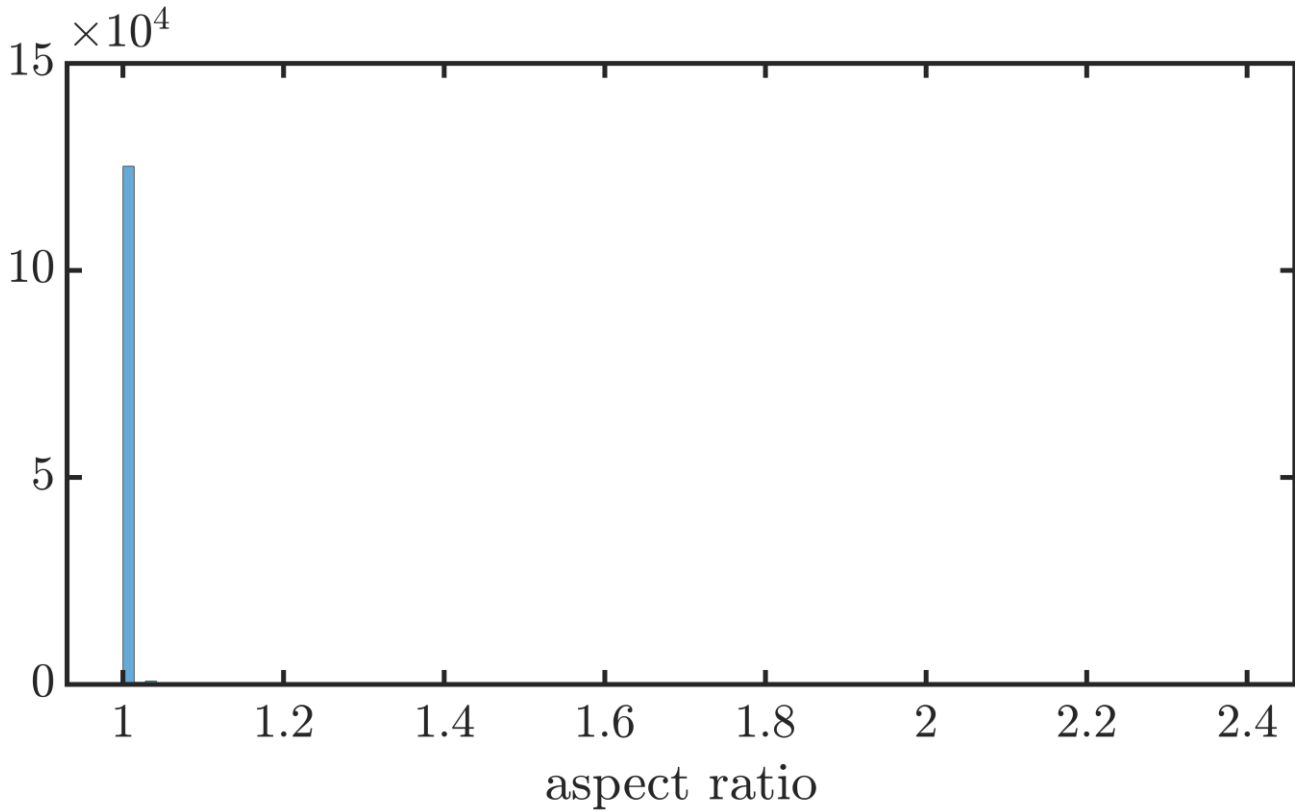


Figure A. 9 Histogram aspect ratio for the 2D isoAdvectord case of $H=0.10$ m, $T=2.44$ s

Results of aspect ratio for all time steps for the case WIF-015196
Mean 1.01, Median: 1.00

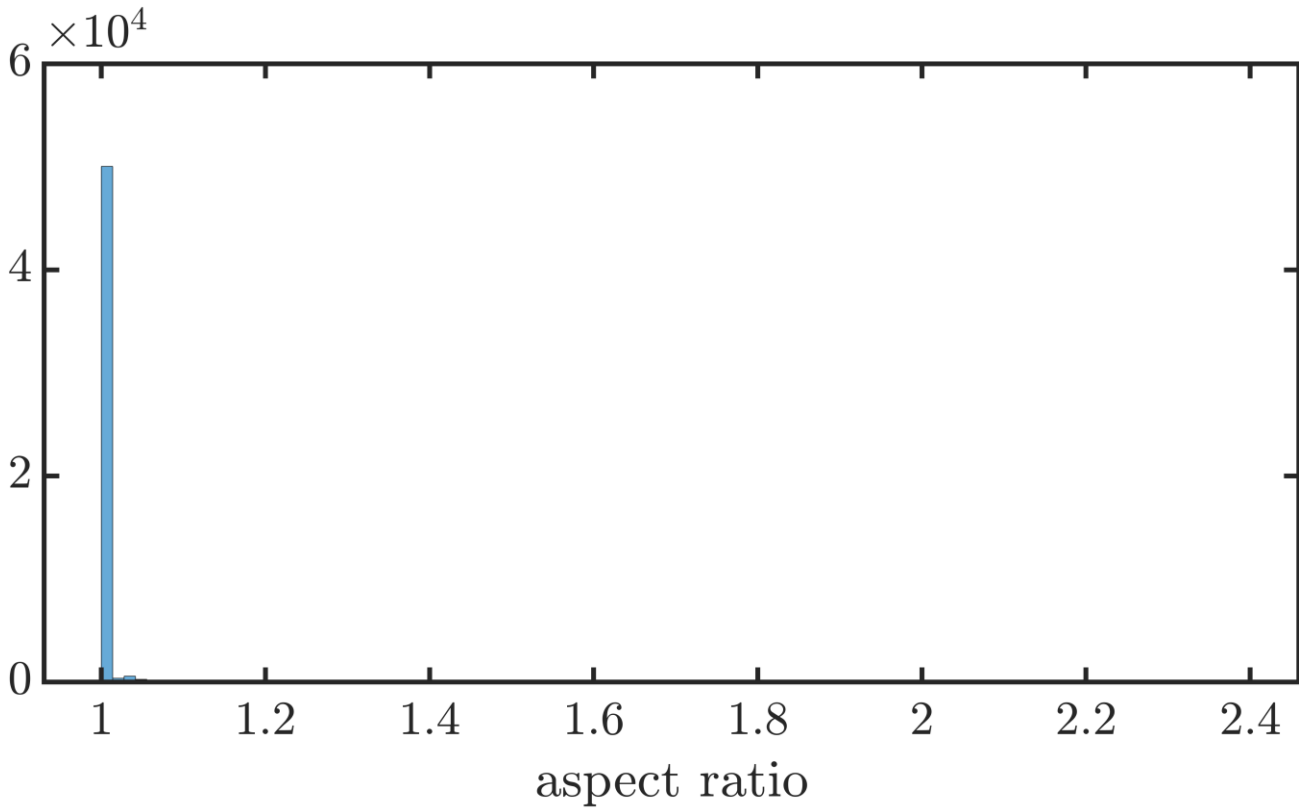


Figure A. 10 Histogram aspect ratio for the 2D isoAdvectord case of $H=0.15$ m, $T=1.96$ s

Results of aspect ratio for all time steps for the case isoAdvectord
Mean 1.07, Median: 1.00

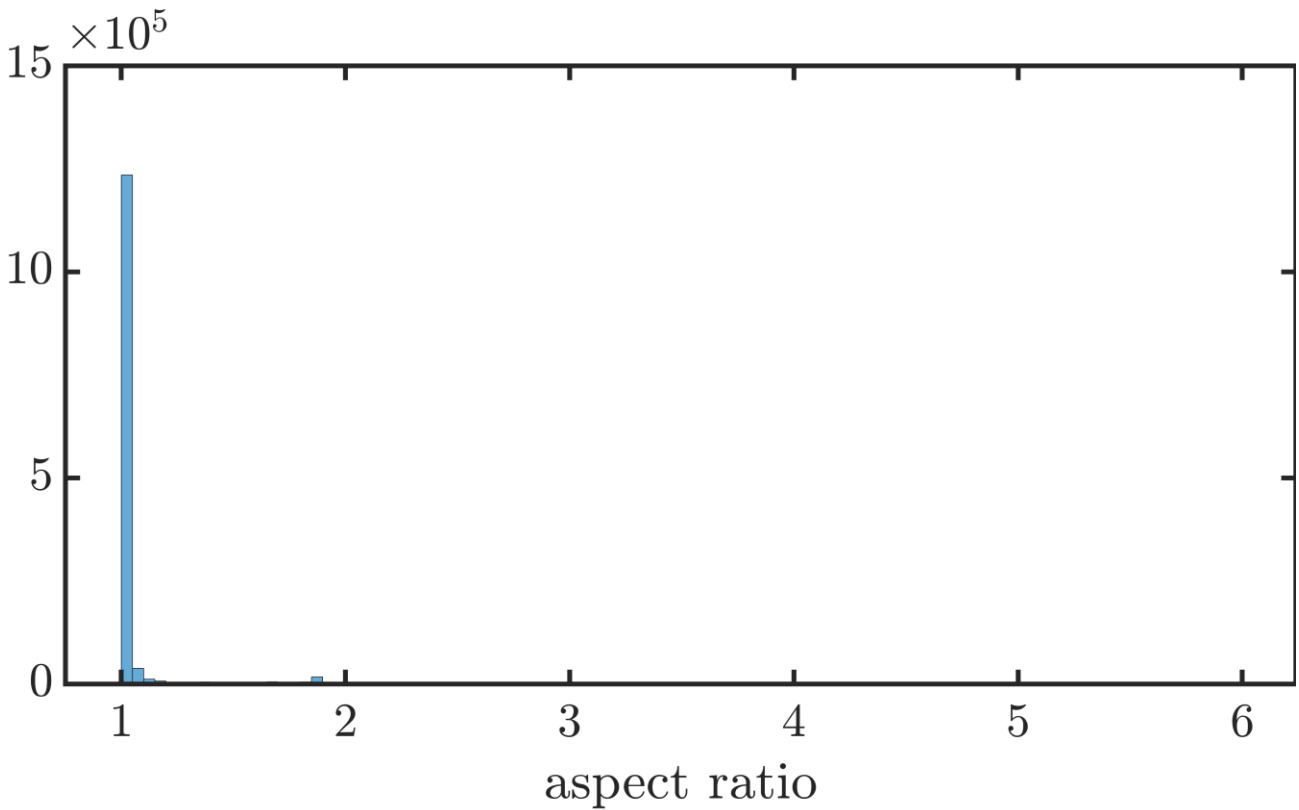


Figure A. 11 Histogram aspect ratio for the 3D case with 15 CPWH

Appendix B Results wave gauges

In this appendix the plots related to the convergence analysis for the different wave gauges in the domain can be found. This data is shown in the order of the wave gauges present in the domain. Per wave gauge the water level elevation, FFT of the water level elevation, the aligned data and average wave shape is shown.

- WG08: $x = 23.08$ m
- WG09: $x = 23.40$ m
- WG10: $x = 23.70$ m
- WG11: $x = 23.82$ m (this wave gauge is not shown as it is already in the main document)
- WG12: $x = 24.07$ m

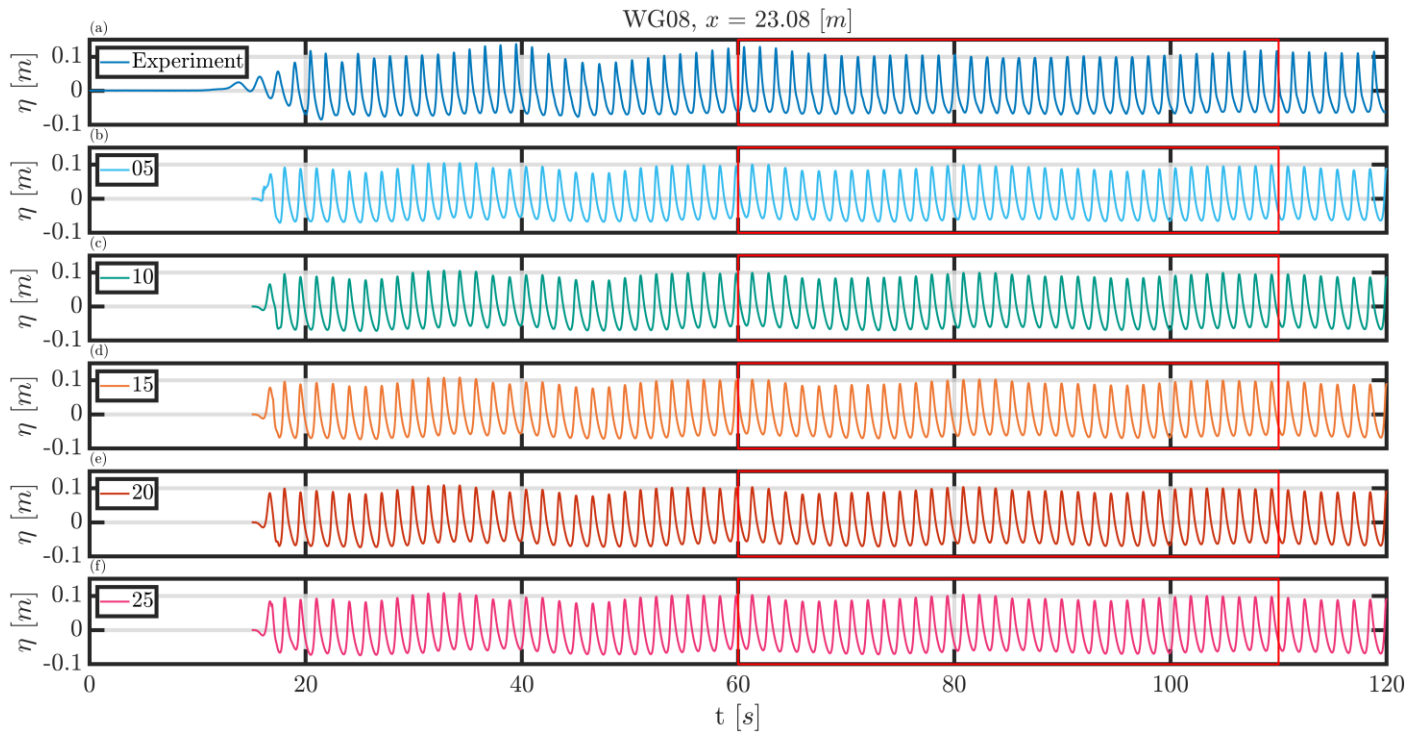


Figure A. 12 Overview of data at WG08. (a): the water level elevation as measured during the experiment. (b-f): the water level elevation measured with a resolution of respectively 5, 10, 15, 20 and 25 CPWH.

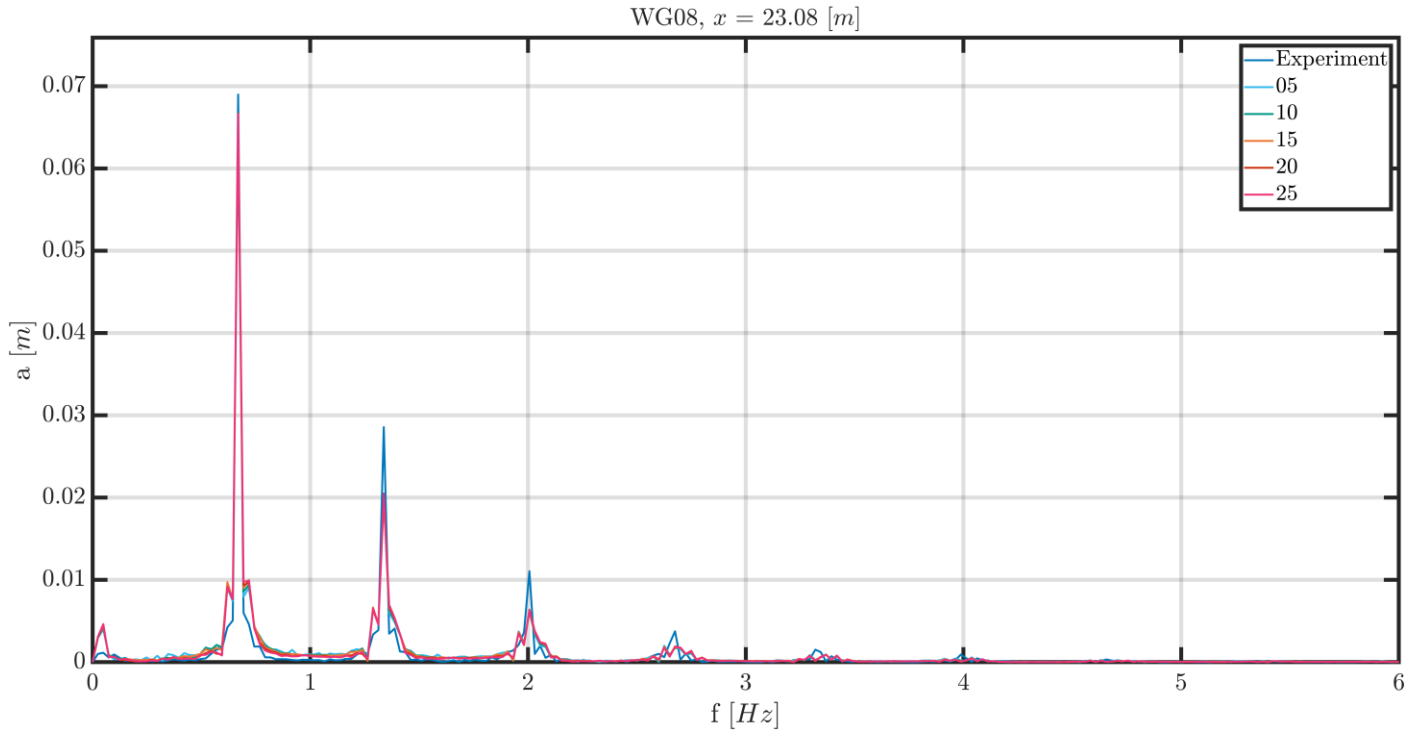


Figure A. 13 Overview of data at WG08. FFT of all resolutions compared with the experiment. Also, the theoretical input frequency and the peaks in the data sets can be found in this plot.

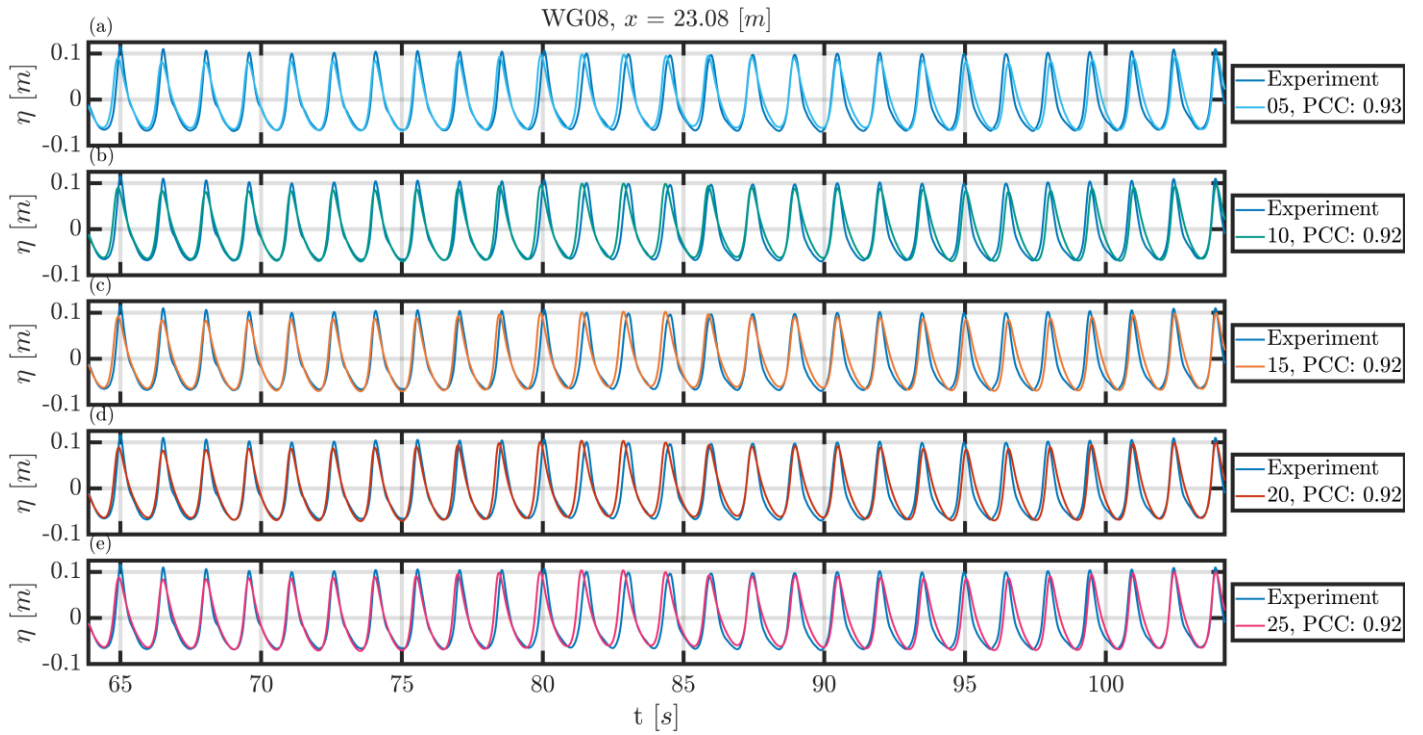


Figure A. 14(a-e): Overview of the selected time series for the different resolutions per wave height compared to the experiment results for WG08.

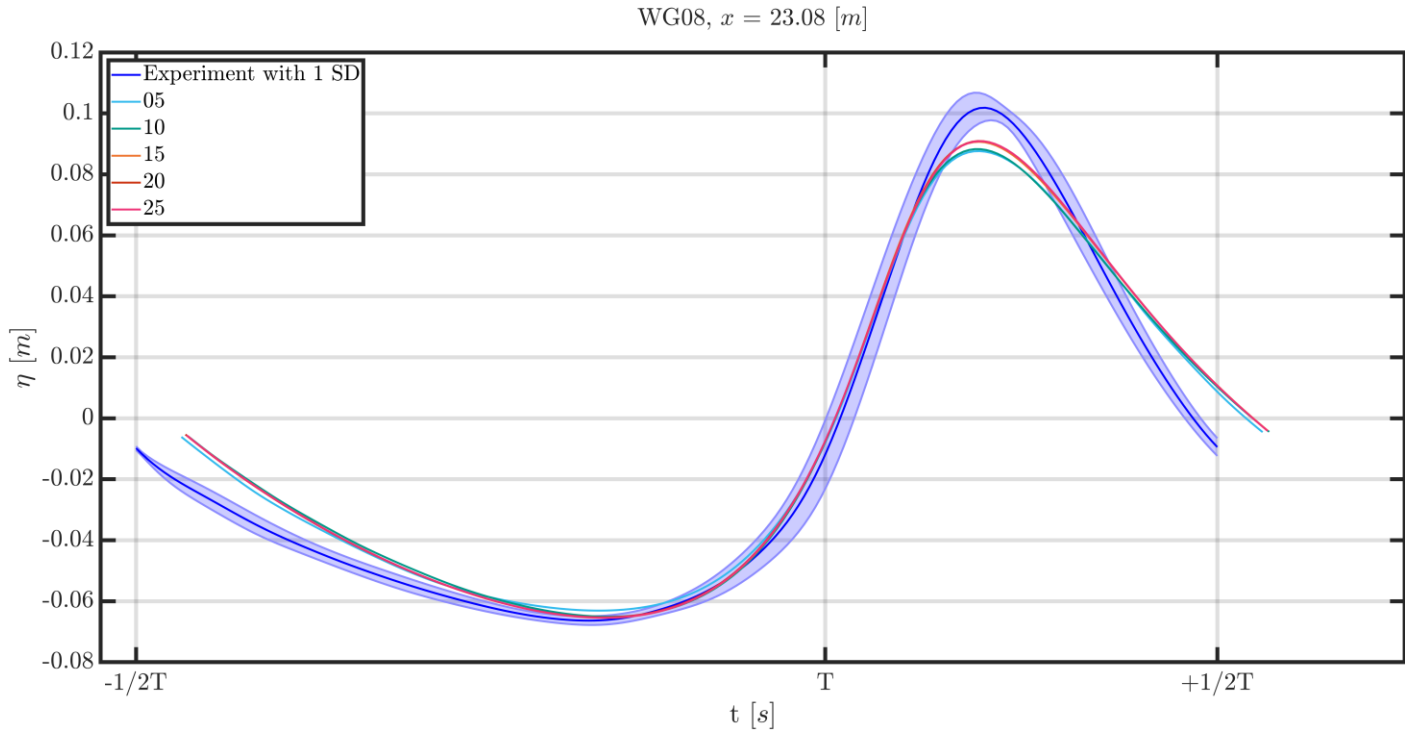


Figure A. 15 Comparison of the ensemble average wave shape at the location of WG08 where the experiment result is shown with 1 standard deviation.

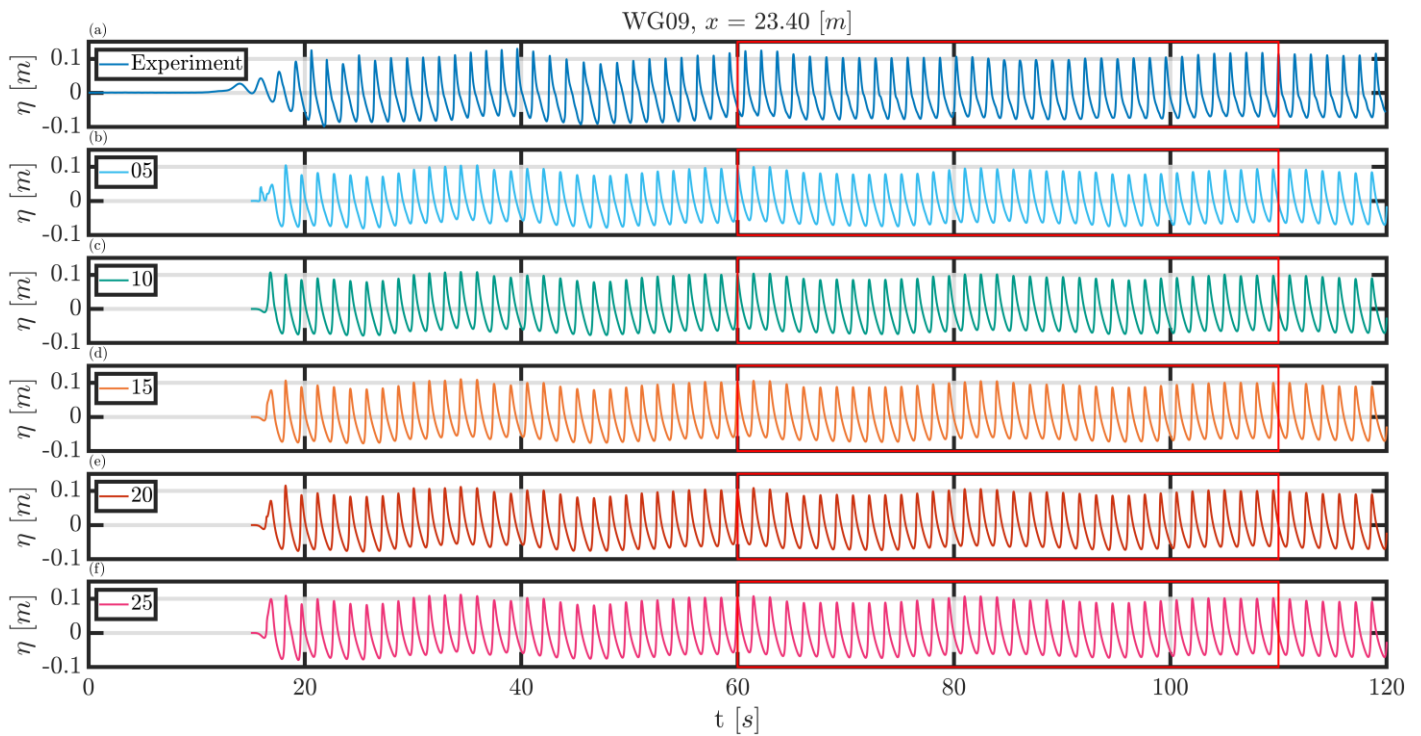


Figure A. 16 Overview of data at WG09. (a): the water level elevation as measured during the experiment. (b-f): the water level elevation measured with a resolution of respectively 5, 10, 15, 20 and 25 CPWH.

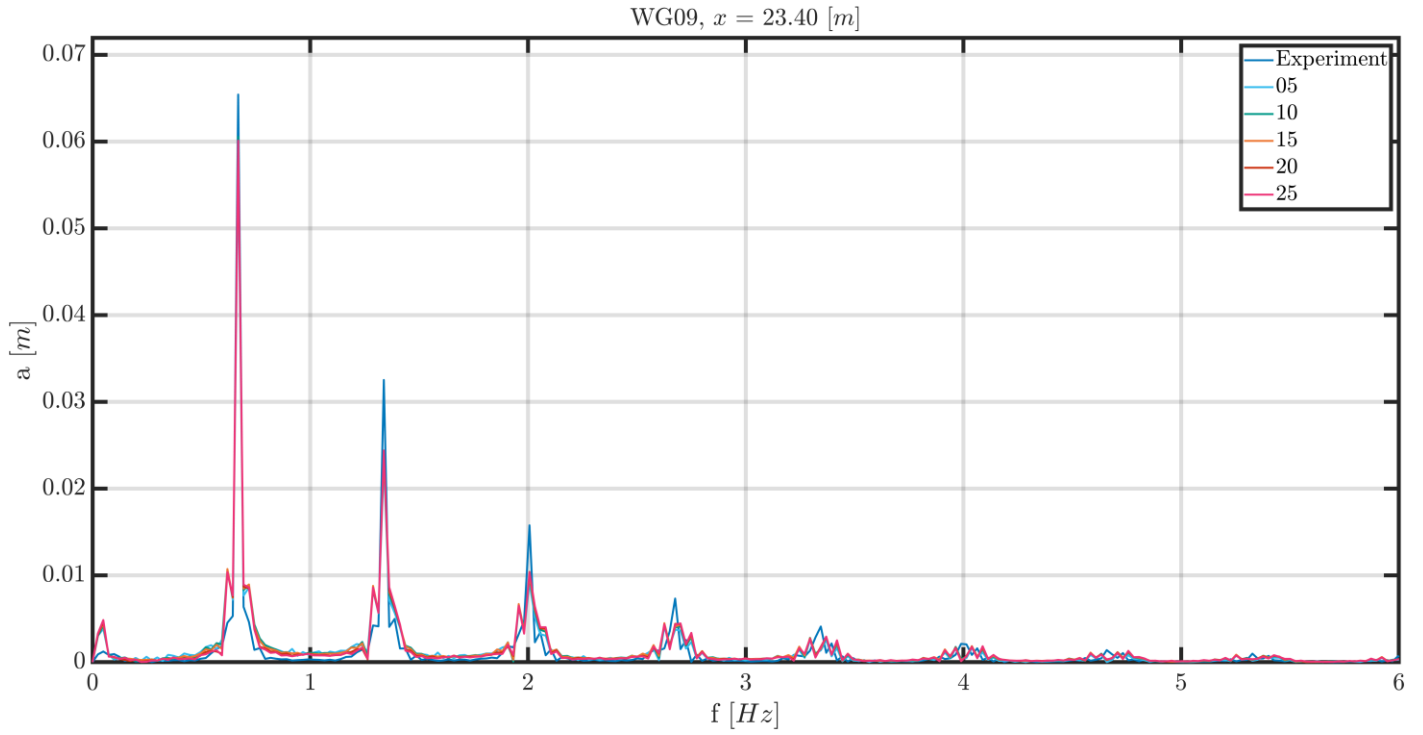


Figure A. 17 Overview of data at WG09. FFT of all resolutions compared with the experiment. Also, the theoretical input frequency and the peaks in the data sets can be found in this plot.

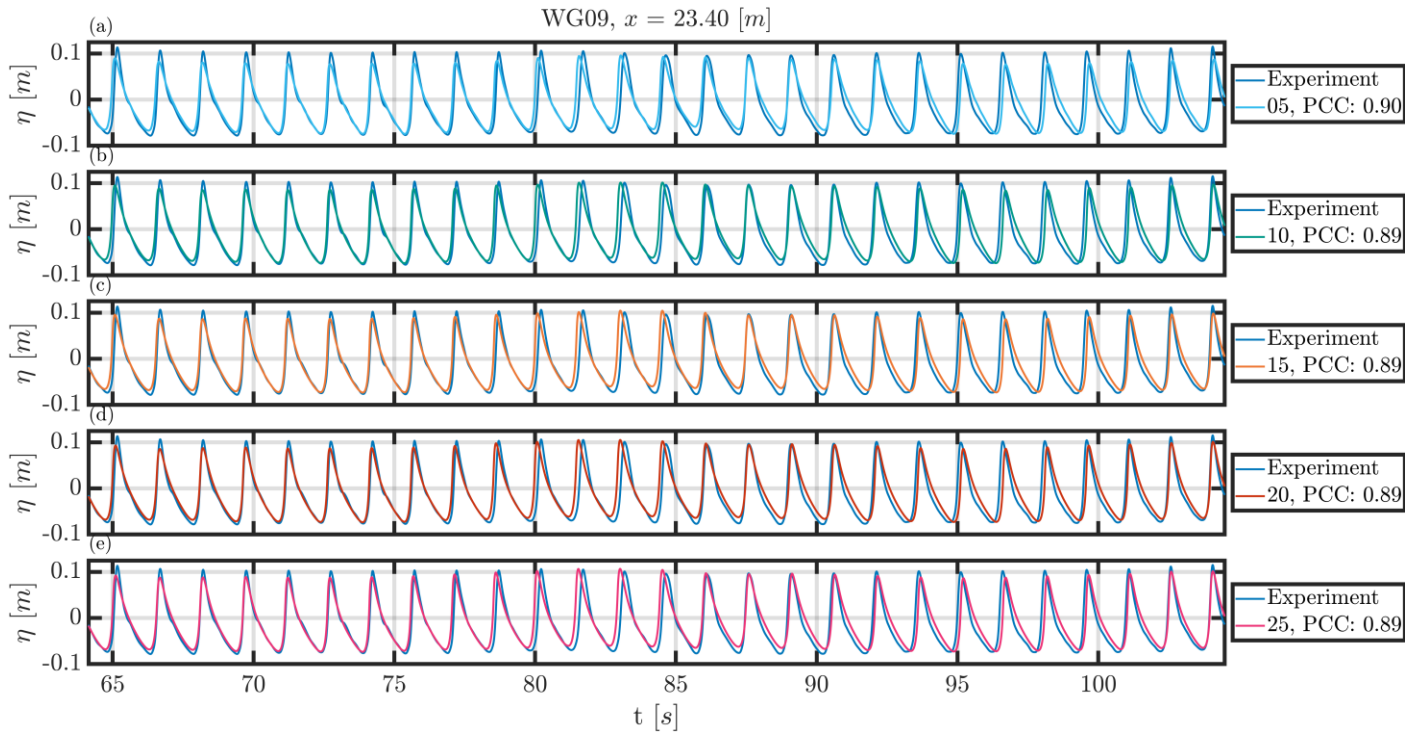


Figure A. 18(a-e): Overview of the selected time series for the different resolutions per wave height compared to the experiment results for WG09.

WG09, $x = 23.40$ [m]

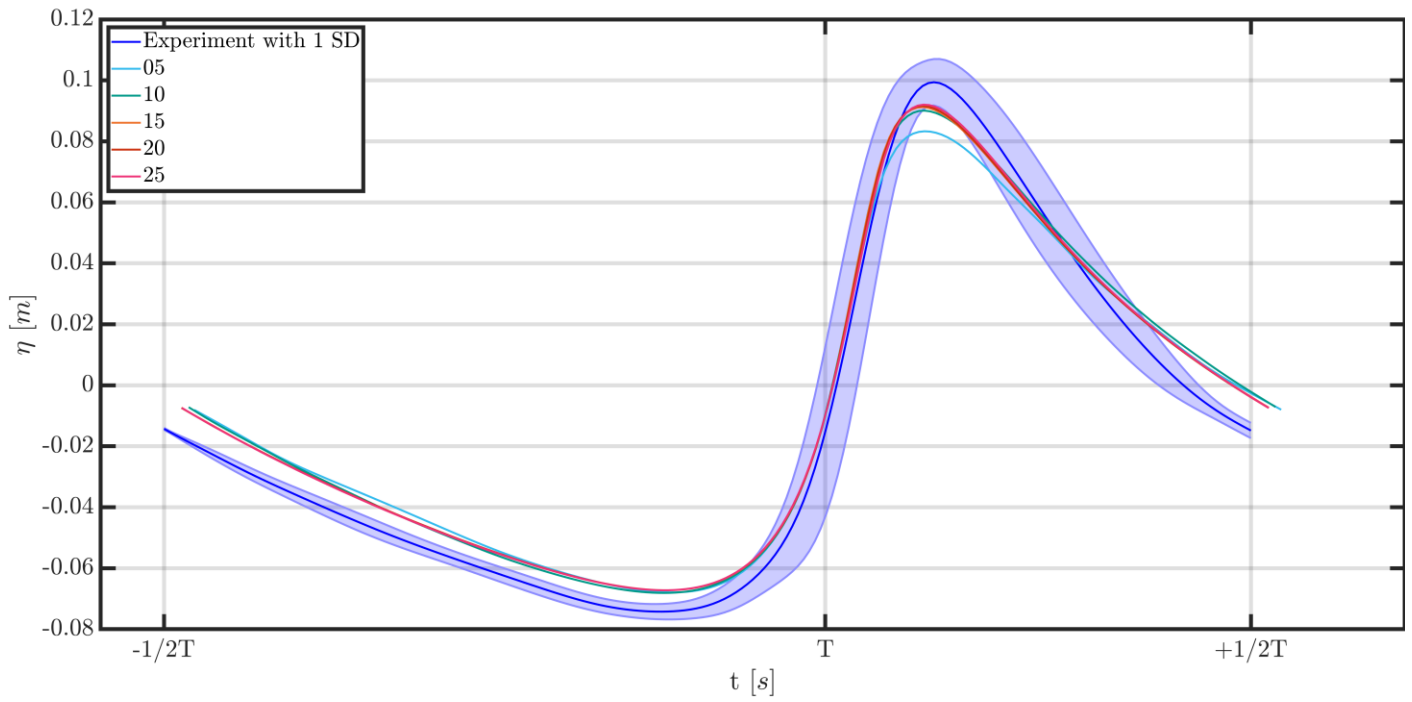


Figure A. 19 Comparison of the ensemble average wave shape at the location of WG09 where the experiment result is shown with 1 standard deviation.

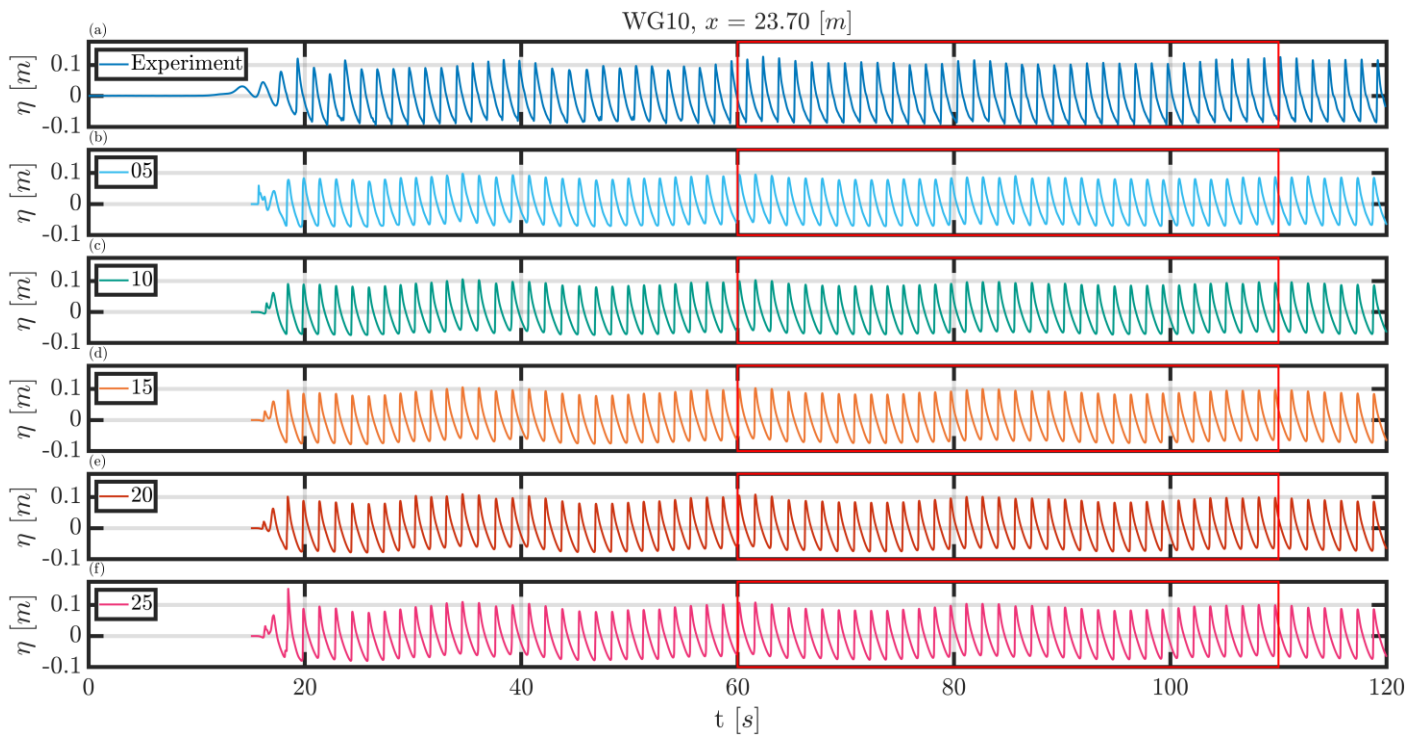


Figure A. 20 Overview of data at WG10. (a): the water level elevation as measured during the experiment. (b-f): the water level elevation measured with a resolution of respectively 5, 10, 15, 20 and 25 CPWH.

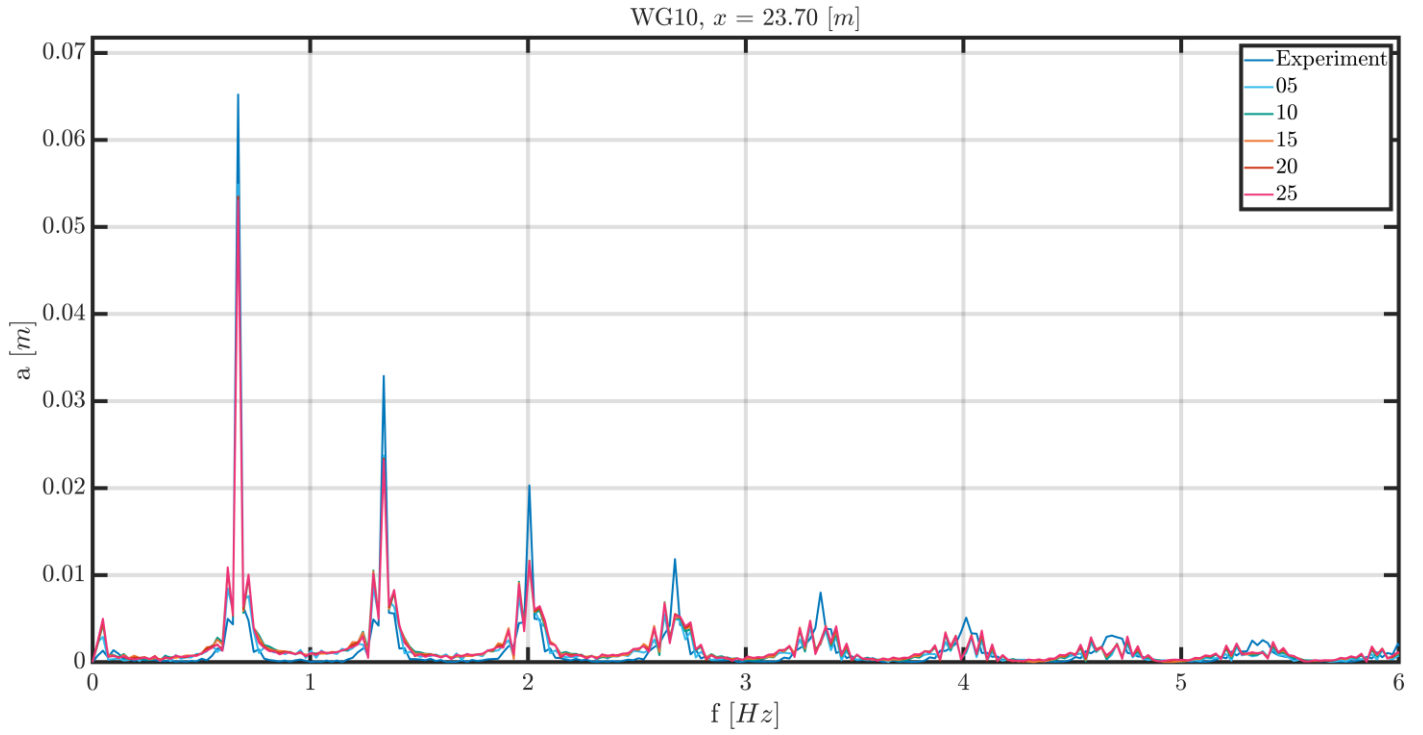


Figure A. 21 Overview of data at WG10. FFT of all resolutions compared with the experiment. Also, the theoretical input frequency and the peaks in the data sets can be found in this plot.

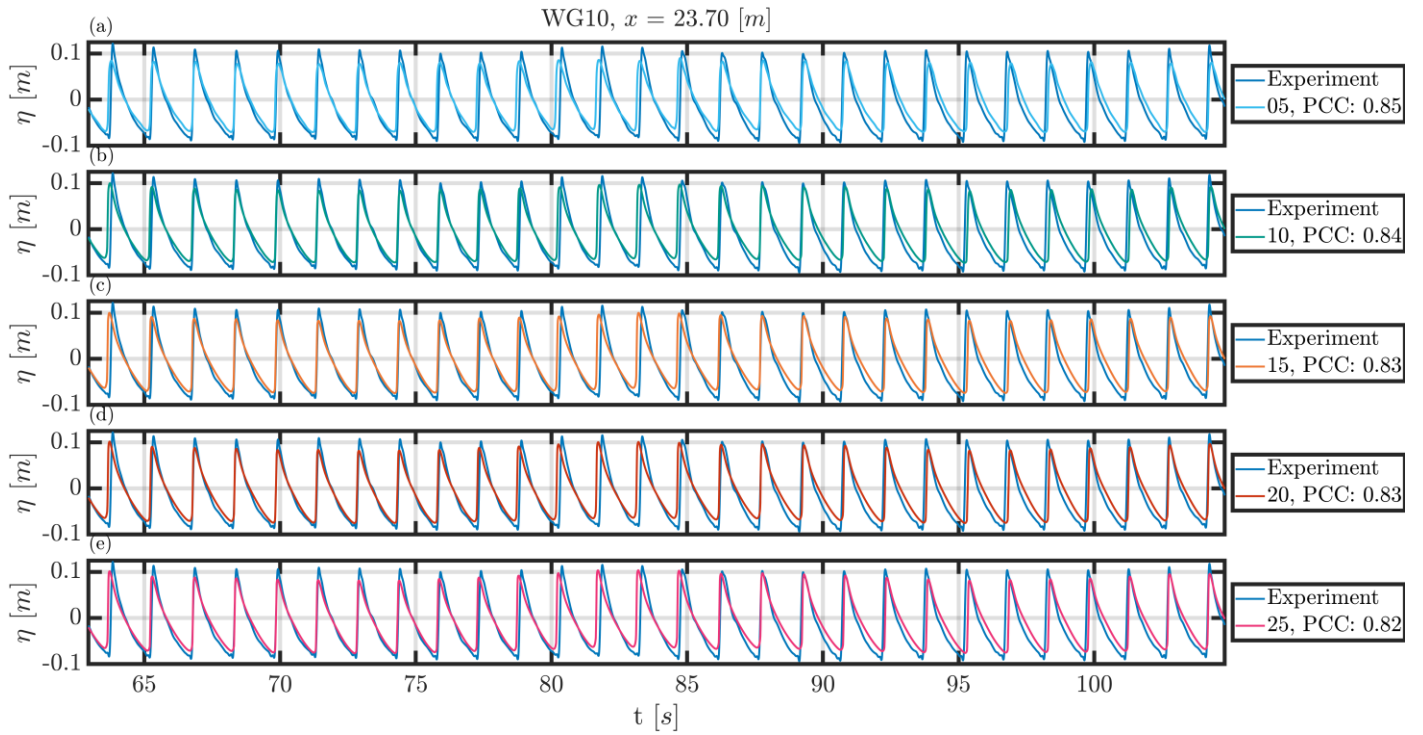


Figure A. 22(a-e): Overview of the selected time series for the different resolutions per wave height compared to the experiment results for WG10.

WG10, $x = 23.70$ [m]

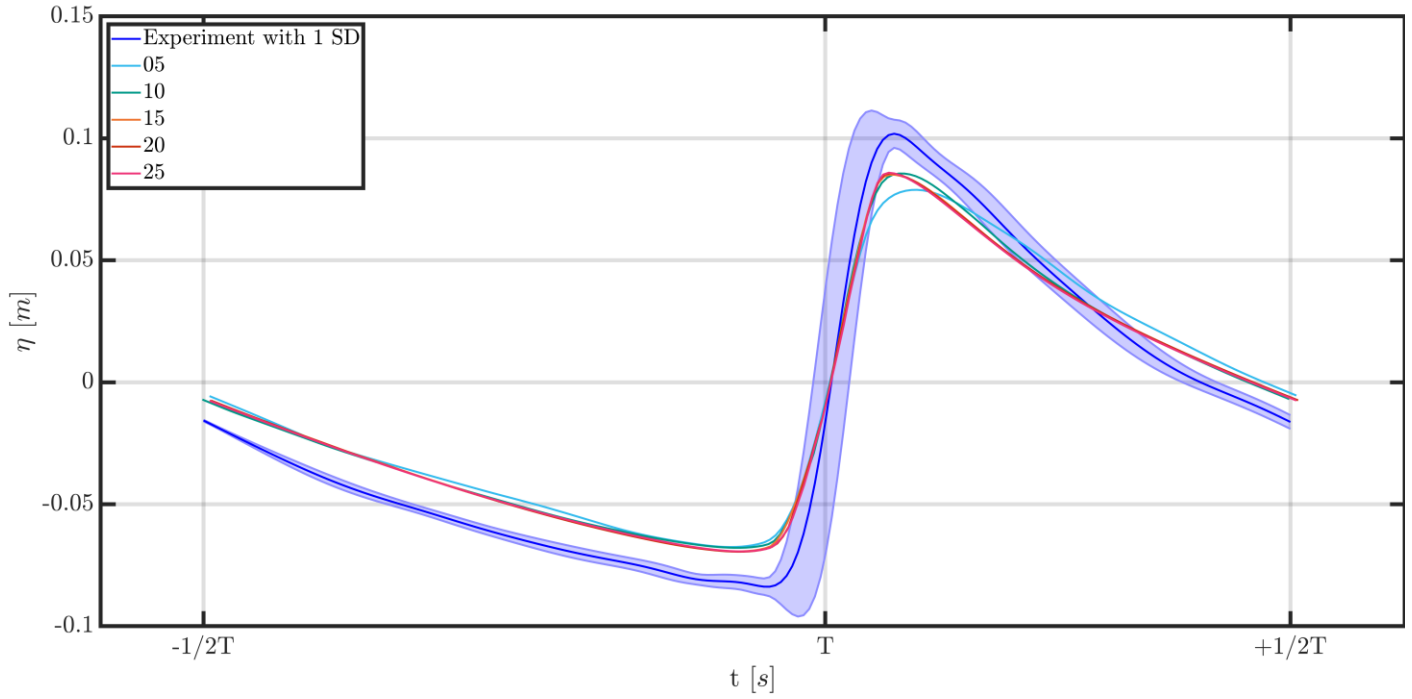


Figure A. 23 Comparison of the ensemble average wave shape at the location of WG10 where the experiment result is shown with 1 standard deviation.

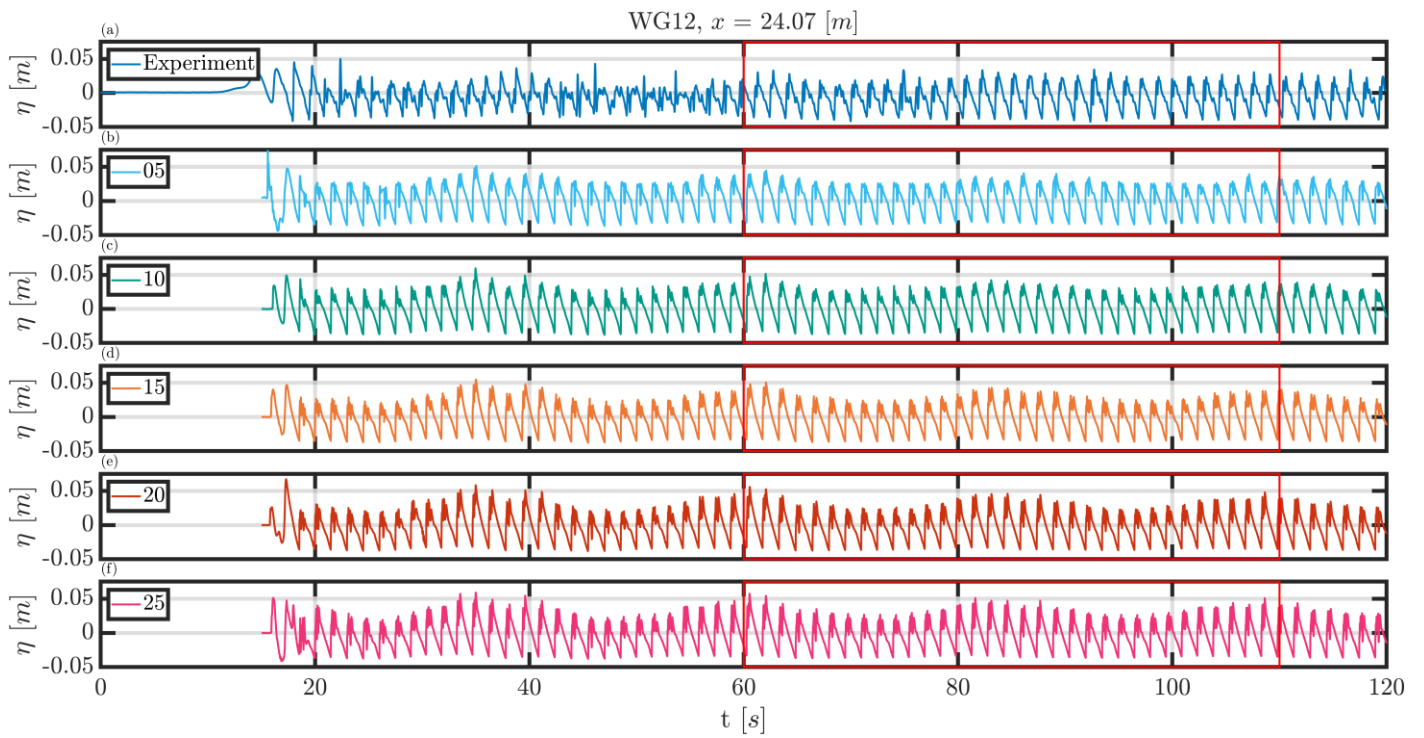


Figure A. 24 Overview of data at WG12. (a): the water level elevation as measured during the experiment. (b-f): the water level elevation measured with a resolution of respectively 5, 10, 15, 20 and 25 CPWH.

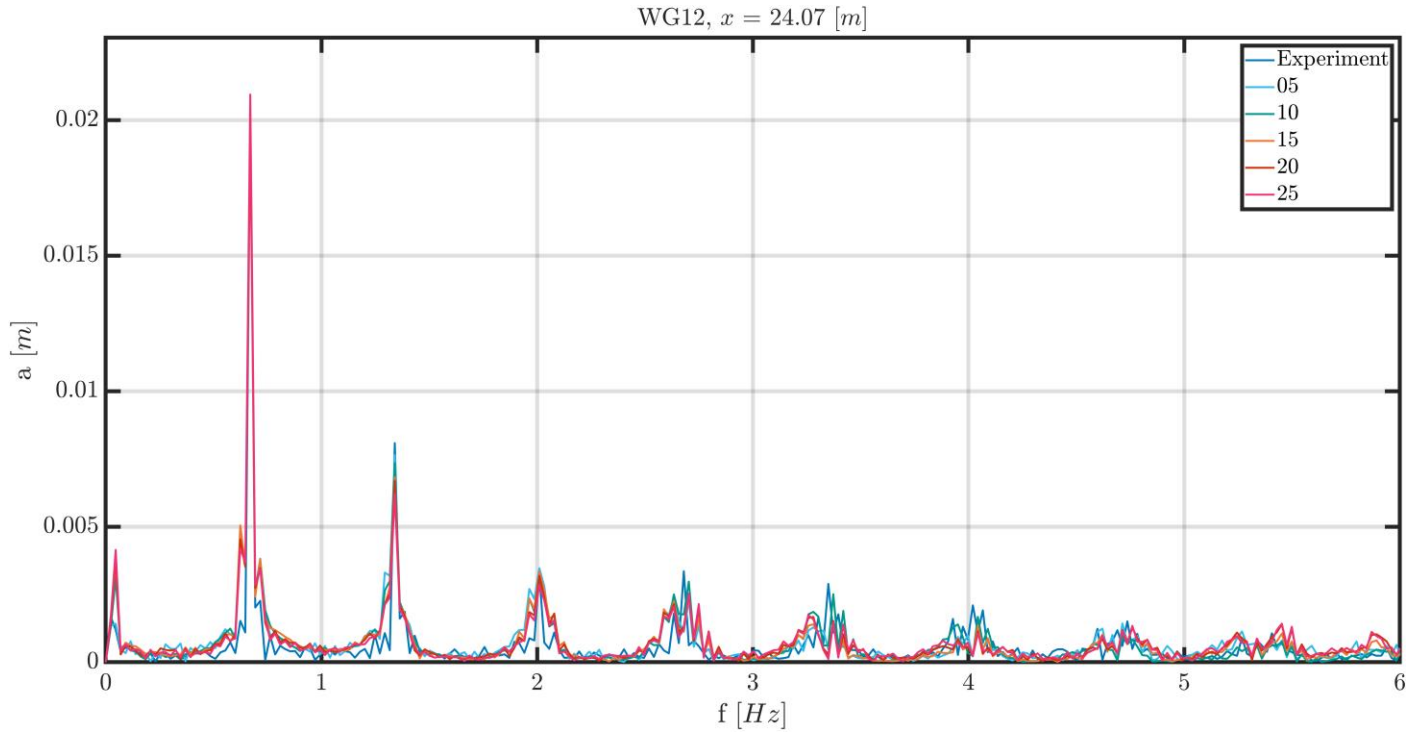


Figure A. 25 Overview of data at WG12. FFT of all resolutions compared with the experiment. Also, the theoretical input frequency and the peaks in the data sets can be found in this plot.

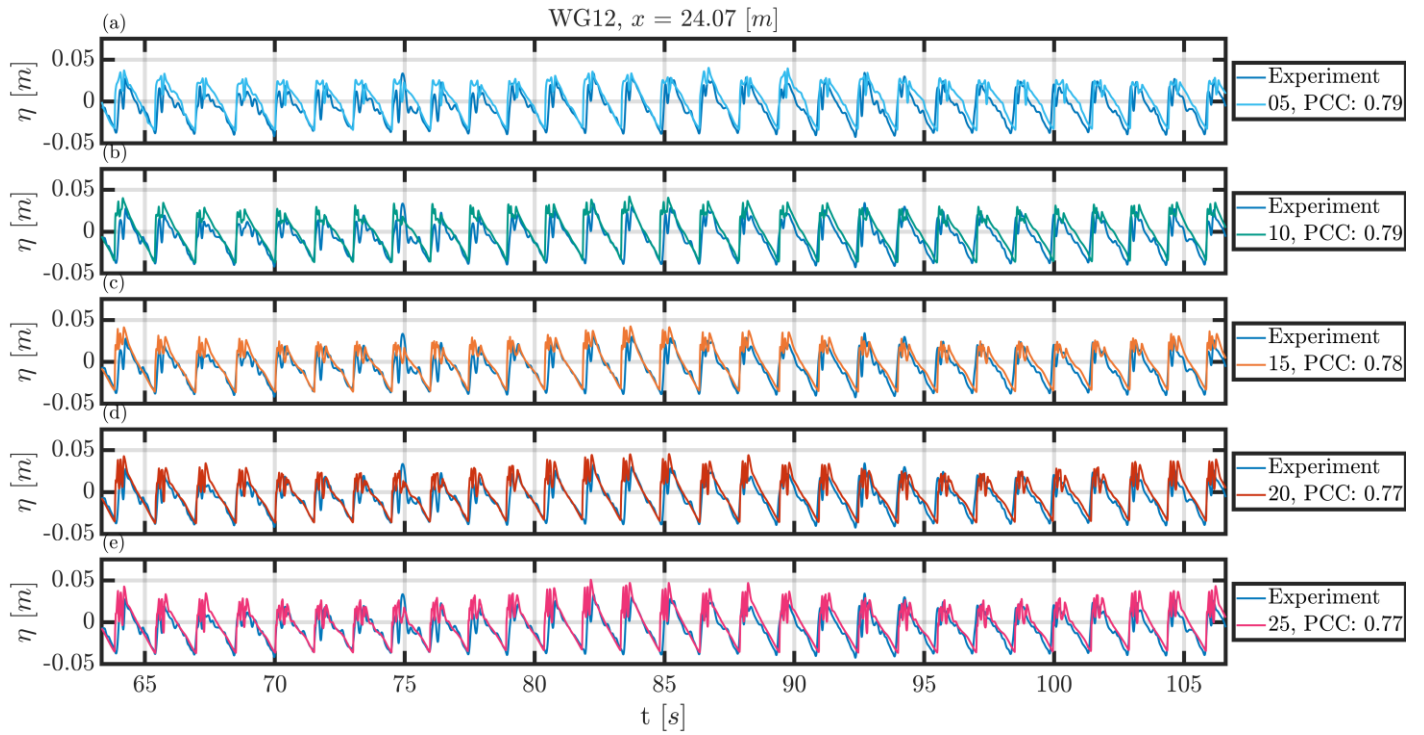


Figure A. 26(a-e): Overview of the selected time series for the different resolutions per wave height compared to the experiment results for WG12.

WG12, $x = 24.07$ [m]

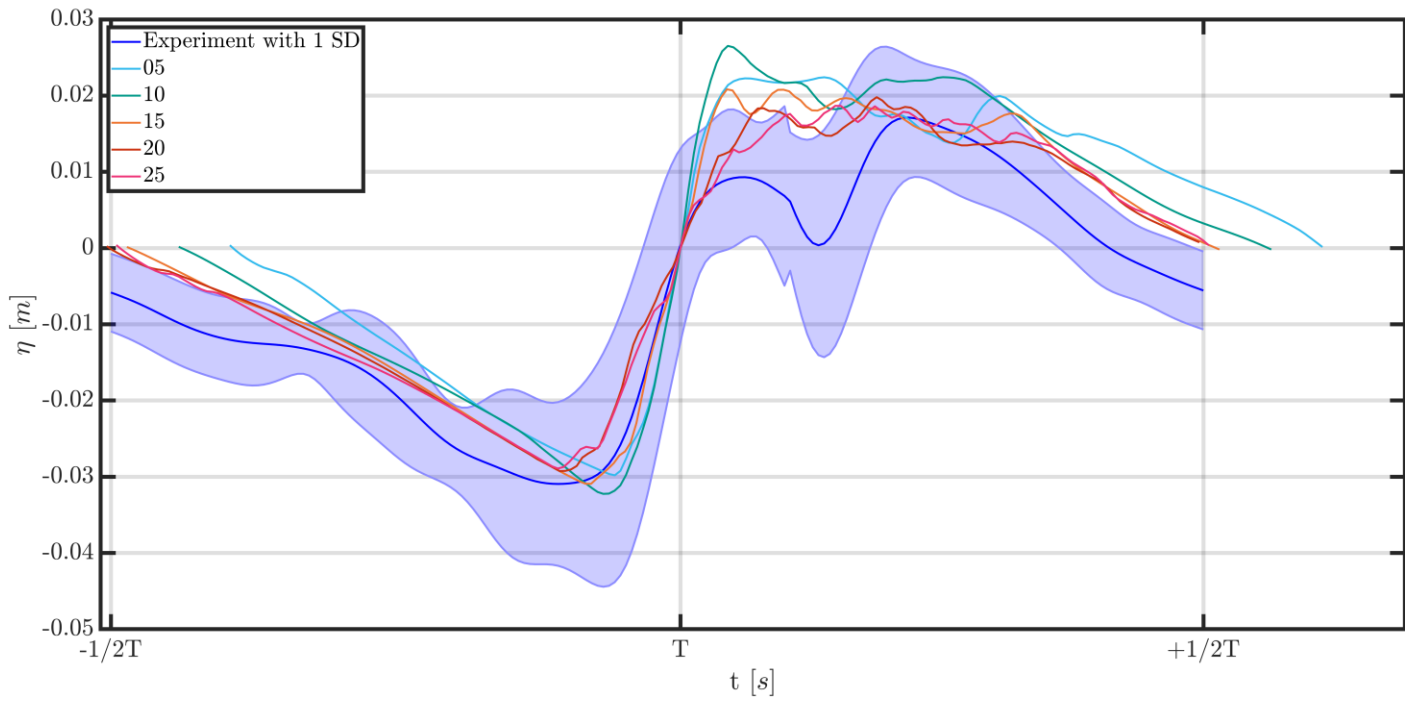


Figure A. 27 Comparison of the ensemble average wave shape at the location of WG12 where the experiment result is shown with 1 standard deviation.

Appendix C y^+ values 2D model validation

This appendix contains the y^+ values for the different meshes in the 2D model validation.

Results of y^+ Plus for all time steps for the case WIF-2D-05
Mean 100.29, Median: 53.05

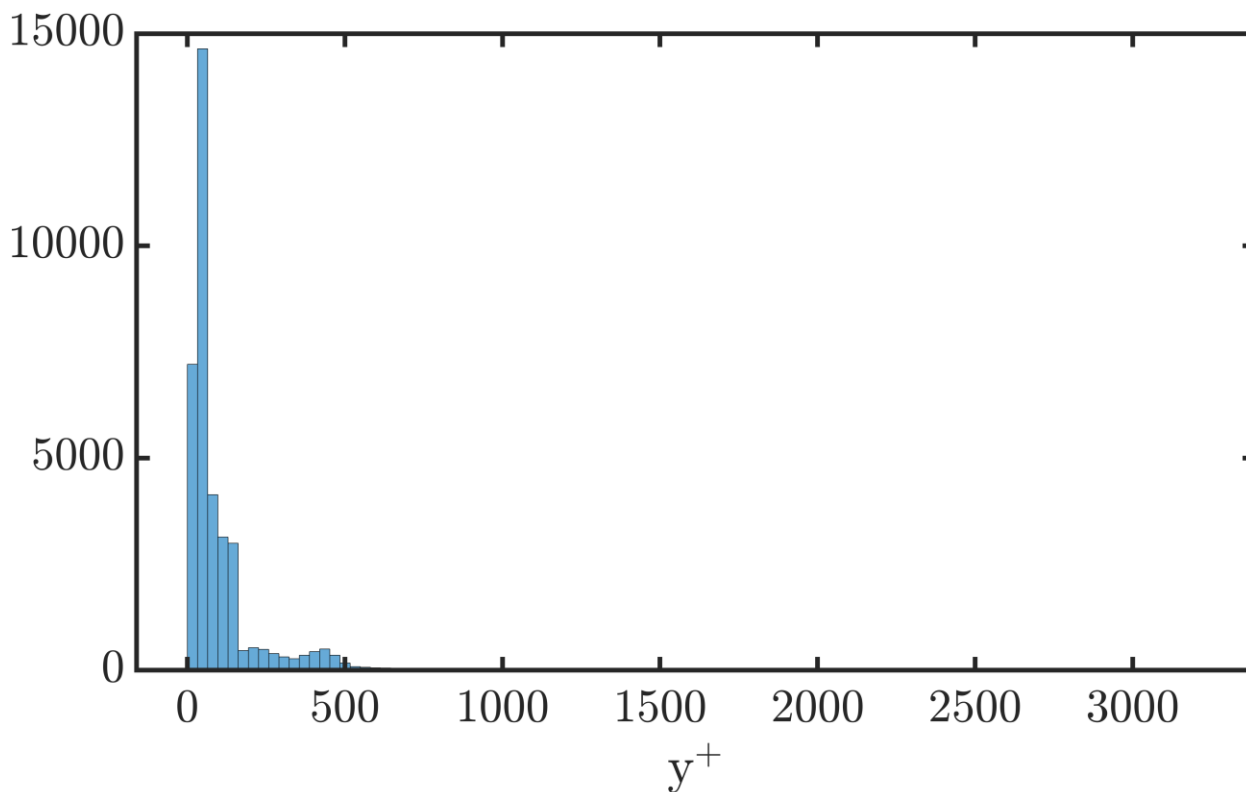


Figure A. 28 Histogram y^+ for the 2D isoAdvect case with 05 CPWH

Results of y^+ Plus for all time steps for the case WIF-2D-10
Mean 60.62, Median: 31.42

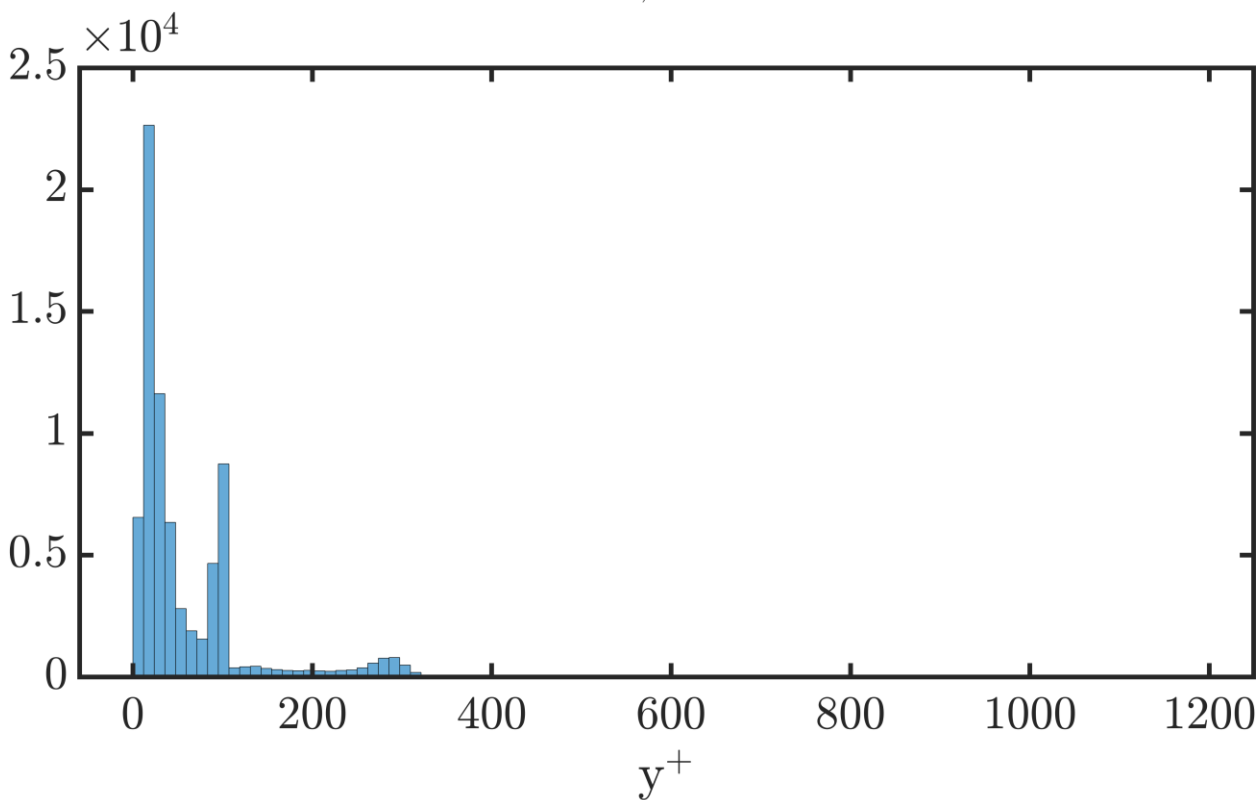


Figure A. 29 Histogram y^+ for the 2D isoAdvectord case with 10 CPWH

Results of y^+ Plus for all time steps for the case WIF-2D-15
Mean 46.62, Median: 23.60

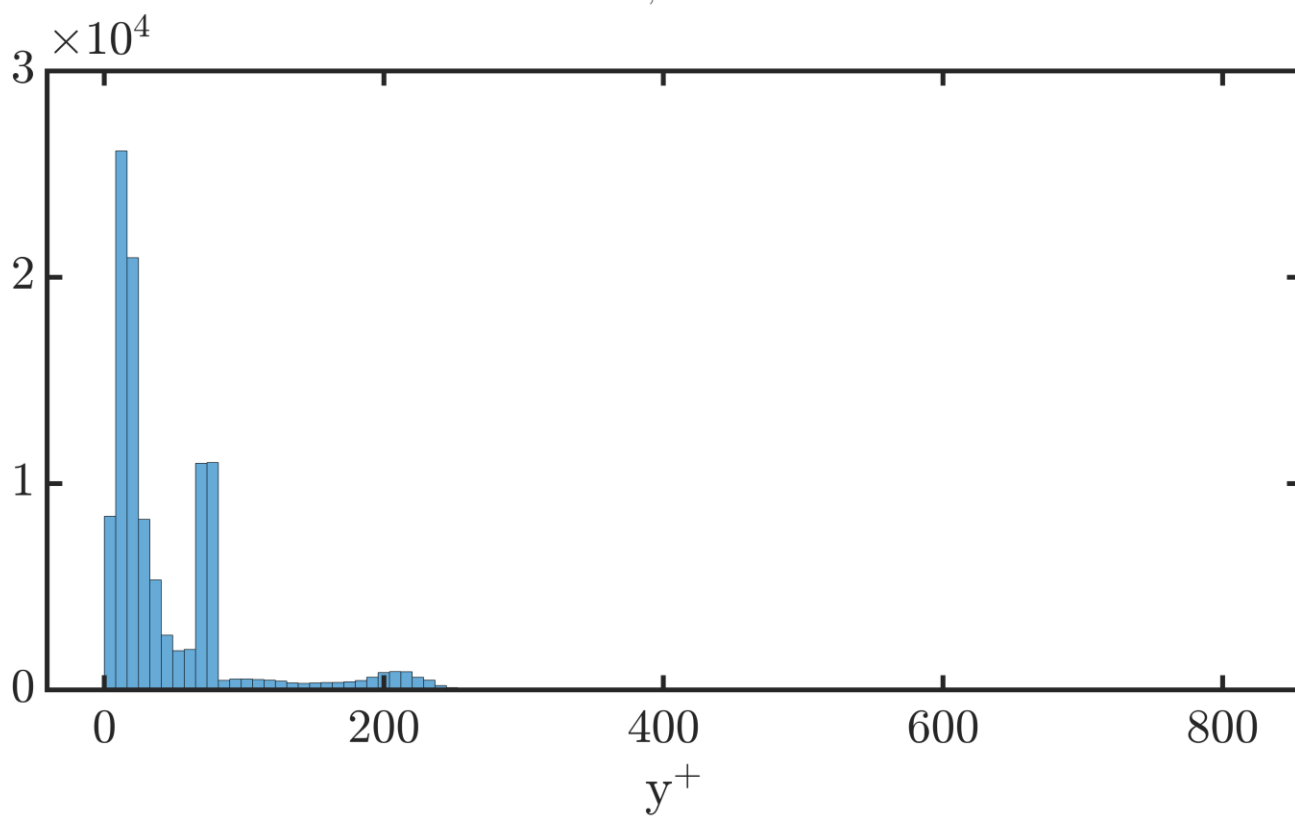


Figure A. 30 Histogram y^+ for the 2D isoAdvectord case with 15 CPWH

Results of y^+ Plus for all time steps for the case WIF-2D-20
Mean 36.43, Median: 17.55

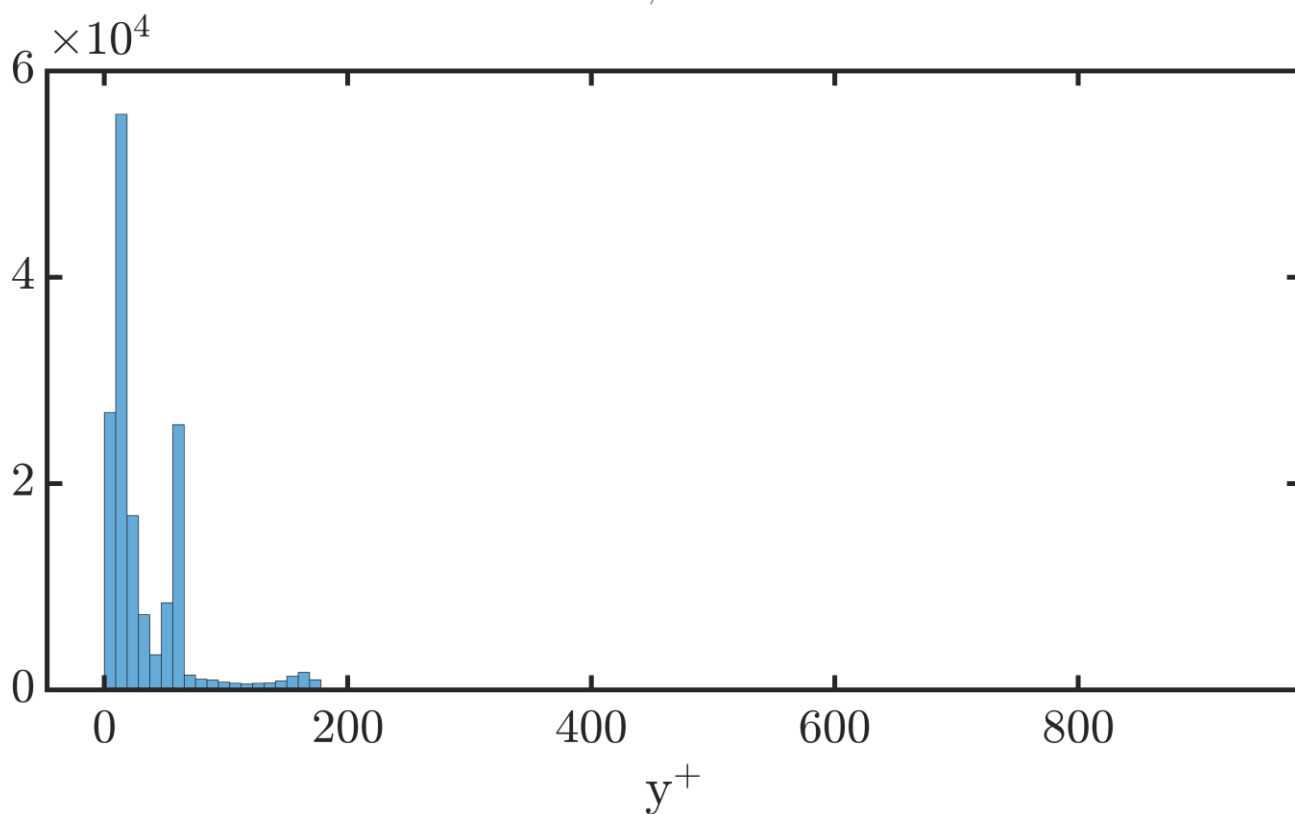


Figure A. 31 Histogram y^+ for the 2D isoAdvectord case with 20 CPWH

Results of yPlus for all time steps for the case WIF-2D-25
Mean 29.10, Median: 14.91

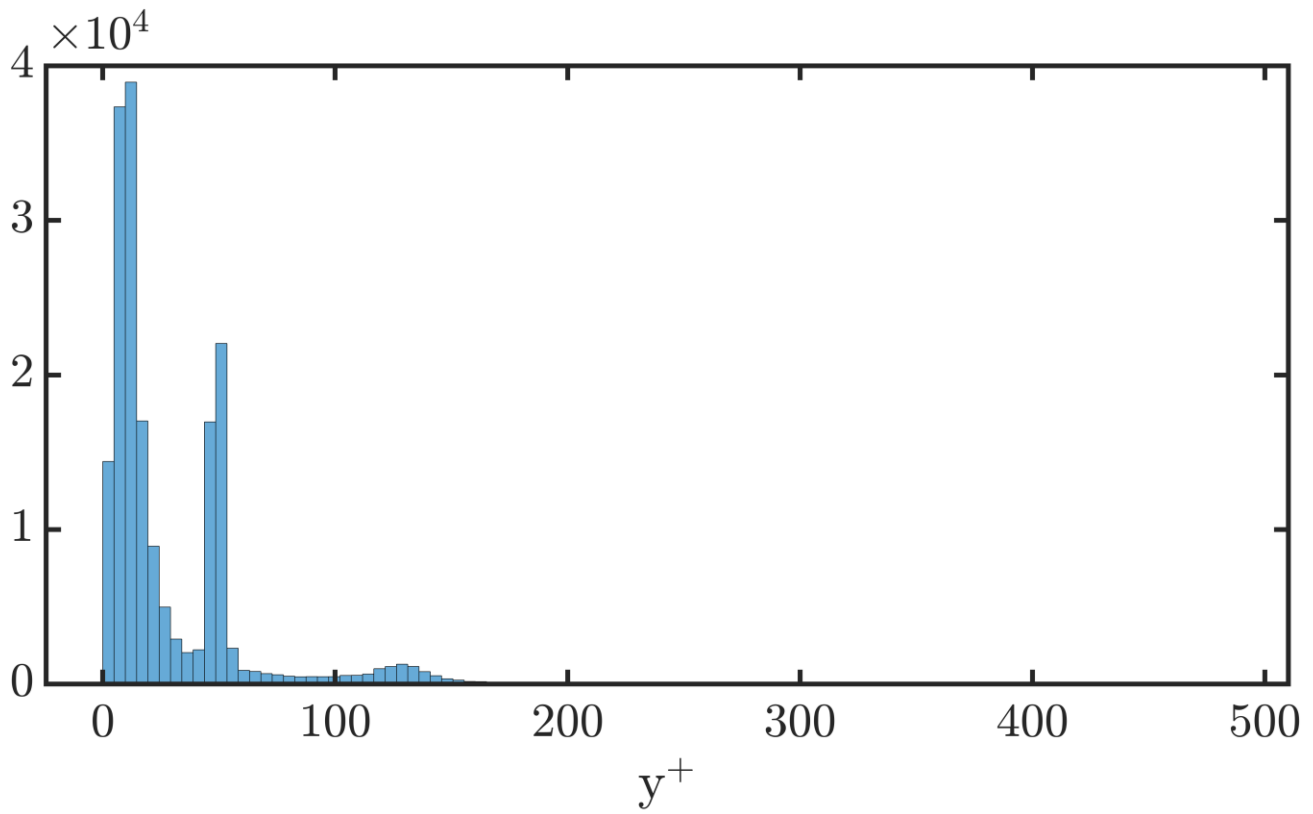


Figure A. 32 Histogram y^+ for the 2D isoAdvect case with 25 CPWH

Appendix D Wave states

This appendix contains the results for all wave gauges for the other wave states assessed in the 2D simulations. Next to the results of the wave gauges the average y^+ of the simulations is also shown. The following wave states can be found in this appendix:

- Wave state $H=0.05$ m, $T=1.20$ s
- Wave state $H=0.05$ m, $T=2.44$ s
- Wave state $H=0.10$ m, $T=1.20$ s
- Wave state $H=0.10$ m, $T=2.44$ s
- Wave state $H=0.15$ m, $T=1.96$ s

For all wave states and all wave gauges the total overview of the data, selected data, aligned data, FFT and an ensemble average wave shape is shown.

Table A. 1 shows the y^+ values for the different cases averaged out for the total simulation.

Table A. 1 Overview y^+ values other wave states

Data set	Median [-]	Mean [-]
$H=0.05$ m, $T=1.20$ s	3.07	5.12
$H=0.05$ m, $T=2.44$ s	10.68	8.09
$H=0.10$ m, $T=1.20$ s	10.40	17.48
$H=0.10$ m, $T=2.44$ s	22.80	30.62
$H=0.15$ m, $T=1.96$ s	30.69	51.16

Appendix D.1 $H=0.05$ m, $T=1.20$ s

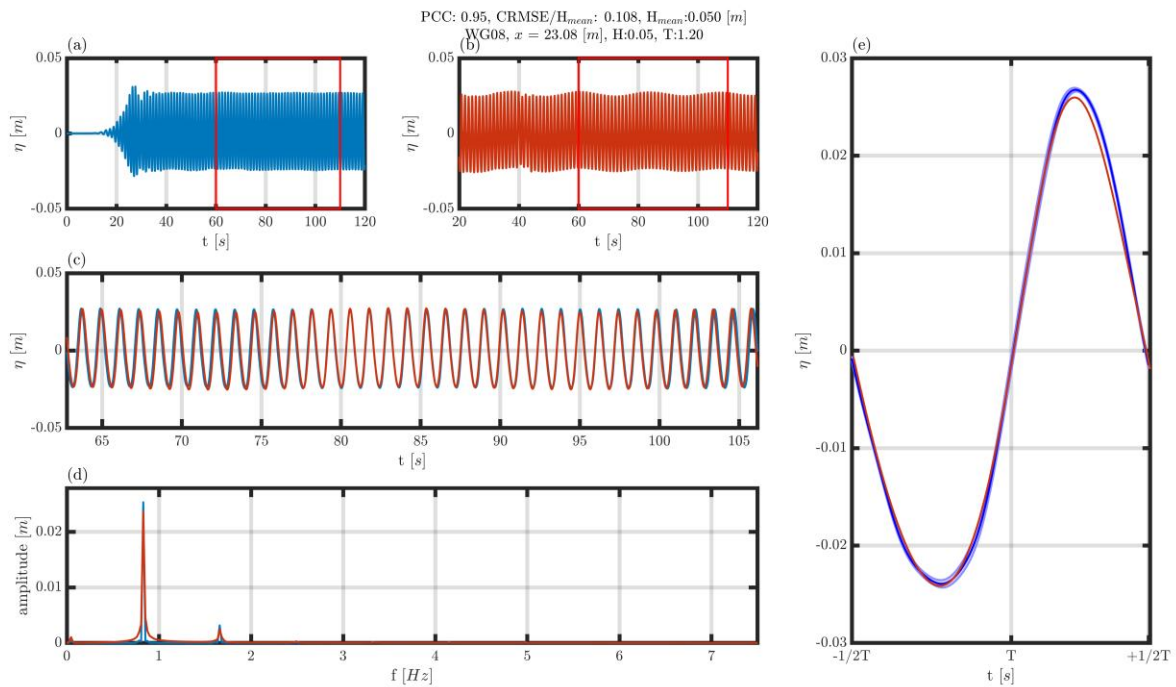


Figure A. 33 Overview of a comparison between the OpenFOAM data and the experiment for WG08. (a) Overview water level elevation from the experiment and the selected part. (b) Overview water level elevation from OpenFOAM and the selected part. (c): Aligned water level elevation signal. (d): Amplitude spectral analysis for both data sets. (e): Overlapped ensemble average wave shape.

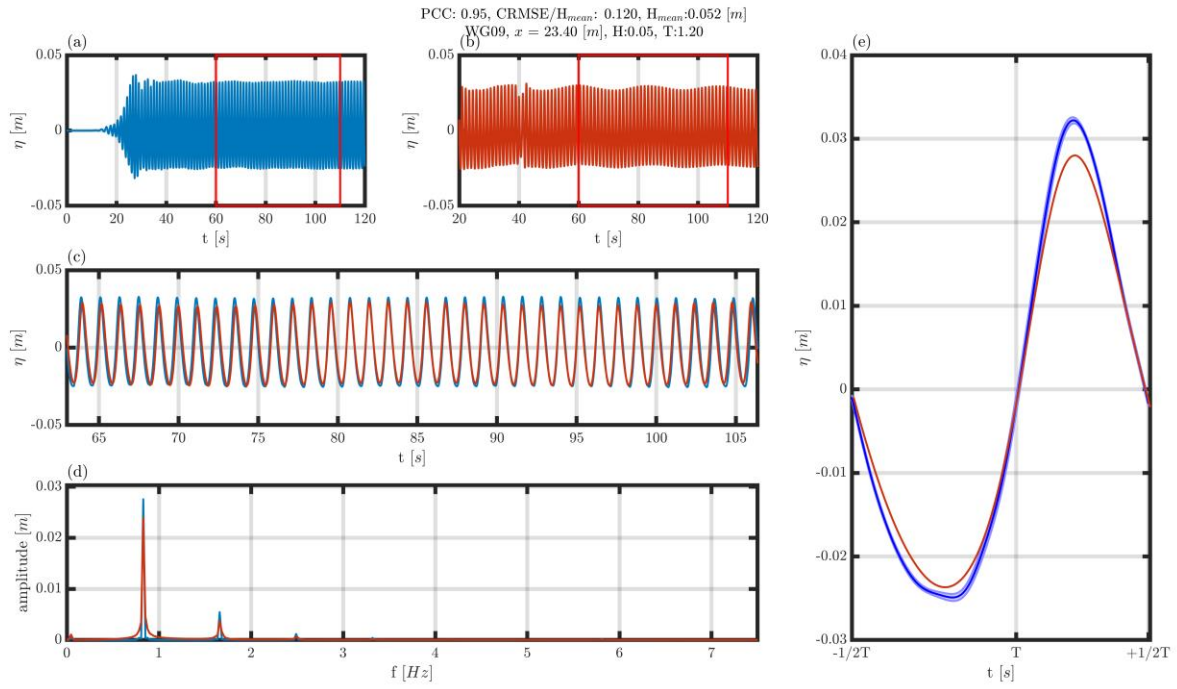


Figure A. 34 Overview of a comparison between the OpenFOAM data and the experiment for WG09. (a) Overview water level elevation from the experiment and the selected part. (b) Overview water level elevation from OpenFOAM and the selected part. (c): Aligned water level elevation signal. (d): Amplitude spectral analysis for both data sets. (e): Overlapped ensemble average wave shape.

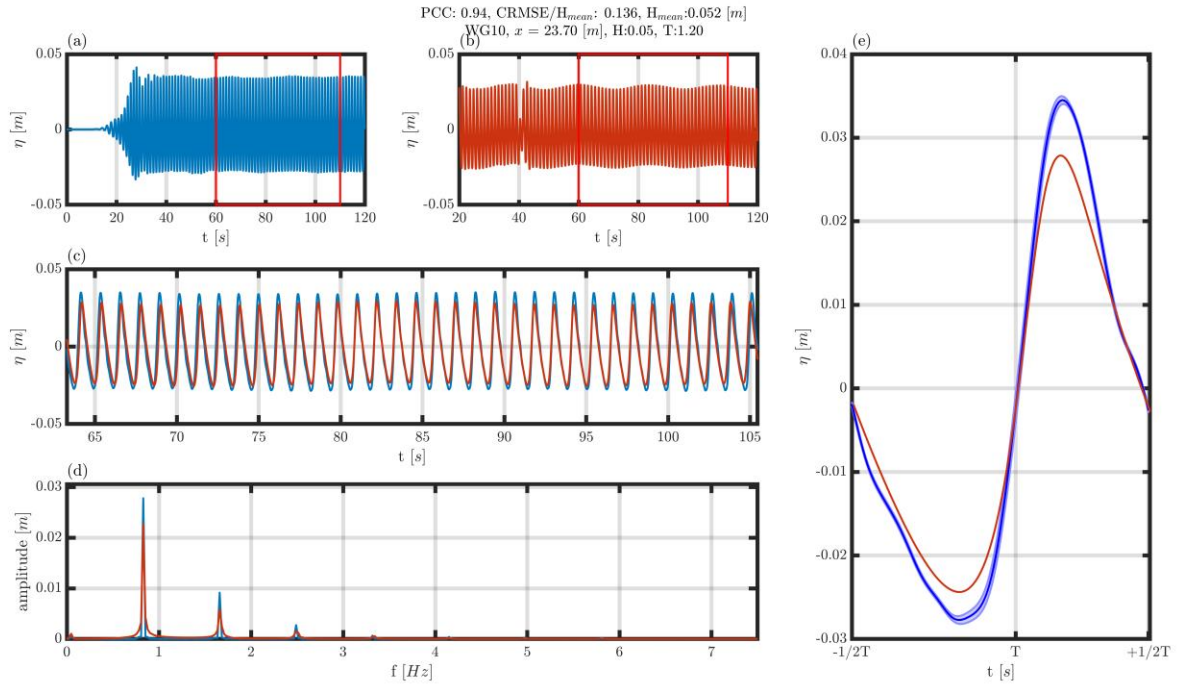


Figure A. 35 Overview of a comparison between the OpenFOAM data and the experiment for WG10. (a) Overview water level elevation from the experiment and the selected part. (b) Overview water level elevation from OpenFOAM and the selected part. (c): Aligned water level elevation signal. (d): Amplitude spectral analysis for both data sets. (e): Overlapped ensemble average wave shape.

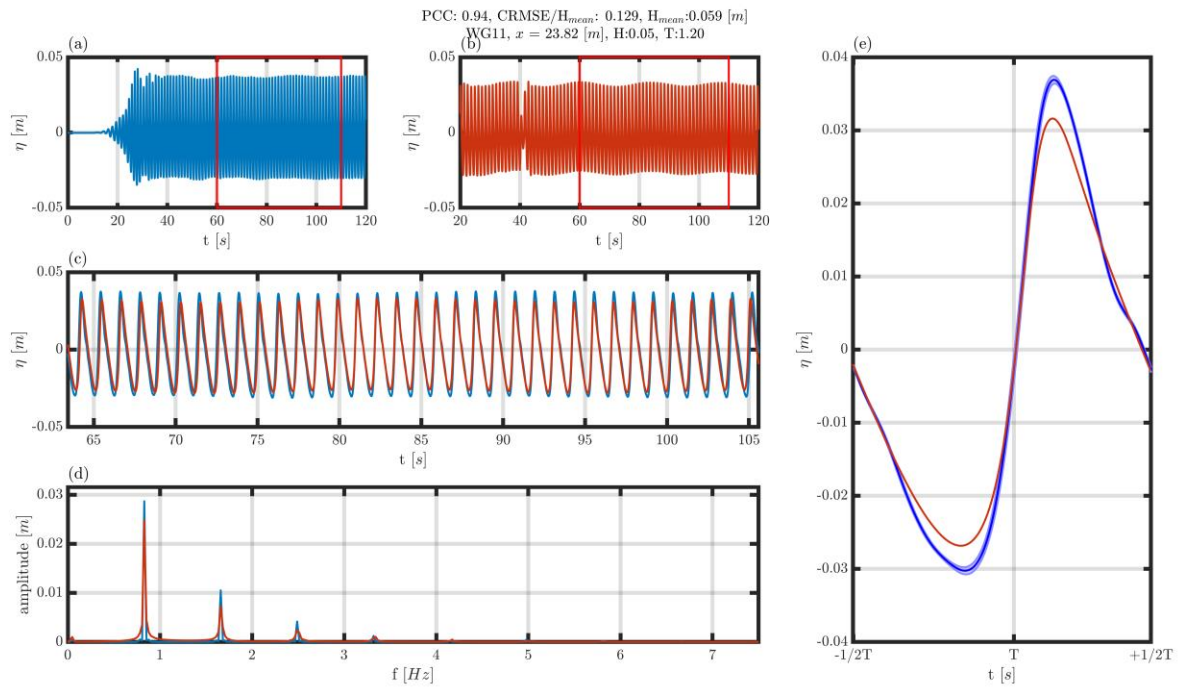


Figure A. 36 Overview of a comparison between the OpenFOAM data and the experiment for WG11. (a) Overview water level elevation from the experiment and the selected part. (b) Overview water level elevation from OpenFOAM and the selected part. (c): Aligned water level elevation signal. (d): Amplitude spectral analysis for both data sets. (e): Overlapped ensemble average wave shape.

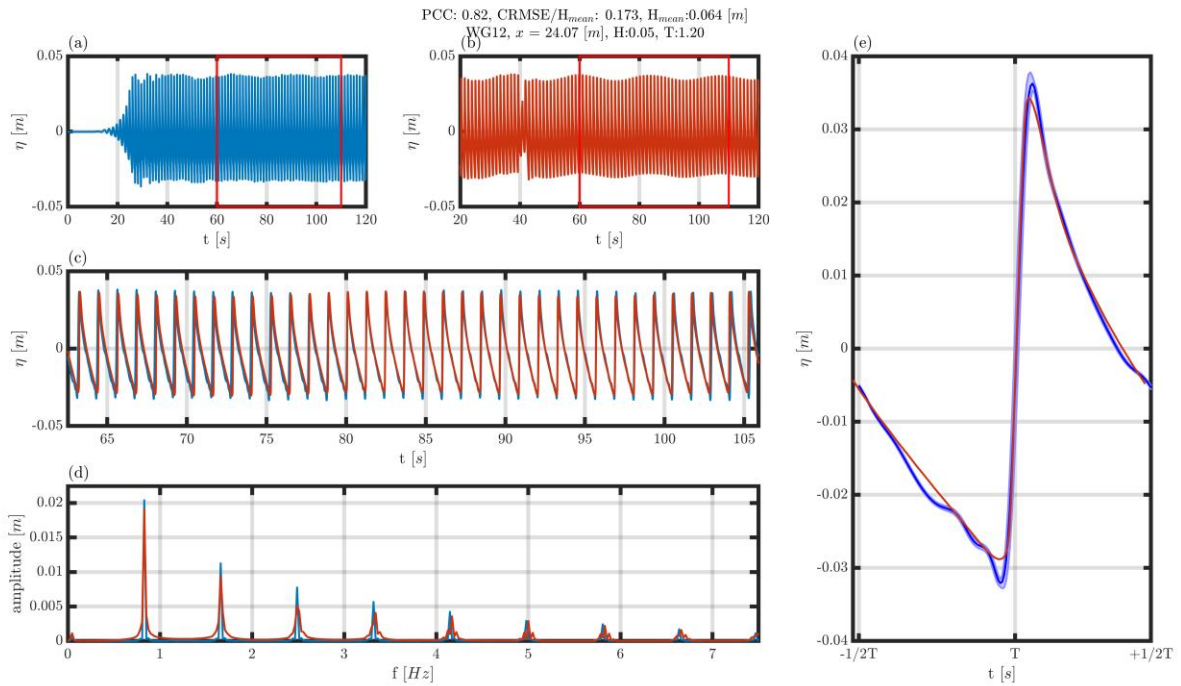


Figure A. 37 Overview of a comparison between the OpenFOAM data and the experiment for WG12. (a) Overview water level elevation from the experiment and the selected part. (b) Overview water level elevation from OpenFOAM and the selected part. (c): Aligned water level elevation signal. (d): Amplitude spectral analysis for both data sets. (e): Overlapped ensemble average wave shape.

Results of yPlus for all time steps for the case WIF-005120
 Mean 5.12, Median: 3.07

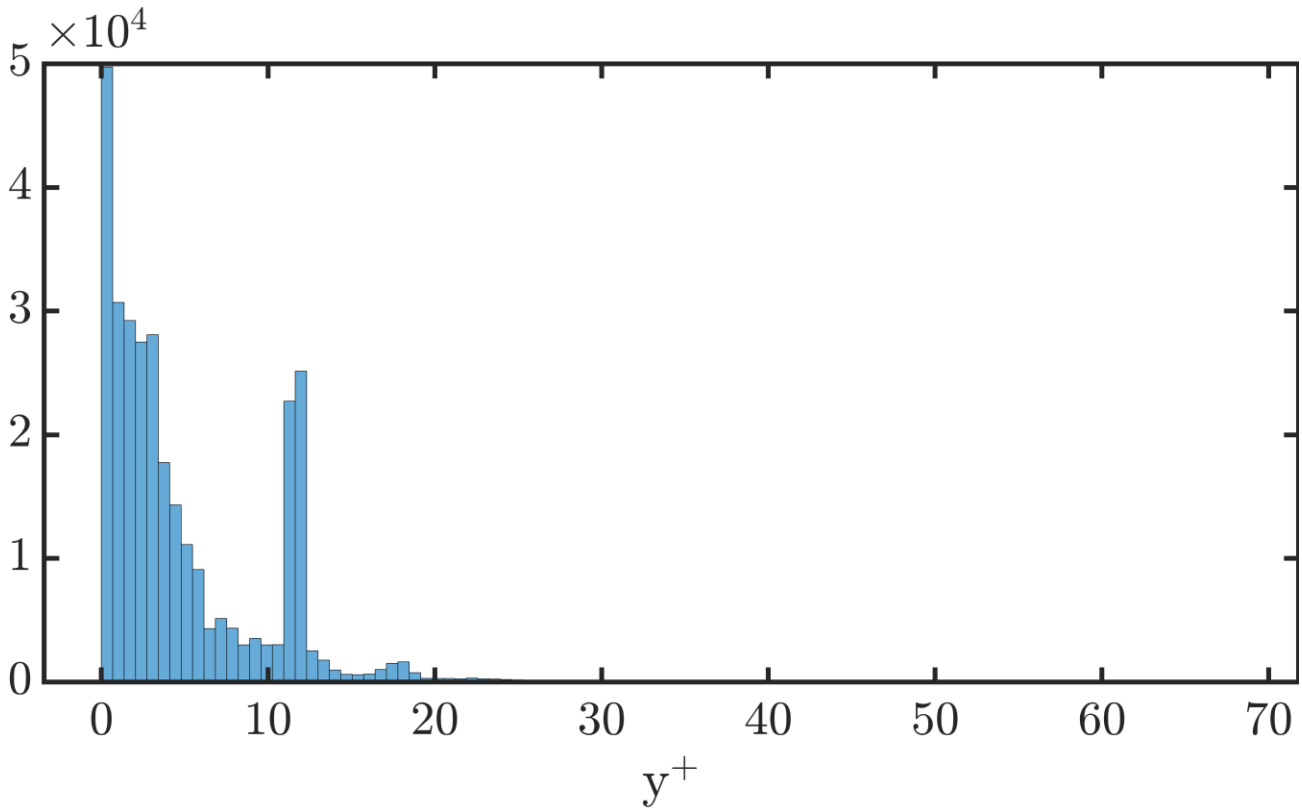


Figure A. 38 Histogram y^+ for the 2D isoAdvector case of $H=0.05$ m, $T=1.20$ s

Appendix D.2 $H=0.05$ m, $T=2.44$ s

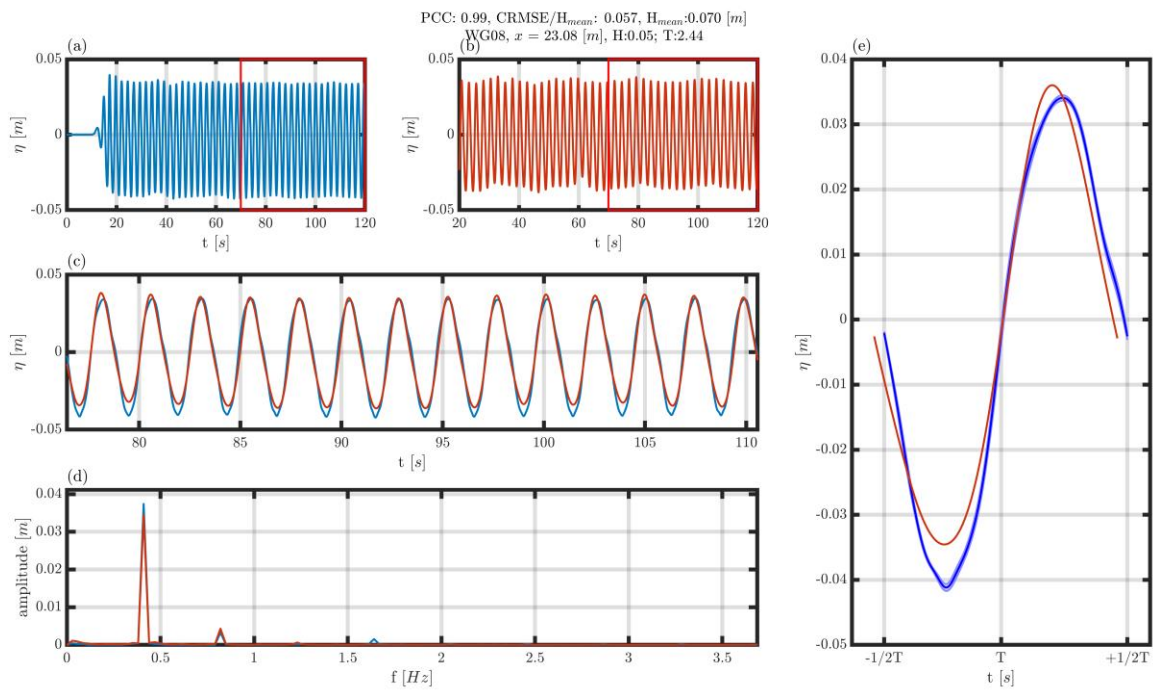


Figure A. 39 Overview of a comparison between the OpenFOAM data and the experiment for WG08. (a) Overview water level elevation from the experiment and the selected part. (b) Overview water level elevation from OpenFOAM and the selected part. (c): Aligned water level elevation signal. (d): Amplitude spectral analysis for both data sets. (e): Overlapped ensemble average wave shape.

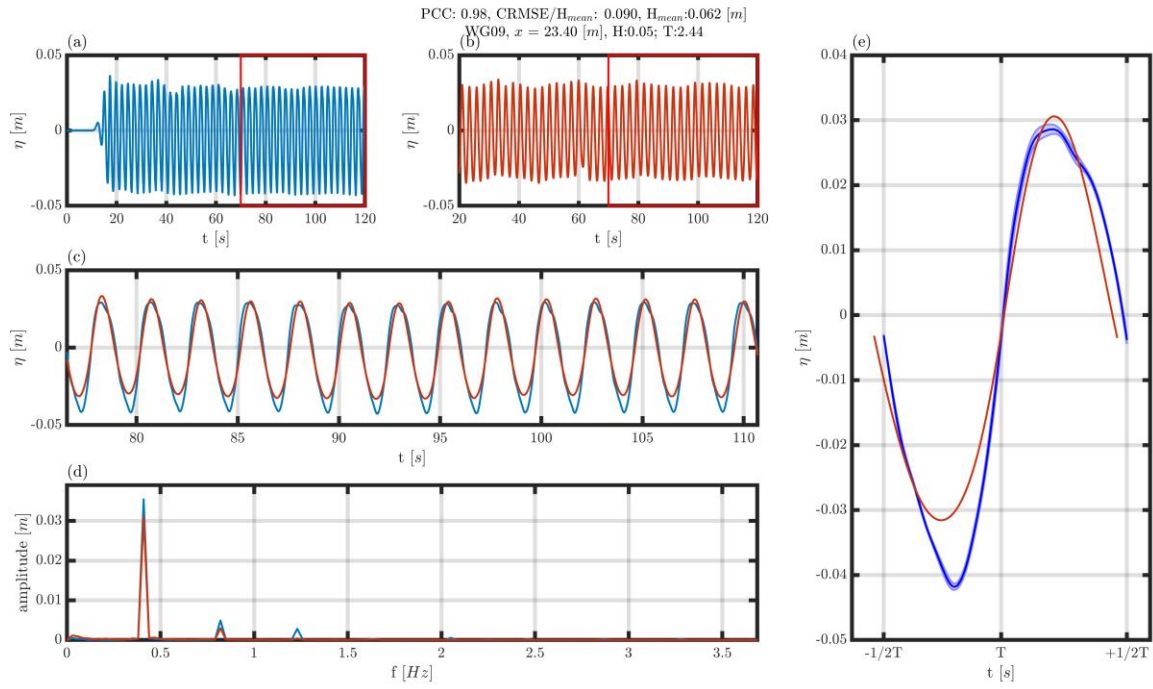


Figure A. 40 Overview of a comparison between the OpenFOAM data and the experiment for WG09. (a) Overview water level elevation from the experiment and the selected part. (b) Overview water level elevation from OpenFOAM and the selected part. (c): Aligned water level elevation signal. (d): Amplitude spectral analysis for both data sets. (e): Overlapped ensemble average wave shape.

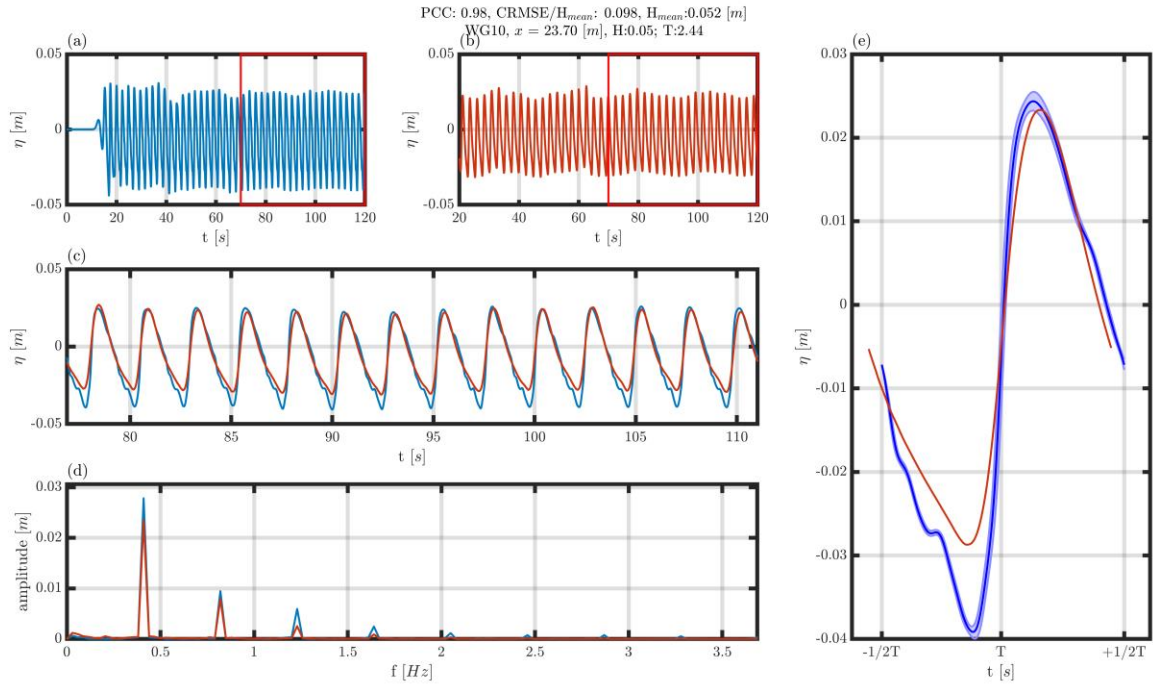


Figure A. 41 Overview of a comparison between the OpenFOAM data and the experiment for WG10. (a) Overview water level elevation from the experiment and the selected part. (b) Overview water level elevation from OpenFOAM and the selected part. (c): Aligned water level elevation signal. (d): Amplitude spectral analysis for both data sets. (e): Overlapped ensemble average wave shape.

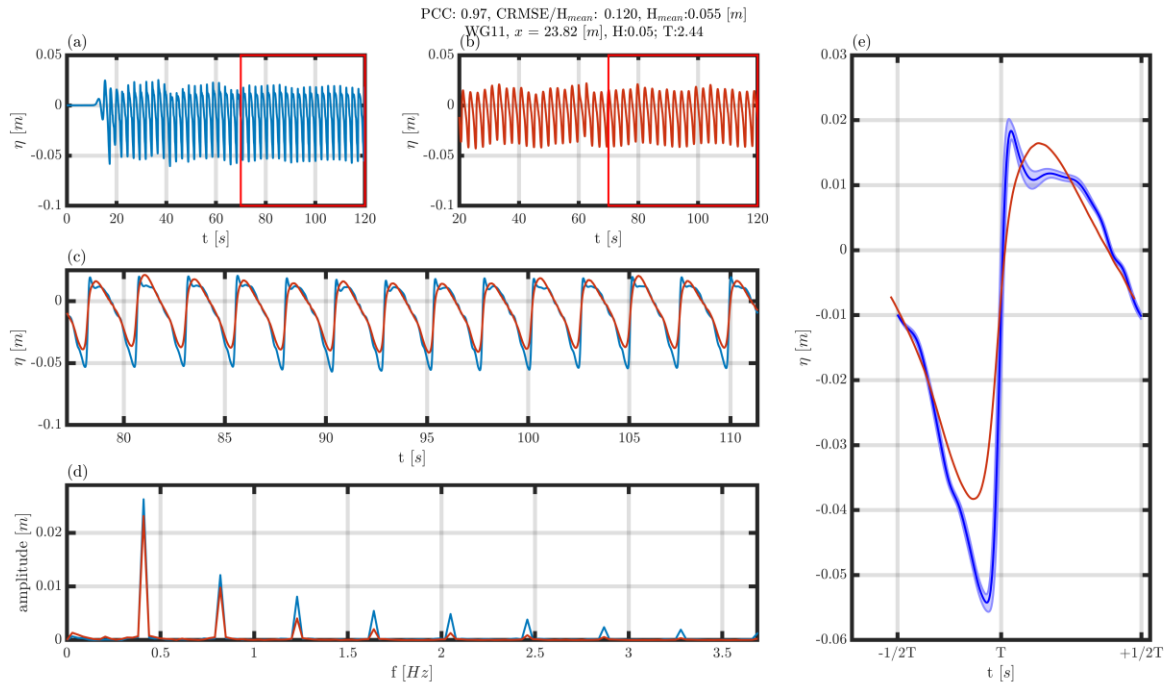


Figure A. 42 Overview of a comparison between the OpenFOAM data and the experiment for WG11. (a) Overview water level elevation from the experiment and the selected part. (b) Overview water level elevation from OpenFOAM and the selected part. (c): Aligned water level elevation signal. (d): Amplitude spectral analysis for both data sets. (e): Overlapped ensemble average wave shape.

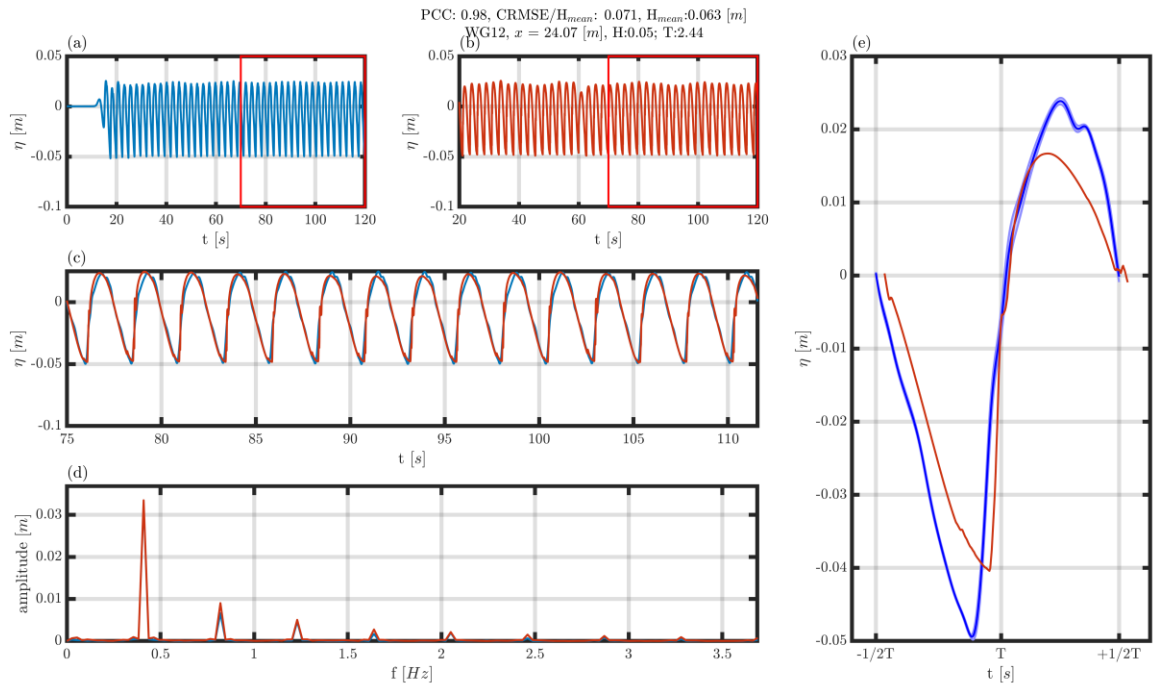


Figure A. 43 Overview of a comparison between the OpenFOAM data and the experiment for WG12. (a) Overview water level elevation from the experiment and the selected part. (b) Overview water level elevation from OpenFOAM and the selected part. (c): Aligned water level elevation signal. (d): Amplitude spectral analysis for both data sets. (e): Overlapped ensemble average wave shape.

Results of yPlus for all time steps for the case WIF-005244
 Mean 10.68, Median: 8.09

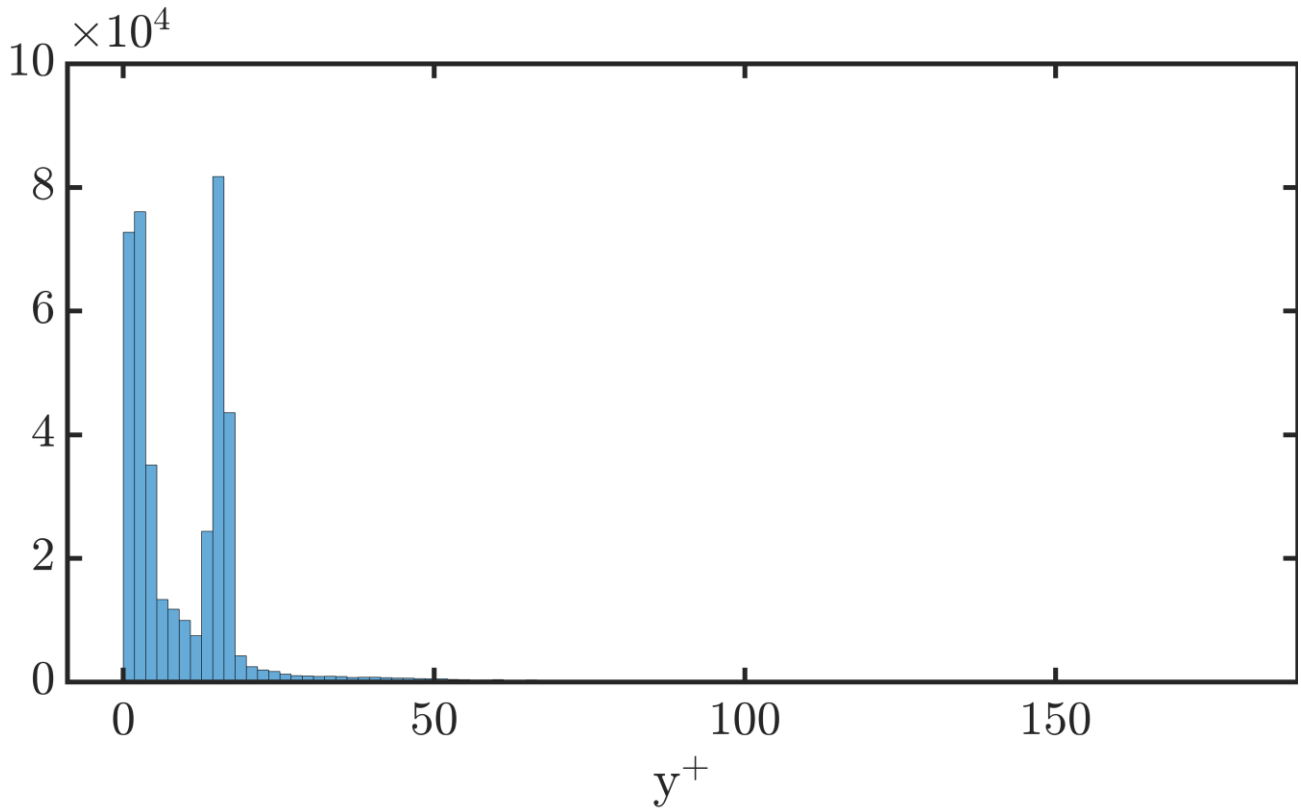


Figure A. 44 Histogram y^+ for the 2D isoAdvector case of $H=0.05$ m, $T=2.44$

Appendix D.3 $H=0.10$ m, $T=1.20$ s

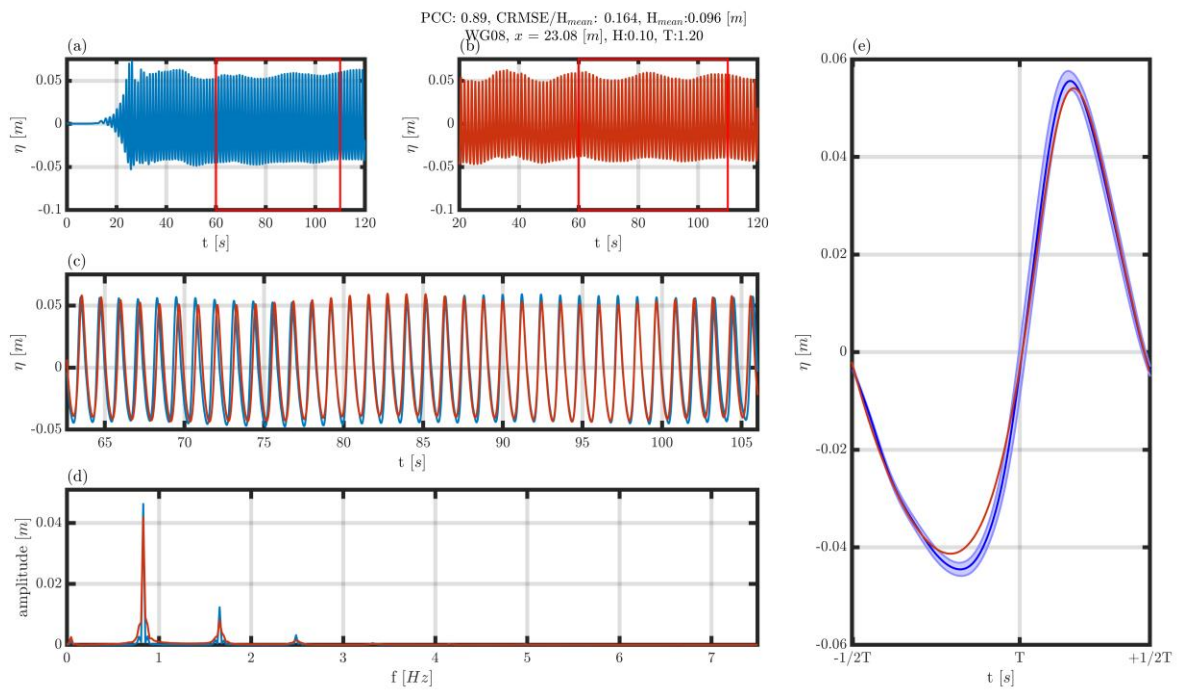


Figure A. 45 Overview of a comparison between the OpenFOAM data and the experiment for WG08. (a) Overview water level elevation from the experiment and the selected part. (b) Overview water level elevation from OpenFOAM and the selected part. (c): Aligned water level elevation signal. (d): Amplitude spectral analysis for both data sets. (e): Overlapped ensemble average wave shape.

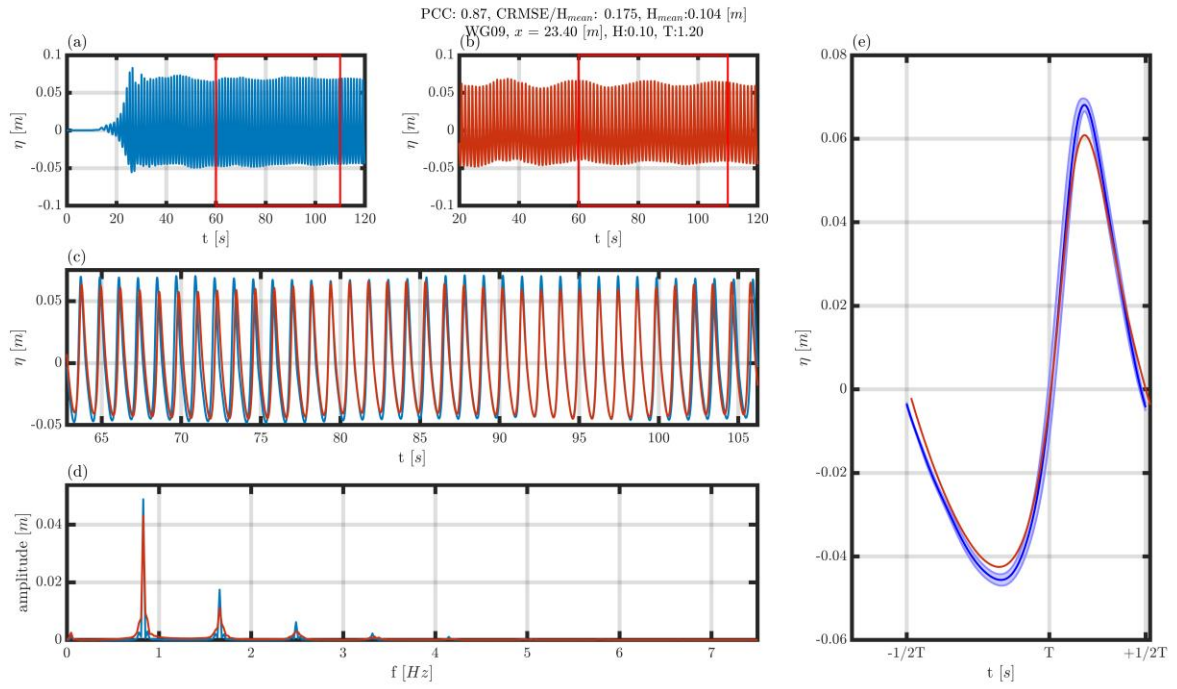


Figure A. 46 Overview of a comparison between the OpenFOAM data and the experiment for WG09. (a) Overview water level elevation from the experiment and the selected part. (b) Overview water level elevation from OpenFOAM and the selected part. (c): Aligned water level elevation signal. (d): Amplitude spectral analysis for both data sets. (e): Overlapped ensemble average wave shape.

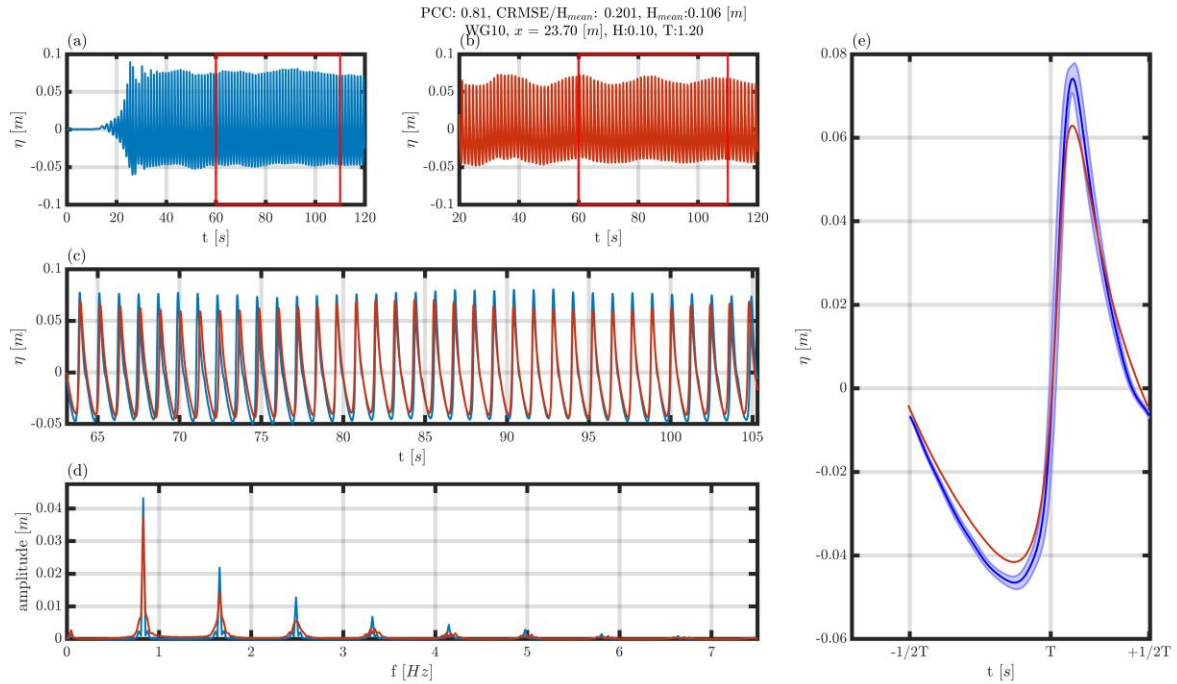


Figure A. 47 Overview of a comparison between the OpenFOAM data and the experiment for WG10. (a) Overview water level elevation from the experiment and the selected part. (b) Overview water level elevation from OpenFOAM and the selected part. (c): Aligned water level elevation signal. (d): Amplitude spectral analysis for both data sets. (e): Overlapped ensemble average wave shape.

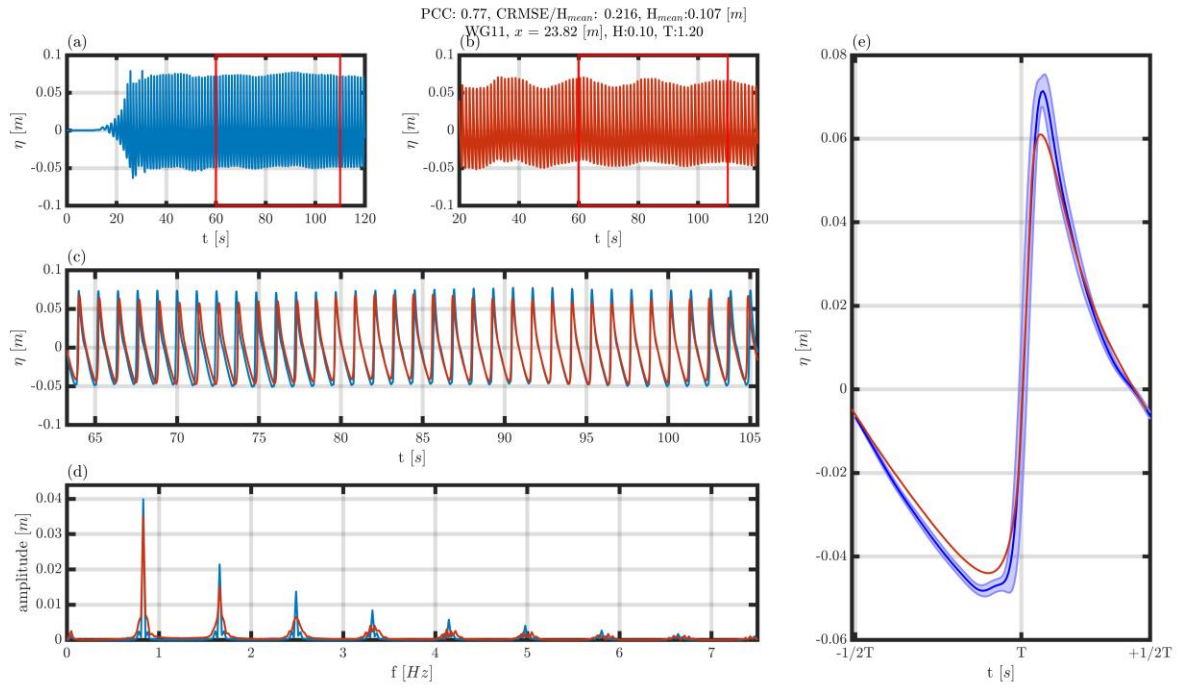


Figure A. 48 Overview of a comparison between the OpenFOAM data and the experiment for WG11. (a) Overview water level elevation from the experiment and the selected part. (b) Overview water level elevation from OpenFOAM and the selected part. (c): Aligned water level elevation signal. (d): Amplitude spectral analysis for both data sets. (e): Overlapped ensemble average wave shape.

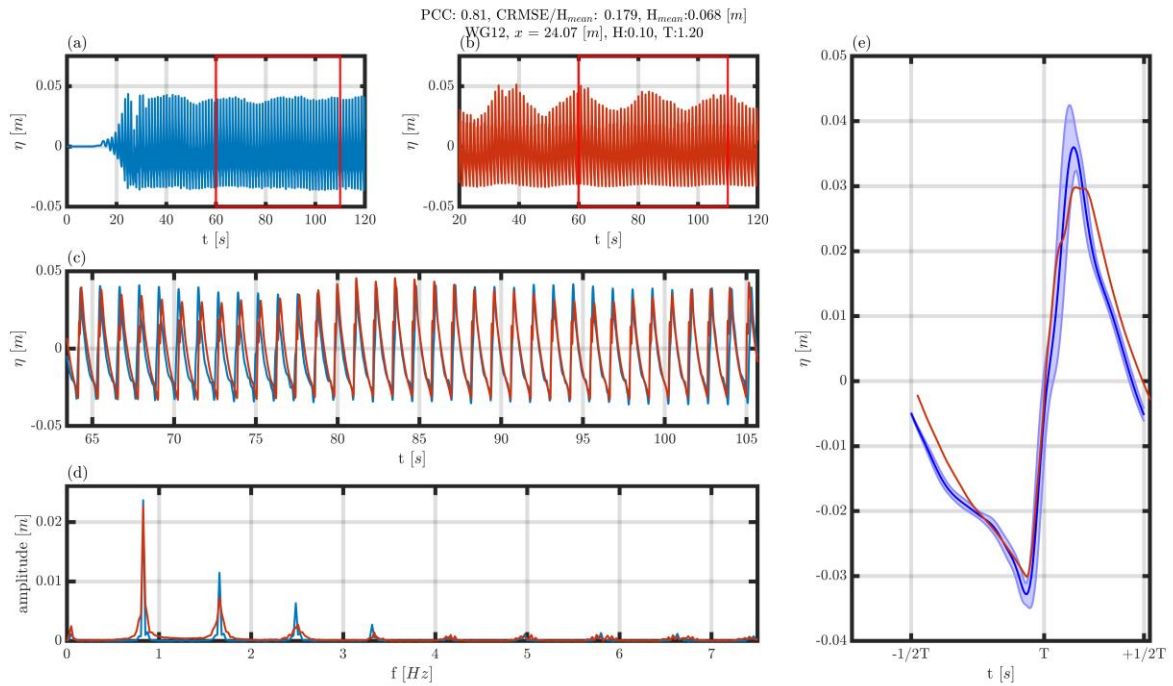


Figure A. 49 Overview of a comparison between the OpenFOAM data and the experiment for WG12. (a) Overview water level elevation from the experiment and the selected part. (b) Overview water level elevation from OpenFOAM and the selected part. (c): Aligned water level elevation signal. (d): Amplitude spectral analysis for both data sets. (e): Overlapped ensemble average wave shape.

Results of y^+ Plus for all time steps for the case WIF-010120
 Mean 17.48, Median: 10.40

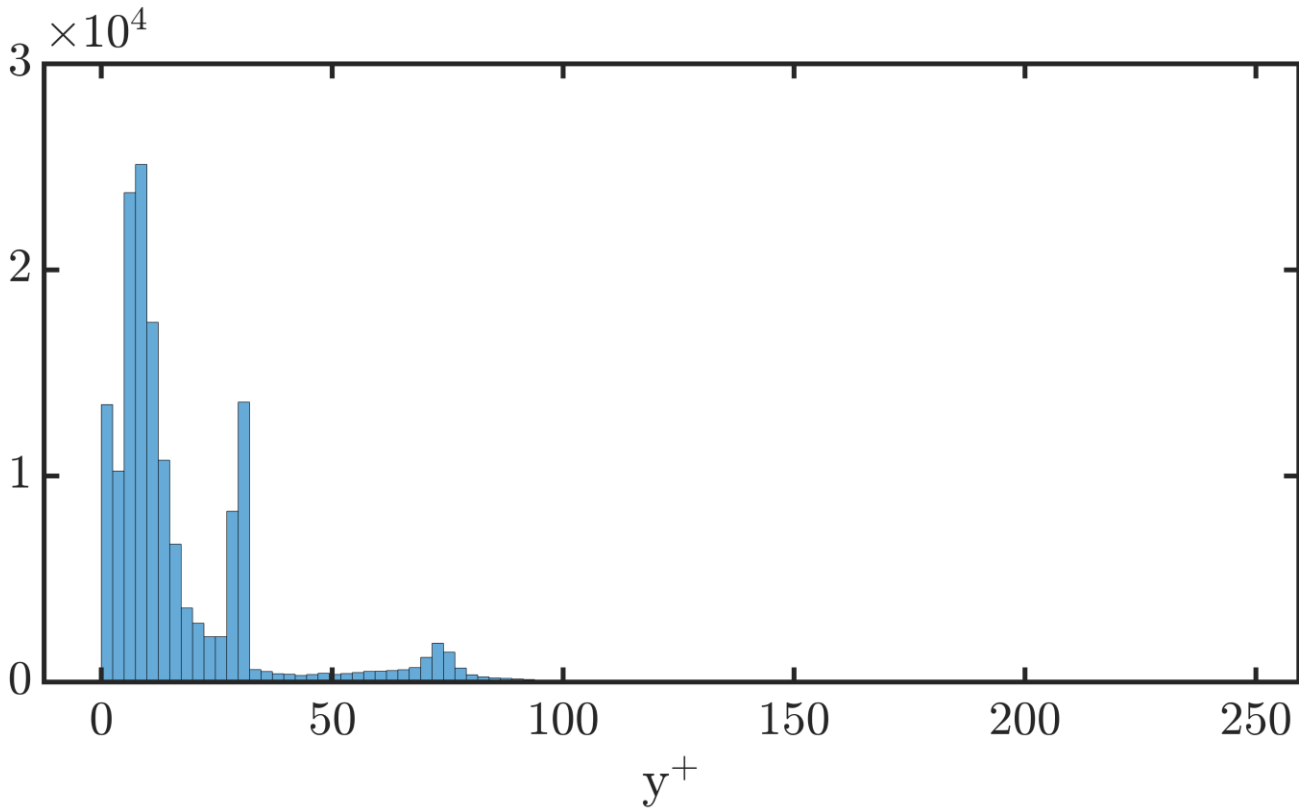


Figure A. 50 Histogram y^+ for the 2D isoAdvector case of $H=0.10$ m, $T=1.20$ s

Appendix D.4 $H=0.10$ m, $T=2.44$ s

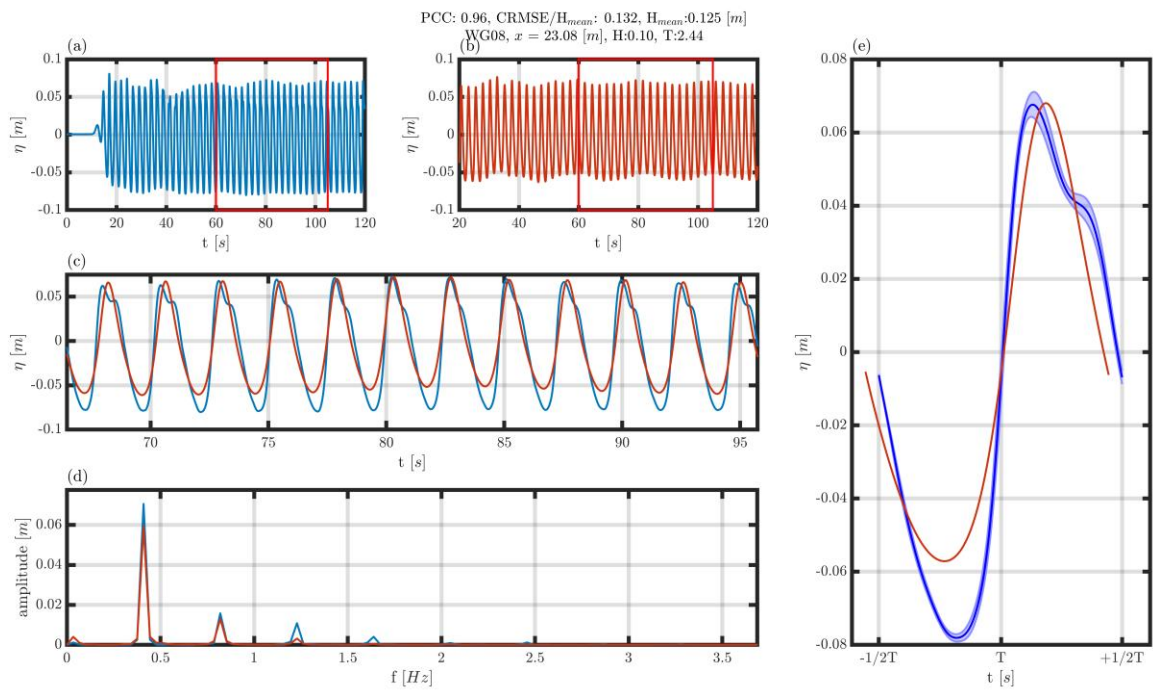


Figure A. 51 Overview of a comparison between the OpenFOAM data and the experiment for WG08. (a) Overview water level elevation from the experiment and the selected part. (b) Overview water level elevation from OpenFOAM and the selected part. (c): Aligned water level elevation signal. (d): Amplitude spectral analysis for both data sets. (e): Overlapped ensemble average wave shape.

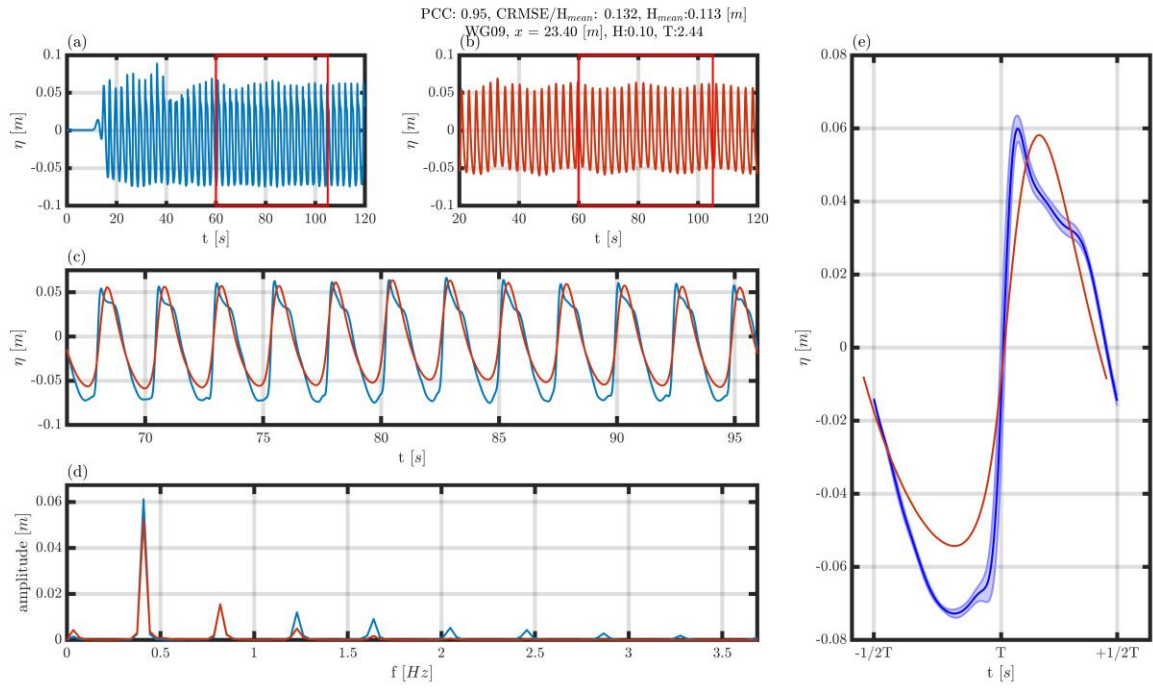


Figure A. 52 Overview of a comparison between the OpenFOAM data and the experiment for WG09. (a) Overview water level elevation from the experiment and the selected part. (b) Overview water level elevation from OpenFOAM and the selected part. (c): Aligned water level elevation signal. (d): Amplitude spectral analysis for both data sets. (e): Overlapped ensemble average wave shape.

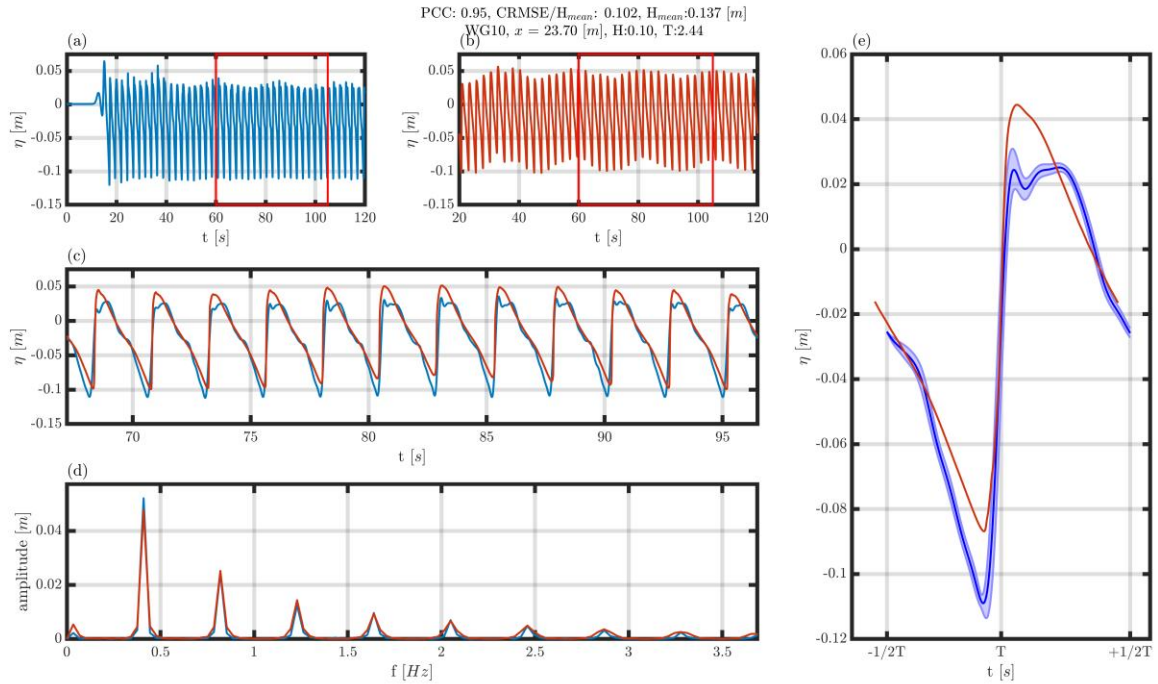


Figure A. 53 Overview of a comparison between the OpenFOAM data and the experiment for WG10. (a) Overview water level elevation from the experiment and the selected part. (b) Overview water level elevation from OpenFOAM and the selected part. (c): Aligned water level elevation signal. (d): Amplitude spectral analysis for both data sets. (e): Overlapped ensemble average wave shape.

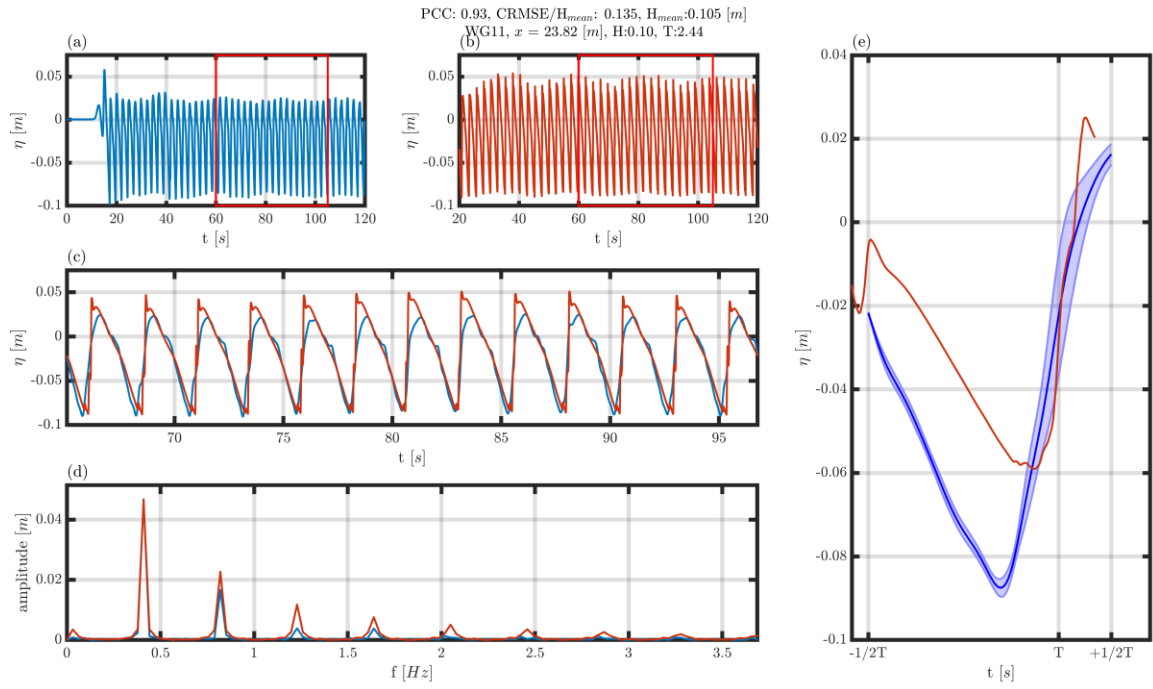


Figure A. 54 Overview of a comparison between the OpenFOAM data and the experiment for WG11. (a) Overview water level elevation from the experiment and the selected part. (b) Overview water level elevation from OpenFOAM and the selected part. (c): Aligned water level elevation signal. (d): Amplitude spectral analysis for both data sets. (e): Overlapped ensemble average wave shape.

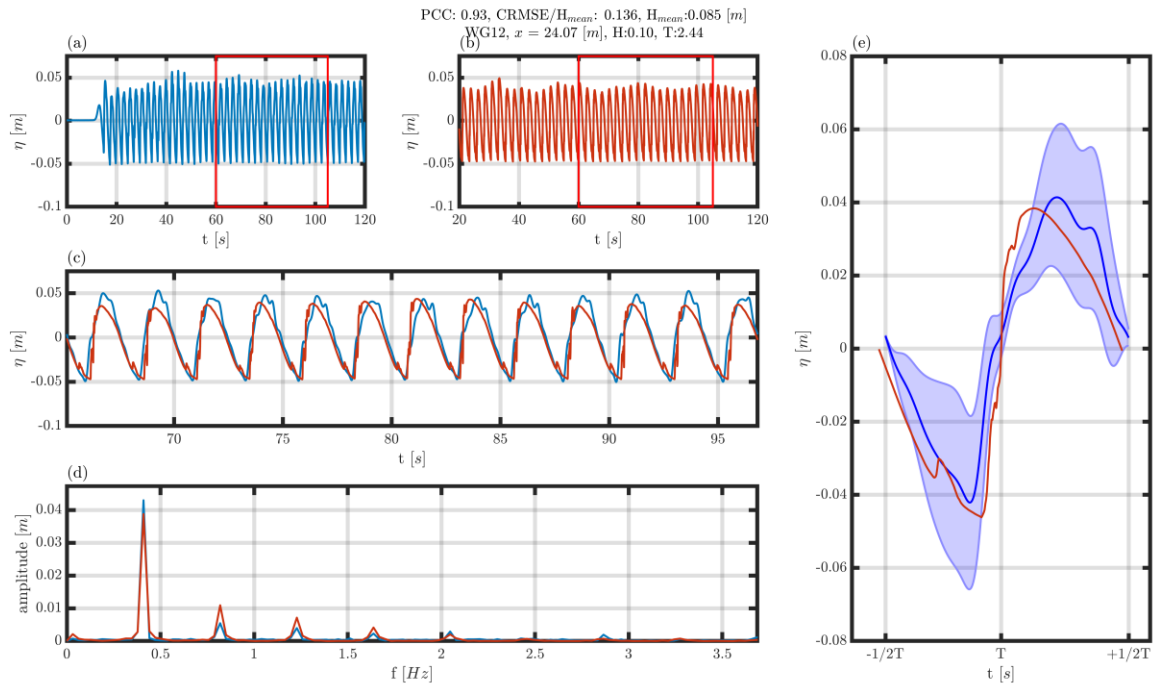


Figure A. 55 Overview of a comparison between the OpenFOAM data and the experiment for WG12. (a) Overview water level elevation from the experiment and the selected part. (b) Overview water level elevation from OpenFOAM and the selected part. (c): Aligned water level elevation signal. (d): Amplitude spectral analysis for both data sets. (e): Overlapped ensemble average wave shape.

Results of yPlus for all time steps for the case WIF-010244
 Mean 30.62, Median: 22.80

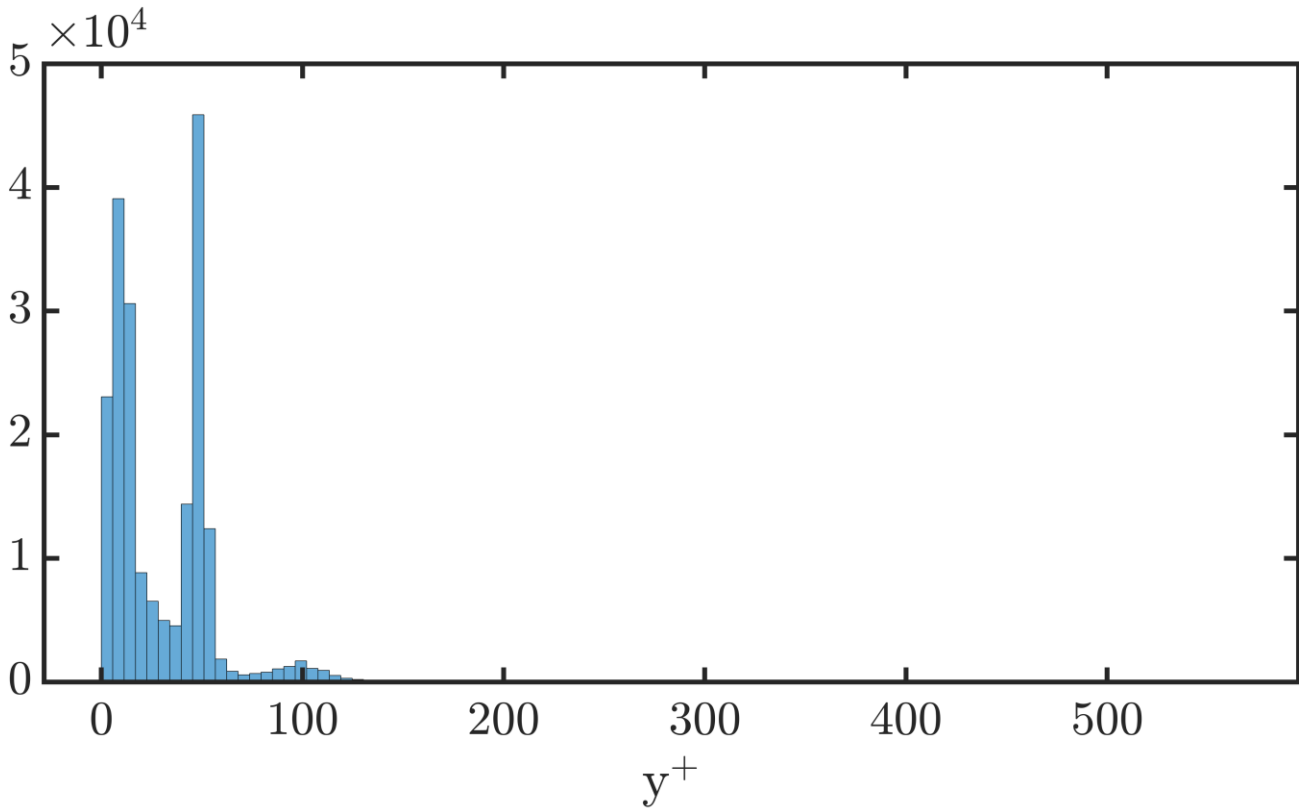


Figure A. 56 Histogram y^+ for the 2D isoAdvect case of $H=0.10$ m, $T=2.44$ s.

Appendix D.5 $H=0.15$ m, $T=1.96$ s

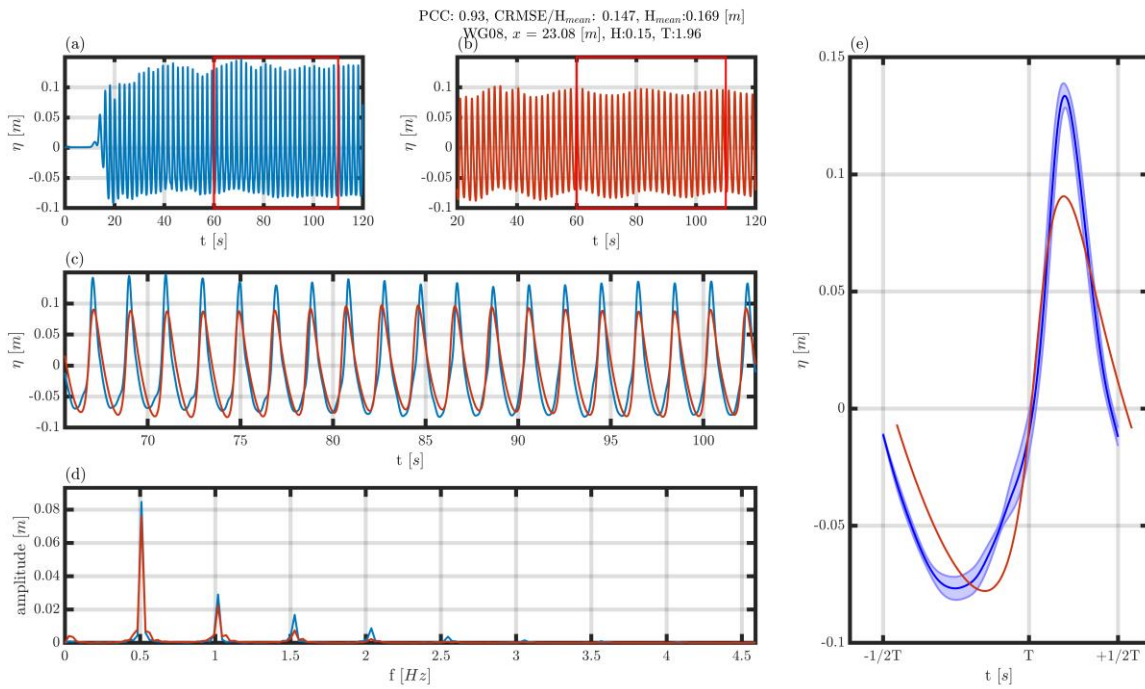


Figure A. 57 Overview of a comparison between the OpenFOAM data and the experiment for WG08. (a) Overview water level elevation from the experiment and the selected part. (b) Overview water level elevation from OpenFOAM and the selected part. (c): Aligned water level elevation signal. (d): Amplitude spectral analysis for both data sets. (e): Overlapped ensemble average wave shape.

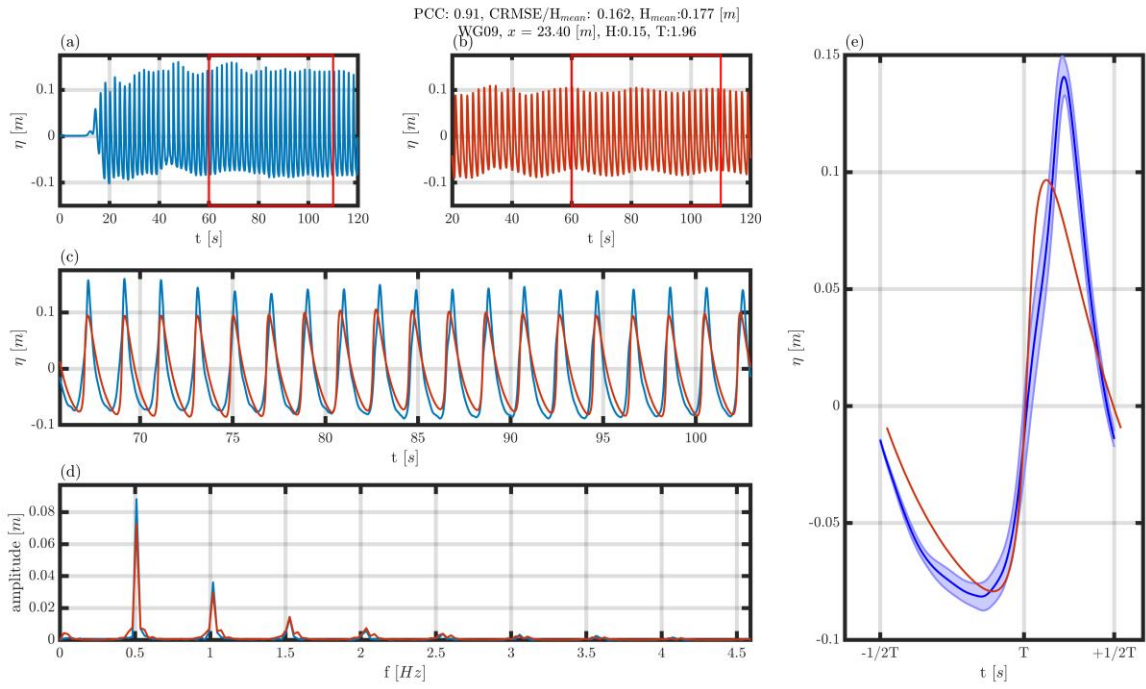


Figure A. 58 Overview of a comparison between the OpenFOAM data and the experiment for WG09. (a) Overview water level elevation from the experiment and the selected part. (b) Overview water level elevation from OpenFOAM and the selected part. (c): Aligned water level elevation signal. (d): Amplitude spectral analysis for both data sets. (e): Overlapped ensemble average wave shape.

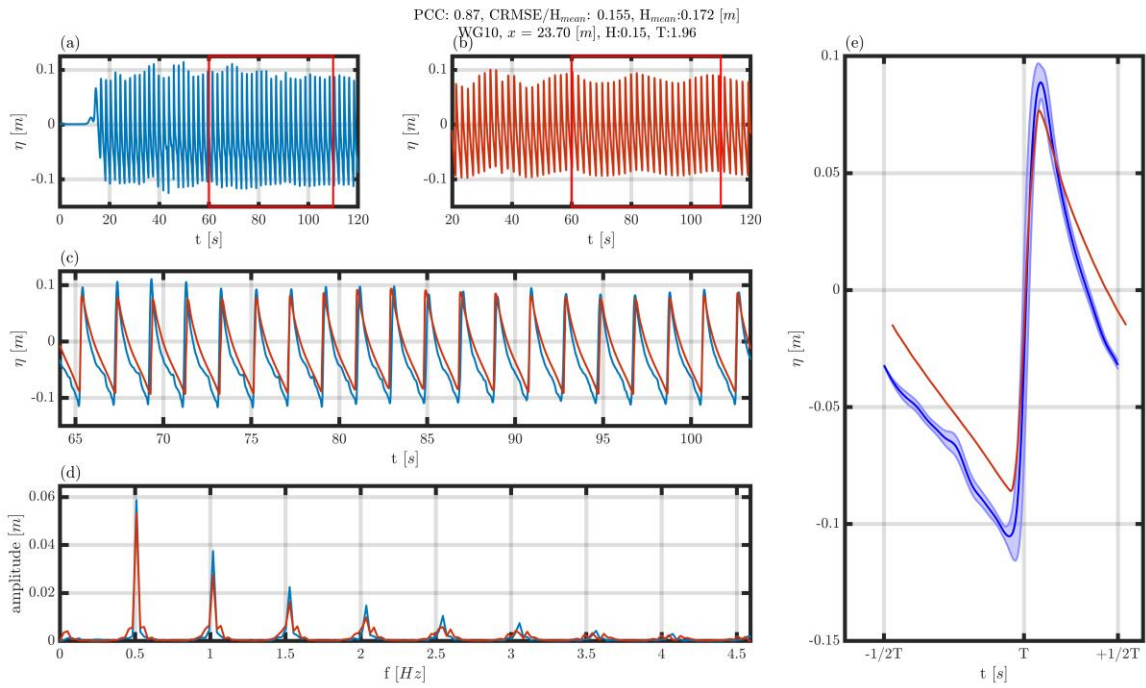


Figure A. 59 Overview of a comparison between the OpenFOAM data and the experiment for WG10. (a) Overview water level elevation from the experiment and the selected part. (b) Overview water level elevation from OpenFOAM and the selected part. (c): Aligned water level elevation signal. (d): Amplitude spectral analysis for both data sets. (e): Overlapped ensemble average wave shape.

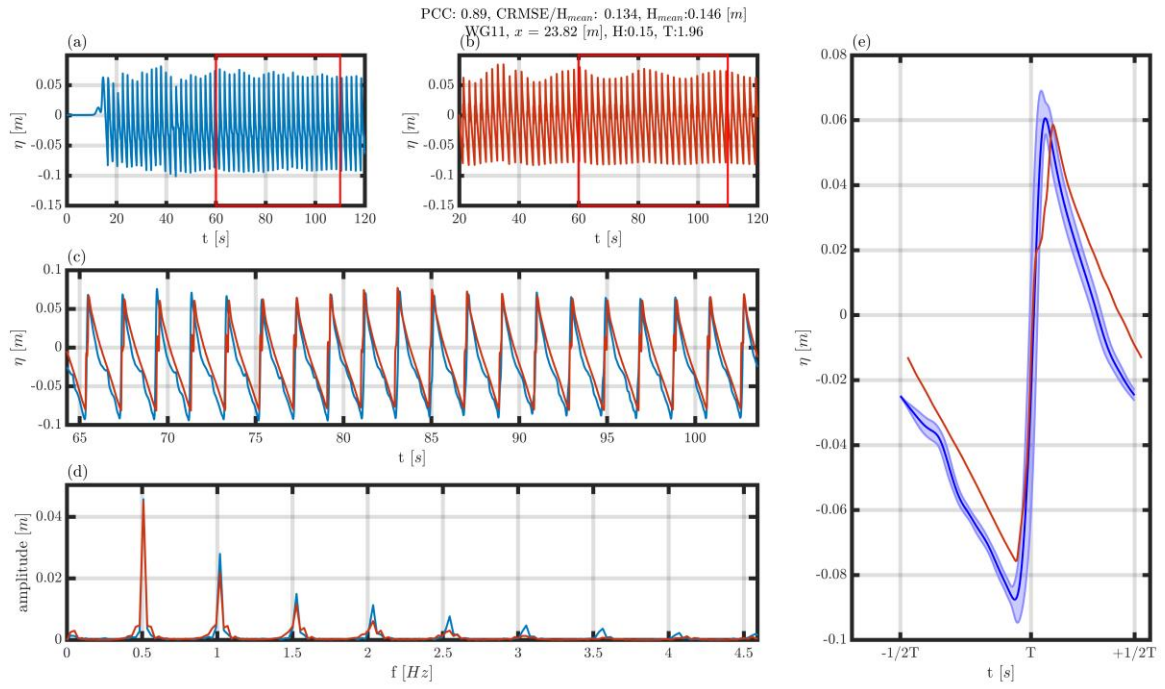


Figure A. 60 Overview of a comparison between the OpenFOAM data and the experiment for WG11. (a) Overview water level elevation from the experiment and the selected part. (b) Overview water level elevation from OpenFOAM and the selected part. (c): Aligned water level elevation signal. (d): Amplitude spectral analysis for both data sets. (e): Overlapped ensemble average wave shape.

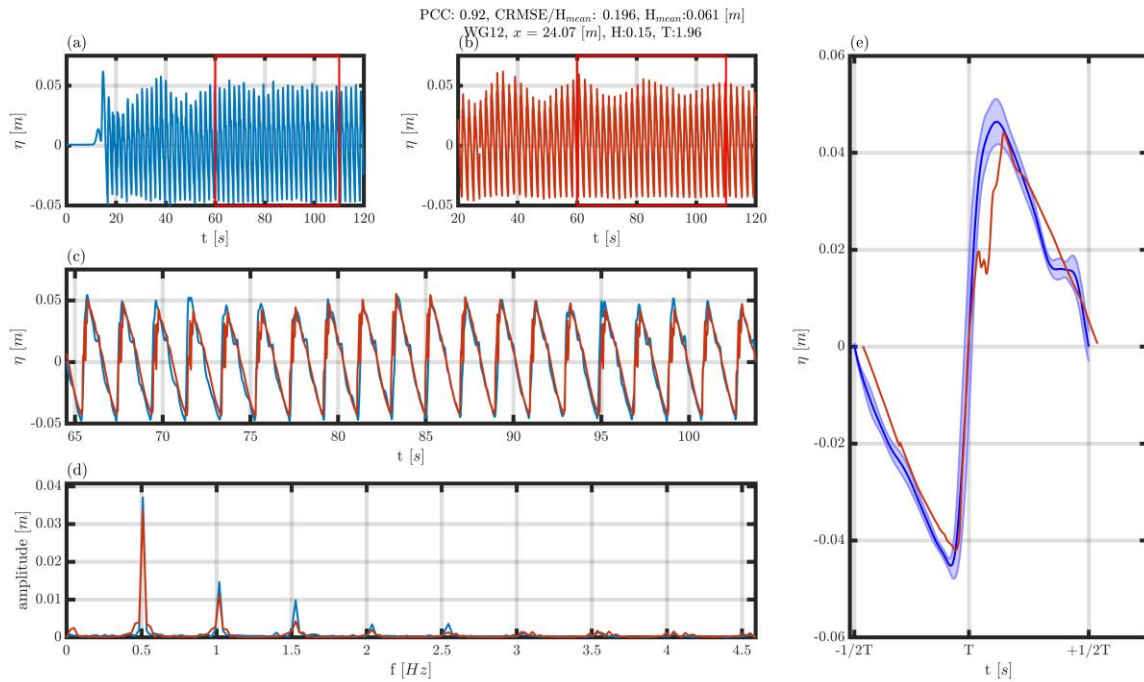


Figure A. 61 Overview of a comparison between the OpenFOAM data and the experiment for WG12. (a) Overview water level elevation from the experiment and the selected part. (b) Overview water level elevation from OpenFOAM and the selected part. (c): Aligned water level elevation signal. (d): Amplitude spectral analysis for both data sets. (e): Overlapped ensemble average wave shape.

Results of yPlus for all time steps for the case WIF-015196
Mean 51.16, Median: 30.69

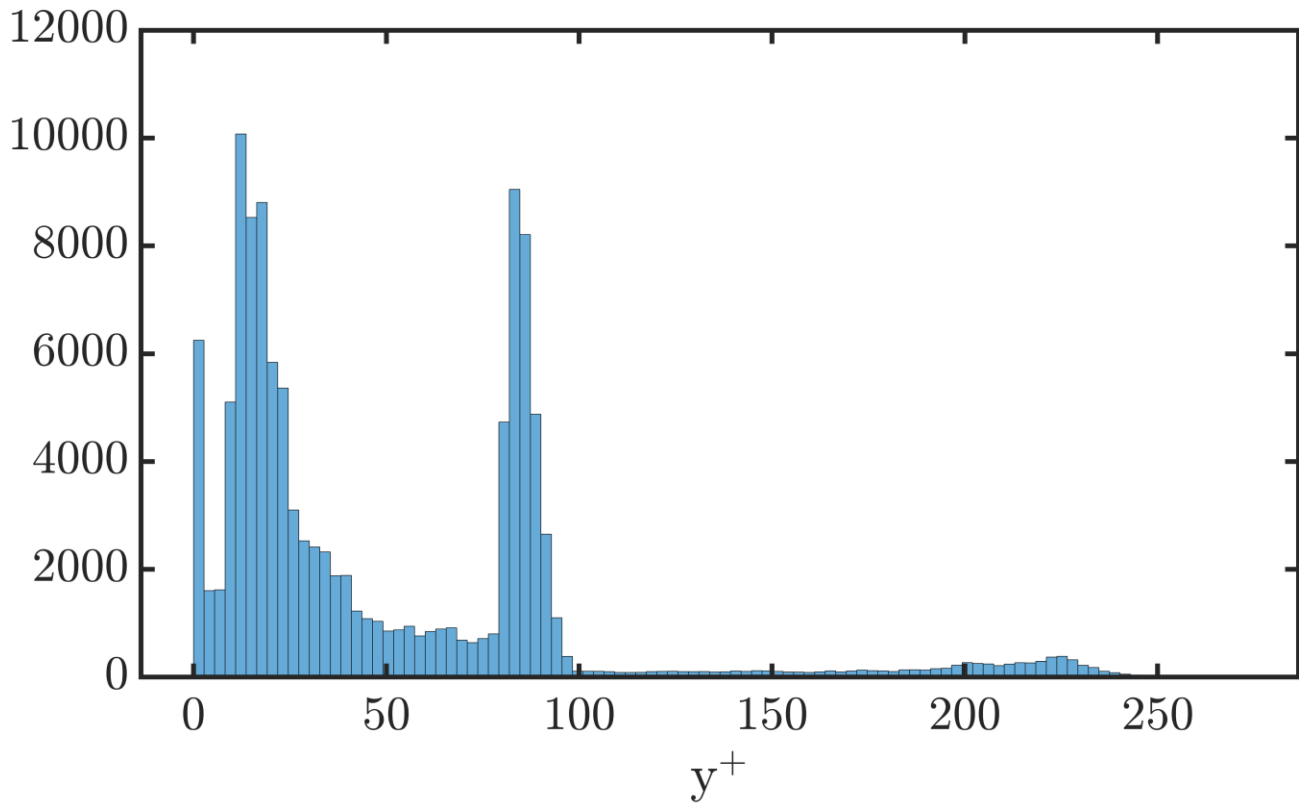


Figure A. 62 Histogram y^+ for the 2D isoAdvect case of $H=0.15$ m, $T=1.96$ s

Appendix E Results of water level analysis 3D simulation

This appendix contains the 3D model validation for the water level elevation of the 3D simulations. Per wave gauge an FFT of the water level elevation is shown, the aligned and overlapped time series and an ensemble average wave shape.

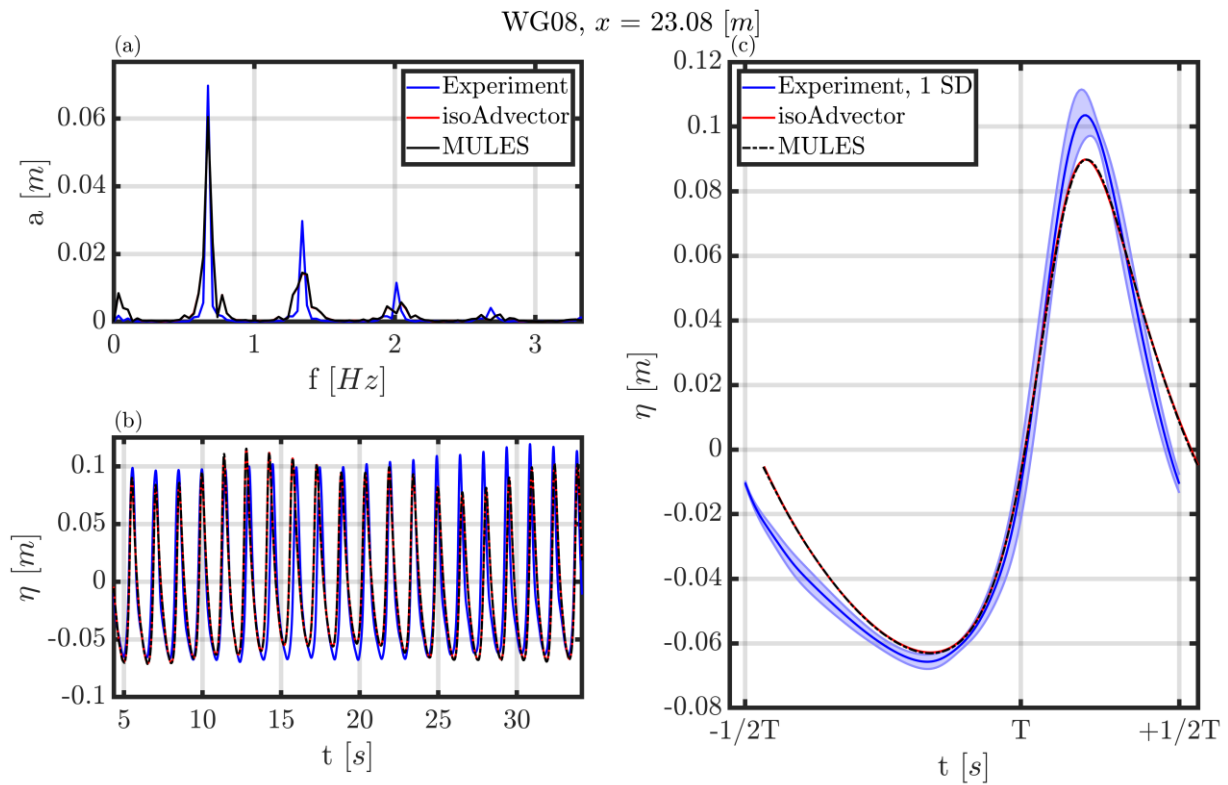


Figure A. 63 Data of wave gauge 08. (a): Spectral amplitude analysis. (b): water level elevation aligned. (c): Average wave shape.

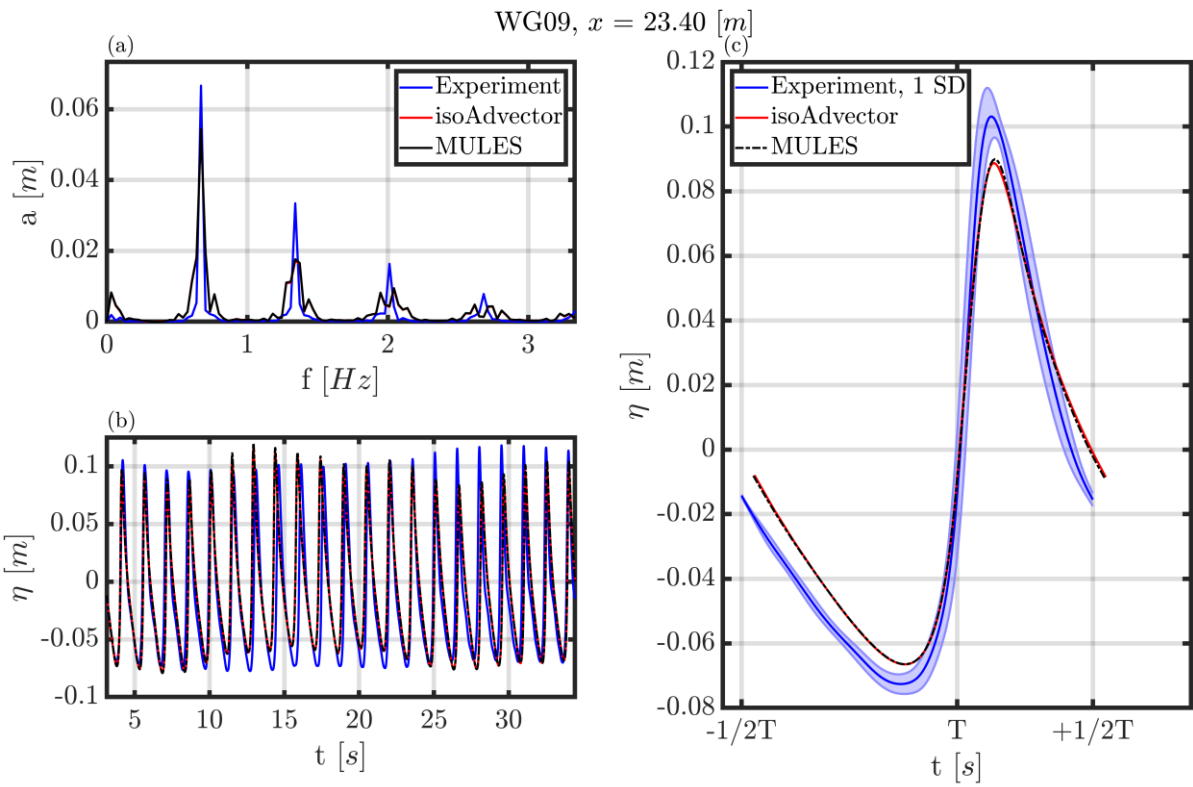


Figure A. 64 Data of wave gauge 09. (a): Spectral amplitude analysis. (b): water level elevation aligned. (c): Average wave shape.

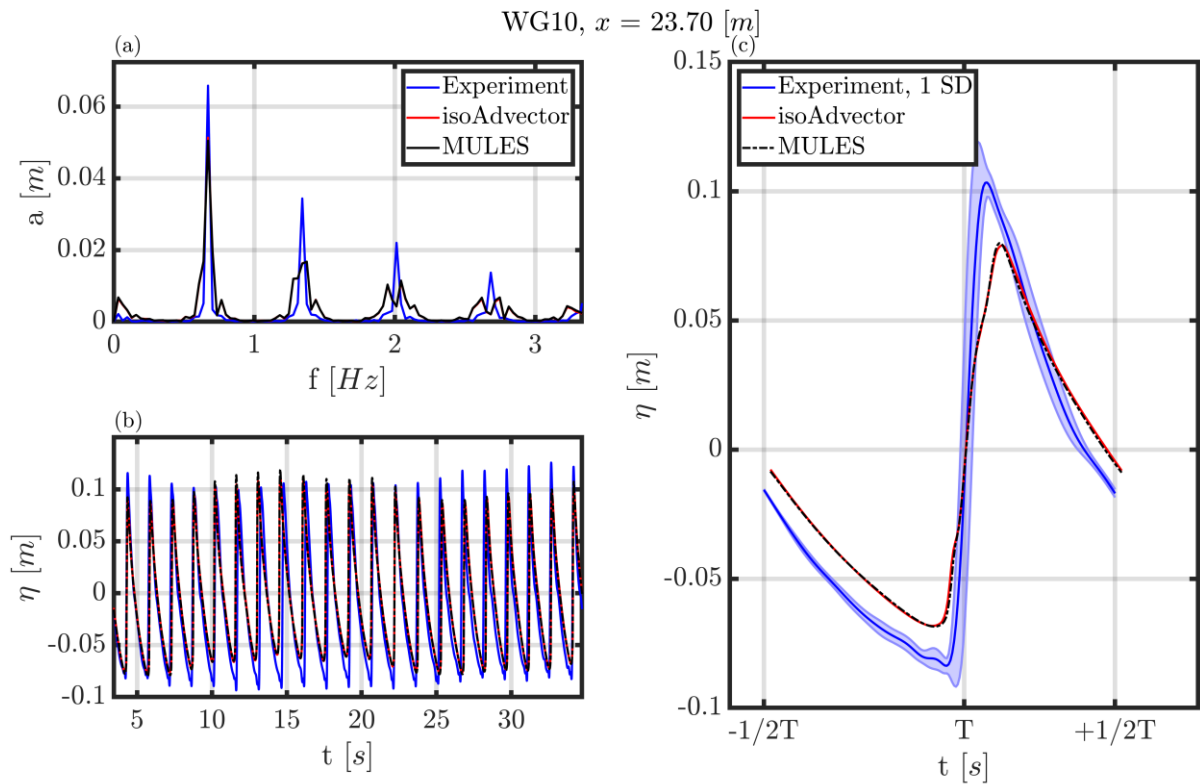


Figure A. 65 Data of wave gauge 10. (a): Spectral amplitude analysis. (b): water level elevation aligned. (c): Average wave shape.

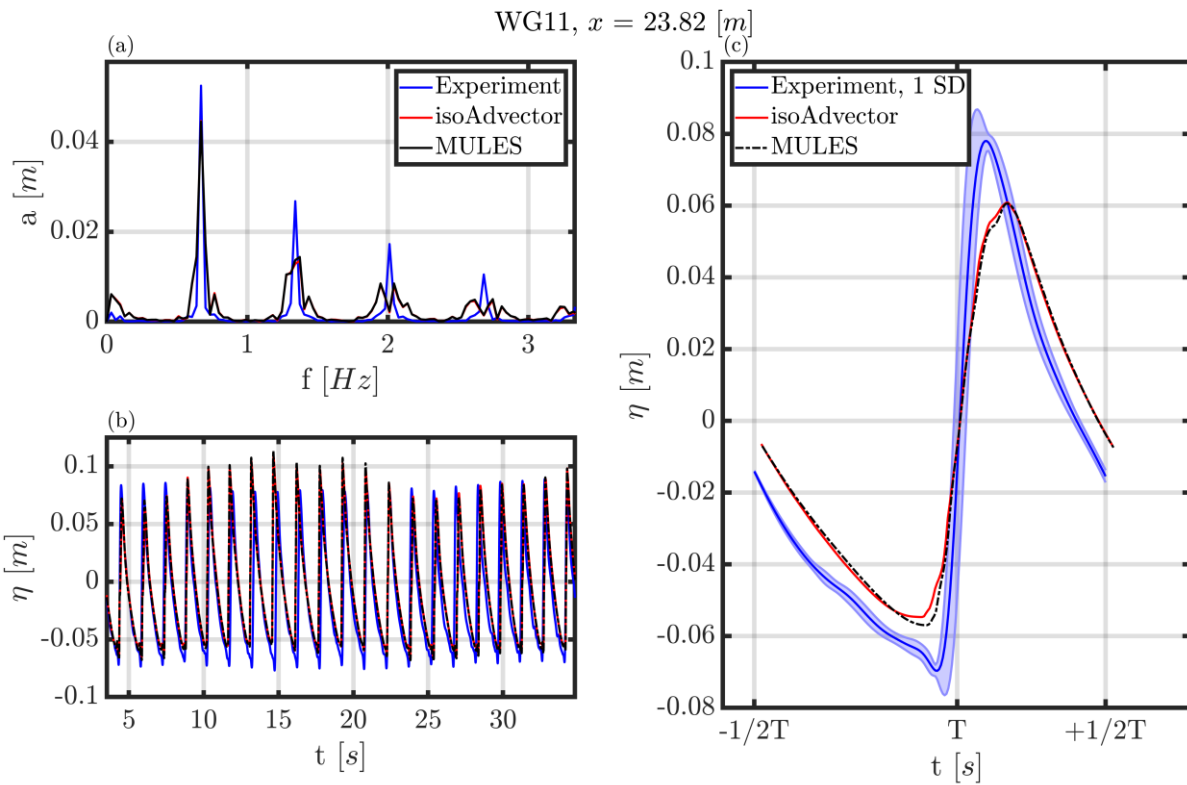


Figure A. 66 Data of wave gauge 11. (a): Spectral amplitude analysis. (b): water level elevation aligned. (c): Average wave shape.

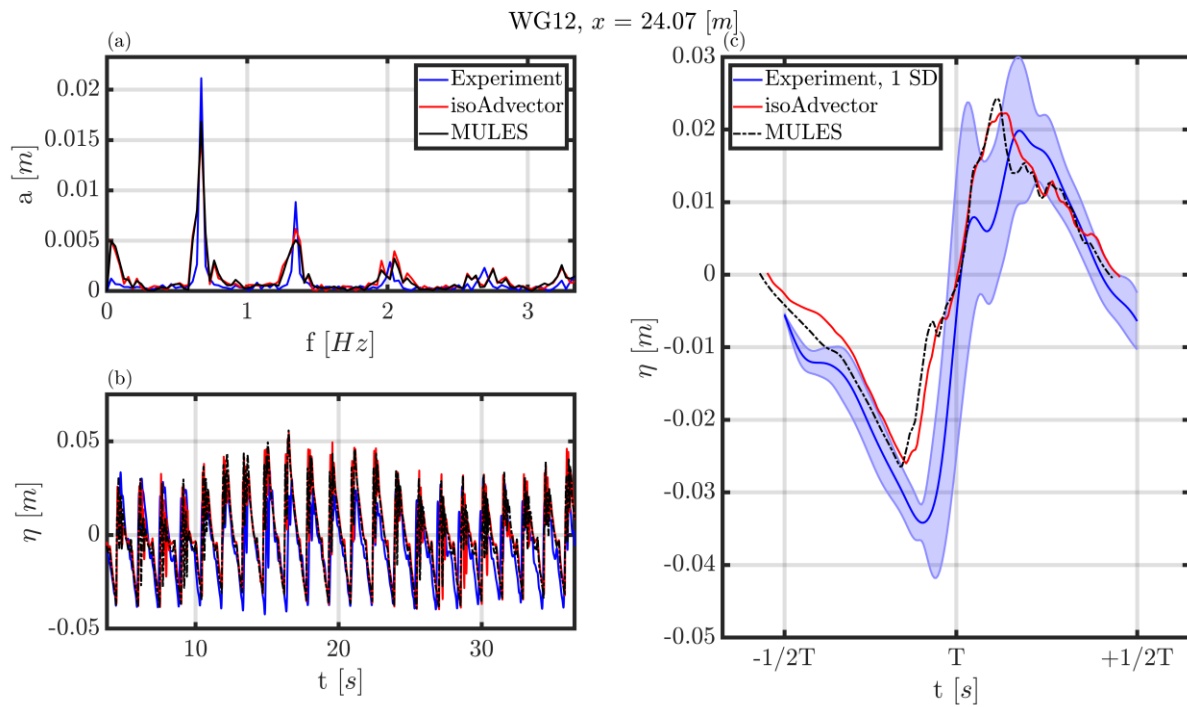


Figure A. 67 Data of wave gauge 12. (a): Spectral amplitude analysis. (b): water level elevation aligned. (c): Average wave shape.

Appendix F y^+ values 3D model validation

This appendix contains the y^+ values for the different meshes in the 3D simulations. The y^+ values in the histograms entail the y^+ values for the entire simulation. The snapshots of the mesh show the average value for y^+ in the total domain.

Results of y^+ Plus for all time steps for the case isoAdvectord
Mean 35.45, Median: 20.56

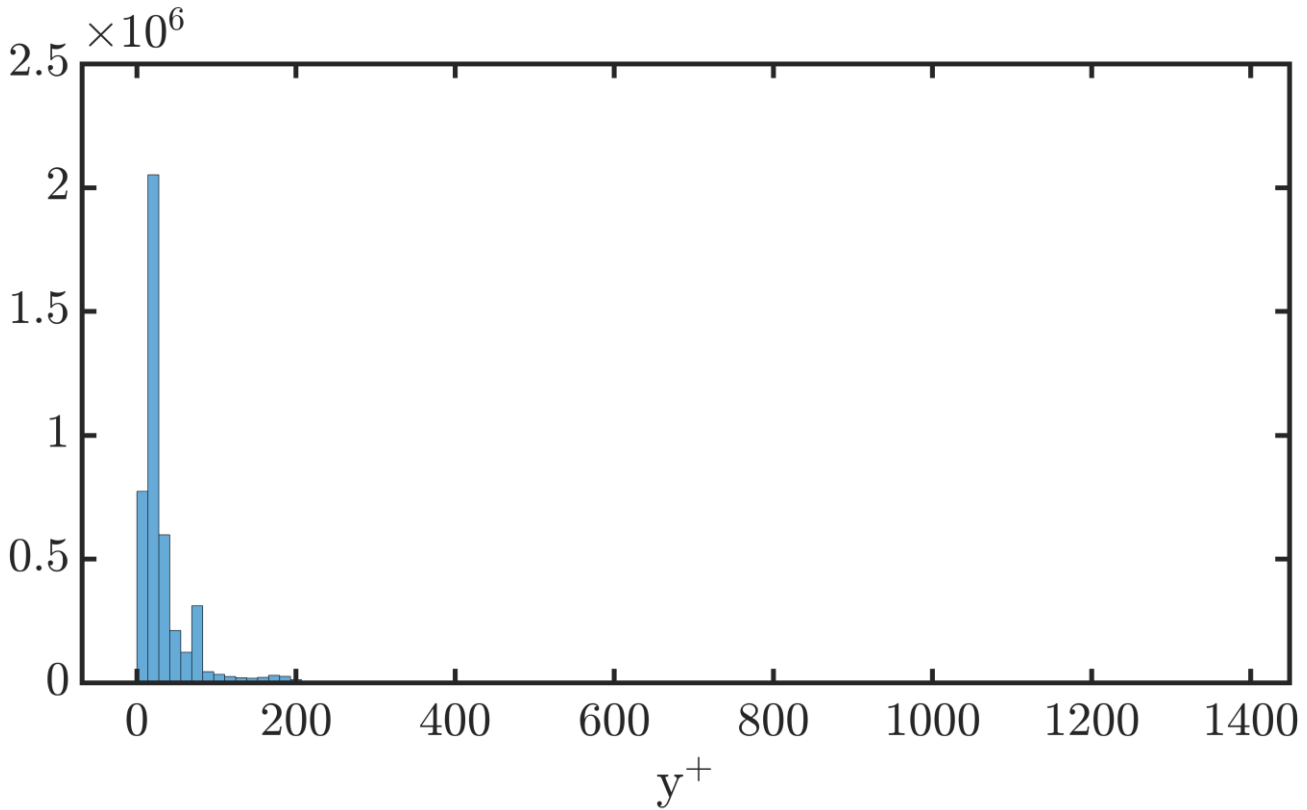


Figure A. 68 Histogram y^+ for the 3D isoAdvectord case with 15 CPWH

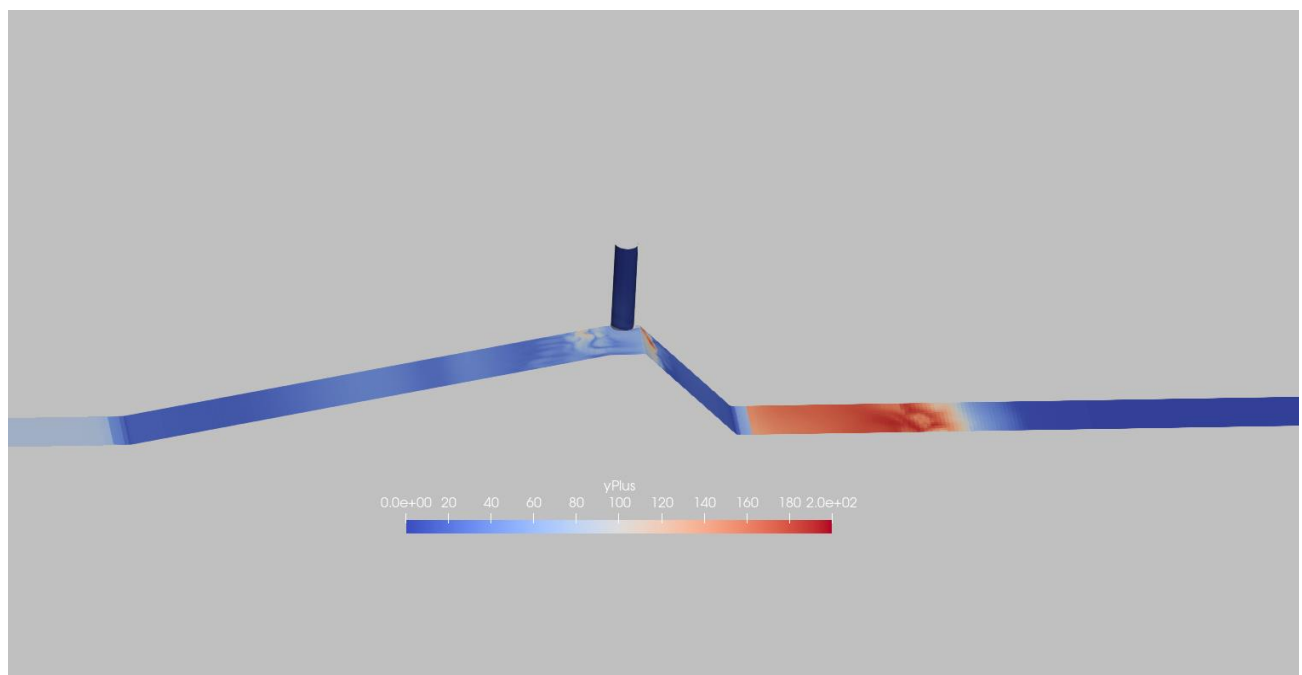


Figure A. 69 The average value for y^+ for the 3D isoAdvectord case for the areas that utilise a wall function.

Results of yPlus for all time steps for the case MULES
Mean 33.59, Median: 19.97

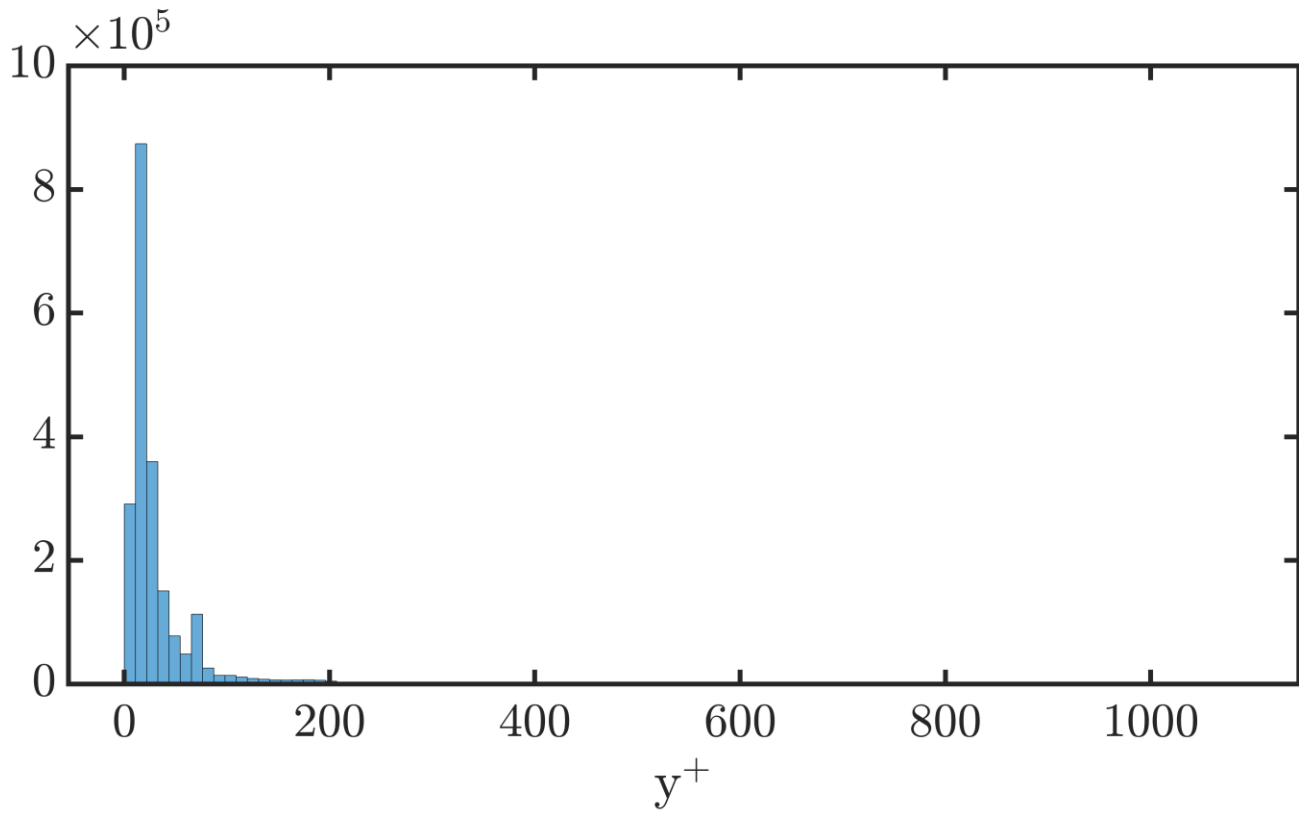


Figure A. 70 Histogram y^+ for the 3D MULES case with 15 CPWH

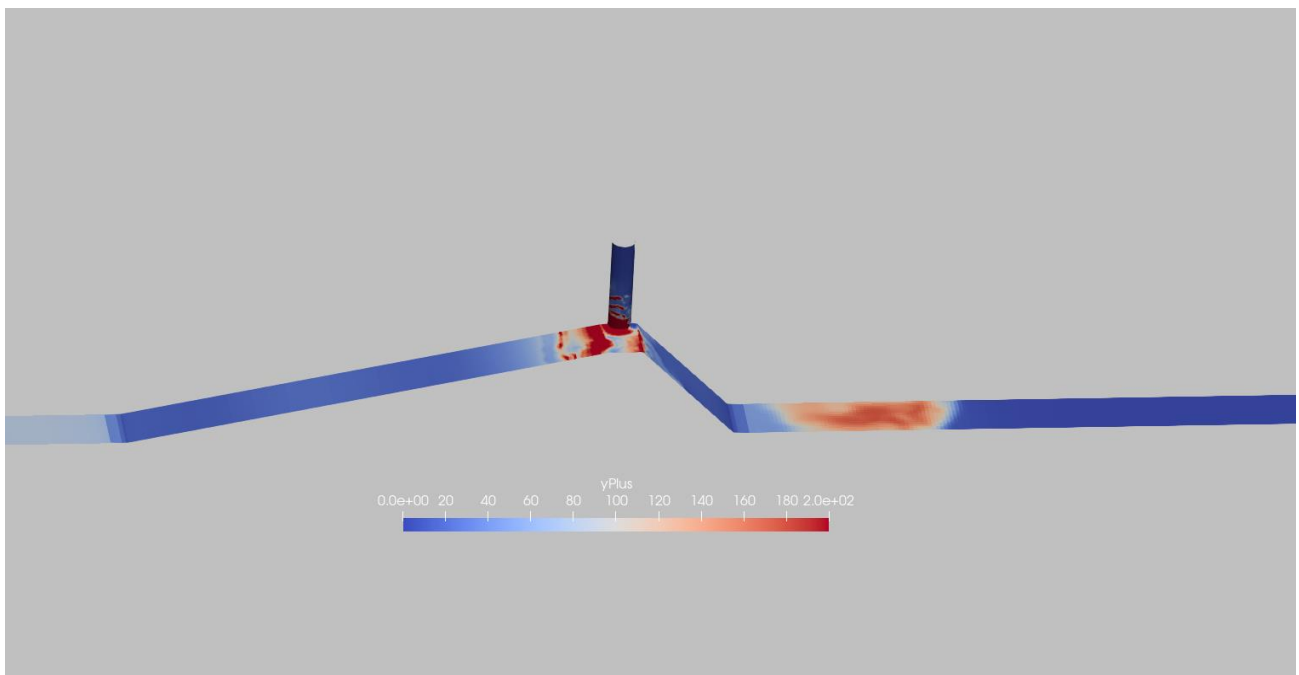


Figure A. 71 The average value for y^+ for the 3D MULES case for the areas that utilise a wall function present.

Appendix G Overview selected data force time series

This appendix shows the total force series and the data that is selected from it in the 3D model validation and analyses for the slamming coefficient and curling factor.

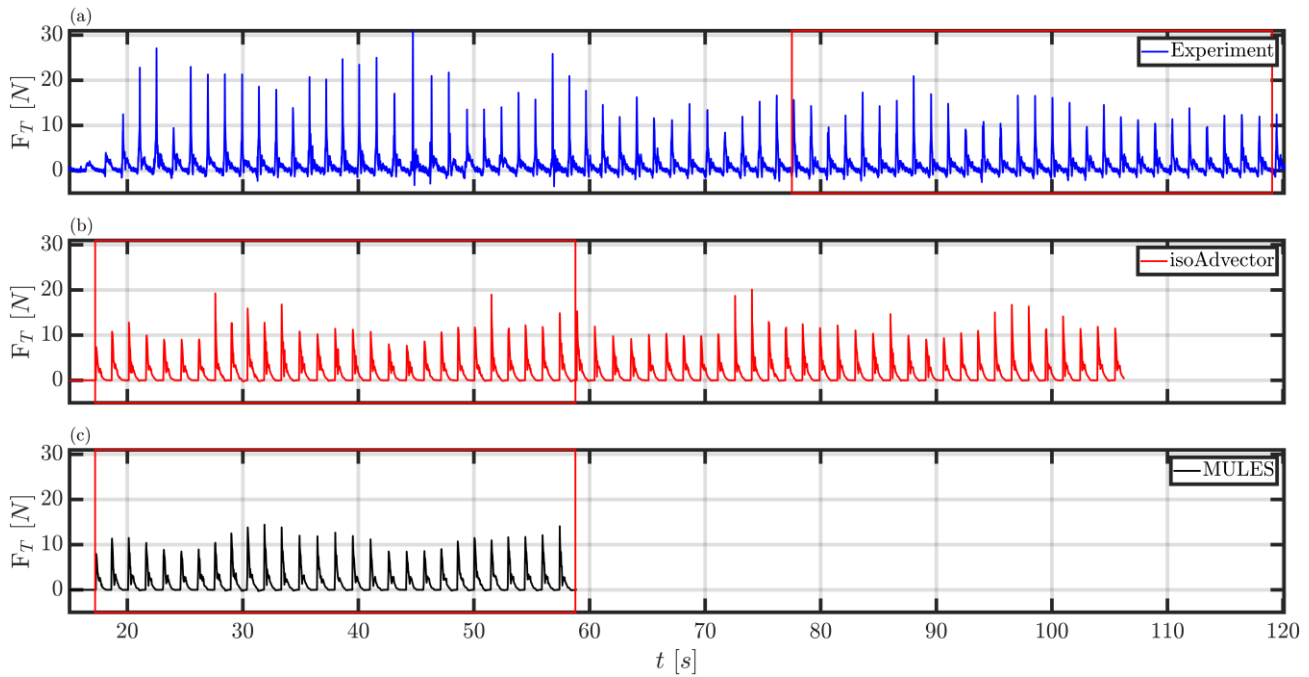


Figure A. 72 Overview of selected data of the total force time series